University of Glasgow

College of Science & Engineering

Fabrication of Plasmonic Nanostructures for Healthcare Applications

By

Iliyana Samardzhieva

Submitted in fulfilment of the requirements for the
Degree of Doctor of Philosophy

School of Engineering
College of Science and Engineering
University of Glasgow

September 2024

Abstract

This thesis investigates high-throughput injection-moulded periodic arrays for high refractive index (RI) sensitivity and biosensing applications. The recent pandemic has underscored the critical need for early sensor diagnosis for effective treatment, emphasizing the importance of accessible and efficient healthcare services. Novel biosensors, especially optical biosensors based on localized surface plasmon resonance (LSPR), are emerging as promising diagnostic tools due to their real-time, cost-effective analytical capabilities.

Despite advances, there is a gap in developing LSPR sensors that combine high sensitivity with low fabrication costs for broad applications. This research aims to address this gap by developing and optimizing LSPR sensors with enhanced sensitivity and practical usability.

The study focuses on the coupling between LSPR and surface plasmon polaritons (SPP) in periodic nanostructures on metal films under normal light incidence. This hybridization model was explored using a double gradient plasmonic array library (DGPAL), systematically transitioning from SPP to hybrid SPP-LSPR and predominantly LSPR properties. Hundreds of nanostructures with varying sizes and periodicities fabricated on a single platform, allowed comprehensive experimental studies of their plasmonic resonance.

Key methods involved advanced nanofabrication techniques, including electron beam lithography (EBL), UV-Nanoimprint Lithography (UV-NIL) and injection moulding, to create high-resolution periodic arrays. Two fabrication approaches were compared: a simplified method using "dot writing" exposure commands and an advanced method using graphic data files for optimized design. The advanced approach, employing the Raith EBPG 5200 system, demonstrated superior quality and precision.

The findings reveal that the DGPAL platform significantly improves RI sensitivity and biomolecular detection capabilities. The nanopillar arrays achieved a sensitivity of 358 nm/RIU, closely matching state-of-the-art values reported in the literature. Sensitivity increased with both diameter and interspacing of the nanostructures, suggesting potential for further optimization.

A severe condition involving organ dysfunction due to an abnormal immune response called sepsis is reliably diagnosed by the levels of IL-6. Early detection is crucial given the high mortality rate and in this context a label-free IL-6 immunosensor was developed and tested, demonstrating real-time detection with high reusability, enhancing both efficiency and affordability.

In conclusion, this research presents a cost-effective, high-performance optical biosensor platform. The developed LSPR sensors offer high sensitivity, ease of use, and low-cost hardware, making them ideal for point-of-care applications and advancing healthcare diagnostics, thereby enhancing global health outcomes.

Table of Contents

List of Figures

List of Tables

COVID-19 Impact Statement

The progress of this project was significantly affected by the pandemic. As the thesis is experimentally focused, it relies heavily on access to labs and facilities. The initial lockdown and the subsequent restricted access to the JWNC cleanroom facilities and biomedical labs greatly hindered my progress. At the onset of the pandemic, we devised temporary mitigation plans that allowed me to perform some limited experimental work at home and analyse already acquired data. However, the project's milestones, which are directly connected with an industrial partner, were significantly disrupted. Since the facilities reopened with limited access, I utilized the available time on campus as much as possible. Nonetheless, it has been very challenging, if not impossible, to maintain the originally planned pace of work.

Acknowledgement

I would like to begin by thanking my supervisor Prof Nikolaj Gadegaard for his continued professional support throughout this process. It has been a pleasure working with you, and I appreciate the opportunity. Your advice and guidance over the years have been instrumental in shaping my mindset into that of an independent researcher, capable of sharp and critical evaluation. Above all, thank you for selecting me for this project, which has profoundly changed my life and revealed to me the beauty of interdisciplinary research.

I would also like to express my sincere thanks to Prof. Steven Beaumont, my second supervisor, for his valuable input and guidance within the NWCAM collaboration.

I am also extremely grateful for all the talented researchers I worked with within the BIG group. Special thanks to Dr Johnny Stormonth-Darling for introducing me to the project and dedicating so much time to training me. Dr Marie Cutiongco and Dr Eline Huethorst, your care and exemplary professionalism have been inspirational. I would like to thank also Dr Ramesh Ghosh with whom I have had the pleasure to work on and my fellow PhD students in the group – Pedro Duarte Carvalhal Calhau De Menezes, Soren Hecht and Dr Nghia Huynh. It was a pleasure to share this journey with you, learning and supporting each other despite our fundamentally different projects. And, of course, sharing a box of chips at lunch was always a delight!

A special thanks also goes to the JWNC staff for all their hard work and support. The work outlined in this thesis would not have been possible without them. I am particularly grateful for the invaluable patience and assistance from Dr Paul Reynolds and Dr Stephen Thoms.

I am also deeply thankful to Dr Affar Karimullah, who gave me the opportunity to work as a research assistant in his group. It was fantastic collaborating with you, and I appreciate your scientific input and the intriguing projects on plasmonics.

I would also like to acknowledge the MSc students I had the pleasure to supervise during their projects – Anji Galabova, X Cang, Devang Kashikar, Jieyao Zhang, and the lovely Rebecca Bean. Their ambition and passion for research made this experience unforgettable.

A special place in my PhD journey belongs to my dear friend and mentor, Dr Aamir Khan. You taught me that everything in life can be achieved with the right amount of determination, concentration, and training. Thank you for every lesson, for breaking the barriers of my own limitations, and for believing in me.

Finally, I would like to thank my family back in the Bulgaria for the support they have given me throughout my PhD (and their patience with me). Being so far away and having the opportunity to visit home probably only for a few days in a year has been a challenge. But you've always been there for me, supporting each decision and believing in my eventual success. Lastly, a special thanks to my husband, Kosta, for bearing with all my tempers at home and encouraging me to keep going.

Dedication

This thesis is dedicated to my parents and my brother. Without their endless love and encouragement, I would never been able to complete my studies. I love you all and I appreciate your kindness and compassion, and everything you sacrificed to support my academic journey.

'In loving memory of my dear mother, Gergina Petkova, with boundless love and eternal gratitude'

(1957 – 2024)

Author's Declaration

'I declare that, except where explicit reference is made to the contribution of others, this thesis is the result of my own work and has not been submitted for any other degree at the University of Glasgow or any other institution.'

Conferences

- University of Glasgow – James Watt Nanofabrication Centre (JWNC) Conference - Innovation Award 2024 – **award winner** - https://www.gla.ac.uk/research/az/jwnc/jwnc-chris-wilkinson-award/headline_1112045_en.html

- Nano-Micro-Lithography Symposium – June 30th, 2021 (on-line presentation) - https://www.genisys-gmbh.com/events-detail/joint-online-symposium-on-direct-write-optical-ion-and-electron-beam-lithography-2021.html

- International Summer School on Nanoscience and Nanotechnologies - NANOSUM 2024 – (University of Tübingen, Germany) - https://nanosum.org/

Posters

- University of Glasgow – James Watt Nanofabrication Centre – (JWNC) Conference – September 20th, 2024 (poster)

- Nano-Micro-Lithography Symposium – November 4th, 2021 (poster) - https://www.genisys-gmbh.com/events-detail/nano-micro-lithography-symposium-november-2021.html

Publications

- O. Guselnikova et al., " Reading and Writing Chirality with a Chiral Plasmonic Nanosponge," (paper submitted for publication)

- S. Wallace *et al.*, "Multiplexed Biosensing of Proteins and Virions with Disposable Plasmonic Assays," *ACS Sensors*, vol. 8, no. 9, pp. 3338-3348, 2023/09/22 2023, doi: 10.1021/acssensors.2c02238.

- Iliyana Samardzhieva and Ramesh Ghosh. Investigating Refractive Index Sensing and Metal-enhanced Fluorescence Using a Plasmonic Array Library. (NWCAM Conference paper, 2021)

- Convery, N., Samardzhieva, I., Stormonth-Darling, J.M., Harrison, S., Sullivan, G.J. and Gadegaard, N. (2021), 3D Printed Tooling for Injection Molded Microfluidics. Macromol. Mater. Eng., 306: 2100464. https://doi.org/10.1002/mame.202100464

Definitions/Abbreviations

SDG - Sustainable Development Goals

POC - Point-Of-Care

OOAC - Organ-On-A-Chip

MPS - Microphysiological System

AI - Artificial Intelligence

EDC - Endocrine Disrupting Chemicals

IUPAC - International Union of Pure and Applied Chemistry

GOD - glucose oxidase

Abs – Antibodies

NAs - Nucleic Acids

LNAs - Locked Nas

SPR - Surface Plasmon Resonance

LSPR – Localized Surface Plasmon Resonance

SERS - Surface-Enhanced Raman Scattering

EM – Electromagnetic

PSPP – Propagating Surface Plasmon Polaritons

ATR - Attenuated Total Reflection

NPs – Nanoparticles

RA - Rayleigh Anomaly

GMR - Guided Mode Resonances

SLR - surface lattice resonances

m/C PhCs - metallic/colloidal Photonic slabs

S – Sensitivity

RI – Refractive Index

RIU – Refractive Index Unit

FWHM – Full Width Half Maximum

NIL – Nanoimprint Lithography

UV-NIL – Ultraviolet Nanoimprint Lithography

EBL – Electron Beam Lithography

DGPAL - Double Gradient Plasmonic Array Library

CAD – Computer Aided Design

GDS - Graphic Data System

CD - Critical Dimension

VRU – Variable Resolution Unit

FF – Fill Factor

BELLE - Beamwriter Exposure Layout for Lithographic Engineers

CNST - Centre for Nanoscale Science and Technology

GUI - Graphical User Interface

PEC – Proximity Effect Correction

PSF - Point Spread Function

SR - Short-Range

LR - Long-Range

MFS - Minimum Figure Size

IPA - Isopropyl Alcohol

RO - Reverse Osmosis

MIBK - Methyl Isobutyl Ketone

PMMA - Polymethyl-Methacrylate

MW - Molecular Weight

RIE - Reactive Ion Etching

RF -Radiofrequency

PPE - Personal Protective Equipment

PET - Polyethylene Terephthalate

SEM - Scanning Electron Microscopy

BSS - Beam Step Size

ASL - Anti-Sticking Layer

PDMS – Polydimethylsiloxane

EBR – Edge Bead Removal

PGMEA - Propylene Glycol Monomethyl Ether Acetate

WEC - Wedge Error Compensation

PS – Polystyrene

AFM - Atomic Force Microscopy

T – Transmission

A – Absorbance

NIR - Near-Infrared

BW-SPP – Bloch-wave Surface Plasmon Polariton

Γp - Drude damping factor

FOM - Figure of Merit

EOT - Extraordinary Optical Transmission

SEOT – Surface enhanced Extraordinary Optical Transmission

TM – Transverse Magnetic

WA - Wood's Anomaly

RWA – Rayleigh-Wood's Anomaly

FEA - Finite Element Analysis

E – Extinction

TE – Transverse Electric

PML - Perfectly Matched Layer

ROI - Region of Interest

SAMs - Self-Assembled Monolayers

RU - Response Units

RIS - Refractive Index Sensitivity

SA - Streptavidin

BREs – Biorecognition Elements

LOD - Limit of Detection

MTL - Mass Transport Limitation

MAb - Monoclonal Antibody

IL-6 - Interleukin-6

IL6-R - Interleukin-6 receptor

MEF - Metal-Enhanced Fluorescence

TCSPC - time-correlated single photon counting

Chapter 1 Introduction

1.1 Introduction and background

1.1.1 Motivation - Biosensing for healthcare applications

There is a tremendous demand in medical diagnosis and early disease detection to improve health care. Countless people, particularly those with social disadvantages and marginalized and vulnerable populations, face steep economic, environmental, and social barriers to healthy living on a daily basis. Ensuring good health and well-being aligns with one of the Sustainable Development Goals (SDGs) set by the United Nations, which member states are mandated to implement over the next 15 years. SDG3 specifically targets the promotion of healthy lives and well-being for individuals across all age groups. This underscores the importance of accessible and effective healthcare services, including **robust diagnostic capabilities**, to achieve the overarching goal of enhancing global health outcomes.

Additionally, another objective within SDG3 is to provide **support for research and development initiatives focused on vaccines and medicines**, further emphasizing the commitment to advancing healthcare and medical innovation.

Furthermore, human health relies on ecosystem health. Preserving and improving ecosystems can serve as a sustainable strategy for effectively managing vector-borne diseases, while the conservation of biodiversity ensures the continued availability of natural resources for traditional and modern medicinal purposes. The multidimensional scope of the SDGs has emphasized the goal of substantially reducing the number of deaths and illnesses caused by exposure to hazardous chemicals, as well as pollution and contamination of air, water, and soil, by the year 2030. This is highlighting the need for implementing **robust monitoring systems to track environmental pollution and contaminants**.

All three objectives within the SDG3 goal highlighted above can benefit from the variety of novel biosensors providing portable, in-situ application, in real-time as cost-effective analytical tools. Moreover, they boast several additional benefits, including remarkably low detection limits, high stability, reduced reagent volumes, rapid detection times, with user-friendly applicability.

Novel biosensors are essential as diagnostic tools for analysing patient samples, such as blood, saliva, and urine in non-laboratory settings, and real-time patient data. These sensors can greatly enhance the capabilities of primary care physicians, nurses, pharmacists, and other health care practitioners, as well as patients, to rapidly determine and deliver the appropriate treatments and prevention strategies. The implementation of these smart devices holds the potential to save lives, aid in controlling bacterial and viral outbreaks, and reduce healthcare costs. Looking ahead, the near future will witness the development of diagnostic systems, particularly point-of-care (POC) technologies, involving portable devices for medical examination during consultations.

Additionally, drug development and vaccines are revolutionised by harnessing the potential of organ-on-a-chip (OOAC) technologies for disease modelling and drug efficacy. OOAC or microphysiological system (MPS) is a microfabricated device which facilitates the development of 3D tissue-engineered architectures considered to authentically mimic physiologically relevant conditions and functionalities of human native organs. This advanced technological innovation, holding the promising potential of filling the large gap between in vitro and in vivo conditions can transform biological research, drug and vaccine development trials, and precision medicine models. Sensor integrated technologies on OOAC platforms can provide critical feedback information and end point measurements during the workflow. This would avoid variations between replicates, decrease cost and time-consuming labour, and sophisticated monitoring tools providing spatially and temporally resolved read-outs about cell physiology and microenvironment can be obtained without sacrificing samples at specific time points throughout the duration of a study. Future monitoring perspectives are considered, implementing multiplex sensing achieved by the fusion of state-of-the-art sensors and artificial intelligence (AI) data science technologies generating meaning from data one step further.

Detection and monitoring of pollutants in the environment is crucial for assessing the harmful effects of potential toxicants to people, flora, and fauna. High performing biosensors are robust in both specific and total responses to environmental pollutants achieving on-site monitoring. Different types of biosensors were successfully applied for specific detection of heavy metals,

industrial, chemicals, detergents, antibiotics, and organic pollutants such as endocrine disrupting chemicals (EDCs) originating from different industrial, household, and agricultural activities. In this context, biosensors can actively contribute wider to the SDG framework and find implementation also in SDG6: clean water and sanitation, SDG12: responsible consumption and production, SDG13: climate action, SDG14: life below water and SDG15: life on land. Biosensing technologies provide the durability, sensitivity, and rationale for on-site environmental analysis as groundwater surveillance, monitoring soil extracts, agricultural run-offs, waste stream effluents.

Recognizing the growing call for sustainable future, highlights the reliable application of biosensor for achieving SDGs initiative (Figure 1.1).

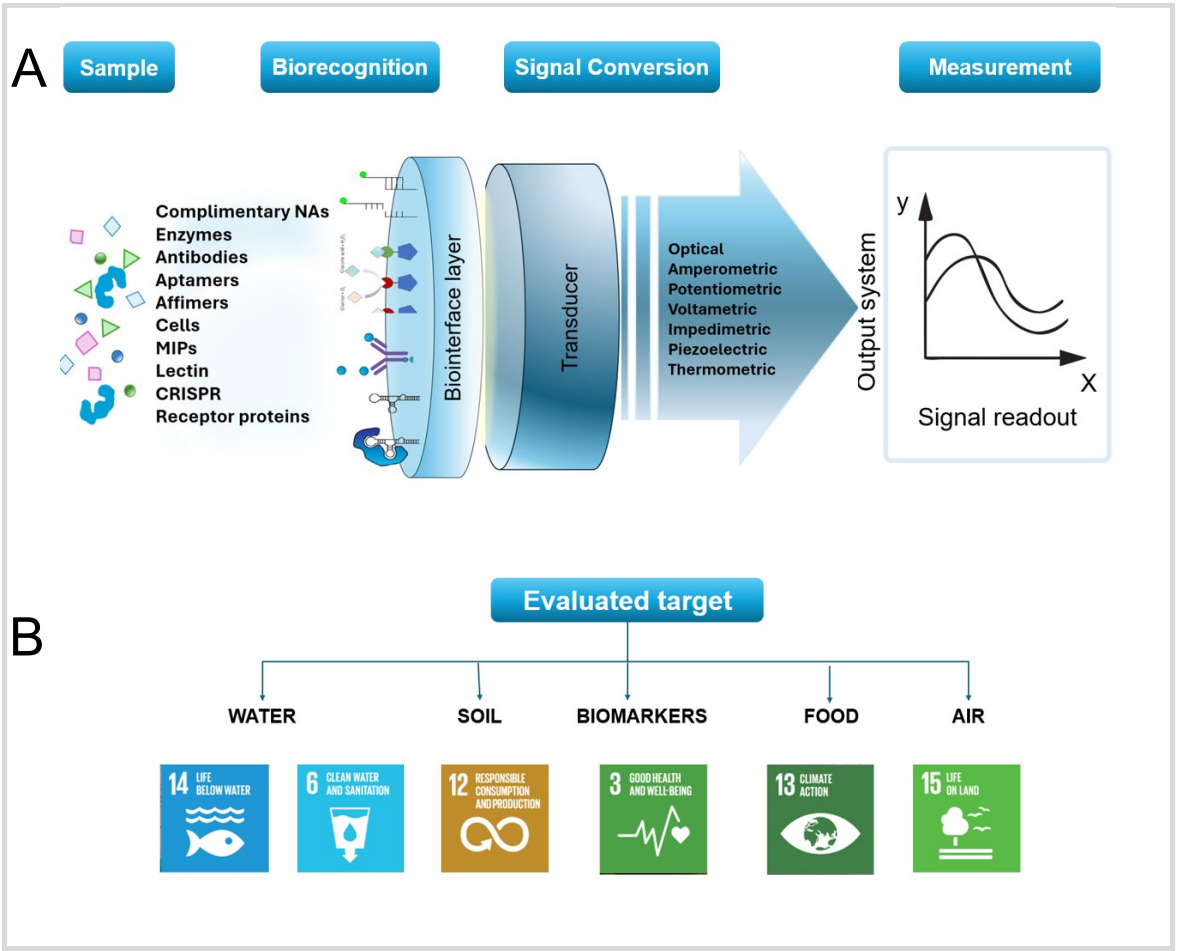

Figure 1.1 Plot A - Diagram depicting the structure of a biosensor and its principle of action. The diagram is also presenting the diversity of biosensor configurations based on variety of biorecognition elements and types of transducer component. Plot B – illustrate the extensive array of applications that biosensors can serve, reflecting the diverse range of targets they can evaluate. It is evident that biosensors play a crucial role in expediting the implementation of the SDGs framework, given their versatility and adaptability across multiple domains.

1.1.2 Types of biosensors

1.1.2.1 Definition

At the beginning of the evolving concept of a biosensor, many authors considered it as an analytical device that detect concentration of chemical species in biological samples, without regard of the role of biologically active recognition material involved in the process. This misconception of the term enabled chemical sensors with biochemical recognition system to be interchangeably named as biosensor. Chemical sensors are measurement devices that convert a chemical or physical property of a specific analyte (mass, volume, density, solubility, colour, acidity, etc.) into a measurable signal, whose magnitude is proportional to the concentration of the analyte [1]. This obviously caused confusion in the use of the term, but the problem was addressed by the International Union of Pure and Applied Chemistry (IUPAC) which framed recommendations of the definition. According to the document the definition of a biosensor is as follows: “a self-contained integrated device, which is capable of providing specific quantitative or semi-quantitative analytical information using a biological recognition element (biochemical receptor) retained in direct spatial contact with an electrochemical transduction element” (Figure 1.1A) [2]. The preposition bio- in the principle of a biosensor employs a biological recognition process of the particular analyte [3].

1.1.2.2 Classification

Biosensors being an integrated receptor-transducer device, which can convert a biological response into an electrical signal are classified according to the type of their biological or alternatively their transducer component.

- Classification of Biosensors Based on Bioreceptors

Bioreceptors are considered as the primary component in biosensor construction. According to the biorecognition principle, biosensors are classified as catalytic biosensors and affinity or non-catalytic biosensors. The left hand side of Figure 1.2 is illustrating the variety of biorecognition elements that could be implemented on the sensor surface.

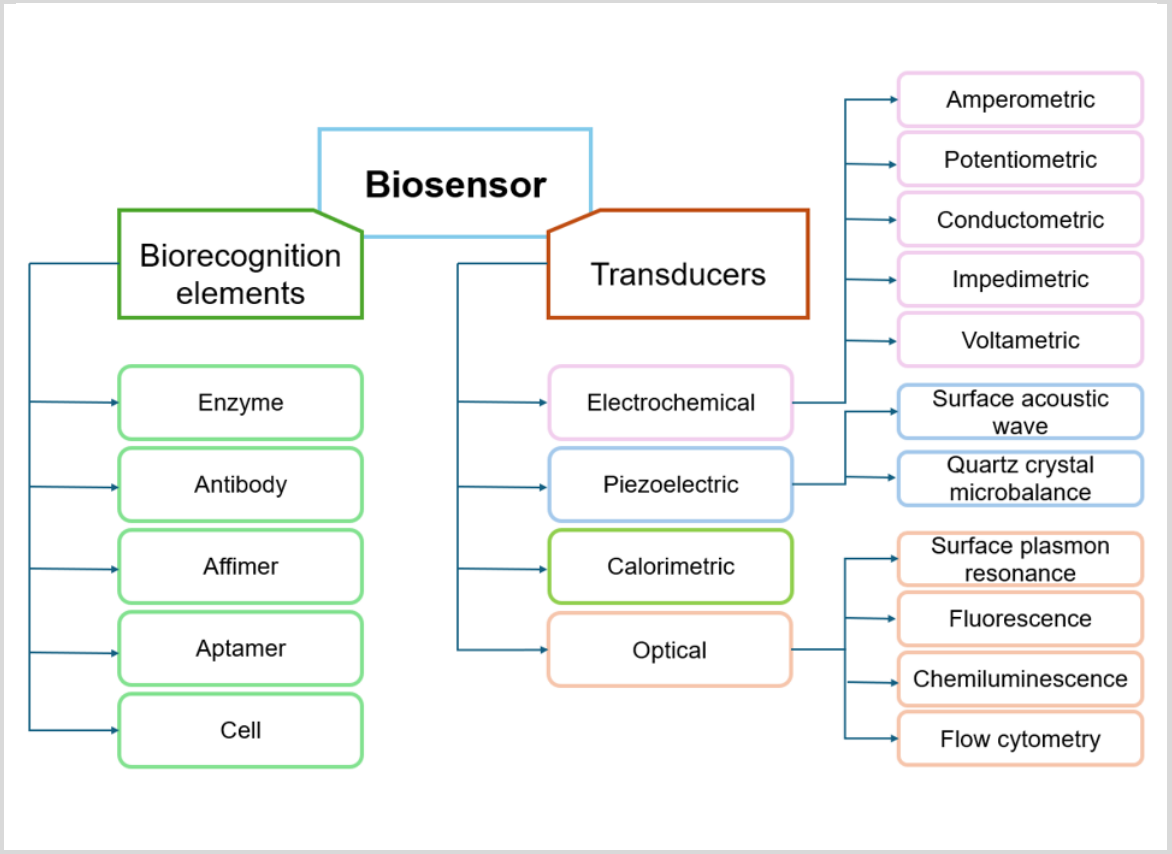

Figure 1.2 Classification of sensors based on biorecognition elements immobilized on the transducer component and signal conversion.

The biocatalytic-based biosensors are the best-known and most studied, and there are three commonly used biocatalysts – enzymes, whole cells, and tissue with enzymatic properties [2]. Historically the first molecular recognition elements implemented in biosensors are enzymes as they are known to catalyse more than 5000 biochemical reaction types [4]. They are highly specific proteins that accelerate a particular reaction where the substrate is converted into a product without being consumed in the process [5]. The integrity of the native enzyme structure provides the biosensor with the ability to detect much lower limits of the interrogated analyte [6]. The first glucose biosensor, proposed by Clark and Lyons in 1962, involved immobilised enzyme recognition element namely the glucose oxidase (GOD) on the surface of an oxygen electrode. The metabolic reaction suggests that from the reduced concentration of oxygen, it is possible to correlate and measure glucose quantity in blood.

The conferring mechanism of affinity-based biosensors is based on the highly specific interaction of the target analyte with the biorecognition receptor as they

form a complex [2]. Thus, biorecognition receptors in affinity-based biosensors are also known as biocomplexing elements and these are either macromolecules like antibodies or organised molecular assemblies such as nucleic acids. Their origin can be from their original biological environment or engineered [7].

Antibodies (Abs), specifically the IgG type are 150 kDa and 15 nm in length, are the most commonly used binding proteins [8]. Because of the strong binding forces between these biomolecules, immunosensors present high selectivity and very high sensitivity, making them very attractive for many applications in different science fields. The way in which an antigen and its antigen-specific antibody interact may be understood as analogous to a lock and key fit, by which specific geometrical configurations of a unique key enable it to open a lock. In the same way, an antigen-specific antibody “fits” its unique antigen in a highly specific manner. They are being able to detect an analyte even in the presence of other interfering substances. This unique property of antibodies is the key to their usefulness in immunosensors where only the specific analyte of interest, the antigen, fits into the antibody binding site. Antibodies have varying stringency of binding depending on their clonality. Monoclonal Abs are highly specific to a single epitope whereas polyclonal Abs are highly sensitive but less specific since they can recognise different epitopes of the same target subjecting them to cross-reactivity [9]. However, Ab production is generally expensive, relies upon the use of animals and mammalian cell culture, while for clinical applications they must be engineered as humanised versions. Nevertheless, the high selectivity and high sensitivity of an antigen-antibody immunoreaction represents the gold standard in biosensors [10].

Protein engineering has been exploited to develop alternative non-antibody binding proteins which mimic the molecular recognition properties of antibodies but with some improved properties. Affimer reagents are small non-antibody binding proteins, with a molecular mass (12 kDa) ~10 times smaller than antibodies. Nanobodies are similarly sized (12–14 kDa and less than 4 nm in length) antigen-binding proteins derived from the variable antigen-binding domains of heavy chain only antibodies [11]. Affimers and nanobodies are both examples of small probes that are becoming increasingly widely used in diagnostics. Characteristics that make them irreplaceable is their excellent stability and

straightforward labelling for downstream applications and affinities typically in the nanomolar range [11].

Nucleic Acids (NAs) are macromolecules that store genetic information and NA research continues to receive enormous attention from scientists since they are associated with various genetic diseases and cancer. The organisation of NAs structure and specifically the complementary binding motif of double stranded molecules makes them appropriate for the purposes of biorecognition components in a biosensor [12]. The nitrogenous bases adenosine and thymine as well as cytosine and guanosine in DNA are in unique complementary relationship and enables a DNA fragment to achieve specificity, capable of detecting trace amounts of the interrogated target [13]. Recent advances in using NA recognition elements include – single-strand DNA, peptide NA, locked NA, G-quadruplexes, aptamers, and DNA zymes [14]. NA probes are biorecognition elements for NA detection based on hybridisation events. Aptamers are synthetic strands of nucleic acid that can be designed to bind amino acids, peptides, proteins, carbohydrates, or live cells [10]. Aptamers poses distinctive binding characteristics. The three-dimensional structure after folding assist aptamers to bind target through hydrogen bonds, electrostatic interactions, pi bond ($\boldsymbol{\pi}$- $\boldsymbol{\pi}$) stacking and variations of the aforementioned [15]. The aptamer sequence can be tailored for the identification of targets spanning heavy metals [16], small molecules [17], proteins [18] and whole cells [19]. Further advantages to their profile are low cost of synthesis, ease of chemical modification, high thermal stability, and high binding affinities [20].

Locked NAs (LNAs) are also with modified structure, analogue of RNA where LNAs become resistant to cleavage by nucleases and more applicable in real samples [21]. G-quadruplexes resemble guanine-rich, single-stranded DNA, which can fold, and form stacked structures. The unique property exploited in biosensing technologies is their ability to bind anionic porphyrins, enabling the detection of metal ions (e.g., K+, Ca2+, Hg2+, Cu2+, Pb2+) [22]. DNAzymes are another class of NA probes characterised by their property to catalytically cut, ligate, and phosphorylate a specific NA substrate depending on a designated cofactor introduced in the process [23].

Cellular structures and organisms serve as a diverse array of bioreceptors employed in the advancement of biosensors and biochips. Typically, microorganism-based biosensors function by assimilating specific chemicals into their metabolic processes. This ingestion of chemical compounds enables the development of class-specific biosensors. Bacteria and fungi, among other microorganisms, serve as indicators of toxicity or for the quantification of specific substances. For example, evaluating cell growth/inhibition, cell viability, substrate uptake, cell respiration and bacterial bioluminescence have been used to evaluate the effects of toxic heavy metals [24, 25].

The measurable parameter generated by the biological recognition process can be optical, electrical, electrochemical, piezoelectric, or other and can serve for quantification. The subsequent section categorizes biosensors according to the diverse types of transducer elements they employ.

- Classification of Biosensors Based on Transducer component

The term transduction is derived from the Latin word “transducere” meaning “to transfer or translate” and in the context of a biosensor the transducer device simply translates information from one kind of system (e.g., immunochemical) to another (e.g., optical) [26]. The definition comprehensively outlines the importance of this component in the design of a biosensor since it is the device that converts biorecognition signal events into measurable physical quantity.

The right hand side of Figure 1.2 is illustrating the variety of transducer components. Regarding the transduction principles, biosensors can be classified as electrochemical, piezoelectric, thermometric/calorimetric and optical. In this work, we will focus exclusively on optical transduction mechanisms, as they are particularly advantageous for healthcare applications involving plasmonic biosensing.

Optical transduction - Optical transduction refers to the induction of change in the phase, frequency, absorption, transmission, reflection, refraction, polarisation, or amplitude of the input light in response to the physical or chemical change produced by the biorecognition process [27]. Research and technological development of optical biosensors has experienced an exponential growth over

the last decade and multiple advanced concepts and highly multidisciplinary approaches are applied in the implementation of new optical biosensors. In this regard a huge number of variations in their construction exist where experts in microelectronics, nanotechnologies, molecular biology, biotechnology and chemistry develop and refine the concept of biosensing [28]. Therefore, optical biosensors are the most diverse class of biosensors because they can be fabricated using surface plasmon resonance (SPR), localised surface plasmon resonance (LSPR), fluorescence, biochemical/luminescence, ellipsometry, surface-enhanced Raman scattering (SERS), and reflectometric interference [29]. The broad diversity of optical biosensors makes their classification based on different parameters but generally they can be divided into two main clusters based on label-free detection and fluorescence detection [30].

1.1.3 Project concept

Among the vast diversity of biosensing techniques discussed above, optical biosensors offer great advantages over conventional analytical techniques. Specifically, plasmon enhanced optical sensors are finding increasing application in detection of analytes in biomedical diagnosis, homeland security, food safety and environmental monitoring [31]. They can be outlined as powerful, simple-to-operate, analytical tools which can fulfil all requirements needed for a robust analytical measurement. A very promising example in this field are the LSPR biosensing platforms, considered as next generation portable plasmonic devices. LSPR-based detection is more easily miniaturised to increase throughput of detection and reduce operational costs as well as more adaptable in terms of biosensor fabrication compared with commercial SPR biosensors and other transducer systems. Reducing the size of the biosensor to the nanoscale can result in a better signal-to-noise ratio as well as the possibility of using smaller sample volumes, thereby reducing assay costs. Plasmonic nanostructures offer the ability to manipulate and control optical fields at the nanoscale with great precision [32]. In addition, the affinity driven biorecognition process can be adapted to label-free detection as well as to be enhanced with fluorescence-based signal transduction, suited for the detection of very low concentrations of bioanalytes since it is one of the most sensitive spectroscopic techniques.

Based on the arguments listed above, the concept for the biosensor design in this research project is based on the optical transduction mechanism for the creation of an LSPR immunosensor allowing protein biomarker detection.

The first stage of the project focuses on the development of a large-scale plasmonic library comprising hundreds of geometric variations on a single chip, enabling the systematic investigation of plasmonic behaviour and the rapid, quantitative detection of biological analytes. The fabrication of these high-resolution periodic arrays is particularly suited for cost-effective mass production through injection moulding—a highly reliable, high-performance technique capable of producing large quantities of uniform devices.

By extracting comprehensive plasmonic data from a single sample, this approach minimizes data variability and enhances the robustness of analytical results. The next phase of research involves leveraging phase-coherent coupling of localized electromagnetic fields and integrating the template-assisted plasmonic array device with a commercially available SPR instrument. This integration aims to facilitate real-time kinetic analysis, enabling the precise study of protein-protein interactions, thus advancing the capabilities of plasmonic biosensing technologies.

Illustrated in Figure 1.3 is an image of the gradient plasmonic device with the size of a standard microscope slide 75 mm x 25 mm (or 3x1 inch) and 1 mm thickness. The nanopatterned area is nearly 2.1 cm^2 encompassing all 400 nanopillar arrays. The dimension of the device makes it compatible with any optical system as most microscopes are equipped with a stage and/or a holder fitting a microscope slide.

The white arrows are indicating the direction of the two orthogonal gradients. Horizontally, from left – to – right, the periodicity in nanoarrays increases while maintaining a constant diameter size. Vertically, from top to bottom, the diameter size increases while maintaining a constant periodicity.

For enhanced visualisation, three white squares for each direction are mapping the locations of the top-view nanopillar SEM inserts, illustrating the double gradient design relationship explained above in a nanoscale format.

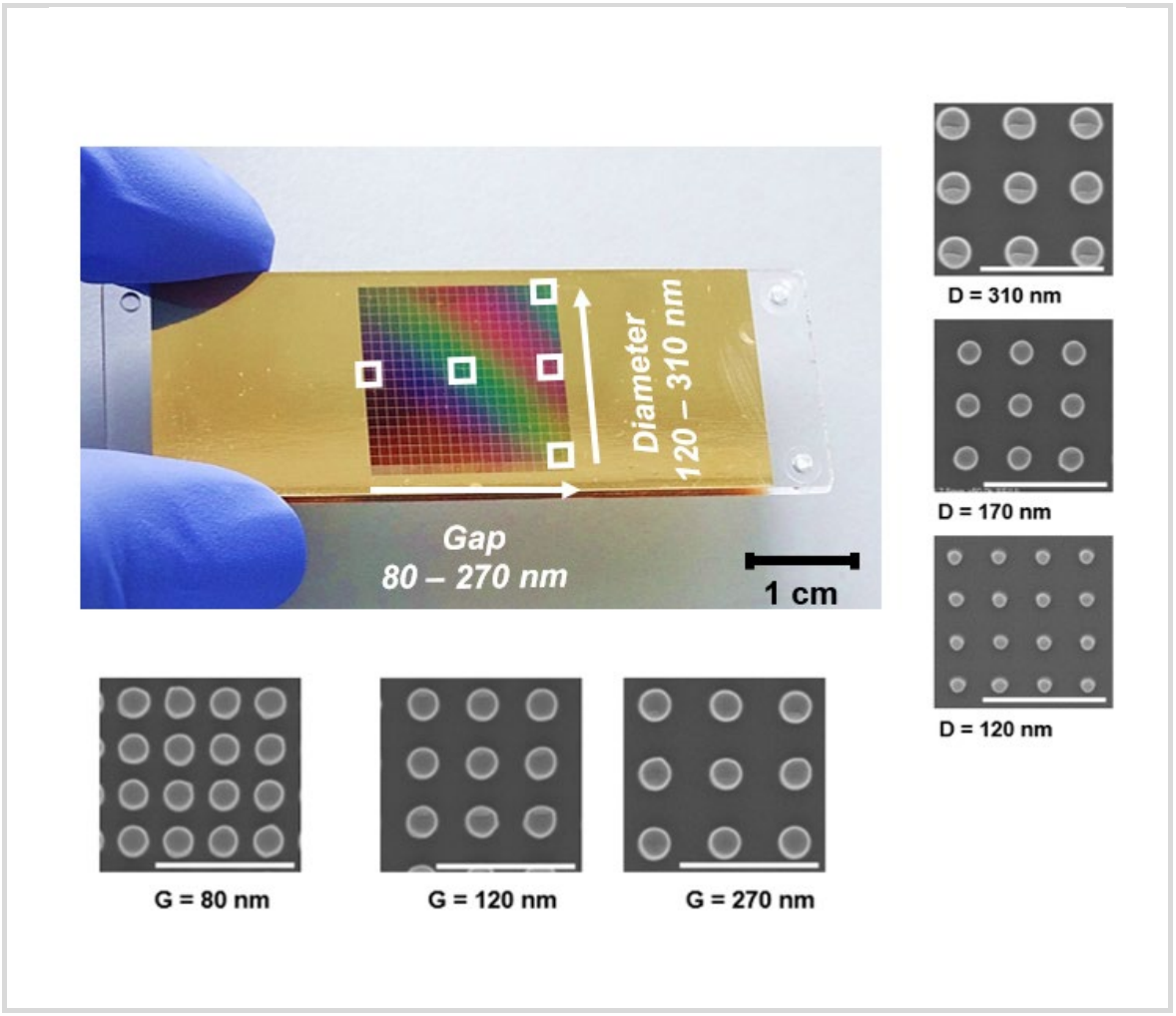

Figure 1.3 Double gradient plasmonic array library (DGPAL) consisting of 400 locations arranged in 20x20 columns and rows enabling the systematic investigation of the flexibility in tunning the optical properties of nanopillar arrays. Scale bar in DGPAL photo is 1 cm, scale bar in SEM inserts is 1 μm.

1.2 Theory

1.2.1 Historical development and Fundamental of plasmonics

Surface Plasmon Resonance (SPR) is a fundamental optical phenomenon that has been widely explored for applications in sensing, spectroscopy, and nanophotonics. SPR has evolved significantly, driven by advances in theoretical understanding, experimental techniques, and technological applications. The integration of SPR sensors in various scientific domains has underscored their importance, particularly in bio-sensing applications where they are used to monitor interactions between biomolecules in real-time. The significance of SPR sensors is highlighted by their ability to provide label-free detection, which is

crucial in maintaining the integrity of biological specimens. This subsection provides an in-depth historical analysis of the key milestones in SPR research, from its discovery to the development of state-of-the-art SPR sensors.

Historically, the development of SPR technology can be traced back to the early 20th century, with major breakthroughs occurring in the latter half of the century. The foundations of SPR begins with the early works of Wood (1902), who observed anomalous diffraction patterns in metallic gratings [33]. These anomalies, later termed as “Wood’s anomalies,” were the first experimental evidence of surface plasmons, though their physical origin was not yet understood. Physical interpretation of the phenomenon was initiated several years later by Lord Rayleigh (1907) who provided a theoretical explanation of Wood’s anomalies [34], further refined by Fano (1941) attributing them to resonance effects involving electromagnetic waves and surface electron oscillations in metallic films [35]. A major breakthrough in the understanding of SPR occurred in the 1950s and 1960s with the work of Ritchie (1957), who formally described the concept of surface plasmons as collective electron oscillations confined to a metal-dielectric interface [36].

The experimental validation of surface plasmons was achieved through innovative optical configurations. In 1968, Otto and in the same year Kretschmann and Raether developed a prism-coupling method that allowed for efficient excitation of surface plasmons [37] [38]. This configuration, known as the Kretschmann-Raether configuration, remains one of the most widely used techniques for SPR excitation in contemporary research and sensor applications. Their work demonstrated that by using a thin metal film coated on a glass prism, surface plasmons could be excited by an incident light wave under total internal reflection conditions. This configuration enabled precise control of plasmonic resonance conditions and paved the way for practical applications of SPR.

By the 1980s, the potential of SPR for sensing applications became evident. Liedberg, Nylander, and Lundström (1983) were among the first to demonstrate SPR as a biosensing platform for detecting biomolecular interactions in real-time [39]. Their pioneering work established SPR as a label-free detection method, allowing for the measurement of molecular binding events at metal surfaces without the need for fluorescent or radioactive labels. This innovation marked the

beginning of SPR-based biosensing, which has since become an indispensable tool in medical diagnostics, environmental monitoring, and pharmaceutical research.

Following its initial application in biosensing, SPR sensor technology experienced rapid advancements. The 1990s saw the commercialization of SPR-based instruments, led by companies such as Biacore [40]. These instruments integrated SPR detection with microfluidic systems, enabling high-throughput analysis of biomolecular interactions with exceptional sensitivity and specificity. Researchers also explored alternative configurations for SPR excitation, including waveguide-based and optical fibre-based SPR sensors, expanding the applicability of SPR beyond traditional prism-based systems.

The optoelectronic phenomenon of SPR was established from studies involving excitation of surface plasmons on nanoscale metallic surfaces, especially noble metals. When metallic surfaces are exposed to light, a photon is trapped near the metallic surface and prompts the electrons to move as a single electrical entity, which is known as surface plasmon (SP) [41]. The electron movements are due to excitation resulting from coupling with a portion of the light energy. The electron movements are called plasmon and the plasmon oscillation in turn generates an electromagnetic field (EM) that exist in two distinct forms [42]. At planar surface e.g. thin metal films is known as propagating surface plasmon polaritons (PSPP). Differently, when a surface plasmon is confined on a nanostructure with dimensions less than the wavelength of an incident light, this unique physical property is highly localized around the nanoparticle, leading to a non-propagating localized surface plasmon with a specific frequency [43]. This novel physical property is not found in their molecular or bulk precursors and has attracted the interest of scientists for generations.

1.2.2 Propagating surface plasmon polaritons

In order to excite PSPPs, energy and momentum conservation should be fulfilled. Excitation of PSPPs by photons is only possible when the wavevector or momentum of incident light is equal to the wavevector of the PSPP [44]. PSPP on a plane interface cannot be excited by light of any frequency that propagates in free space [45]. The reason is that the wavevector of the massless photons is always lower than the large surface plasmon momentum. If the wavevector component of light

is increased above its free-space value and gain extra momentum, coupling conditions would be complied.

The optical excitation can be generated by several ways but conceptually the simplest one is when polarized light passes through a high-reflective index prism - (Kretschmann configuration, discovered in 1971) with a flat metallic film on top [46]. The optical dense medium of the prism increases the photon wavevector and at a certain angle it matches the PSPP wavevector on an (optical less dense) air-metal interface. Prism couplers are used to establish the phase matching between an incident light beam and surface plasmons, relying on the attenuated total reflection method (ATR) [47]. In Kretschmann configuration, the metal film strongly reflects the light except at a specific angle θ when the intensity of the reflected light passes through a minimum (Figure 1.4-A). The photons are absorbed, and the energy is transferred to the free electrons of the metal layer, inducing a wave-like oscillation, or travelling parallel surface charge waves at the interface between the metal and a dielectric material. The absorption of light photons causes a dip in the intensity of reflected light obtained by a detector and the position of the dip in the reflectivity curve can be used as an indicator for biological binding assays [31]. At this precise angle, PSPP excitation conditions are satisfied and thus it is called resonance angle or SPR angle [48].

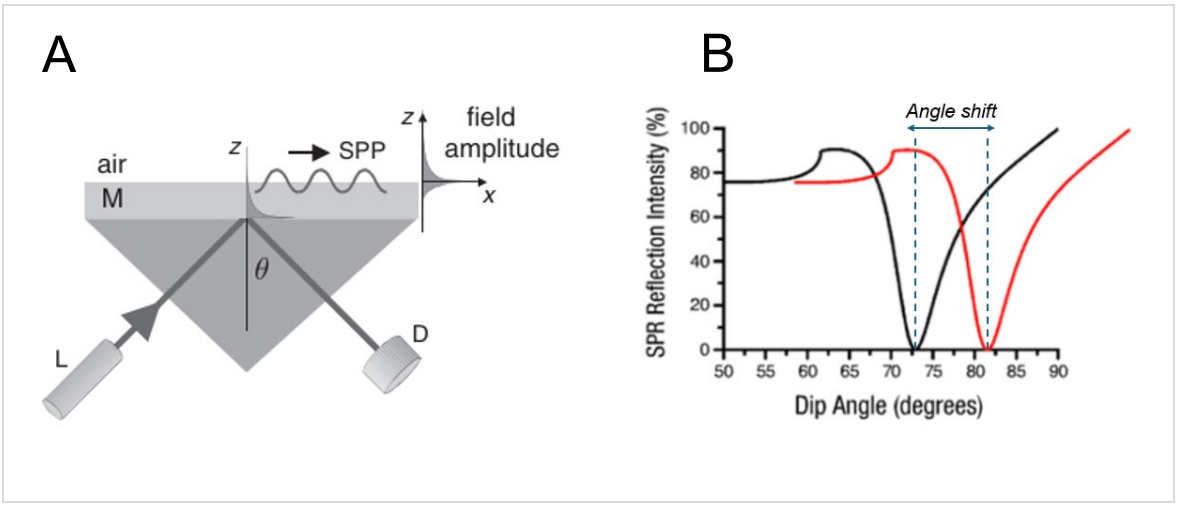

Figure 1.4 Panel A - Excitation of propagating surface plasmons with Kretschmann configuration. L, laser; D, detector; M, metal layer [45]. Panel B - SPR Scanning Angle Response. SPR causes an intensity dip in the reflected light at the sensor surface. A shift in the curve represents molecular binding [49].

For example, in the case of a planar surface, the binding of bio/chemical molecules perturbs the plasmon and leads to a shift of the resonance angle of the incoming photons (Figure 1.4-B). Although these optical phenomena have attracted interest in various fields, their use is most prominent in the field of biosensor development.

The enhancement factor in the Kretschmann configuration can be evaluated by calculating the ratio of EM intensity above the metal and the input light intensity [45]. Typically, the electromagnetic field of an SPPs is distributed in a highly asymmetric fashion and the propagation depths and lengths are with higher values [50]. The evanescent field decay length can extend 100-500 nm from the metal-dielectric interface [51]. This leads to the detection of weakly bound non-specific interactions and convective thermal fluxes with less orientation/conformation-based sensitivity. SPPs are highly sensitive to bulk refractive index changes in solutions [52].

1.2.3 Localized surface plasmon resonance

LSPR occurs when metal nanostructures are significantly smaller than the wavelength of incident light and give rise to strongly enhanced optical near-fields [45]. In this case, the incident electric field will be constant across the nanoparticles (NPs) and will induce a uniform overall displacement of the conducting electrons leading to a strong restoring force from the positively charged ion lattice (Figure 1.5) [31]. As the conduction electrons are with significantly lower mass compared to the ion cores, upon excitation, they move freely producing net positive charge from one side of NPs and net negative charge on the other side – a dipole moment.

Due to those displaced charges, a restoring force (Coulomb attraction) arises responsible for re-establishing the system to its equilibrium state. The restoring force creates a characteristic oscillation frequency in the metal electrons which are spatially confined to the interface of the nanoscale object and hence are defined as localized a phenomenon known as LSPRs.

LSPRs are strongly dependant on the size, shape, structure, and composition of the 3D nanoscale object properties since they all determine the LSPR excitation

wavelength (Figure 1.6) [53]. The latter is mainly governed by the strength of Coulombic restoring force while the damping determines its width [54].

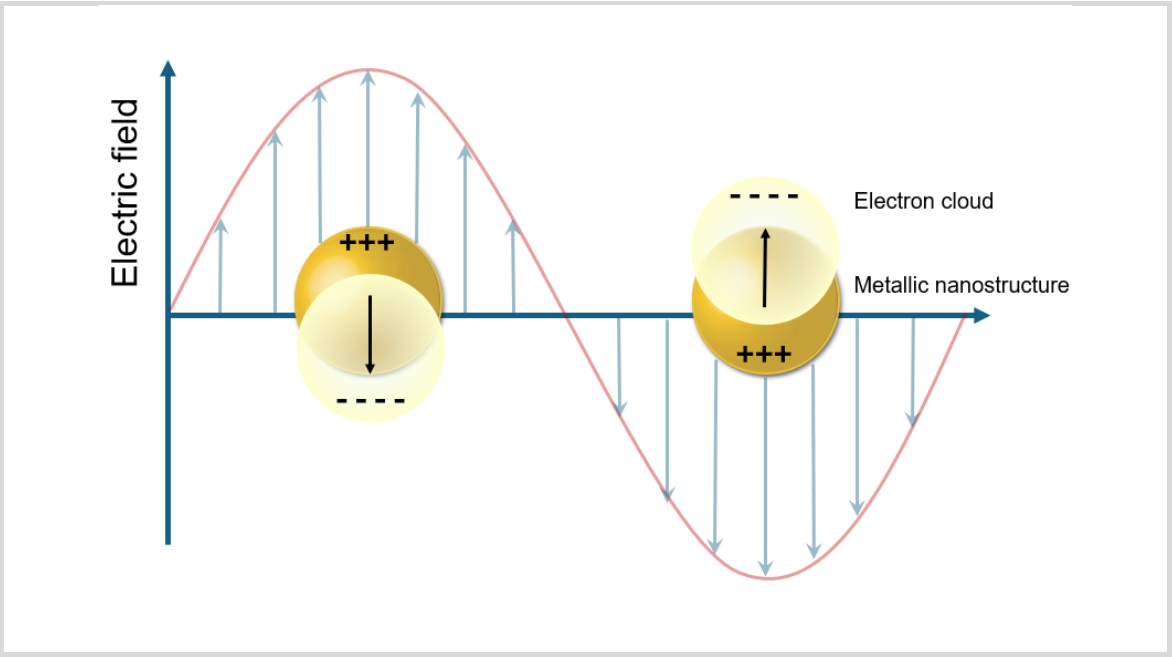

Figure 1.5 Schematic illustration of LSPR for a plasmonic nanosphere. The illustration is depicting the formation of a dipole plasmon mode. When an electromagnetic field is applied, it moves the free electrons in one direction but the restoring forces from positively charged nuclei return the movement to equilibrium position. The momentum makes the electrons oscillate, creating the plasmon resonance – adapted from [55].

The larger the NPs, the weaker the Coulomb attraction for electrons will be and the plasmon resonance red-shifts (Figure 1.6 A).

The energy removed from the incident beam of light creating LSPRs in metal NPs is due to the strong scattering and absorption. The sum of scattering and absorption is known as extinction. In large metal NPs, extinction is dominated by scattering, provided by their larger optical cross sections, and have peaks that broaden significantly and shift towards longer wavelengths (known as red shifting). In small NPs, electron-electron scattering quickly converts the energy of the LSPR into heat, which translates into a strong absorption. By changing the diameter of the NPs, a transition can be observed between the two regimes characterized by a colour change. For instance, small gold NPs absorb green and blue and thus appear in red, where large NPs mostly scatter in the green and appear greenish.

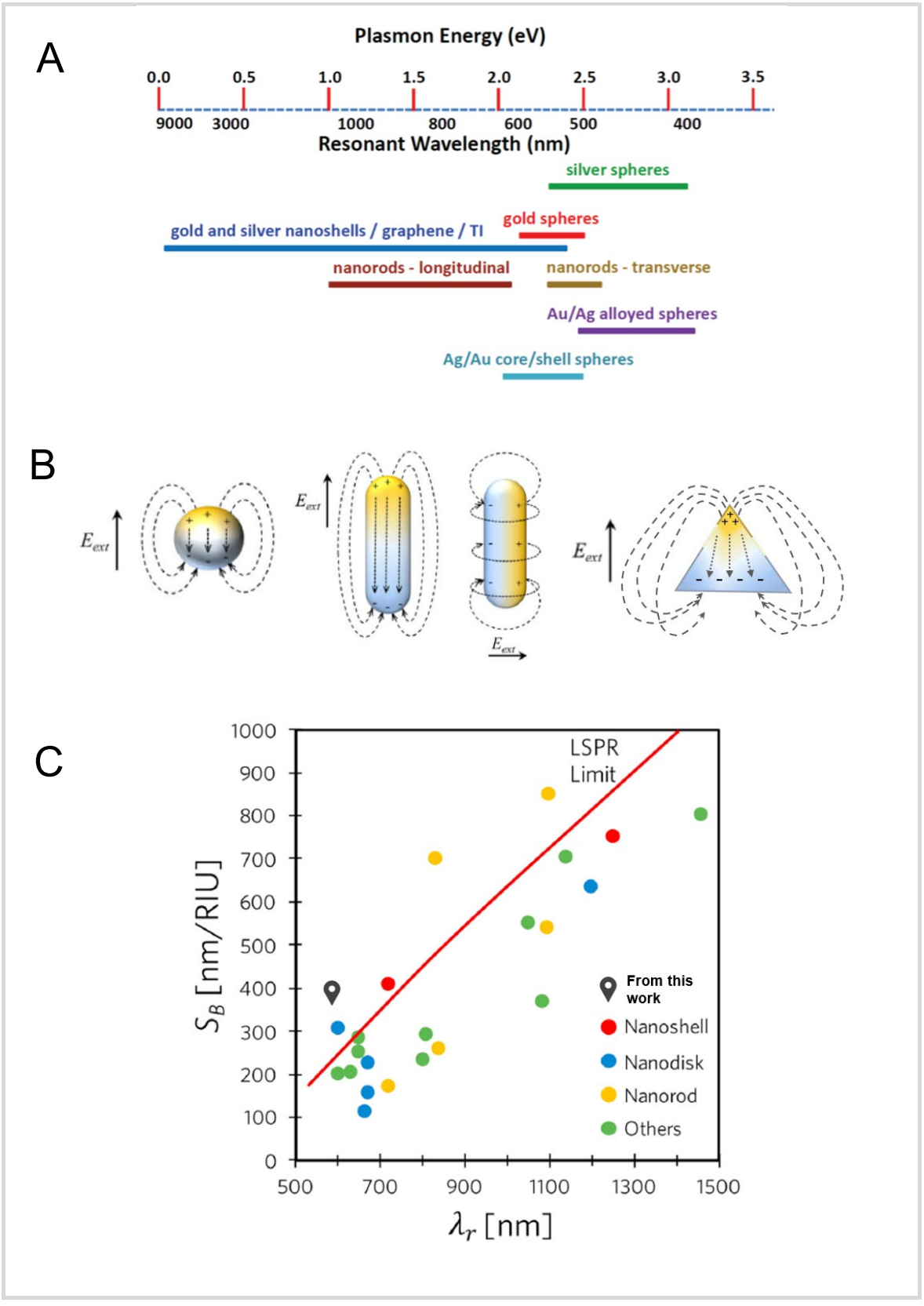

Figure 1.6 Diagram illustrating the strong dependence on the size, shape, structure, and composition of the 3D nanoscale object properties. Plot A – demonstrating how these determine the LSPR excitation wavelength [56]. Plot B – demonstrating how these determine the dipole EM field distribution – adapted from [57]. Plot C - demonstrating how these determine the experimental bulk refractive index sensitivities (S_B) of Au nanostructures. The black marker indicates the (S_B) achieved within this project. The plotted red line represents the theoretically calculated limit S_B for LSPR structures as a function of their resonance wavelength [52].

The dependence of the NP size on the ratio of scattering to the absorption, was simulated with the MNPBEM toolbox [58], where had been observed that absorption contributes significantly if diameter is up to 70-80 nm after which scattering starts to prevail [59]. Plasmonic materials, primarily composed of noble metals, are chosen for their biocompatibility, resistance to corrosion in aqueous environments and oxidation in air, crucial factors for maintaining device sensitivity. Therefore, gold has been specifically chosen as the primary nanostructure composition in this project. Gold possesses a small imaginary dielectric constant and a substantial negative real dielectric constant (with values within the range -20 to -1) implying low loss in the visible and NIR ranges. The real component of the dielectric function, *Re* [ε'], dictates the resonance frequency (wavelength) of electron oscillations, while the imaginary component, *Im* [ε"], characterizes the dephasing and damping (loss) of these oscillations [60]. These conditions imply a relatively high Q-factor for gold, which corelates to efficient light-matter interaction time as well as enhancement of the electric field and sharper resonance signal typically desirable for plasmonic metasurfaces [61].

Additionally, the LSPR frequency of gold lies in the visible and near-infrared (NIR) region of the spectrum [62]. In many biological applications, it is desirable to work in the near-infrared (NIR) region of the spectrum, specifically within the range 650-900 nm, due to the high transmission of proteins, tissue, blood, and water in this window [63].

Extensive research has provided theoretical and experimental evidence of the optical properties of nanoparticles. It is well-known that their plasmon resonance is strongly sensitive to the nanoparticle size, shape, composition, and the dielectric properties of the surrounding medium. Another interesting outcome is that the tunability of the wavelength can be extended to a wider range by altering the structural composition. For example, nanospheres offer a limited resonance wavelengths in the visible region and this can be extended to NIR region with nanoshells. The tunning conditions with this approach are either changing the total nanoshell size or the ratio of the core/shell radius. The optical characteristics can be significantly changed when instead of a nanoparticle, an elongated rod is used. Gold nanorods possess a band at longer wavelengths due to the plasmon oscillation of electrons along the long axis. The corresponding

longitudinal LSPR wavelength can range from about 600 nm to 1200 nm by simply increasing their aspect ratio. However, chemical synthesis of colloidal nanoparticles can be an unreliable process leading to poor reproducibility, lack of uniformity in composition and size in combination with small scale production volumes [64]. Their application for biochemical sensing exploiting the shift of the LSPR upon changing the refractive index (RI) of the surrounding medium is usually over dominated by nanoparticle aggregation and fails to discriminate variations in RI [65]. The uniformity in spatial separation is a major limitation and nanoparticle aggregation in physiological solutions is a of concern because can be observed in the absence of an analyte [31]. The reaction is noticeable with naked eye as cluster formations would cause drastic change in the colour of the colloidal solution [66].

The shape of the particle significantly influences the resonance modes. Spherical structures are extensively studied due to their ability to produce simple optical spectra. However, more complex structures can display intricate spectra with multiple resonances (Figure 1.6 B). For particles elongated in specific directions, such as spheroids and rods, the mode frequencies will have dependence on the polarization direction of the incident field with respect to each principal axis. Nanorods provide two distinct dipolar modes - longitudinal and transversal mode.

The combination of shape and size together give rise to even more intricate interaction. The retardation effect is significantly important for large nanostructures. Theoretically, as the size of the nanoparticle is comparable to the wavelength of light, the nanoparticle is no longer homogeneously polarized by the light due to the electromagnetic retardation, which results in the excitation of higher-order oscillation modes. The emergence of higher oscillation mode peak (quadrupole, octupole etc.) is always located at shorter wavelength relative to the dipolar one [67].

As depicted in Figure 1.6 C, the refractive index sensitivity of nanostructures is also varying. First, the plasmonic composition defines the upper limit of the RI sensitivity independent of the nanostructure shape. The LSPR limit is plotted as a solid red line and it was evaluated with Equation 17 published at Hasan Kurt et al [52]. Secondly, the variations in shapes of gold nanostructures are compared, and the dependence between their resonant wavelength and their sensitivity

performance is analysed. This analysis provides insights into how different geometries influence the optical properties and detection capabilities of the nanostructures, offering a pathway to optimize their design for enhanced biosensing applications.

Both SPR and LSPR structures are attracting platforms in the field of biosensor development due to their strong confinement and enhancement of the electromagnetic field near the surface. This is true because they both cover different sensitivity ranges of the analysed solution and can be adapted to perform accurate surface and bulk assays.

Surface assays are characterised with the detection of molecular binding events (e.g., antigen-antibody interactions), which usually happen at extremely close proximity to the surface of the sensor and disregard the bulk effects. They are highly sensitive and allow for real-time monitoring of biomolecular interactions, making them useful for kinetic studies and label-free detection [68].

However, when characterizing RI variations in solution in the sample medium these are categorized as bulk refractive index assays.

Based on that the sensitivity of the assay can be significantly enhanced when considering the penetration depth of the plasmonic field which determines how far into the sample the sensor can detect refractive index changes.

The typical decay length of SPR thin films is of 100 – 1000 nm, and the LSPR has much shorter decay length of 5- 60 nm. Typically, the electromagnetic field of an SPPs is distributed in a highly asymmetric fashion and the propagation depths and lengths are with higher values [50]. This leads to the detection of weakly bound non-specific interactions and convective thermal fluxes with less orientation/conformation-based sensitivity (Figure 1.7-A). Thus, it is regarded that the SPR structure is more suitable for bulk assays - detecting the refractive index changes within the volume of the solution or for the detection if larger biomolecules and whole-cell pathogen detection [52]. The LSPR with metastructures offers a strongly confined and enhanced electromagnetic field sensitive to changes in the local dielectric environment which is huge advantage when the analyte in question is on the nanoscale, or when refractive index changes occur very close to the nanoparticle surface.

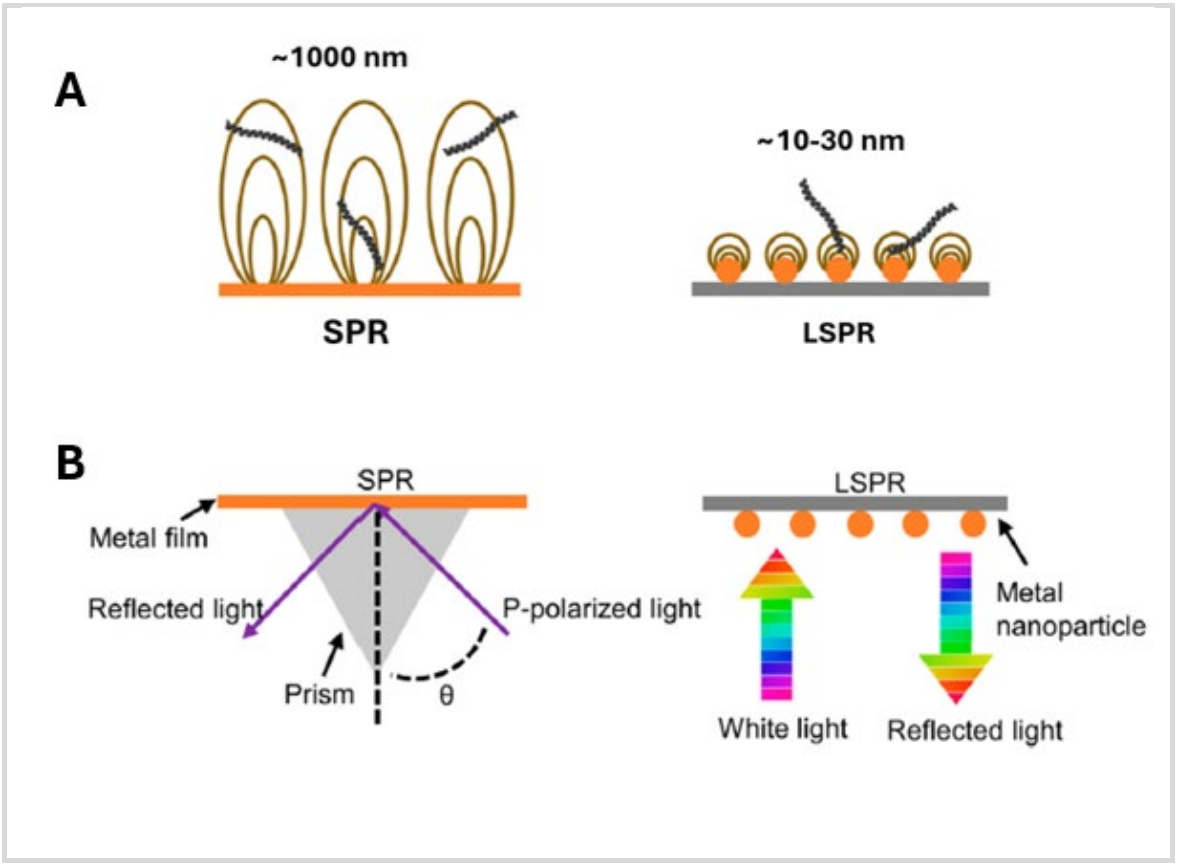

Figure 1.7 A -The perception range in LSPR compared to SPR. The significantly extended evanescent field leads to the detection of weakly bound non-specific interactions B-Differences between adaptive optics in LSPR and SPR. Adapted with permission from [69].

However, despite LSPR has a shorter field decay length, it still senses RI variations beyond immediate molecular interactions at the surface [70]. Thus, LSPR refractive index measurements are also often categorized as bulk assays despite their surface-based sensing mechanism.

For example, in bulk refractive index calibration, LSPR sensors respond to variations in glycerol or sucrose concentration, even if no biomolecules are binding to the nanoparticle surface [71]. While the sensitivity of LSPR arises from near-field interactions at the nanoscale, LSPR-based sensors exhibit both bulk and surface sensitivity. This dual nature means that LSPR-based assays can be optimized for either surface-specific detection (biomolecular interactions) or bulk RI sensitivity (medium composition analysis), making it a hybrid technique with applications in both localized surface sensing and bulk refractometry.

The trend in the design of LSPR sensors is to use hybrid modes, for example, LSPR -SPR, to improve the sensitivity and FOM simultaneously [72]. The strong polarization-dependent sensing performance of the hybrid mode demonstrates higher sensitivity, achieved at longer wavelength resonance.

As mentioned earlier plasmonic nanostructures can exhibit multiple types of resonances, and these may also couple or hybridise with each other. When two or more NPs are in close vicinity, the LSPR of the individual nanostructure interact with via their optical near fields, creating coupled LSPR mode. A useful analogy for understanding the plasmon response of metal-based nanostructures is to compare plasmons to molecular orbitals of atoms. According to molecular orbital theory, atomic orbitals can hybridize with neighbouring atoms to form bonds. Similarly, plasmonic oscillations from metallic particles or structures can hybridize to form new resonances. The introduction of plasmon hybridization (PH) was proposed by Peter Nordlander and colleagues in 2003 predicting the resonant properties of interacting LSPR nanostructures [73]. The PH theory can be applied to identify the possible eigenmodes of two strongly coupled metallic nanorods. Figure 1.8 presents the eigenmodes in a hybridization diagram for two identical nanorods treated as an electrical dipole, where four different eigenmodes are possible.

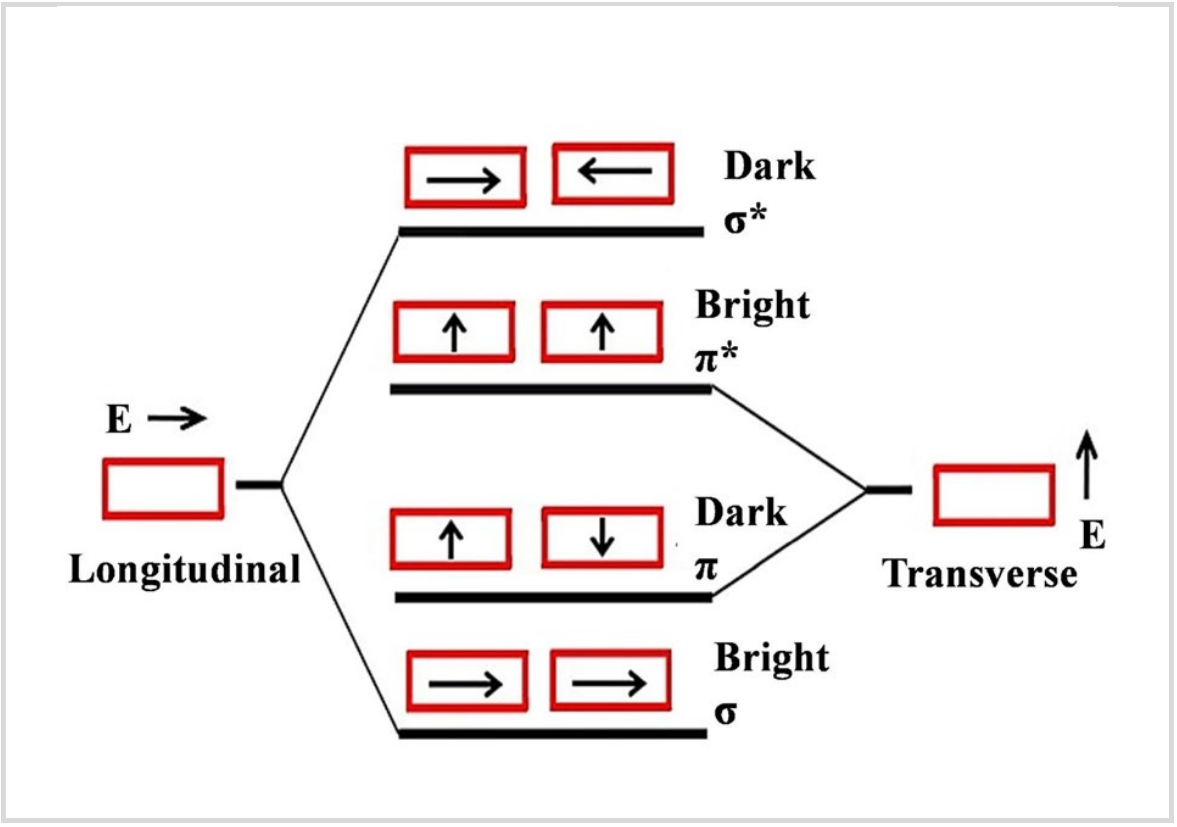

Figure 1.8 Plasmon hybridization diagram for both the longitudinal and the transverse plasmonic modes of nanorods in proximity illuminated with an electromagnetic plane wave [74]. The plasmonic oscillations generate charged regions which can couple with the neighbouring nanorod in a favourable (bonding) interaction or unfavourable (anti-bonding) interaction.

Two of the modes, σ and π*, involve in-phase oscillation of the electric dipoles in both nanorods. These modes are known as symmetric or bright eigenmodes, capable of radiating into the far field and exhibiting super-radiant behaviour. The bonding plasmon mode is formed through a constructive interference of two in phase plasmon states, resulting in reinforcement or the addition of their wave functions. The associated hybridized electric fields are stronger and more localized in the gaps between the particles. The modes, which couple with incident light and scatter, are bright. The other two modes, σ* and π, feature out-of-phase oscillation of the electric dipoles in both nanorods. These are referred to as asymmetric or dark eigenmodes because they cannot radiate into the far field, and their optical response is primarily governed by absorption, thus exhibiting sub-radiant behaviour. The interaction in this case is destructive causing their wave functions to cancel out, resulting in a region of no electron density between plasmon nanoparticles. The lack of electron density is described as node between the plasmon nanoparticles. This renders the antibonding plasmonic mode energy to increase. The symmetric hybridized plasmon occurs at a lower energy level, while the anti-symmetric hybridized plasmon appears at a higher energy level [75]. The resonant frequencies of coupled NPs depend strongly on the interparticle distance and configuration. The strength of plasmon coupling decays exponentially as the gap is increased [76]. At larger separations, hybridization effects disappear, and plasmonic NPs are supposed as non-interacting.

The local electric field enhancement in the gap region is much more significant than the enhancements for individual NRs [77]. The symmetric oscillations are coupled with the external optical fields and have greater RI-sensitivity than asymmetric plasmonic oscillations [78]. Therefore, the study of the plasmon coupling between NRs of different configurations and different metals has great importance.

A metamaterial composed of a periodic array of metallic nanostructures can generate both SPP and LSPR phenomena. This dual resonance capability enhances the material's sensitivity and functionality in various applications, including sensing and photonic devices. Additionally, the interaction between these resonances can lead to unique optical properties, such as enhanced

electromagnetic fields at specific wavelengths, which are critical for the development of advanced plasmonic technologies. Understanding these coupled plasmonic modes through plasmon hybridization mechanism provides a framework for designing metamaterials with tailored optical responses, paving the way for innovations in areas like biosensing, imaging, and telecommunications.

The thin, continuous gold film enables grating-coupled excitation of SPPs under normal incidence, while the gold-coated nanopillars provide the geometrical confinement necessary to support LSPR modes. The SPP response remains relatively stable and is primarily governed by the grating periodicity and the gold-dielectric interface, often coinciding with Rayleigh anomalies (RA) of the underlying continuous gold film and less sensitive to discrete nanostructure dimensions. In contrast, the LSPR peak exhibits a characteristic redshift with changes in nanopillar geometry—specifically variations in diameter and inter-pillar spacing—highlighting its sensitivity to local field confinement and confirming its localized nature.

The excitation of SPPs at the interface between a thin gold film and a dielectric medium is fundamentally determined by the complex dielectric function of gold. Specifically, in the visible region of the spectrum, gold exhibits a negative real part of its dielectric constant, with values that become sufficiently large in magnitude around 550–580 nm to satisfy the phase-matching condition required for SPP excitation [79]. This characteristic wavelength range, corresponds to the condition where the in-plane momentum of photons under total internal reflection matches the momentum of the surface plasmon mode, enabling efficient energy transfer [80] [81].

In the context of nanostructured hybrid platforms, such as gold-coated nanopillar arrays on a continuous gold film, the SPP mode observed at ~550 nm reflects the phase-matching condition imposed by the periodicity of the structure and the refractive index contrast between the gold and the surrounding medium (e.g., water). Unlike localized surface plasmons, this resonance is relatively insensitive to changes in nanopillar geometry, which further supports its attribution to a propagating SPP mode (Chapter 3, Figure 3.9 C-D and Figure 3.10).

LSPR excitation has a much higher field enhancement relative to surface area and much stronger coupling interaction with photons at more specific wavelengths/frequencies. It can be achieved by an incident field of light (Figure

1.7-B) without the need of a coupling prism as the geometry of the NP supplies the additional momentum, making the electron oscillations in phase. LSPR results in an enhancement of fields around the surface of the nanoparticles where field intensity can be between 10-10,000 times greater than the intensity of the incident field. LSPR can provide higher surface sensitivity due to its shorter field decay length of 10-30 nm, making it less sensitive to bulk refractive index changes and convective temperature fluctuations (Figure 1.7-A) [31]. Consequently, LSPR-based biosensing systems can effectively track analytes near their surfaces without interference from distant molecules in the analyte solution. The significantly short evanescent field decay into the surrounding dielectric medium and the lack of requirement for highly complex optics offer a higher potential for miniaturization and multiplex detection.

The SPP-LSPR hybridization results in stronger plasmonic resonance, which exhibit superior electromagnetic field enhancement compared to either resonance alone especially in the near field, which is advantageous for biosensing applications due to improved sensitivity to molecular binding events occurring close to the metal surface [82]. The choice of gold is critical in this context, as its plasmonic response is well-matched to the visible and near-infrared spectrum, and its negative real part of permittivity with relatively low imaginary losses in this range allows efficient coupling and minimal damping [79]. The enhancement is a result of constructive interference between the electric fields of the SPP and LSPR, which is governed by phase matching and plasmon hybridization theory (Chapter 3, Figure 3.9 C-D). This interaction can be viewed analogously to coupled oscillators, where bonding (low energy) and anti-bonding (high energy) hybrid plasmonic modes are formed depending on the phase relation and coupling strength [73].

The amplitude or intensity of the SPP resonance peak is strongly influenced by the thickness of the gold film. As the thickness increases—particularly within the range of 40–80 nm—the optical losses within the gold layer decrease, thereby enhancing both the propagation length and coupling efficiency of SPPs. Thicker continuous films reduce the impact of ohmic losses and minimize grain boundary scattering, resulting in more coherent plasmon propagation and stronger resonance signals [80] [83] (Chapter 3, Figure 3.10). This correlation between gold film thickness and SPP peak amplitude is consistent with previous studies, which have shown that

continuous films thicker than ~50 nm support more efficient plasmon propagation due to reduced ohmic losses and fewer grain boundary disruptions [84]. Specifically, in this study, it was observed that gold films of 60–80 nm provided significantly stronger SPP-related peaks compared to thinner films (e.g., 40 nm), where incomplete film formation and increased surface roughness led to increased damping and broadened spectral features.

The mathematical derivations related to thin-film SPPs, LSPRs in nanoparticles, and surface polaritons on periodically structured surfaces are extensively covered in existing literature. Key references include Novotny et al., 2012 [45], Chandreyee Manas Das et al., 2023 [67], Yao, Kan et al., 2023 [55], and Zayats, Anatoly V., et al., 2005 [48]. Since these mathematical explanations have been thoroughly discussed in numerous papers, they are omitted from this thesis to avoid repetition. This research focuses primarily on the experimental outcomes derived from the SPP/LSPR phenomena, and thus, mathematical equations are not included and will not be utilized throughout the investigation.

1.2.4 Surface-Enhanced Raman Scattering (SERS)

Understanding Surface-Enhanced Raman Scattering (SERS) requires examining how light interacts with both molecules and metal nanostructures—an area explored through the field of plasmonics. SERS is an advanced spectroscopic technique that significantly enhances the Raman signals of molecules adsorbed on metallic nanostructures. This enhancement allows for ultra-sensitive molecular detection, making SERS a powerful tool in analytical chemistry, biomedical diagnostics, environmental sensing, and materials science [85] [86]. Since its discovery in the 1970s, the field of SERS has witnessed remarkable advancements in both theoretical understanding and practical applications, with continuous developments in nanostructured substrates and detection methodologies [87].

When the energy associated with polarization does not interact with molecular vibrations, the scattered photon retains the same frequency and energy as the incident photon, a phenomenon known as Rayleigh scattering (Figure 1.9-B). Conversely, if polarization couples with molecular vibrations, leading to a change in the electronic energy state from its original condition, the frequency and energy

of the scattered photon deviate from those of the incident photon. This process is identified as Raman scattering.

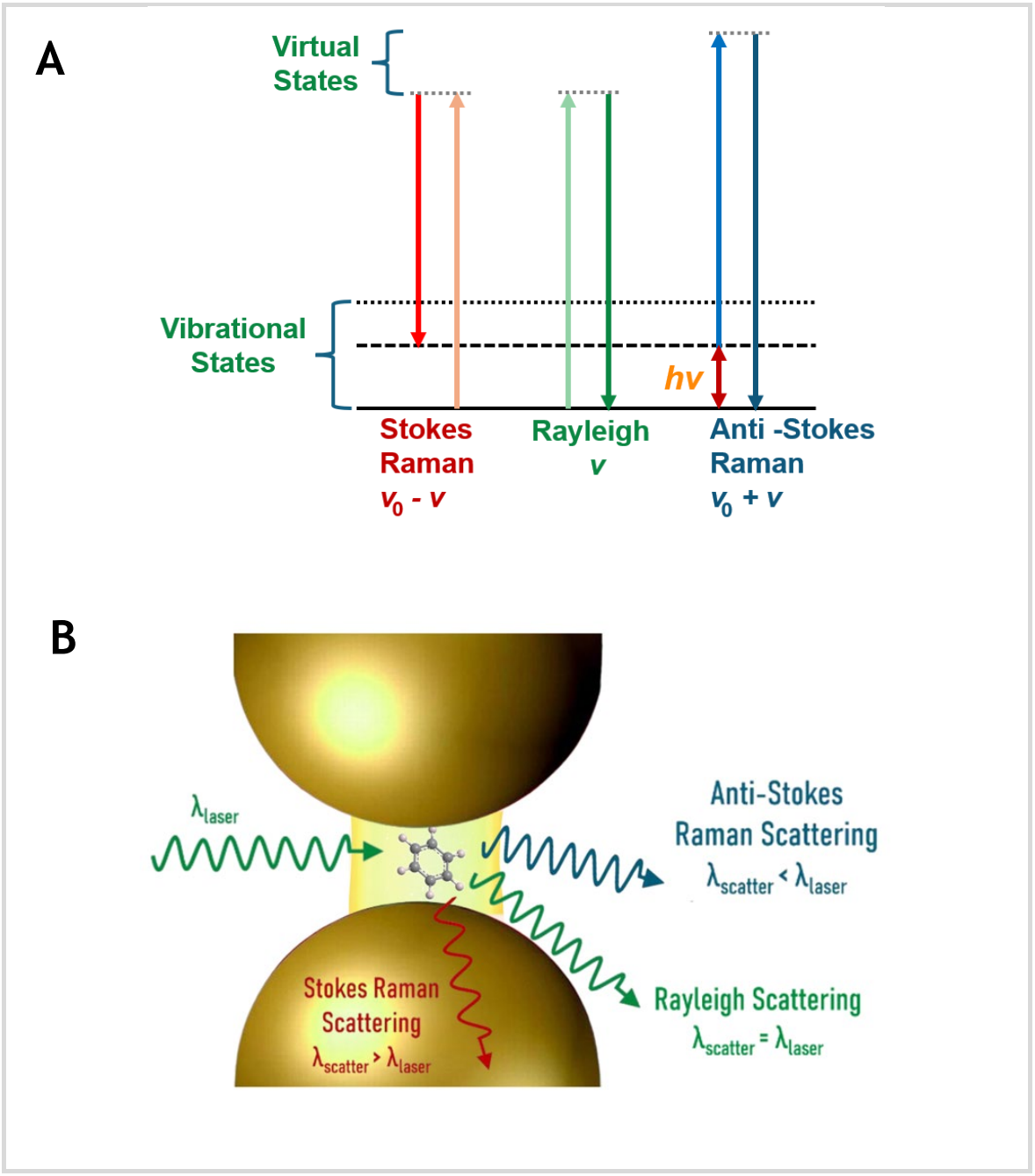

Figure 1.9 A - Energy level change for different scattering: the energy level of Rayleigh scatter remains unchanged; the energy level of Stokes Raman scatter decreases; the energy level of anti-Stokes Raman scatter increases. B - Types of light scattering demonstrated in SERS supported by plasmonically active nanostructures - all three different ways in which light can be re-emitted. Adapted with permission from [88].

Raman scattering is an inelastic scattering process where incident photons interact with molecular vibrations, leading to shifts in the scattered light

frequency, providing a unique spectral fingerprint of the material [89]. The inelastic-scattered photons can either lose (Stokes) or gain (anti-Stokes) energy (Figure 1.9 - A). However, conventional Raman spectroscopy suffers from low signal intensity due to the weak inelastic scattering cross-section.

SERS overcomes this limitation by exploiting the enhancement effects produced by nanostructured metal surfaces, increasing Raman signal intensities by factors as high as 10^11 [90] [91]. This enhancement arises when molecules are placed near metallic nanostructures that support localized surface plasmon resonances (LSPRs), leading to strong electromagnetic field confinement (Figure 1.9 – B) [91].

The development of SERS can be traced through several historical milestones in SERS Research:
The foundation of SERS can be traced back to the Raman effect, first discovered by C.V. Raman in 1928 forming the groundwork for vibrational spectroscopy, allowing molecular fingerprinting based on inelastic scattering of light.
1974 – Initial Observation: Fleischmann et al. (1974) [92] first reported unexpectedly high Raman signals from pyridine adsorbed on a roughened silver electrode. Initially, the enhancement was attributed solely to an increased surface area.
1977 – Theoretical Foundations: Jeanmaire & Van Duyne (1977) [87] and Albrecht & Creighton (1977) [93] independently proposed that the enhancement was not due to surface area alone but resulted from an interaction between the molecule and the metal surface, marking the beginning of theoretical SERS studies.
1985 – Plasmonic Explanation: Moskovits (1985) [90] provided a thorough theoretical framework, attributing SERS enhancement to localized surface plasmon resonances (LSPR) and the strong electromagnetic fields they generate.
1997 – Single-Molecule SERS: Kneipp et al. (1997) [85] and Nie & Emory (1997) [91] independently demonstrated that SERS could be used to detect single molecules, proving the technique's extreme sensitivity and marking a breakthrough in nanoscale spectroscopy.
2000s – Advancements in Nanofabrication: The emergence of lithography and chemical synthesis techniques enabled the reproducible fabrication of highly efficient SERS substrates, improving both sensitivity and reliability [86] [94].

Fundamental Principles of SERS interaction between incident light and surface plasmons in noble metal nanostructures, leading to a massive enhancement of Raman scattering signals. Two primary mechanisms contribute to this enhancement:

Electromagnetic Enhancement

The predominant mechanism behind SERS is electromagnetic enhancement, which arises due to localized surface plasmon resonances (LSPR) in nanostructured metals like gold (Au) and silver (Ag). When the frequency of incident light matches the plasmonic resonance of the nanostructure, a highly confined and amplified electromagnetic field is generated (Figure 1.9). These collective oscillations of conduction electrons generate intense local electromagnetic fields, which amplify the Raman scattering of nearby molecules. Surface of nanoscale roughened or artificial nanoengineered metal surfaces usually made of gold or silver convert the inherently weak Raman scattering to be significantly amplified and thus the name of the phenomenon. The enhancement factor (EF) can reach up to 10^8-10^{11}, enabling the detection of single molecules.

$$EF \approx |E_{local}|E_{incident}|^4$$

where E_{local} is the enhanced electric field near the nanostructure, and $E_{incident}$ is the incident field [95].

At spatial regions, the localized electric field between the particles is maximal compared to the excitation field [96]. These regions where the maximum Raman enhancement between or on the sharp apexes and edges of the plasmonic nanostructures are called hotspots. The LSPR hotspots of the SERS substrate are the core of electromagnetic enhancement. The following step is the energy transfer from the plasmon to the analyte to facilitate the scattering process. The energy is transferred back to the plasmon with a scattering in a new form of wavelength-shifted light (enhanced Raman signals) which is reduced or increased by the amount of the molecular vibrations [97]. The SERS enhancement depends on factors such as the energy of the incident radiation, the electric properties of the metal, the distance of the molecule from the surface, and the orientation of the molecule with respect to the surface [98]. The best SERS enhancement comes from proper pairing of metal and laser. It should be noted that the size of roughness features is important. The laser generates the surface plasmons when it interacts with the metal, and the surface roughness features of the metal affect

the strength of the surface plasmons and the resulting enhancement. If the laser and metal are not properly matched, the signal will be weak, noisy or not produce any enhancement at all.

Chemical Enhancement

A secondary contribution to SERS is the chemical enhancement mechanism, which results from charge transfer interactions between the adsorbed molecule and the metal surface [99].

The charge transfer enhancement is analyte dependent, so the analyte molecules must directly bind to the metal surface. In this case, the charge transfer (electron donor/acceptor) phenomenon occurs when there is electron exchange between the Fermi level of a metal substrate and the lowest unoccupied molecular orbital-highest occupied molecular orbital (LUMO–HOMO levels) of an analyte molecule. The charge transfer can be from metal to analyte molecules or vice versa, depending on their relative energies, and then the de-excitation process is accompanied by releasing Raman photons [100].

While weaker than electromagnetic enhancement, chemical enhancement plays a role in selective molecular detection [101]. This mechanism typically contributes an EF of 10^2-10^4. The performance of SERS is strongly influenced by the substrate used. In the next section the variety of SERS substrates is discussed.

Nanoparticle-Based Substrates

Most metals exhibit plasmonic properties and can therefore be used as SERS substrates. Although Cu-and Al-based nanostructures are cheaper than the other metals, easy oxidation and relatively low enhancement factor are serious disadvantages. Up to date, plasmonic nanostructures based on Au and Ag are most commonly used due to their higher enhancement factors and availability of plasmonic resonances in the visible and NIR regions [98]. Therefore, the plasmon frequencies of these metals are easy to combine with commercial lasers with wavelength at such range can be applied as the excitation source. UV SERS is not widely used in biosensing because the high frequency of UV light can cause damage on biomolecules.

In addition to the specific materials used in analytical SERS, the physical characteristics of the material structures, such as size, shape, type (colloidal, 2D, and 3D), and composition, are also extremely important. The main challenge of the reproducibility of SERS substrates can be mitigated by development in

nanotechnology. Recent advancements have focused on designing nanostructured platforms with high reproducibility, uniformity, and sensitivity.

1. Colloids

Metallic nanoparticles, particularly Au and Ag colloids, have been extensively studied as SERS-active substrates. Their optical properties can be tuned by adjusting size, shape, and aggregation states. For instance, NP clusters enhance SERS signals through plasmonic coupling effects.
The variation in hotspot location and/or density can cause irreproducible results [102]. Colloidal solutions have a significant drawback as the random distribution of nanoparticles prevents the hotspots from even spread.

2. Nanostructured Thin Films and Arrays

Nanostructured thin films and periodic arrays present significant advantages for SERS applications due to their high reproducibility, tunability, and ability to support large-area uniformity [102]. These features enable the fabrication of SERS-active substrates with ultrafine nanoscale structures, contributing to consistent and reliable SERS signal outputs. By precisely engineering the geometrical parameters of the nanostructures, their plasmonic resonance can be finely tuned to match the wavelength of the excitation laser, thereby maximizing the localized electric field enhancement and improving signal intensity.
Typically, these substrates consist of a metallic film rich in electromagnetic hotspots, supported by a rigid backing material. However, this high-resolution fabrication approach often involves complex techniques, slow production rates, and considerable manufacturing costs. As an alternative, highly ordered SERS substrates can also be produced via template-assisted methods, which offer advantages such as lower cost, high reproducibility, scalable throughput, and minimal background signal interference [103].
Compared to colloidal nanoparticle-based systems, rigid SERS substrates not only deliver superior signal stability but also exhibit enhanced sensitivity and reproducibility, making them more suitable for practical and repeatable analytical applications [102] [104].

3. Hybrid and Functionalized Substrates

Hybrid substrates incorporating metal-organic frameworks (MOFs) or graphene have been explored for enhanced sensitivity and selectivity. Functionalization of SERS substrates with biorecognition elements (e.g., antibodies, aptamers) further improves molecular specificity.

Another promising advancement is the integration of SERS with ultrafast techniques like femtosecond stimulated Raman spectroscopy (FSRS) [105]. This fusion allows for the real-time study of ultrafast photochemical reactions and structural dynamics at the molecular level. Recent experiments achieved notable enhancement using engineered SERS nanotags, although the precise mechanisms remain under investigation.

Tip-Enhanced Raman Spectroscopy (TERS) presents a third frontier, enabling nanoscale spatial resolution by localizing the enhancement to a metallic probe tip. While TERS has been applied to diverse samples, including RNA and carbon nanotubes, challenges such as tip reproducibility and spatial resolution remain. Developments in UV-TERS and ultrahigh-vacuum TERS could further expand the technique's applicability to molecular imaging and dynamic reaction monitoring [106].

SERS has undergone remarkable advancements, solidifying its status as a pivotal analytical tool across diverse scientific and industrial fields. Recent significant publications have further expanded its applications and deepened our understanding of its mechanisms. In the biomedical arena, SERS has been instrumental in detecting and mapping cellular biomarkers with high sensitivity, offering rich chemical fingerprint spectra for multiplexed detection.

The fusion of nanotechnology with SERS has catalysed profound advancements. By amplifying Raman signals from molecules adsorbed on metallic nanostructures, or semiconductor metasurfaces, SERS offers unprecedented insights into nanoscale environments and interactions, spurring breakthroughs across various affiliated domains. These structures, designed with materials like titanium oxide (TiO_2), leverage optical bound states in the continuum to achieve ultrahigh electromagnetic field enhancement, significantly boosting Raman signal intensity.

In summary, SERS has emerged as a rapidly evolving and transformative analytical technique, solidifying its role as an essential tool in both scientific research and

industrial applications. Its scope of utilization continues to expand, driven by ongoing advancements. As improvements in sensitivity, selectivity, reproducibility, and spatial-temporal resolution progress, SERS is expected to play an increasingly crucial role in biomedical and clinical fields, facilitating the resolution of critical biological inquiries and addressing life-threatening medical challenges.

1.2.5 Extraordinary Optical Transmission (EOT)

Another phenomenon increasing compression of light into subwavelength structures, finding solution with nanotechnology, is the Extraordinary Optical Transmission (EOT) [107] [108] [109]. This enhancement in transmission of light happens under the condition of opaque metal films comprising regular arrays of plasmonically active shapes [110]. Light does not normally couple to a smooth metal-air interface due to the momentum mismatch. Interaction and mutual excitation of the light and surface plasmons (SPs) requires a photon-plasmon coupling/decoupling interface to overcome the momentum mismatch. A flat metal–dielectric interface already presents transverse magnetic (TM) surface modes, called surface plasmon polaritons (SPP) [111] [83]. However, these SPPs cannot be excited by incident radiation, as it is not possible for this process to simultaneously conserve energy and momentum. The existence of roughness, holes or periodic structure can fulfil this need [112]. In this project, diffractive coupling is made possible with periodic subwavelength corrugations such as the nanopillar arrays.

The existence of a periodic array of nanopillars has two effects: it modifies the characteristics of the surface modes, and it relaxes momentum conservation (which now is only fulfilled up to a vector of the reciprocal lattice), thus allowing the coupling between incident radiation and EM surface modes of the corrugated interface. A conventional diffraction grating requires the grating period to be larger than one-half of an optical wavelength λ ($> \lambda/2$) to ensure the presence of at least one diffraction order [113].

The accepted explanation considered for such anomalous behaviour is that the incident light couples via diffraction (scattering) into surface plasmon polaritons (SPPs) which then propagate across or along the coating through the metallic

nanostructures. Thus, the intense field of SPPs can be changed from nonradiative to radiative, and the resonance mode leads to strong emission of light. As a result of the foregoing, it is now well known that these systems display anomalous transmission and reflection spectra compared to those of a flat metal surface with the same coverage of metal [112].

1.2.6 LSPR sensors

Plasmonic sensors directly utilising shifts in their spectral properties to provide sensing signals can be generally classified as colloidal nanoparticle-based plasmonic sensors and planar 2D chip-based plasmonic sensors with periodic architectures.

1.2.4.1 Colloidal nanoparticle-based plasmonic sensors

Research on colloidal nanoparticles synthesized from noble metals and alloys has revealed that these nanoparticles, available in various shapes, sizes, and structures (including both solid and shell-like configurations), exhibit exceptional LSPR absorption and scattering properties. These properties make them highly effective for sensing applications. The primary mechanism of sensing involves monitoring shifts in the LSPR peak wavelength, which occur when an analyte binds to the surface of the nanoparticle. Additionally, when analytes bring multiple nanoparticles into close proximity, the plasmonic fields of these nanoparticles can couple, leading to a shift in the LSPR peak. This shift often results in a colour change. Colorimetric detection is a simple and facile method for the detection of analytes in a solution because it provides a direct way to visualize the analyte concentration through the colour change that can be easily detected with the naked eye.

Among the various plasmonic nanoparticles, colloidal Au nanoparticles are the most commonly used plasmonic transducer. Functionalized Au nanoparticles have already been used in colorimetric detection of heavy metal ions such as Pb^{2+}, Cd^{2+} and Hg^{2+}, biological small molecules and biomacromolecules [114] [115] [116].

Nanoparticle-based colorimetric sensors are typically operated in a vial, requiring professionals in a laboratory. Real-world samples also need to be pre-treated in a laboratory prior to testing. To solve these problems, nanoparticle-based colorimetric sensors have been incorporated into lateral-flow strips to make a point-of-care device.

Lateral flow assays (LFAs) have become increasingly popular due to their simple operation, rapid results, minimal interference, affordability, and suitability for use by non-specialists. Originally introduced in the late 1960s for monitoring serum proteins, LFAs later evolved into practical diagnostic tools [117]. In 1976, the first laboratory-based LFA was developed for detecting human chorionic gonadotropin (hCG) in urine, utilizing the principle of specific antibody-antigen interactions [118]. Over time, these assays have been extensively applied in various fields, including the detection of cancer biomarkers, pathogens, toxins, heavy metals, and pesticides.

The lateral flow device comprises several key components (Figure 1.10): the sample pad, conjugation pad, test line, and control line, each playing a critical role in the assay process [119]. The sample pad serves as the entry point for the liquid sample, ensuring uniform flow across the device. It often contains buffer salts and surfactants that help optimize sample conditions for efficient migration. When a sample is dropped to the sample pad, the sample moves via capillary force towards the end of LFA strip.

Next, the conjugation pad houses labelled detection molecules, typically antibodies or aptamers conjugated to nanoparticles (e.g., gold or latex beads). When the sample reaches this region, the target analyte binds to the conjugated detection probe, forming a complex that migrates along the strip via capillary action.

The reaction membrane, typically made of nitrocellulose, houses both the test line and the control line, which facilitate antigen-antibody interactions. The test line is coated with immobilized capture molecules specific to the analyte of interest. If the target is present, nanoparticle accumulation at this site produces a visible signal.

The control line, positioned further along the strip, ensures assay validity by capturing excess conjugates, producing a detectable signal regardless of analyte presence. The absence of a control line signal indicates assay failure, making it a crucial quality control measure.

Usually, a positive control antigen is placed on the strip so that it is encountered after the test antigen to confirm that the sample has diffused a sufficient distance to interact with the test antigen. Absorption pad maintains flow of liquid over the membrane and prevents sample backflow. All these components are fixed in a backing card serving as a support.

The ability to visually interpret the test outcome is what defines the lateral flow assay as an immunochromatographic assay, a term derived from the combination of immunological recognition and chromatographic separation principles.

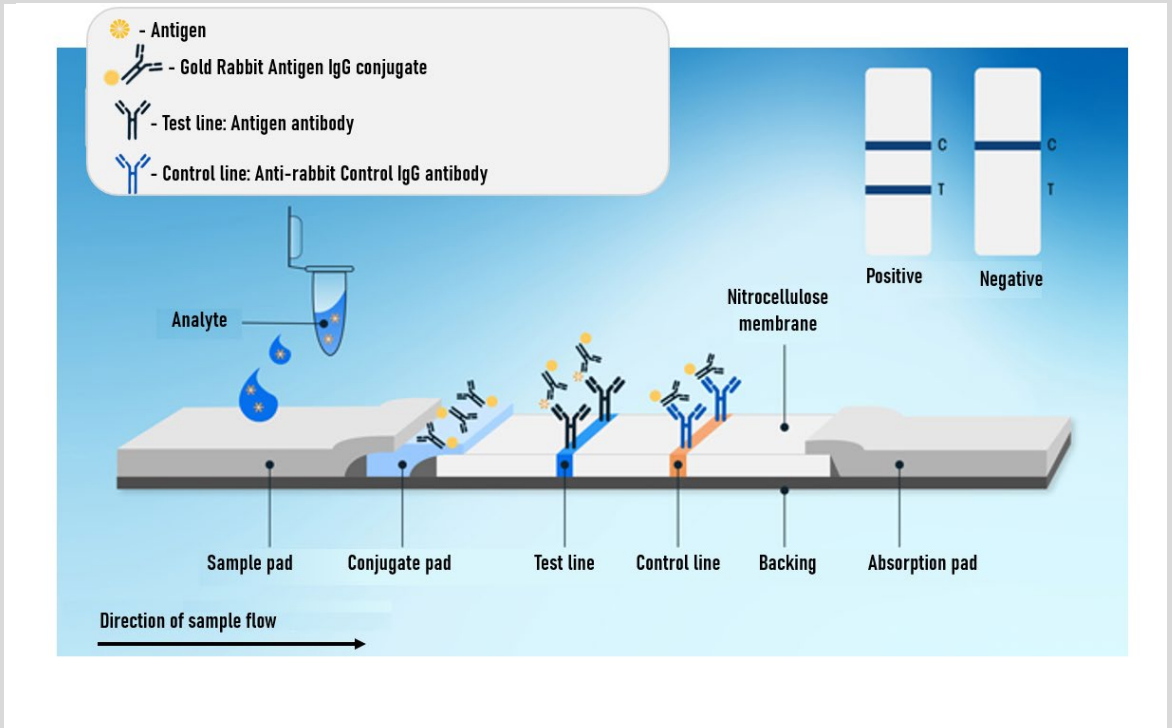

Figure 1.10 Diagram summarizing lateral flow assay architecture. Samples containing the analyte flow through the nitrocellulose membrane by capillary flow, carrying reporter antibodies (labelled with gold) until the mixture interacts with the test line (containing antibodies that bind the analyte of interest) and the control line (containing anti-IgG antibodies that bind to human IgG molecules). If the control line shows a positive reaction, it is a valid test. Adapted from [120]

While plasmonic colloidal nanoparticle-based sensors provide a facile and rapid way to detect molecular or ionic targets using just the naked eye, this ease of use

comes with the trade-off of their sensitivity. The yielded response is often low to detect a clear colour contrast. In addition, colorimetric detection typically suffers from interference problems when used in complex matrices which may hinder application at point-of-care; and their low uniformity of their structure and poor stability in a physiological solution is of concern because aggregation can occur in the absence of an analyte [121]. Moreover, the solution-based synthesis and growth mechanism of colloidal nanoparticles is usually performed by reducing metal ions into uncharged nanoparticles using hazardous reducing agents [122]. Lastly, the synthesis process can be adapted to produce small range of variations in small volumes with a coefficient of variation in their diameter which makes it difficult to investigate thoroughly their properties. Although significant advances have been made involving the use of colloidal nanoparticle-based sensors for diagnostics applications, technical and practical problems need to be solved [123].

1.2.4.2 Chip-based plasmonic sensors with periodic architectures

Plasmonics has become a vigorously researched field, driven by recent advancements in nanofabrication techniques. The geometry of on-chip periodic arrays can be fabricated precisely by using modern lithographic methods. Such exquisite synthetic control yields highly organized arrays, with stable and controllable optical properties, facilitating us to investigate the plasmonic effects both experimentally and theoretically [124]. Furthermore, advancements in theoretical approaches and the development of quantitative electromagnetic modelling tools have significantly enhanced the understanding of the optical properties of isolated nanostructures and electromagnetically coupled nanostructures of various sizes and shapes [125].

The formation of periodic arrangements on a chip allows precise control over spatial distribution of nanostructures and coupling of individual nanostructure resonant modes together (plasmonic or photonic) due to proximity or specific configuration. The newly formed coupled modes with altered properties are believed that can achieve high optical quality required for advanced biosensing. Figure 1.11 is reviewing optical sensor exhibiting the four fundamental modes that can be intercoupled to realize several advanced sensing schemes. As outlined in the inner circle these are - 1. Rayleigh anomaly (RA) associated with periodic photonic structures, 2. LSPR occurring in isolated metallic nanostructures, 3.

guided mode resonances (GMR) generated in grating-waveguide structures, and 4. surface plasmon polaritons (SPP) appearing at metal–dielectric interfaces.

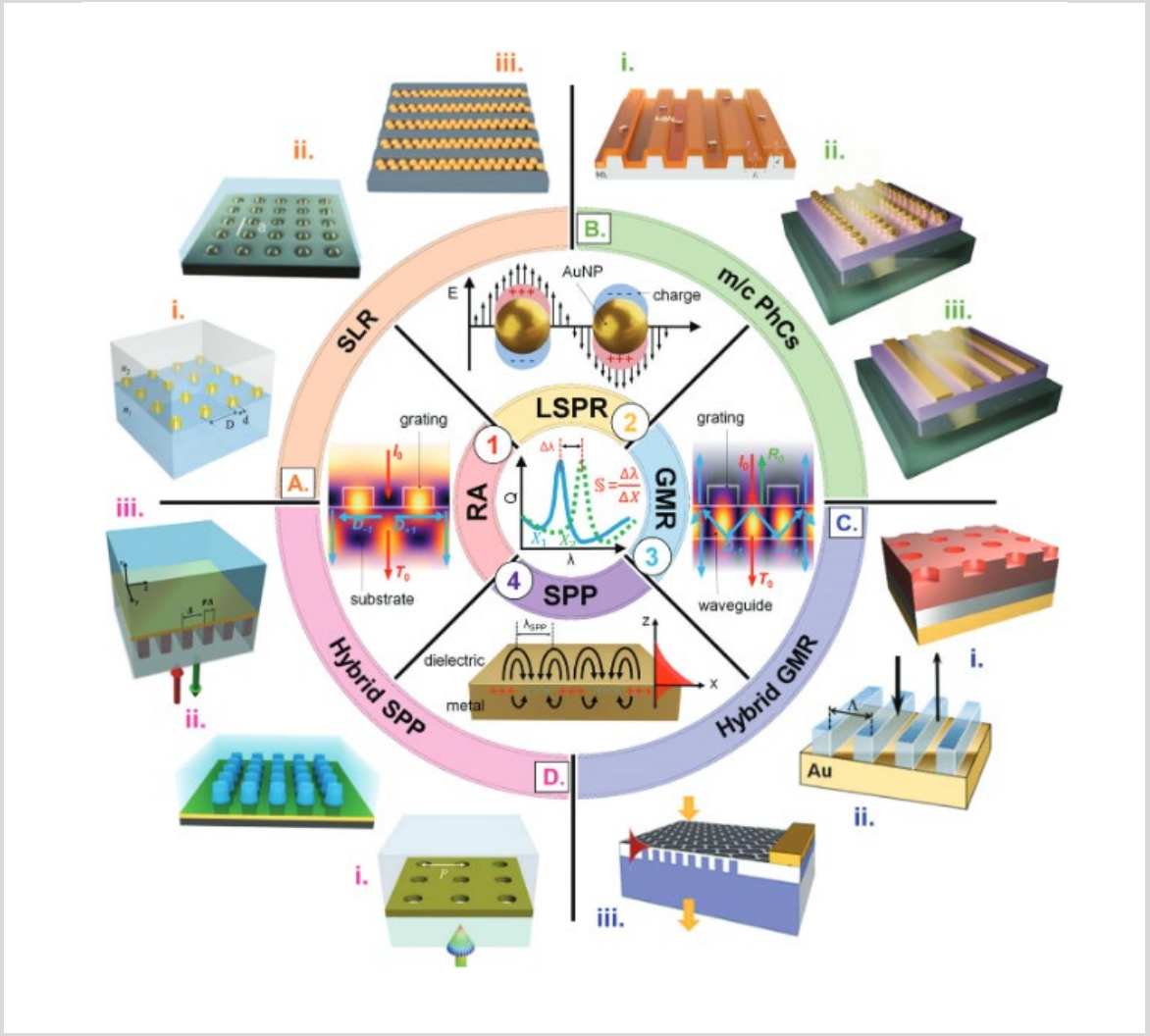

Figure 1.11 Diagram summarizing the planar periodic architectures for advanced optical sensing application [126]. The inner circle reviews the four fundamental modes that can be inter-coupled that can achieve high optical quality required for advanced biosensing - 1. Rayleigh anomaly (RA), 2. LSPR, 3. guided mode resonances (GMR) and 4. surface plasmon polaritons (SPP). The outer circle displays the hybrid mechanisms generated by combining the fundamental resonances. A - surface lattice resonances (SLR), B. metallic/colloidal photonic slabs (m/C PhCs), C. hybrid guided-mode resonances (hybrid GMR), and D. hybrid SPP.

In addition to the fundamental photonic resonances, such as Rayleigh anomalies (RA) and guided mode resonances (GMR), and plasmonic resonances, such as LSPR and SPP, recent research has demonstrated that combining these fundamental resonances can lead to the emergence of various hybrid mechanisms. This hybridization is facilitated through plasmon-photon and plasmon-plasmon coupling, which is only enabled by specifically engineered chip-based

metallodielectric nanostructures, as depicted in the outer circle of Figure 1.11. The plasmonic hybridization resulting from the fundamental modes are - A. surface lattice resonances (SLR), B. metallic/colloidal photonic slabs (m/C PhCs), C. hybrid guided-mode resonances (Hybrid GMR), and D. hybrid surface plasmon polariton (Hybrid SPP).

This hybridization model offers significant sensitivity improvements but the requirements for an optical sensor are high. For example plasmonic-plasmonic hybridizations in a split ring stacking consisting of two gold split ring with orthogonal gap orientation along with a sandwiched dielectric (SiO2) disk spacer offer a sensitivity (S) of 3024 nm per RIU [127]. Despite the high sensitivity, the major drawback in both these structures is the operational wavelength (≈2.25μm) limiting its applicability in the visible optical range.

LSPR offers extreme sensitivity but one of the significant challenges with LSPR is the intrinsic losses associated with metallic nanostructures due to strong radiative damping [68] and shorter plasmon lifetimes (2–10 fs) [128]. Such losses result in broad FWHM of the line shapes (>50nm), implying low quality factor of the resonant modes. In contrast, photonic modes like GMR are constrained with considerably lesser sensitivity while characterized by ultralow spectral linewidth due to their extreme confinement inside the dielectric medium.

Hybrid GMR sensing (GMR and SPP) with a material composition of Ag/Si3N4/Ag/Si3N4/SiO2 metallic grating, demonstrating a sensitivity of 1084 nm per RIU and a FOM of≈23 has only been studied numerically [129]. However, while the theoretical hybridization of guided mode resonances (GMR) and surface plasmon polaritons (SPP) has been identified, experimental fabrication of such hybrid structures would not meet the requirement for ultralow fabrication costs.

Using hybrid SPP sensing (plasmon–photon interaction of SPP modes with the RA), the sensitivity can be enhanced by orders of magnitude while maintaining high-Q modes for improved resolution [130]. The plasmonic LSPR and SPP-based sensors can offer higher bulk RI sensitivities, in general, because of the more extensive interaction of the resonant modes and the analyte in the cover region, along with options to tune the resonant wavelength over the visible and NIR wavelength [126].

With the advent of nanotechnology, SPR research entered a new era. The incorporation of nanostructured materials, such as metallic nanoparticles and nanohole arrays, enabled enhanced sensitivity and tunability of SPR sensors. The localized surface plasmon resonance (LSPR) effect, a nanoscale counterpart of conventional SPR, was extensively studied in the early 2000s [131]. LSPR-based sensors, which rely on the plasmonic properties of metallic nanostructures rather than thin films, provided significant advantages, including miniaturization, improved sensitivity, and compatibility with diverse sensing environments.

Biosensing technologies are actively researched for integration into scalable, mass-producible platforms. The fabrication techniques employed across these studies include electron beam lithography (EBL), nanoimprint lithography (NIL), soft lithography, and hybrid lithographic processes, each offering trade-offs between performance, resolution, and suitability for industrial-scale replication.

Segervald et al. [132] developed gold-coated nano-well arrays using thermal nanoimprint lithography on polymer substrates, optimized for large-area SERS enhancement. Zhao et al. [133] fabricated silver-coated silicon nanopillar arrays integrated with microfluidic chips to perform real-time in situ SERS detection. Although the method offers strong enhancement and integration potential, the reliance on silver limits long-term stability, and the complex lithographic fabrication is not ideal for scalable mass production.

Seo et al. [134] utilized electron beam lithography to fabricate gold nanopillar arrays for thermoplasmonic PCR, achieving rapid and specific nucleic acid amplification via plasmonic heating. Despite its functional sophistication, the fabrication process is low-throughput and less suitable for disposable diagnostics.

T. Lednický et al. demonstrated a different approach to fabricate ordered gold nanoparticle arrangements on epoxy substrate which are selectively etched resulting in nanomushrooms arrangements resonating in the VIS spectrum [135]. While the approach demonstrates promise in terms of fabrication cost-effectiveness, it is not yet compatible with high-throughput mass replication technologies such as injection moulding, where production cycles can be completed within minutes. This limitation constrained the scope of their study, as only a limited number of nanoarray configurations could be fabricated and

analysed. The resulting nanomushroom structures exhibited a bulk refractive index sensitivity ranging from 83 to 108 nm/RIU.

Zheng et al. [136] presents a cost-effective fabrication method for large-area plasmonic biosensors using transfer nanoprinting with anodic aluminium oxide membranes to create Ag-ZnS nanodisk arrays on gold films. The resulting platform demonstrates a high refractive index sensitivity of 438 nm/RIU and supports surface plasmon polariton Bloch modes under normal light incidence, highlighting its potential for scalable, high-performance biosensing applications.

Chu et al. [137] employed nanoimprint lithography (NIL) on a flexible PDMS substrate followed by metal deposition (90 nm gold) to create a hexagonal nanopillar array with bilayer cap–nanohole architecture. The bilayer gold cap–nanohole configuration exhibited an ultranarrow resonance linewidth of 4.5 nm due to strong coupling between Wood's anomaly and Fabry–Perot cavity modes. This resulted in a high figure of merit (FOM) of 140.6 and bulk refractive index sensitivity of 632.8 nm/RIU. The device also demonstrated label-free detection of bovine serum albumin (BSA) with a limit of detection as low as 0.27 μM. While the fabrication route offers advantages such as flexibility, scalability, and high uniformity, the reflectance-mode setup and relatively thick gold layer limit its compatibility with transmission-based biosensing configurations common in transparent chip designs. PDMS is soft and deformable, which may cause long-term mechanical instability, alignment challenges, and limited reusability. Chu et al.'s PDMS-based method, although innovative and suitable for research or flexible electronics, lacks the long-term stability and throughput capacity needed for standardized biosensor production pipelines.

In another study, R. S. Moirangthem et al. [138] reported a flexible plasmonic sensor featuring a gold-coated polymer nanograting structure fabricated via soft UV nanoimprint lithography on a PET substrate. The device demonstrated a significantly enhanced bulk refractive index sensitivity of 788 nm/RIU. Similar to the platform developed in this thesis, their nanograting sensor operates under normal incidence with white light illumination, which simplifies the optical setup. However, it should be noted that the resonance dip in their reflectance spectrum is positioned in the near-infrared (NIR) region, which contributes to the enhanced sensitivity compared to sensors operating in the VIS spectrum.

Although these nanograting-based sensors show strong potential for point-of-care (PoC) applications, they also face limitations. The fabrication process, while cost-effective, is not readily scalable. Additionally, reflectance-based measurement setups typically require thicker gold films than transmission-based sensors, which could increase the overall cost and complexity of the final device.

Minopoli et al. [139] reviewed various plasmonic nanostructures—such as nanodisks, nanopillars, and nanoholes—fabricated through EBL, NIL, and colloidal methods. While highlighting the trade-offs between performance and fabrication scalability, the review concludes that cost-effective, reproducible, and scalable methods like injection moulding are essential for commercial biosensor deployment.

Other researchers like Wei et al., [140] similarly to the work presented in this thesis adopted injection moulding as low-cost, rapid, and high-throughput fabrication method in order to fulfil commercial applications. The optical setup for transmission measurements was also simplified to normally incident polarized light on the nanoslit-based SPR chip. The refractive index sensitivity was 460 nm/RIU, and a FOM of 58 was achieved. Protein–protein interactions between BSA and anti-BSA demonstrated the proof of concept of the biological detection capability of the sensors. A platform as such, has the capability to modify the number of sensing arrays to 96, 384, or more. This would benefit various multiplex sensing applications such as clinical disease diagnosis, drug screening, and protein biomarker discovery. The expectations for an optical sensor include reliability, speed, sensitivity, and simplicity, without the necessity of expensive equipment. These features must be achieved at ultralow fabrication costs. To meet these requirements, and after carefully reviewing the chip-based sensor configurations, in this project we focused on the coupling between LSPR and SPP of periodic nanostructures on a metal film, operating under normal light incidence. This hybridization model offers significant sensitivity improvements and requires careful investigation of its full coupling potential.

Hundreds of periodic nanostructures with varying sizes and periodicities were fabricated on a single platform, allowing for experimental study of their plasmonic resonance. This platform, known as the double gradient plasmonic array library (DGPAL), systematically demonstrates how the geometry of the arrays transitions

from predominantly SPP mode exhibiting photonic Rayleigh anomalies (RA) to hybrid SPP-LSPR combinations, and finally to predominantly LSPR properties. The intriguing results extracted from the DGPAL analysis show improvements in high bulk refractive index (RI) sensitivity and biomolecular detection.

Undoubtedly, while periodic metasurfaces with high-quality detection are typically associated with high costs, this project also addresses the cost factor by adapting the process to a high-throughput replication approach. With advancements in nanoengineering technologies, chip-based nanostructures can meet all requirements for a reliable optical sensor. Compared to other works in literature, the combination of injection moulding and thin gold film deposition presented in this thesis demonstrates several advantages. It incorporates prices control over the size, shape and distribution in a large surface area with a reproducible technology resulting in high sensitivity for a minimal cost per device. The strategy employed in this work offers a clear path to industrial-scale replication of nanostructured biosensors.

1.3 Thesis objectives

This thesis explains the high-throughput fabrication of highly ordered nanostructure arrays for LSPR biomolecular detection. Investigate their plasmonic and optical properties, study generated hybridized plasmon modes and evaluate their sensing performance. The objectives are listed below:

1. Develop large-scale nanofabrication by implementing EBL technique to fabricate periodic plasmonic array pattern in a controlled fashion.

2. Investigate the plasmonic and optical properties of nanostructures and their correlation with LSPR performance.

3. Examine the hybridized plasmon modes within the parametric sweep for refractive index (RI) sensitivity and biosensing applications.

4. Demonstrate the performance of optimised plasmonic biosensors.

1.4 Thesis overview

Chapter 2 – explains the fast and cost-effective method of nanofabrication allowing pattern transfer and mass-replication of high-resolution periodic arrays. In such manner, the fabrication of a plasmonic library containing hundreds of geometry combinations on a single chip becomes an achievable task and a vast number of characteristic properties of the plasmonic behaviour can be extracted systematically.

Chapter 3 – dedicated to the spectroscopy analysis of the double gradient plasmonic library. A comprehensive resonance characterisation explains the dual plasmonic capabilities of the arrays. Since both SPP and LSPR have local fields, coupling can occur between SPP/SPP, SPP/LSPR, and LSPR/LSPR when the supporting metal structures are brought within the local field decay length.

Chapter 4 - a label-free immunosensor based on the LSPR of gold nanopillars was designed and tested. The design was specifically accommodated to be compatible with the Open SPR instrument from Nicoya for real-time measurements.

Chapter 5 - conclusions and future remarks - this final chapter will summarise the presented results, as well as consider possible future prospects for applications.

Chapter 2 Nanofabrication of injection moulded plasmonic nanostructures

2.1 Introduction

This project relates to the creation of injection moulded plasmonic nanopillars or nanostructure arrays for integration into a plasmonic biosensor device for rapid quantitative sensing of biologic analytes.

Systematic approach to identify the optimal design parameters for the plasmonic biosensor. To do so instead of performing tens or hundreds of experiments separately we devised a library with all the design parameters on a single device. This allows us to systematically explore the plasmonic performance of the design parameters.
The array-based screening approach was made possible with the fabrication of a double gradient plasmonic array library (DGPAL) with 400 distinct combinations. The DGPAL with orthogonally increasing diameter and periodicity was arranged in 20x20 columns and rows of 1 mm2 fields spaced apart by 50 µm. The total area of the DGPAL formed approximately a 21x21 mm2 pattern (see Figure 1.3).

The selection of the design sweep, encompassing variations in nanopillar diameter and interspacing, was guided by prior research on nanopatterned devices exhibiting resonance wavelengths within the visible spectrum. Notably, the study by Cosmin et al. [141] presented experimental and simulated results on the resonance performance of gold nanopost-shell arrays closely resembling the nanostructures planned for fabrication in this research. Their work investigated polymer nanopillar cores with widths of 190 nm and 240 nm, periodicities of 300 nm and 400 nm, and a 50 nm gold coating. Using finite-difference time-domain (FDTD) simulations, they explored a design sweep encompassing diameters ranging from 130 nm to 240 nm and periodicities between 250 nm and 450 nm. Spectroscopic analysis in water confirmed that both experimental and simulated reflectivity data exhibited resonance peaks within the visible wavelength range.
Building on these findings, we selected nanopillar arrays with diameters ranging from 120 nm to 310 nm and interspacing of 80 nm to 270 nm, corresponding to periodicities between 580 nm and 200 nm. This decision was further influenced by the technological constraints of the fabrication process, particularly NIL and

injection moulding. The resolution capabilities of both techniques were well-suited for achieving feature sizes of 100 nm and above, ensuring both the feasibility of the design and the high-throughput production of devices with robust plasmonic performance. Regarding the upper limit of the design parameters, nanopillar size and periodicity was preferably adjusted to exert subwavelength optical confinement thereby maintaining strong plasmonic coupling which is crucial for achieving high sensitivity in refractive index-based sensing applications.

It is of a great importance to have a fast and cost-effective method of nanofabrication allowing pattern transfer and mass-replication of high-resolution periodic arrays. In such manner, the fabrication of a plasmonic library containing hundreds of geometry combinations on a single chip becomes an achievable task and a vast number of characteristic properties of the plasmonic behaviour can be extracted systematically.

The nanofabrication process was specifically adapted to a high-throughput replication approach i.e., injection moulding as it is a reliable, high-performance method generating large quantities of identical plastic parts, and it is particularly well-suited for mass production. It is a complex, cost-effective technique using a patterned inlay inside the mould shaping the injected thermoplastic material under pressure with nanostructures which subsequently solidifies, and the finished part is ejected. The process repeats multiple times producing hundreds of components quickly at a consistent quality. The inlay itself is a polymer film patterned by nanoimprint lithography (NIL) technique involving a master stamp. The manufacturing of the master stamp is achieved through a sophisticated, high-resolution, multi-step process achieving the nanoscale pattern development.

In summary a single master stamp patterned with high precision can be replicated by inverting the nanopattern into an inlay and reinverting it hundred times through injection moulding into a plastic carrier to provide the original structure from the master stamp.

All steps along the pattern transfer starting with the fabrication of the master stamp, followed by the inlay and finishing with the injection moulded parts are described further in detail in the Appendix (Section A1-A3).

2.2 Fabrication of the nanostructures

The array-based screening approach was made possible with the fabrication of a double gradient plasmonic array library (DGPAL) with 400 distinct combinations. The DGPAL with orthogonally increasing diameter and periodicity was arranged in 20x20 columns and rows of 1 mm^2 fields spaced apart by 50 μm. The total area of the DGPAL formed approximately a 21x21 mm^2 pattern.

Due to the complexity of the plasmonic library, our first goal was to test the feasibility of the full nanofabrication process by simplifying the design and file preparation and thenceforth to implement the optimizations enhancing quality and uniformity of the final device. The patterning of the plasmonic library was carried out using two distinct generations of electron beam lithography (EBL) systems. The Vistec VB6 UHR EWF electron beam tool was employed to scan the simplified design, whereas the Raith EBPG 5200 was used to pattern the high-quality version. Therefore, in the subsequent chapter sections the double gradient plasmonic libraries produced via the simplified and the advanced nanofabrication approach will be referred to respectively as VB6 sample and EBPG sample.

2.2.1 Computer aided design (CAD) of double gradient plasmonic array library (DGPAL) and file preparation.

The nanofabrication of any nanoscale pattern begins with a design package such as L-Edit and involves the creation and careful positioning of shapes aiding the optimisation of the total pattern writing by lithography tools. The 2D design layout data is then stored in a GDS (Graphic Data System) file format as it can be easily used to communicate between different tools and stages of the design process. Secondly, it is necessary for a proprietary software converter as Beamer (GenISys GmbH) to extract the GDS data and translate the layout into a machine-exposable file. All shapes in the design are modified for optimum exposure by fracturing, implementing exposure fields, setting a writing order, and adjusting exposure doses for optimum CD (critical dimension) uniformity and contrast. Lastly, the converted data is uploaded in a specialized graphical user interface to facilitate positioning the design layout on the wafer and creates program scripts for the exposure of patterns onto a substrate. The following steps, after CAD is finalized, is to transfer the job file on the external server where the electron beam

lithography (EBL) tool operates which allows the actual job submission to be performed.

The structure of the DGPA library consisting of hundreds of nanopatterned arrays organized in a single layer render the CAD procedure together with the file preparation steps extremely laborious and time-consuming for manual processing. Therefore, as an optimization was necessary, certain operations regarding the generation of the DGPAL submission file to be automated. As mentioned, above a simplified and advanced nanofabrication approach was developed to test the feasibility of the nanofabrication method, and in this section, a detail description of the CAD/file preparation undertaken for VB6 sample and EBPG sample will be discussed.

2.2.1.1 CAD/file preparation of VB6 sample

For the purposes of this project, one of the most fabricated types of geometries was used – the circle. With the EBL technique shapes are generally defined by building them gradually through the exposure of the resist as a series of pixels. The centre to centre spacing between each exposed pixel, known as the VRU (Variable Resolution Unit), is set slightly smaller than the beam diameter so that subsequent exposures overlap, and the cumulative result is that of a continuous shape.

However, the VB6 UHR EWF lithography tool used for the fabrication of VB6 sample can only expose trapezium shaped elements [142]. This is possible because there are sophisticated software tools e.g., Beamer that allow complex CAD patterns to be split into trapezium shaped elements that an e-beam tool can expose. This process is referred to as “fracturing" since the complex polygons are split-up, or fractured, into trapezium shaped elements. As you might expect, exposing the shape of a circle with the VB6 would be highly inconvenient. Ideally, the curvature of a circular shape should be represented with the maximum number of vertices in order to maintain its original design and be fractured into many polygons. As the fabrication of the VB6 sample is within the nanoscale and part of the nanoarrays approach the resolution limit of the tool, trapezium derived circles become an impossible task as the sufficient number of vertices cannot be met. A simplified version of shape writing is a process known as dot writing [143]. Dot writing utilises the natural shape of the beam of electrons which is circular, and each feature can be defined by a single pixel or a single beam exposure.

The VRU grid is a grid of points which control the beam position in a writing field. The interval between two adjacent points in the VRU grid is called an “exel” and it is often referred to as the resolution. The beam can move within the VRU grid, but the exposures are defined by the beam step size (BSS). The BSS is equal to the VRU multiplied by the resolution (BSS= VRU * resolution). In this case the resolution is 1 nm which technically makes the BSS equivalent to the VRU. In this case the VRU is set to a higher value than the beam diameter and acts as the pitch between adjacent features. Adjusting the VRU with equal increments when using the same beam diameter would result in the formation of nanopatterned arrays with gradient periodicity [144] (Fig 2.1**A)**.

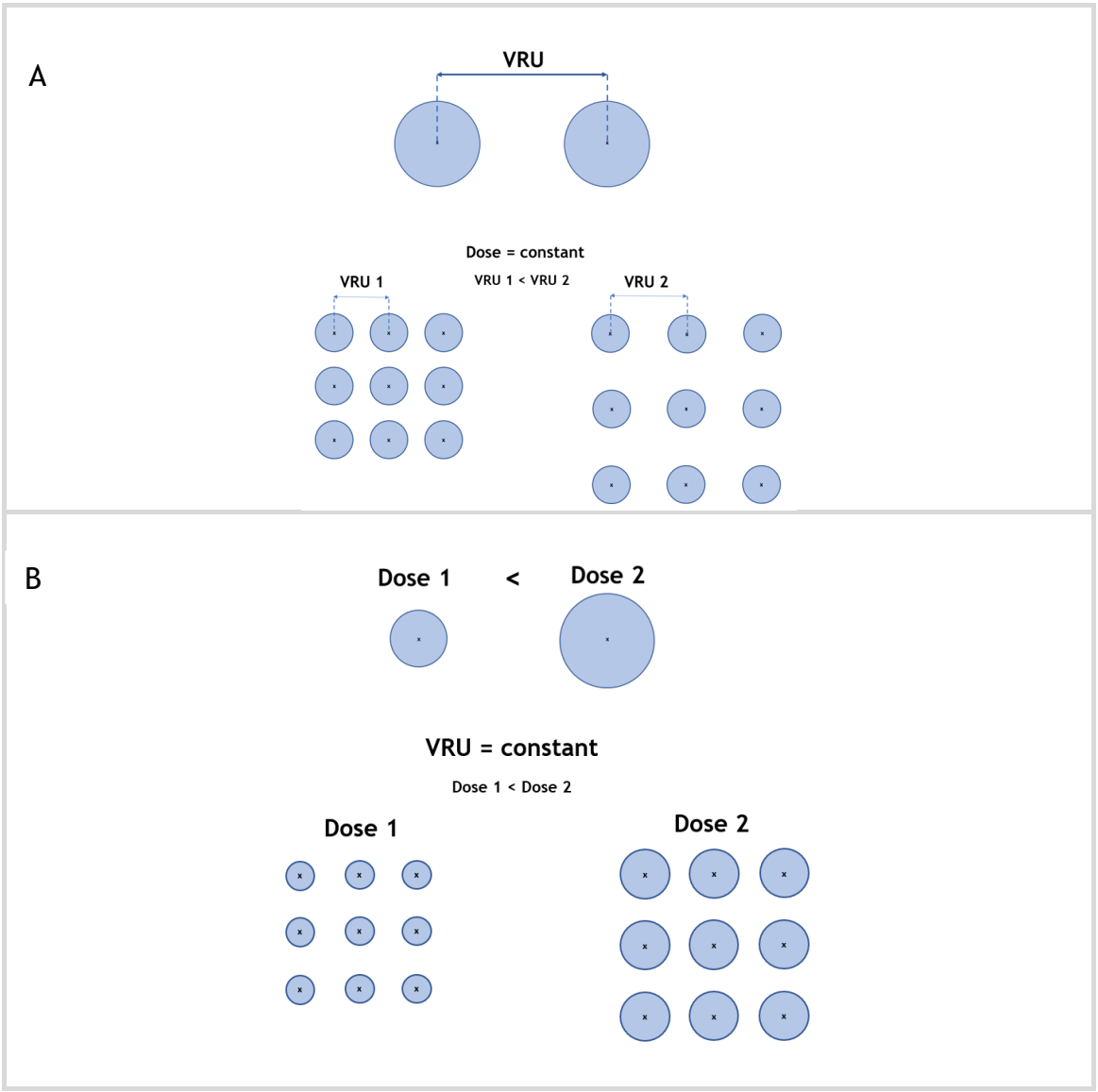

Figure 2.1 Diagram illustrating how VRU (Variable Resolution Unit) and dose create a double gradient within the periodicity and nanostructure size of nanopatterned arrays. A - depicting the change in nanostructure interspacing while keeping the diameter size constant. B – depicting the change in diameter size while keeping the nanostructure interspacing constant.

In order to generate the gradient in the dot diameter, the amount of energy exposing the resist, known as the dose, is adjusted with equal increments. This relationship translates into the following: for a fixed VRU in the array, one would obtain larger dots with higher dose and smaller dots with lower dose (Fig 2.1B).

However, there is one more factor that needs to be taken into consideration when we discuss the dose-VRU relationship, namely the "fill-factor" (FF). The FF is an expression quantifying the percentage area exposed by EBL within a nanoarray or in other words the density of a nanoarray. The FF and density are directly proportional but dose conditions for sparse and dense nanoarrays can differ significantly. This specific relationship translates into the following: denser nanoarrays require lower dose whereas sparse nanoarrays require higher dose.
The dose exposing the resist is conventionally expressed as charge per unit area i.e., μCcm^{-2} instead of charge per dot exposure and thus the database for the DGPA library expressing the relationship of all 400 variations between dose-VRU were adjusted for 1 mm^2 fields.
It becomes apparent that the dot writing style cannot store its database in a GDS file as it does not contain any graphic data. This imply that the dot writing database must be converted into a machine-exposable file by using an alternative file preparation process as it is not compatible with the standard process explained in the beginning of section 2.2.1.
With the intention of addressing this issue, a Python code (Python Software foundation, USA) was written that would provide all necessary instructions for the VB6 UHR EWF pattern generator within a text file. The purpose of the code is to create a grid of 400 cells organized in 20x20 columns and rows and each cell should store its corresponding information regarding dose-VRU. Considerable amount of the dose-VRU information was derived from an extensive experimental work accumulated from various dose tests executed in the past and the rest was based on calculated predictions. The compiled dose-VRU data was then organised in a matrix with 400 cells and imported within the code to create a machine-exposable file. The code also holds commands for the size of each cell – approximately 1 mm, the space between adjacent cells – defined as 50 um and the order in which each one will be exposed – applied as "serpentine" writing order.
Once the library has been designed, the desired exposure may require this single pattern to be exposed in multiple locations on a substrate, or that several patterns

are combined to create one larger exposure. The process of defining which pattern files is to be exposed in which position is usually described as creating a job layout. The proprietary software tool operating at that time was BELLE (Beamwriter Exposure Layout for Lithographic Engineers), creating exposure layouts.
BELLE produces a text “job file" that contains an ordered list of the job settings, pattern positions, exposure parameters, marker positions, marker search parameters, and various other commands to allow the job to be exposed properly. At the time of exposure this file is read by the “Runjob" program which controls the VB6 to perform the required calibrations, alignments, and exposures.

2.2.1.2 CAD/file preparation of EBPG sample

With the latest improvements of the software tool - Beamer, fracturing of complex curved layouts became possible with utmost accuracy and the conversion of circular shapes into multiple polygons was no longer needed. This opportunity opened the possibility to re-create the double gradient plasmonic array library by using graphic data and represent the arrays with actual shapes. Shape writing approach is considered as the “golden standard” in electron beam lithography and the computer aided design together with file preparation in this case follow the classic process blueprint. A detailed description is shown in Figure 2.2 where the three core segments of CAD/file preparation are explained in a flow diagram.
L-Edit IC v2018.3 CAD package is a powerful layout editor extremely useful in micro and nanofabrication. It is an easy to learn draw type layout editor from Tanner Research where the creative process of drafting two dimensional geometries comes with maximised efficiency and numerous useful features. However, manually designing the wide range of graphic data within the library remains a time-consuming obstacle.
In an effort to alleviate the work and significantly shorten the time of graphic data generation, we have exploited the scripting execution feature provided via the CNST Nanolithography toolbox [145]. The Centre for Nanoscale Science and Technology (CNST) at the National Institute of Standards and Technology (NIST) developed the Nanolithography Toolbox to help users design devices with intricate curves and aggressively scaled critical dimensions. As shown in Figure 2.2, Python programming can be used to create such complex CNST scripting files.

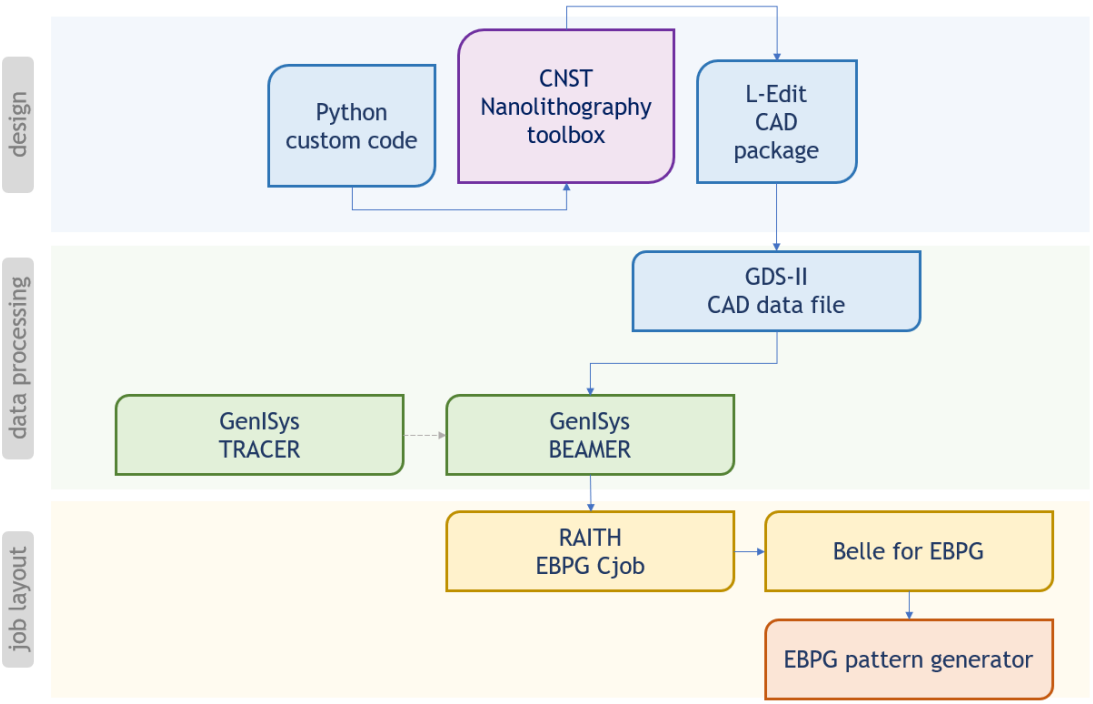

Figure 2.2 Process diagram explaining the CAD/file preparation multistep operations of EBPG sample.

Within the custom code we have shaped the construct of the library by initializing the variables – size of library, size of nanoarray, distance between nanoarrays as well as the construct of the nanoarray taken as "point of origin". The "point of origin" nanoarray consists of the variables – minimum radius of a circle and a minimum pitch or centre-to-centre distance between adjacent circles. As these variables are looped with the conditionals to add a fixed increment to radius while developing a column and add a fixed increment to pitch while expanding a row, we have algorithmically fulfilled the script file to generate the graphical expression of a double gradient library. The output of the code is a cnst file which is further loaded in the CNST toolbox to consequently save and organise the information into a single GDS file. The GDS data can be easily visualised with the L-edit CAD package and design parameters can be verified. The development of the design of all 400 geometries consisting of approximately 5 billion circles across the library becomes effortlessly executable within a few clicks with duration of less than 1 minute.

Consequently, the data processing segment starts by extracting the GDS data with Beamer and translating the layout into a machine-exposable file. Beamer is the most comprehensive and fully integrated e-beam lithography (EBL) software package in use today [146]. The graphical user interface (GUI) allows for a visual

flow to be created with “drag-and-drop” building blocks, inspect results in a viewer window and export results.

An advanced data processing module used in the flow is the proximity effect correction technology (PEC). PEC is essential for improving the exposure quality by automatically adjusting exposure doses for optimum CD (critical dimension) uniformity and contrast. It eliminates the need to experimentally adjust the exposure dose for each layout. Performing traditional “trial and error” optimisation is very expensive and labour-intensive, thereby PEC technology significantly increases the productivity and reproducibility on the wafer. The proximity effect in EBL is due to forward-scattering of electrons in the resist and backward scattering of electrons from the substrate [147]. The electron scattering leads to undesired exposure of the adjacent regions of the resist which in turn results in changes in the pattern dimensions, resolution reduction and line-edge roughness. The process correction is therefore needed to provide uniform energy distribution across the resist which translates in uniform pattern development. This means that the absorbed energy of the resist is analysed in the pattern and dose assignments are made such that the absorbed constant energy at threshold lands at the edge of the intended design.

By definition “proximity effects” are pattern density dependant size variations and are observed especially in arrays greater than 100x100 μm. If no correction is applied, the features in the centre will have a larger size than those at the edge and corners. The additional absorbed energy in the centre area of the resist is from backscattered electrons. Corners and edges are the areas rendered to always absorb less energy. PEC identifies those critical areas and assigns higher dose to compensate for the difference. PEC technology plays a crucial role in data processing stage of the double gradient library. Not only because the nanoarrays qualify as 10 times greater than the threshold size mentioned above but also due to the nature of the design. The rows in the library are designed to gradually change density but should remain with constant diameter. Immediately becomes clear that denser arrays will absorb much more additional energy from backscattering compared to the sparse arrays.

The columns in the library are designed to gradually change diameter but should remain with constant density. In this case the arrays with large diameter would accumulate additional energy from backscattering compared to the arrays with small shapes. The solution to this issue previously would be addressed with

creating a dose matrix similar to the development of VB6 sample. The 20x20 dose matrix would contain higher exposure doses in the cells with sparse arrays and smaller shapes to compensate the difference in absorbed energy. These matrices are based on additional calculations and predictions that solely consider a parameter termed “fill factor”. Fill factor describes what percent of area from the 1x1 mm^2 array is exposed or covered with electrons. Although this is a very good starting point in attempt to perform a proximity effect correction, it is not very accurate as it does not encompass many other intricate events happening on the surface during e-beam exposure.

Dose matrices are no longer required when performing data processing with BEAMER. In this case the fill factor and the corresponding dose assignments are calculated automatically from the software. The correction of the proximity effect does not end here. The most important parameter characterizing this phenomenon is the Point Spread Function (PSF) [147]. PSF specifies the relative energy deposited at the distance *r* from a point exposure. It appears obvious that the spread is an effect of the interaction between the electrons with the resist and the substrate. Its strength and influence have a different range depending on the thickness of materials and acceleration voltage (Figure 2.3).

Monte Carlo simulation is an excellent technique to model electron scattering [148]. Such software performing electron solid interactions simulations to model the energy distribution in a custom specified resist, thickness and substrate is named TRACER [149]. TRACER is also a release by GenISys GmbH, developed to advance the standard in EBL.

The primary function of TRACER is to compute the PSF for a given set of conditions describing the energy deposited into a resist layer as a radial function of distance from the beam incident position. An example PSF is plotted in Figure 2.4, showing the energy absorbed for a 100 keV electron beam in a 300 nm thick layer of PMMA on a silicon substrate.

If the PSF is provided, the absorbed energy at any position *x* can be calculated: $E(x) = P(x) * PSF$. The details from energy distribution are then automatically used in the correction algorithm.

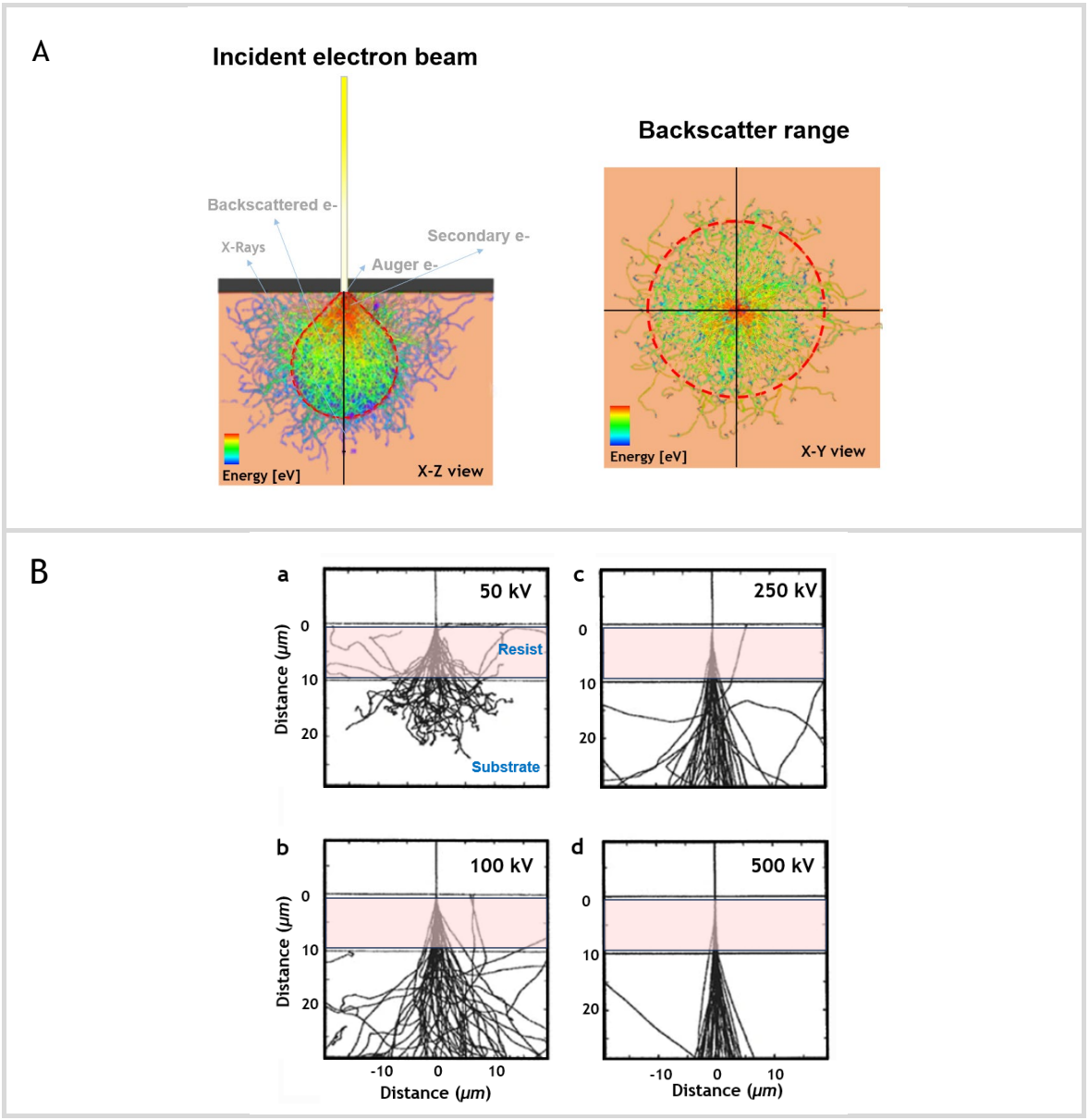

Figure 2.3 Diagram illustrating the electron solid interactions. A – visualizing the electron interaction volume with resist and substrate roughly with a shape of a teardrop in X-Z view as well as the perimeter of the backscattering range in X-Y view. B - Electron trajectory simulations using Monte Carlo for 10 μm of resist on a silicon wafer for different acceleration voltages. The horizontal lines at 0 and 10 μm denote the top and bottom of the resist layer, respectively. As shown there is a significant difference in the spread range of deposited energy between 50 kV, 100 kV, 250 kV and 500 kV electron beams (adapted with permission from [150]).

The simulated PSFs from TRACER can interface directly with BEAMER and can be easily uploaded in the PEC module (Figure 2.5). Once the customised PSF is implemented in the file processing stage, BEAMER software is supplied with the fundamental information of energy distribution within the chosen combination photoresist-substrate material and thus accurately executes the proximity effect correction.

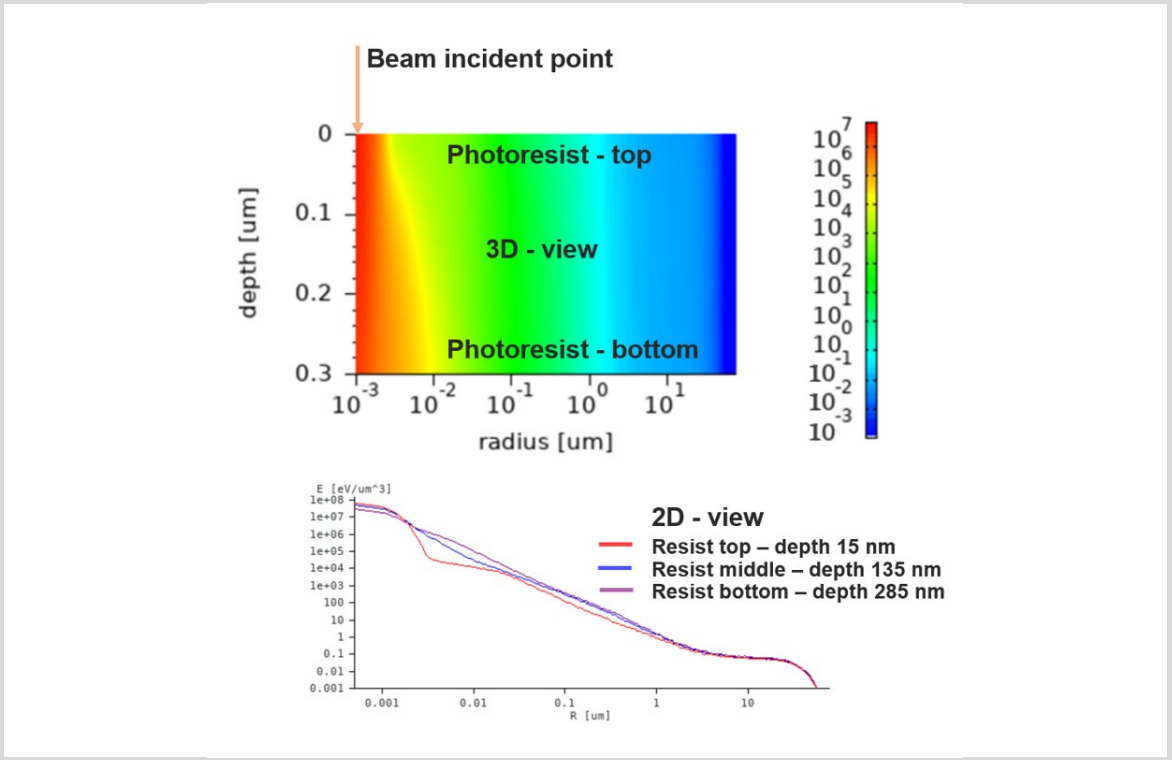

Figure 2.4 3D heat plot viewing the absorbed energy as a function of radius and depth (top) and a 2D-Radial plot viewing the density energy (bottom).

PSF is divided into shape fracturing, correcting for Short-Range (SR) effects and Long-Range (LR) effects by a separation point (at 0.2431 um, Figure 2.5 A). SR effects include electron forward scattering and beam blur while LR effects include electron backscattering. When applying PEC to a layout, LR is always permanently activated while SR can be optionally selected depending on the smallest feature design included. SR correction is used for feature sizes less than twice the effective blur size (Full Width Half Maximum (FWHM) of a Gaussian function) or three times the sigma values of the Gaussian alpha value (PSF).

Tools can expose one square field from the DGPAL with only one dose. This would mean that the energy distribution would not be equalized and features in the middle of the field will develop significantly larger than the features located in the edges and corners. The PEC module corrects the exposure by performing fracturing based on the absorbed energy distribution. Thus, each array in the DGPAL is fractured in thousands of minimum figure size (MFS) fields and further each MFS filed is assigned a dose factor. BEAMER computes a continuous dose spectrum for the correction with more than 250 dose classes which is sufficient to equalize the absorbed energy distribution with a great accuracy. After the PEC fracturing is implemented, instead of one dose, each square field in the DGPAL is

exposed with a spectrum of dose classes (Figure 2.5 B). Dose classes are colour coded and as the value of the dose factor increases the corresponding colour becomes warmer. In substance, Figure 2.5 B depicts the application of the LR PEC module utilizing a customized PSF in the fracturing algorithm. The colour coded diagram of the double gradient library accurately illustrates the absorbed energy distribution as the nanoarrays located in the top left corner with large features arranged densely are assigned with the lowest dose factor whereas the nanoarrays located in the bottom right corner with small features arranged sparsely are computed with the highest dose factor.

Not only the software corrects the DGPA library across by considering the density of electron beam exposures but also performs automated fracturing equalizing the middle area of each array with the edges and corners (Figure 2.5 B).

Consequently, follows the Export module where all shapes in the design are modified for optimum exposure by shape detection, fracturing, implementing exposure fields, setting a writing order and setting resolution and beam step size for optimum CD (critical dimension) uniformity and contrast. In the export settings of the DGPAL file processing stage, 1 nm resolution was applied with a beam step size of 10 nm. In order to avoid field placement and field stitching, the settings for field ordering were activated as automated floating fields. The floating field option will let BEAMER attempt to centre isolated features inside an exposure field. The fracture mode “Shape detection” designed for the detection of basic elements greatly improved the placement of beam shots with curvature e.g., circles and shape filling were set to high resolution. In the final steps of data processing sage, the .GDS file is converted to .GPF and transferred to the e-beam tool server.

Once patterns are converted to the machine specific GPF format, follows the job layout stage. The software tool used for EBPG sample job layout is EBPG RAITH Cjob. Cjob software is a graphical user interface (GUI) that makes program scripts for the exposure of patterns onto a substrate for the EBPG 5200 electron beam tool. The job layout starts by choosing a substrate object e.g., Si wafer and indicating the size and model – 4-inch ((Miller index 100) p-type). The GUI will be able to easily visualize the expected positioning of the patterns on the desired substrate. Patterns are loaded in the layout by choosing their corresponding GPF formats containing the machine-exposable details, and a prompt window gives the opportunity to add the specifications for beam size, dose, and exact location.

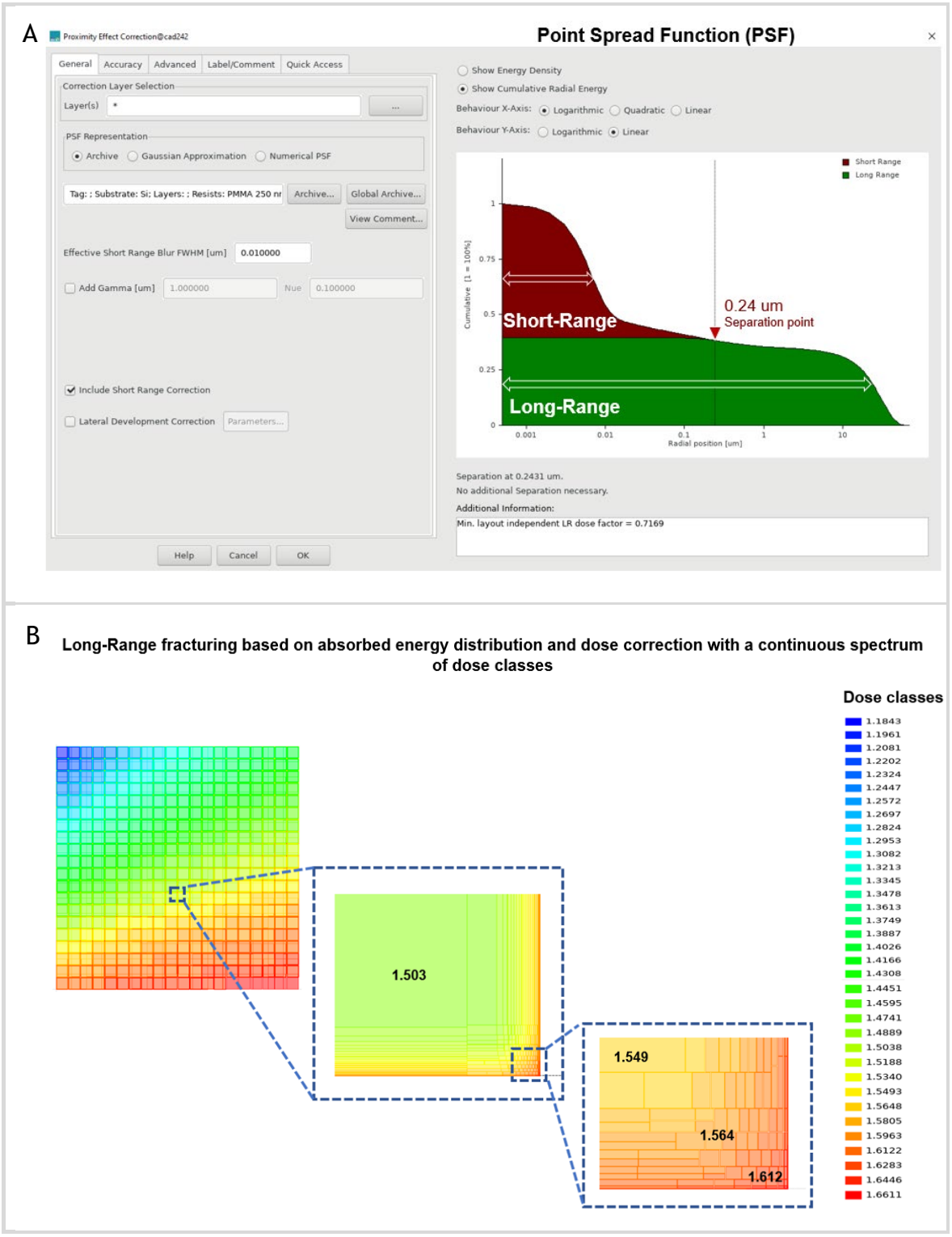

Figure 2.5 A - Customized PSF file from TRACER imported into the PEC module showing the Short-Range and Long-Range energy distribution. The vertical line on the plot is marking the short-range separation point at 0.24 µm. B – Long-Range fracturing based on the absorbed energy distribution extracted from the PSF and automated dose correction. Depending on the algorithms for equalizing the absorbed energy distribution, areas such as the top left corner are assigned with lowest dose class values and areas such the bottom right corner are assigned with highest dose class values indicating the fill factor differences between the nanoarrays. Furthermore, each individual nanoarray is corrected in the periphery and corners with utmost precision.

The exposure of EBPG sample was performed with 100 kV acceleration voltage, 8 nA beam current creating a spot size of approximately 36 nm. The dose was set to 310 μC/cm^2. When the job layout is finalised, the software runs an estimation for the exposure time calculating 3h 36 min for the completion of the plasmonic library.

2.2.1.3 CAD/file preparation of VB6 sample vs EBPG sample

The comparison of CAD/file preparation process flow between VB6 sample and EBPG sample can be summarized as follows (Figure 2.6):

VB6 sample design was based on the exposure commands controlling the electron beam e.g., dose and VRU information known as "dot writing". This would mean that the design stage does not include graphic data and thus cannot be optimised further with any data processing software. The output from the Python code is a script file directly uploaded for a job layout.

The matrices containing exposure commands are in a sense extremely rigid data format and cannot be fine tunned straightforwardly. For each 1 mm^2 field would be applied only a single dose and that inevitably would create the proximity effect of unequalised energy absorption.

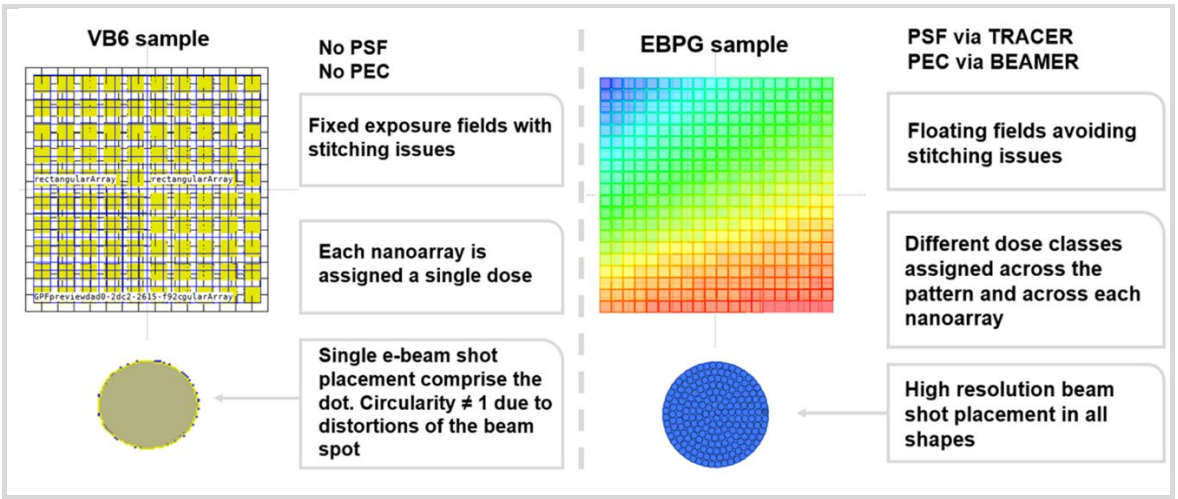

Figure 2.6 Comparison between VB6 sample and EBPG sample data processing flow. VB6 sample represents the "dot writing" approach where the lack of graphic data restricts the file processing stage to further optimization. Proximity effect is not corrected, exposure fields are fixed, and stitching occurs across each nanoarray. Distortions of the e-beam spot leading to reduced circularity. EBPG sample diagram is showing the benefits of the "shape writing" approach. Proximity effect is corrected and utmost accuracy, exposure fields are not interfering with the pattern and each shape remain circular due to the high-resolution shape detection and e-beam shot placement.

The script file does not contain fracturing instructions and thus the EBL tool would implement default settings to divide the pattern to main fields and subfields rendering the stitching process to occur across all nanoarrays.

Each shape was created with a single electron beam shot exposure which interferes with the circularity as the shape of the beam spot varies due to aberrations, distortions and defocus during execution.
EBPG sample design was based on graphic data and represent the arrays with actual shapes. The generation of the graphic data file was automated via customised Python code and CNST toolbox. The output GDS file is generated quickly, and design parameters are accessible for fine tuning. Data in GDS format is readable by various software programs and can be further manipulated for optimisation. TRACER and BEAMER lithography software provided highly efficient proximity effect correction by implementing a customized PSF simulated to be utilised in an absorbed energy distribution algorithm. Additionally, exposure fields placement was positioned automatically avoiding stitching to intersect nanoarrays. High-resolution shape detection facilitated electron beam shots filling with 10 nm BSS which achieving the desired circularity.

As mentioned above the machine-exposable file finalised from the CAD/file preparation process contains all instructions needed by the pattern generator to activate and direct the electron beam gun. The EBL technique is pivotal for the fabrication of the master stamp. A comprehensive overview of the EBL-based fabrication procedure is provided in Section A1 of the Appendix titled Fabrication of the Master Stamp. The subsequent fabrication steps, including the creation of the inlay and the injection moulding process, are detailed in Section A2 and Section A3 of the Appendix, respectively.

2.2.2 Morphological comparative analysis of VB6 sample vs EBPG sample master stamps

EBL patterning of the resist was carried out using two distinct generations of EBL systems. The Vistec VB6 UHR EWF electron beam tool was employed to scan the VB6 sample, whereas the Raith EBPG 5200, being a state-of-the-art EBL system, was used to pattern the EBPG sample. Also, as detailed in section 2.2.1, completely different CAD techniques were implemented, e.g., “dot writing” vs “shape writing” guiding the EBL patterning. After the completion of the master stamp nanofabrication there is an opportunity to physically inspect and analyse their quality.

In order to systematically create an overview of the results, the comparison begins with images of the Si wafers where the detectable differences are observable with naked eye and proceeds with optical images taken from the nanoarray units. Finally, a zoomed in scanning electron microscopy (SEM) data acquisition displays the profile comparison of the nanopillars.

The first detail that grabs the attention as we start the comparison of the Si masters is the unsuccessfully developed top left corner of the VB6 sample outlined as region 1 with a dashed line in Figure 2.7 A. As this specific location of the gradient is designed to hold its largest nanostructures densely packed with the smallest interspacing between each other, it is rendered to be with the highest fill factor compared to the rest of the locations. As discussed in section 2.2.1, this would suggest a very high dose of electrons deposited in the resist which also increases the proximity effect. The excessively high exposure doses would completely degrade the structure of the bottom PMMA layer (with lower molecular weight) which then cause the top PMMA layer to collapse. Upon development with IPA : MIBK solution these areas would be completely washed away and remain “hollow” as shown in the image.

On the other hand, the nanofabrication of EBPG sample delivers the desired objectives across all locations. In this case the critical area is corrected for the proximity effect and the energy distribution is uniform. Every single subfield is assigned a specific dose which would eliminate the probability of energy accumulation in places where it is not needed.

The assignment of a single exposure dose as in the case of VB6 sample proves to be ineffective and a conclusion can be made that the specificities of EBL file preparation stages are extremely critical.

The second region outlined with a magnification glass on Figure 2.7 A focuses the attention on the surface with successfully developed nanoarrays. As shown in the second pair of optical images the surface within the nanoarrays in VB6 sample is somehow granular, displayed with darker and lighter areas compared to the uniform colour in EBPG sample.

After a further investigation, using the SU8240 (Hitachi, Japan) ultra-high resolution scanning electron microscope (SEM), the nature of the defects becomes apparent. The third region in Figure 2.7 B is presented as a pair of SEM images. In order to enhance the differences in the investigated regions the images were adjusted by thresholding in ImageJ (U. S. National Institutes of Health). The SEM image taken from VB6 sample visualize the pattern formed by the dark and light areas.

All lighter spots comprise the successfully developed areas. In the SEM image these can be identified with a white solid contour following identical grid pattern. Everything around, that appears darker, are areas perforated by multiple missing nanopillars. The grid arrangement suggest that each writing subfield repeats the same defect accumulation. A zoomed insert of the same SEM pair of images is displayed at the end of Figure 2.7 B to showcase the missing features in the nanopillar array. After a substantial discussion with JWNC EBL staff on the topic this effect is thought to be due to a noise signal with frequency measured around 70kHz. The noise appeared as common mode noise on the deflector plates, so had a focussing effect, which would make the dot sizes change periodically, and in extreme cases the dots do not fully develop and so disappear.

In contrast, the subfield irregularities are absent in the second master stamp as the design of the EBPG sample is based on graphic data with predefined pitch divisible to the size of the nanoarray and constant BSS of 10 nm. The file is processed with BEAMER software where the user interface visualizes the fracturing of the arrays. As mentioned previously in this case the option automated floating fields was activated. The floating field option will enable BEAMER to autonomously centre isolated features within exposure fields. Uniformity of the exposed features is demonstrated in each level of magnification with both optical and SEM surface inspection.

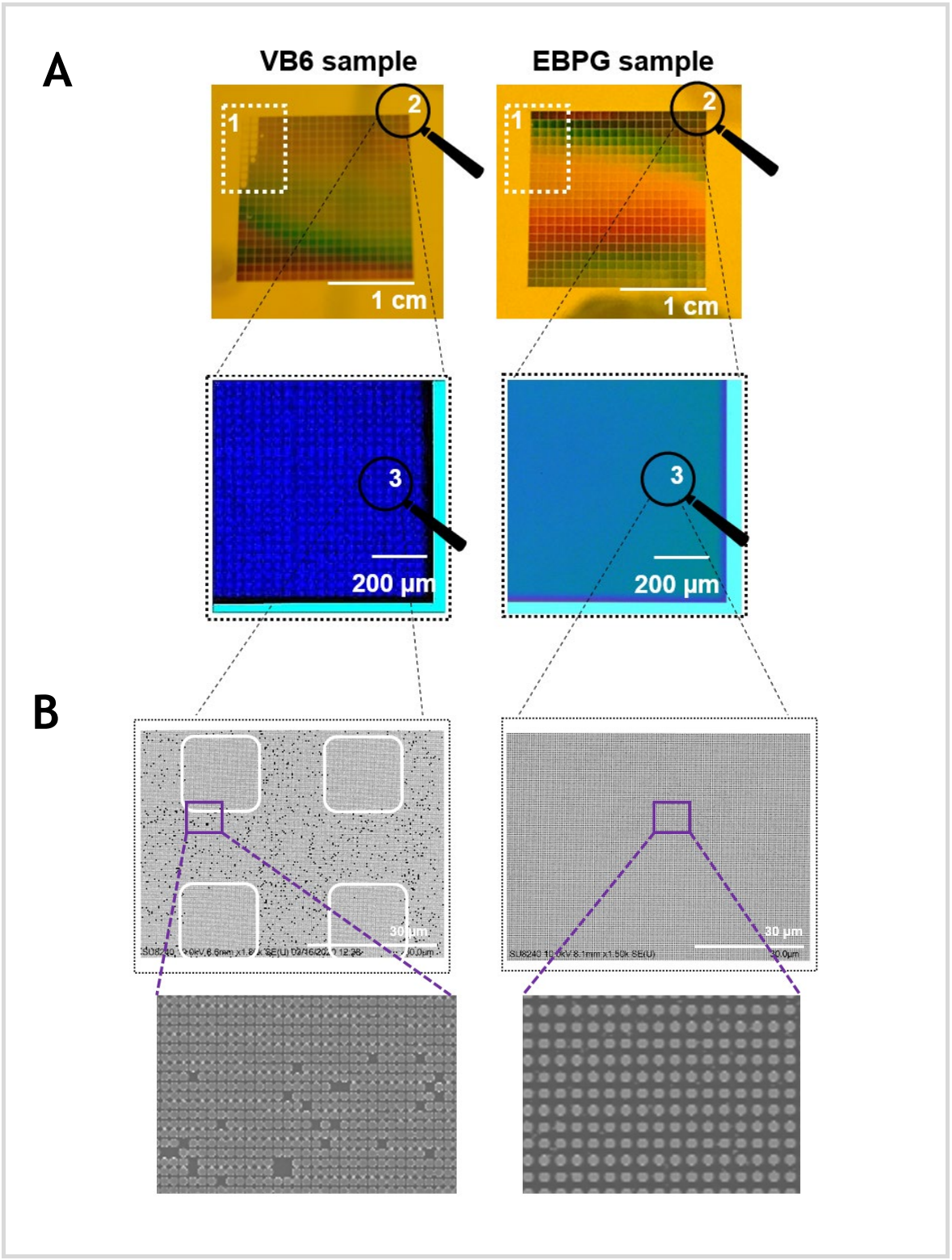

Figure 2.7 Quality comparison of Si master stamps VB6 sample and EBPG sample. The comparison aims to systematically depict differences starting from a larger scale with optical images to a microscale with SEM images, product of two significantly distinct nanofabrication methodologies. Panel A – Optical images of VB6 sample (left) and EBPG sample (right), where two regions of interest are outlined – region 1 (outlined in a white dashed box) comparing critical areas with high fill factor and energy accumulation and region 2 (outlined with a magnification glass) comparing the uniformity of the metasurfaces. Panel B - Region 3 - SEM images visualizing the comparison in more depth. The VB6 sample exhibit a non-uniform surface with multiple missing features. The array of square patches with successfully developed pattern are outlined with white boarders for better visualisation on the SEM image.

Moving forward, Figure 2.8, compares the quality of successfully developed areas by showing SEM images from both master stamps. The comparison aims to demonstrate that the circularity of the nanopillars is impaired in the case of the VB6 single dot exposure.

The extract bellow the SEM images is a smaller area after performing image segmentation where the contours of each nanostructure are outlined in green, and the centroid is shown as a red dot. It becomes more apparent that the single dot exposures in VB6 sample are forming an oval egg-shaped geometry with visibly different diameter in x and y axis. Also, if the pointy side of the dot is followed, the direction of the vector scan becomes apparent.

This suggest that the shape of the dot is very much dependent on the shape of the beam. If the beam is deflected as shown in the diagram in Figure 2.8 A, then each exposed dot will resemble the elongated shape of the beam.

This effect is thought to be caused by beam settling issues. While the subfield deflectors move the beam from one position to another so does the deflection rate from one position to another slows down towards the target position. This leads to the formation of oval-shaped dots changing direction as the vector scan moves through each row.

This issue is addressed in the design of EBPG sample as each circle is comprised by hundreds of focused small-beam sized exposures within the contours of the shape. Thus, the shape of the nanostructures is controlled by the graphic design and does not depend on the current shape of the beam.

To demonstrate how “shape writing” significantly differs from “dot writing” an aspect ratio analysis was performed depicting the differences in the circularity of the nanostructures (Figure 2.8 B). The maximum value is 1, denoting features of a perfect circle and values bellow 0.9 meaning that the aspect ratio deformation is above 10%, exhibit noticeable elongation. The analysis encompasses the entire range of diameter sizes across the vertical axis of both DGAPL matrices. The aspect ratio in VB6 sample for the shapes less than 200 nm shows poor results with values between the range of 0.81-0.91 and improves for the larger shapes up to 0.97 after some quite a few fluctuations with an average error of ±0.02.

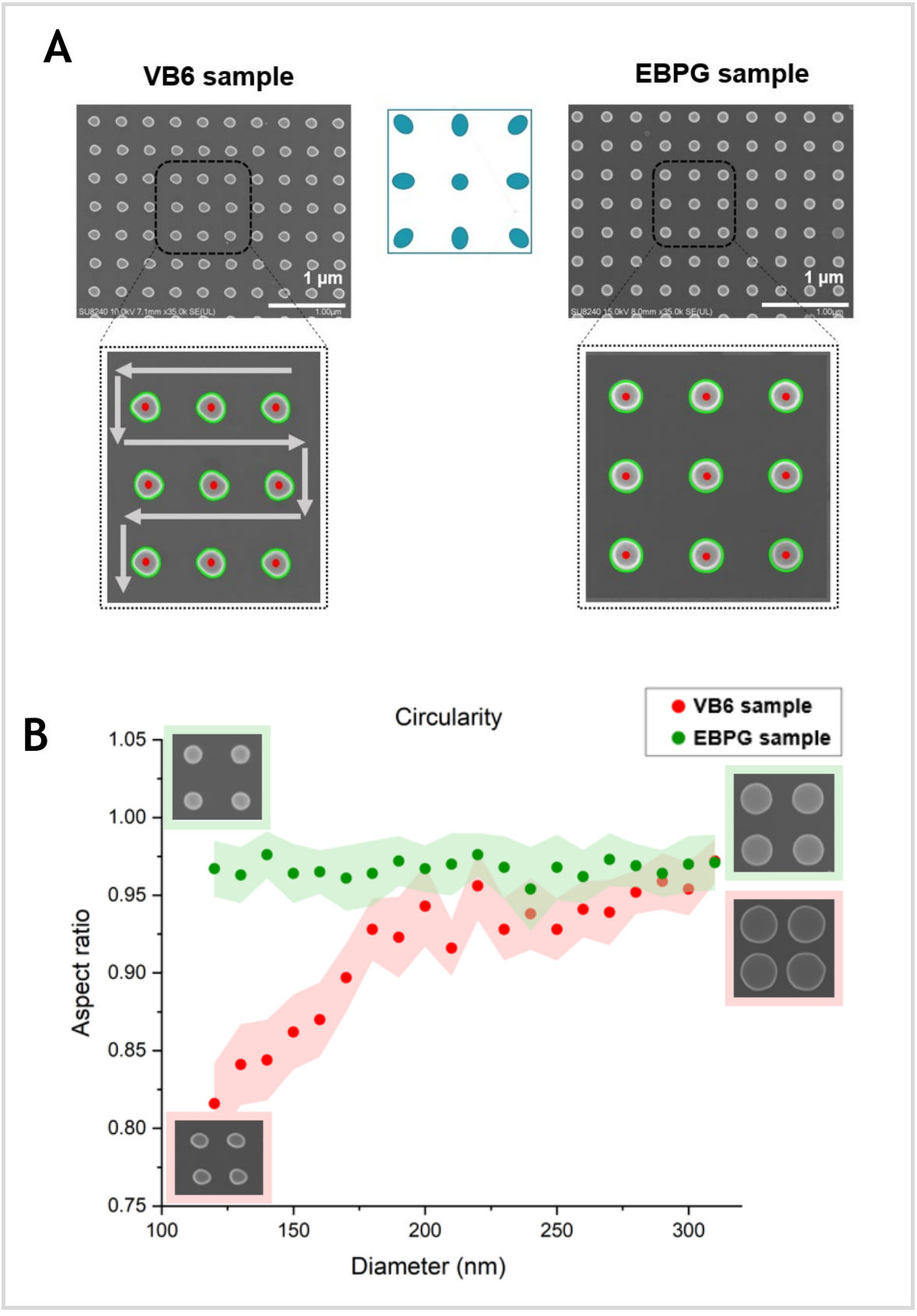

Figure 2.8 B Quality comparison of Si master stamps VB6 sample and EBPG sample. The comparison aims to systematically depict nanoscale differences with SEM images, product of two significantly distinct nanofabrication methodologies. Panel A – SEM image analysis of VB6 sample (left) and EBPG sample (right), comparing the nanopillar circularity and depicting the effect of electron beam deflection. Panel B - The final plot in this figure demonstrates the evaluated aspect ratio of all diameter variations between VB6 sample (red) and EBPG sample (green).

In order to visualize the results, small SEM inserts on the plot are added in the beginning and in the end of each data set. The smallest shapes in the VB6 sample data set are noticeably elongated horizontally and the largest shapes exhibiting good circularity but with a boundary that is irregular. The SEM inserts on the other hand for the EBPG sample depict shapes with high circularity and smooth boundaries in both ends of the data set. The consistently high circularity with values between 0.95-0.98 is supported across the full range of diameter sizes with an average error of ±0.01.

The nanoscale comparison between VB6 sample and EBPG sample is also supported with a comprehensive SEM morphological characterisation summarizing findings through both horizontal and vertical cross-sectional assessments. Each cross-sectional analysis comprises a dataset consisting of twenty SEM images captured at identical magnification, extracted from the central portion of each nanoarray. These assessments focus on two vital design parameters: the diameter size and the gap size. In the context of the dual gradient configuration, it is important to note that, during the assessment of either cross-section, the outcomes should demonstrate that one of the parameters remains constant, while the other parameter varies within a predefined range. For instance, the horizontal cross-section analysis, conducted row wise, reveals nanoarrays with a constant diameter size while exhibiting an increasing interspacing between nanostructures, falling within the range of 60-270 nm. Conversely, the vertical cross-section analysis, performed column wise, showcases nanoarrays with a consistent gap size between nanostructures and a changing diameter size within the 120-310 nm range.

The SEM analysis was performed with ProSEM which is also a release by GenISys GmbH. It is an advanced SEM metrology and automation package for precise and calibrated image analysis. ProSEM is very powerful in measuring similar features and pattern arrays automatically such as the nanoarrays evaluated in the project. It is based on sophisticated algorithms for automatic edge detection and feature fitting. This enables reliable results in multiple measurements and statistical data sets which can be visualized and summarized in data tables.

The morphological cross section analysis is conducted in the middle area of the 20x20 double gradient matrix and thus the assessment includes only row number 10 and column number 10.

In figure 2.9 is illustrated the row wise analysis comparing both Si master stamps subjected for the assessment. As it can be noticed Panel A, evaluates the size of diameter where the expected outcome is to remain constant and thus a reference line signifies the desired result of 220 nm. In accordance with the aspect ratio deformation analysis presented in Figure 2.8, the diameter size is assessed by considering both the major and minor diameters, measured along the longest and shortest axes of the features, respectively.

The scatter plot for VB6 sample reveals significant deviations from the reference point for both major and minor diameters. These deviations follow a similar increasing trend as the gap size expands. The major diameter exhibits an extreme deviation of 17 nm below the baseline and 9 nm above the expected value. Conversely, all data points for the minor diameter fall considerably below the reference.

Another important observation is that there is a substantial separation between the data points for major and minor diameters, underscoring the significance of aspect ratio deformations.

In contrast, the scatter plot for EBPG sample demonstrates a desirable consistency, with values for both major and minor diameters closely aligning with the reference and exhibiting acceptable aspect ratio deformations.

The reason why we observe such differences in the quality of both master stamps originates from the substantial differences in their design and data file preparation.

In the VB6 sample data file, the allocation of e-beam exposure doses, within the assessed row, spans from 60 μCcm^{-2} to 380 μCcm^{-2}. This allocation is primarily informed by dose test analysis, albeit largely reliant on estimations. These assigned doses exhibit a gradual increase as the gap size expands, reflecting the inversely proportional decrease in fill factor along the gradient. However, it is noteworthy that the range of doses is considerably broad and fails to align with the objective, as most nanoarrays either fall below or exceed the 220 nm reference point.

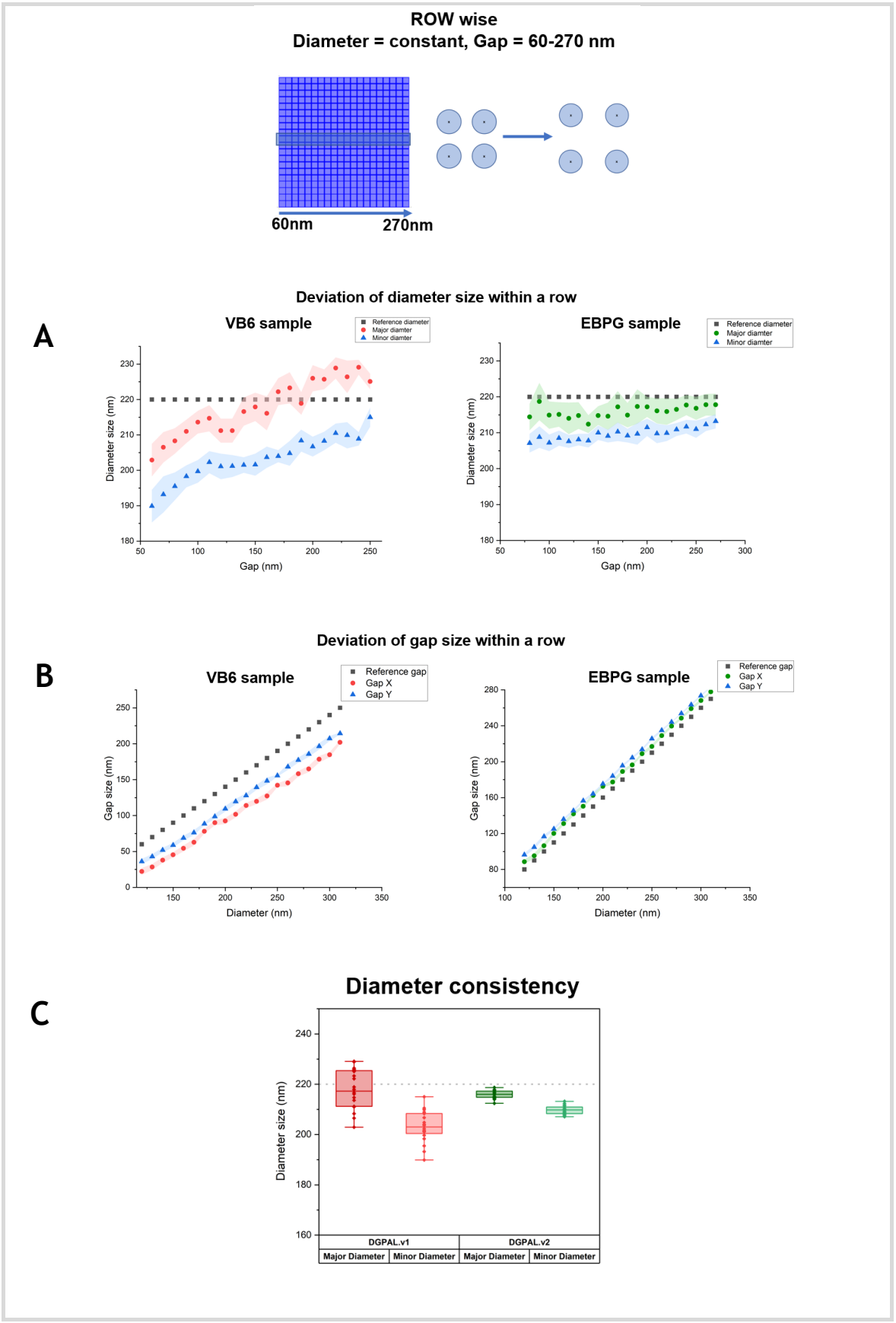

Figure 2.9 Row wise cross-sectional analysis comparison of Si master stamps VB6 sample and EBPG sample. The comparison aims to systematically depicts the variations in quality within a given row, where outcomes of nanoarrays demonstrate constant diameter size while exhibiting an increasing interspacing between nanostructures, falling within the range of 60-270 nm (see top diagram). Panel A – scatter plots showing the outcome when assessing the constant diameter size. Panel B – scatter plots showing the outcome when evaluating the variable parameter, gap size. Panel C – box plot summarizing the diameter consistency.

For instance, in the same row, the nanoarray with the smallest gaps is densely packed with nanostructures, leading to a high percentage of area filled with electrons. Therefore, it is assigned a dose of 60 μCcm^{-2}, which proves insufficient for developing a feature of 220 nm in size. Conversely, the nanoarray with the largest gaps in the same row, being sparser and having the lowest electron coverage, is allocated a dose of 380 μCcm^{-2}. In this case, the exposure dose is excessively high, resulting in features larger than 220 nm.

The distribution of energy is notably challenging to estimate accurately without accounting for the proximity effect, leading to frequent discrepancies in the outcomes.

The assignment of e-beam exposure doses in EBPG sample data file is based on automated proximity effect correction mechanism generated with a customized PSF. BEAMER software utilizes algorithms to accurately assign dose factors across each nanoarray and achieve uniform energy distribution. The outcome is a narrow range of doses spanning from 435 μCcm^{-2} to 468 μCcm^{-2} fulfilling the objective as evidenced by a plot wherein data points closely converge with the reference.

Panel B of Figure 2.9 is dedicated to evaluating gap size within the assessed row, with the expected outcome being variations within the range 60-270 nm, as indicated by a reference line. Similar to the diameter assessment, the gap size is assessed with two descriptors, representing the gap in the horizontal and vertical axes. The scatter plot for VB6 sample reveals that all data points fall significantly below the reference. Conversely, all data points for EBPG sample accurately reflect the gap in both horizontal and vertical axes, demonstrating alignment with the intended range.

This distinction in performance may be attributed to differences in data file preparation for the two samples. In VB6 sample, the separation between adjacent dots is determined by the VRU value. However, even if VRU estimations are conducted accurately, the resulting gap between adjacent dots is critically contingent upon the precision of diameter size outcomes. As previously illustrated, diameter accuracy in VB6 sample did not align with the reference, potentially explaining the observed inconsistencies.

The EBPG sample data file consists of graphic data with predefined interspacing between nanostructures. During the EBL, electrons are precisely deposited within the predefined contours of the designed features, ensuring that the gap size remains consistent. This example underscores another notable advantage of EBPG sample, wherein patterns are organized in a graphical format rather than being generated in real-time. This approach offers increased flexibility for processing and allows for more comprehensive adjustments to be made during fabrication.

The concluding graphic representation in Figure 2.9, Panel C, encapsulates the uniformity in diameter size, presented in the form of a box plot. In the case of VB6 sample, both major and minor diameters are represented by broader boxes, with mean values notably distant from each other, revealing a substantial difference of 14.5 nm. The results imply an inconsistency in the size and circularity of the nanostructures within the evaluated row expected to adhere to constant values.

In contrast, the parameters of EBPG sample exhibit commendable uniformity, characterized by closely clustered data points and mean values that diverge by merely 6 nm. This outcome closely aligns with the objective of the design and demonstrate the desired quality necessary for subsequent experimentation.

Figure 2.10 presents a column-wise analysis that compares two Si master stamps subjected to evaluation. As it can be noticed Panel A, evaluates the size of gap parameter and the expected outcome is to remain constant. Hence, a reference line signifies the desired results of 160 nm and 180 nm, respectively. The assessment of gap size considers both the horizontal and vertical axes, measuring the gaps between adjacent features in both directions. This approach is adopted to ensure that the lattice design maintains a square configuration, necessitating a visual demonstration of the equality between gap x and gap y.

The scatter plot for VB6 sample reveals significant deviations from the reference point for both gap x and gap y. These deviations follow a similar decreasing trend as the diameter size increases. Specifically, the gap x parameter exhibits a substantial deviation between 32 nm and 85 nm below the baseline which accumulates to a standard deviation of 18 nm.

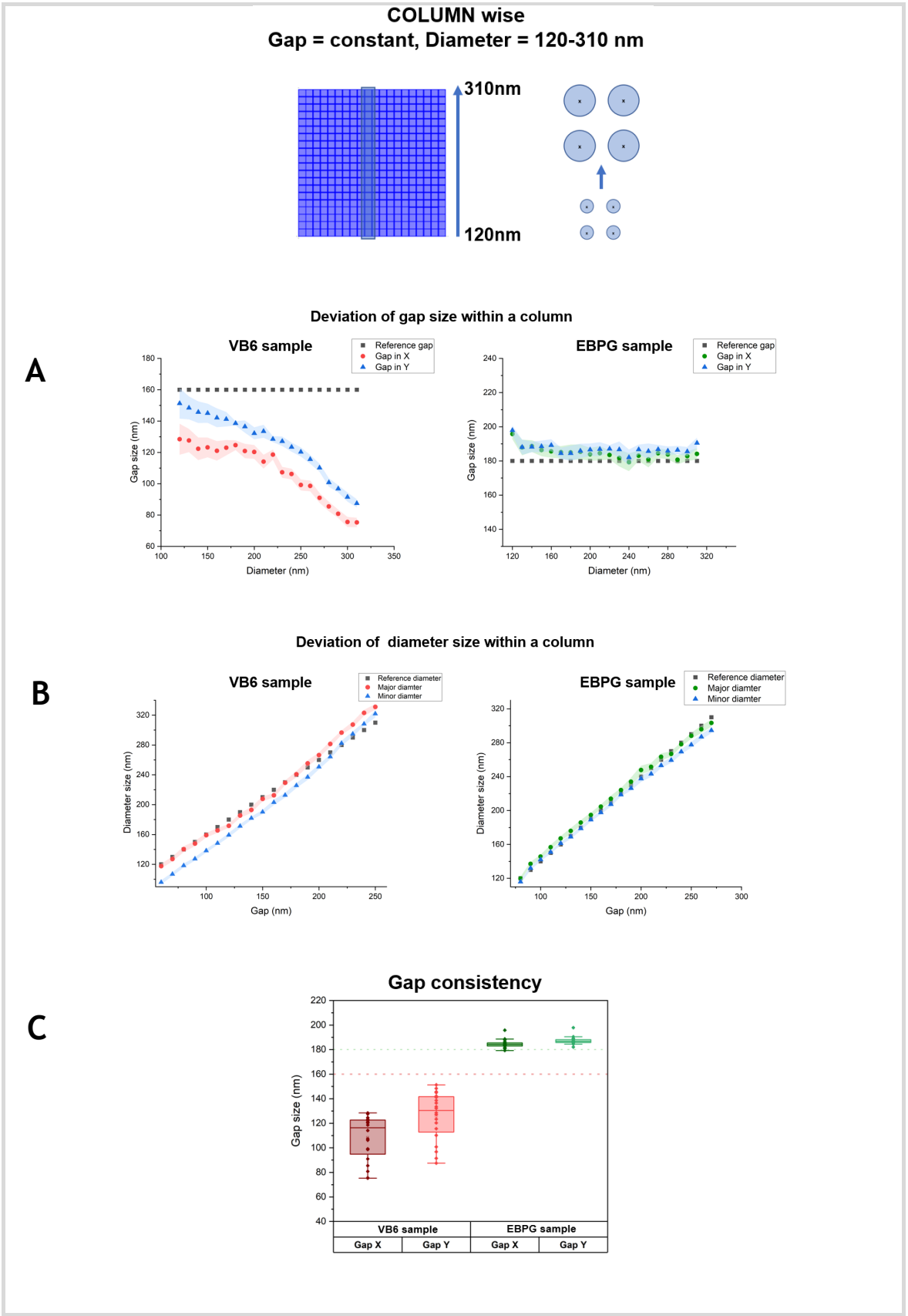

Figure 2.10 Column wise cross-sectional analysis comparison of Si master stamps VB6 sample and EBPG sample. The comparison aims to systematically depicts the variations in quality within a given column, where outcomes of nanoarrays demonstrate constant gap size between nanostructures while exhibiting an increasing diameter size, falling within the range of 120-310 nm (see top diagram). Panel A – scatter plots showing the outcome when assessing the constant gap size. Panel B – scatter plots showing the outcome when evaluating the variable parameter, diameter size. Panel C – box plot summarizing the gap consistency.

On the other hand, gap y parameter demonstrates deviation between 9 nm and 72 nm below the baseline, presented with a standard deviation of 19 nm. Additionally, it is crucial to note a considerable separation between the data points for gap x and gap y, highlighting the notable impact of aspect ratio deformations.

In contrast, the scatter plot for EBPG sample demonstrates a desirable consistency, with values for both gap x and gap y parameters closely aligning with the reference and displaying acceptable aspect ratio deformations. The standard deviation in regard to the reference point for gap in both axes is 3 nm.

The reason why we observe such differences in the quality of both master stamps can be attributed to the interrelation between gap and diameter outcomes. Any deviations in one of these parameters inevitably affect the other, leading to the observed differences. As presented in the row-wise analysis, diameter outcomes in the VB6 sample encounter severe deviations from the baseline, suggesting that these deviations may be pervasive across all nanoarrays. Inevitably, that would be reflected in the gap analysis. Another contributing factor to the inconsistencies in the gap analysis stem from the data file allocating the pitch values or VRU values within the VB6 sample matrix. The pitch values are all the variations in nanoarray periodicity within the library and are also based on estimations, rendering them susceptible to inaccuracies.

Upon revisiting the VB6 sample data file and extracting the pitch values within the assessed column, the range extends from 224 nm to 424 nm. These assigned values exhibit a gradual increase as the diameter size increases, a reflection of the adjustments made to ensure that the gap value remains constant.

However, it is noteworthy that the range of pitch values is inadequately positioned, as it fails to align with the intended objective. Consequently, all nanoarrays fall below the 160 nm reference point. For instance, within the same column, the nanoarray with the smallest diameter is assigned a pitch value of 224 nm. This, however, proves to be excessively low as the resulting features are with major and minor diameter 117 nm and 96 nm and consequently diminishing the size of gap x and y to 128 nm and 151 nm. The deviation amounts to 32 nm for gap x and 9 nm for gap y below the baseline. This outcome relates to the aspect ratio

deformations in the horizontal direction. The nanostructures are with their long axis oriented horizontally and thus the gap in x becomes even further out of range.

Similarly, the nanoarray with the largest diameter in the same column is allocated a pitch value of 424 nm. In this scenario, the centre-to-centre distance again proves to be excessively low for two reasons. Firstly, the expected feature size at this location is 310 nm, leaving a gap distance of only 114 nm, which is 46 nm below the mark. Secondly, features end up larger than anticipated and, consequently, causing gap x and y to diminish by 85 nm and 72 nm, respectively.

In contrast, the pitch values in EBPG sample data file are implemented in the graphic format of the file and accurately represent the intended design. Given the critical interdependence between gap and diameter for the final quality of the master stamp, diameter size accuracy is also addressed through the automated assignment of dose factors across each nanoarray, resulting in uniform energy distribution. Consequently, the reference value of a 180 nm gap is consistently met across all variations of feature sizes within the column, aligning with the intended objective, as evidenced by a plot wherein data points closely converge with the reference.

Panel B of Figure 2.10 is dedicated to evaluating diameter size within the assessed column, with the expected outcome being variations within the range 120-310 nm, as indicated by a reference line.

Upon revisiting the VB6 sample data file and extracting the e-beam exposure doses within the assessed column, the range extends from 300 μCcm^{-2} to 197 µCcm-2. These assigned doses exhibit a gradual decrease as the diameter size increases, reflecting the inversely proportional increase in fill factor along the gradient.

However, it is worth noting that the range of doses is, to some extent, adequately positioned, as it aligns with the intended objective. Consequently, the major diameter for nanoarrays in the 120 nm - 260 nm range aligns with the reference line, while those above 260 nm result in a larger size. Conversely, the minor diameter in the 120 nm - 260 nm range falls below the reference line, whereas those above 260 nm perform as expected. This discrepancy between the major and minor diameter outcomes highlights significant aspect ratio deformations in

the horizontal direction, attributed to the horizontal orientation of the nanostructures' long axis, which consequently affects gap x.

Conversely, all data points for EBPG sample accurately reflect the major and minor diameter in the assessed column, demonstrating alignment with the intended range. The result is yet another proof of the fact that having the design of the nanoarrays in graphic format with predetermined parameters of pitch and diameter, allows for strict control over the file processing and enables BEAMER software to implement computational improvements far more effectively than manual estimations.

The concluding graphic representation in Figure 2.10, Panel C, encapsulates the uniformity in gap size, presented in the form of a box plot. In the case of VB6 sample, both gap x and gap y are represented by broader boxes, with mean values notably distant from each other, revealing a substantial difference of 17.6 nm. The results imply an inconsistency in the gap size and circularity of the nanostructures within the evaluated row expected to adhere to constant values.

In contrast, the parameters of EBPG sample exhibit commendable uniformity, characterized by closely clustered data points and mean values that diverge by merely 2.5 nm. This outcome closely aligns with the objective of the design and demonstrate the desired quality necessary for subsequent experimentation.

The final SEM analysis accessing the quality performance of EBL nanofabrication of the VB6 sample and EBPG sample focus on the consistency within a single nanoarray. Up until now we have discussed the performance across the double gradient library, but it is equally important to identify any deviations within the 1 mm^2 unit of the plasmonic library.

As mentioned in section 2.2.1.2 (CAD/file preparation of EBPG sample), arrays greater than 100 x 100 μm are exhibiting the “proximity effects” during e-beam exposure and if no correction is applied, the features in the centre will have a larger size than those at the edge and corners. This is a result from the additional absorbed energy in the centre area of the resist originating from backscattered electrons. Corners and edges are the areas rendered to always absorb less energy. VB6 sample is not corrected for the “proximity effects” whereas the file

processing of EBPG sample includes this important adjustment. In order to visualize the outcome, we have compared a cluster of 9 areas within a nanoarray where SEM images were obtained namely – corner 1 to 4 taken from all four corners, middle 1 to 4 taken from the middle area and centre which is the most important. A small diagram in the beginning of Figure 2.11 is depicting the map of the sampled zones.

The first piece of analysis in Panel A is showing if the expected consistency in diameter size is met in both Si masters. The VB6 sample bar plot with a reference dotted line at 220 nm perfectly demonstrates the proximity effect issues where diameter results in the periphery is roughly around 180 nm which is 40 nm below the baseline and the cluster sampled from the middle area and centre is around 210 nm, which is 30 nm larger than the periphery but still 10 nm below the reference point.

In contrast, EBPG sample bar plot with a reference dotted line at 250 nm demonstrates perfectly executed proximity effect correction where all sampled areas within the nanoarray hit the mark.

The second piece of analysis in Panel B is showing if the expected consistency in gap size is met in both Si masters. The VB6 sample bar plot with a reference dotted line at 100 nm perfectly demonstrates the diameter – gap interdependence.

As the middle area and centre are with larger diameter size this render the size of gap to significantly diminish to about 65 nm which is 35 nm below the mark. All values for gap size taken from the corners are around 10 nm below the reference point.

In contrast, EBPG sample bar plot with a reference dotted line at 280 nm demonstrates the diameter – gap interdependence. When the consistency in diameter size is maintained that inevitably reflects into a consistent gap parameter.

The concluding graphic representation in Figure 2.11, Panel C, encapsulates two box plots visualising the distribution of data for diameter and gap size respectively.

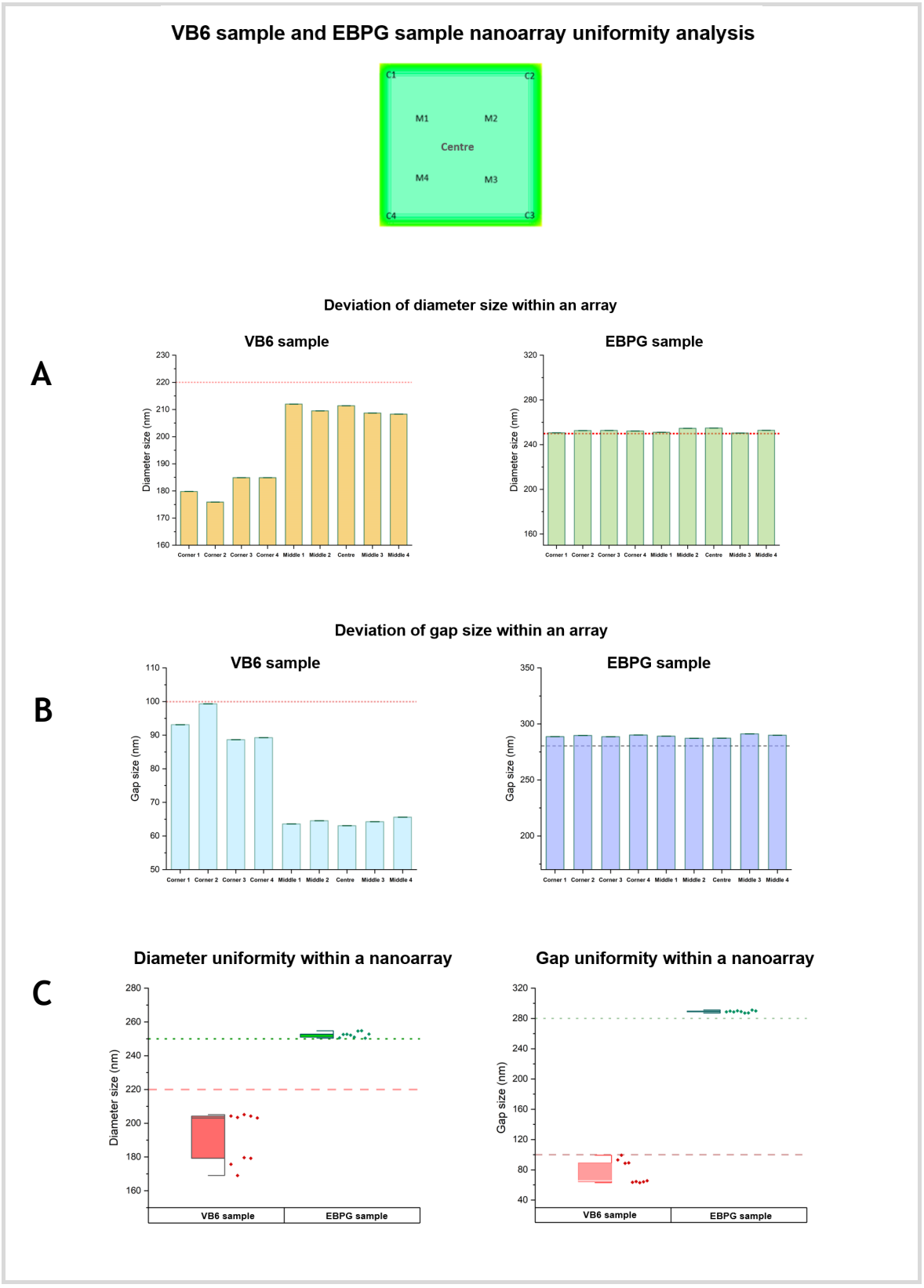

Figure 2.11 Uniformity within nanoarray analysis - comparison of Si master stamps VB6 sample and EBPG sample. The comparison aims to systematically depicts the variations in quality within a given nanoarray. Design parameters of size of diameter and gap taken from all corners, middle area and centre are tested for consistency. Panel A – bar plots showing the outcome when assessing diameter size. Panel B – bar plots showing the outcome when evaluating the gap size. Panel C – box plots summarizing the diameter and gap consistency.

In the case of VB6 sample, both diameter and gap are represented by broader boxes, where data points are divided in two distinct clusters representing the periphery and middle area respectively. The results imply an inconsistency in both parameters within the evaluated nanoarray that was expected to adhere to constant values.

In contrast, the parameters of EBPG sample exhibit commendable uniformity, characterized by closely clustered data points for diameter and gap. This outcome closely aligns with the objective of the design and demonstrate the desired quality necessary for subsequent experimentation.

2.2.3 Morphological comparative analysis of VB6 sample and EBPG sample to its respective polystyrene replica

After the successful production of 100 plastic pieces, the polystyrene devices were subjected to thermal evaporation of thin gold film to make the nanopillar arrays plasmonically active via Plassys MEB 550S electron beam evaporator. Figure 2.12 is depicting a schematic diagram of a plastic replica with nanopillar arrays formed after injection moulding against the PET foil with nanohole arrays used as an inlay.

On the right side of the schematic diagram is shown an actual image of the polystyrene replica with a 20 x 20 double gradient library in the middle section. A schematic diagram of the plasmonically active nanopillars is also depicted in Figure 2.12 with a top and a side view of the device. The thin layer film is continuous, covering the nanostructures as well as the bottom of the surface. As the thermal evaporation of gold is directional, it is worth noting that the thickness of gold deposited on top of the nanopillars, and the bottom of the surface is thicker than the sides of the cylindrical nanostructures.

The second image on Figure 2.12 shows the final product of a high-throughput templet-assisted fabrication of a double gradient plasmonic array library utilized further as a plasmonic sensing platform.

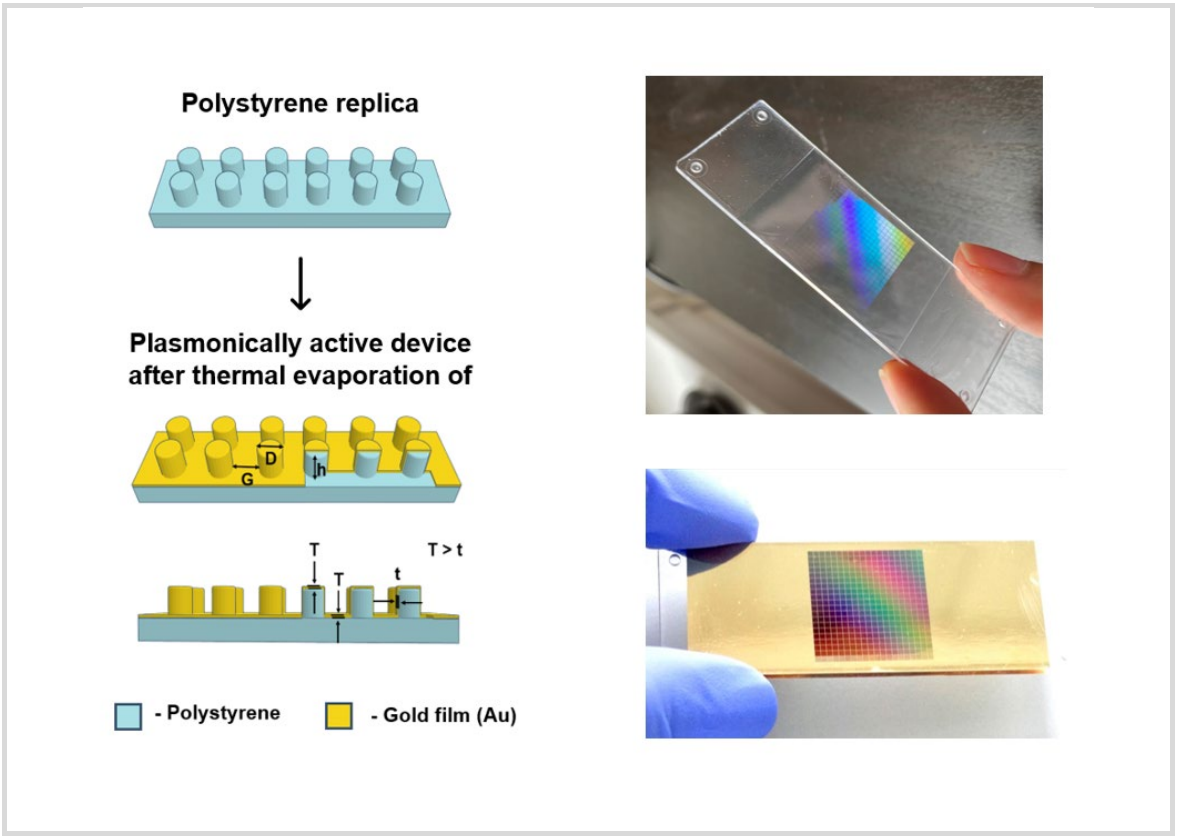

Figure 2.12 Schematic diagram of polystyrene replica (left) and an actual image of it (right), as well as top view schematic diagram of the replica coated with a thin film of gold continuously covering the nanostructures and the bottom of the device. D, G and h - denote the diameter, gap and height of the nanopillars in the square array. The side view of the schematic diagram illustrates the directional deposition of the gold during thermal evaporation that covers the top and bottom of the device with a slightly thicker layer of gold compared to the sides of the nanopillars. An image on the right side demonstrates the DGPAL device coated with gold.

In order to assess the quality of the plasmonic sensing platform a nanoscale comparison between the Si master stamp and the polystyrene replica is performed. As usual, the comprehensive SEM morphological characterisation is detailed for the translation of VB6 sample and EBPG sample to its respective polystyrene replica. We have used the same concept of horizontal and vertical cross-sectional assessment.

In Figure 2.13, we present a row cross sectional analysis that involves the comparative assessment of both silicon master stamps and their corresponding polystyrene (PS) replicas. Panel A is dedicated to the examination of how effectively the quality of VB6 sample is transferred to the PS replica. The objective here is to maintain a consistent diameter, as indicated by a reference line representing the target dimension of 220 nm.

The graphical representation of VB6 sample in the scatter plot reveals substantial deviations from this specified reference point. Notably, these deviations exhibit a consistent increasing trend in tandem with the expansion of the gap size.

This observation aligns with the earlier discussion in Figure 2.9, where we provided a comprehensive clarification of the limitations associated with the selected range of exposure doses for the VB6 sample master stamp. This analysis highlighted how the imprecise exposure doses negatively influence the resulting diameter size.

In line with these findings, it is not surprising that the polystyrene replica, being an exact duplicate of the Si master stamp, mirrors these deviations from the reference diameter. This correspondence underscores the parallel behaviour observed between the two substrates in the nanofabrication process.

The second plot is dedicated to evaluating gap size within the assessed row, with the expected outcome being variations within the range 60-270 nm, as indicated by a reference line.

The scatter plot evaluating the gap size between the VB6 sample Si to PS transcription stage reveals that all data points fall significantly below the reference.

Panel B is dedicated to the examination of how effectively the quality of EBPG sample is transferred to the PS replica. The objectives here are identical, maintaining a consistent diameter at 220 nm and varying gap size within the range 60-270 nm.

In contrast, the scatter plot for EBPG sample demonstrates a desirable consistency, with values taken from both Si and PS substrates, with diameters closely aligning with the reference. The second plot also advocates for high quality achievement as the gap size variations closely align with the baseline.

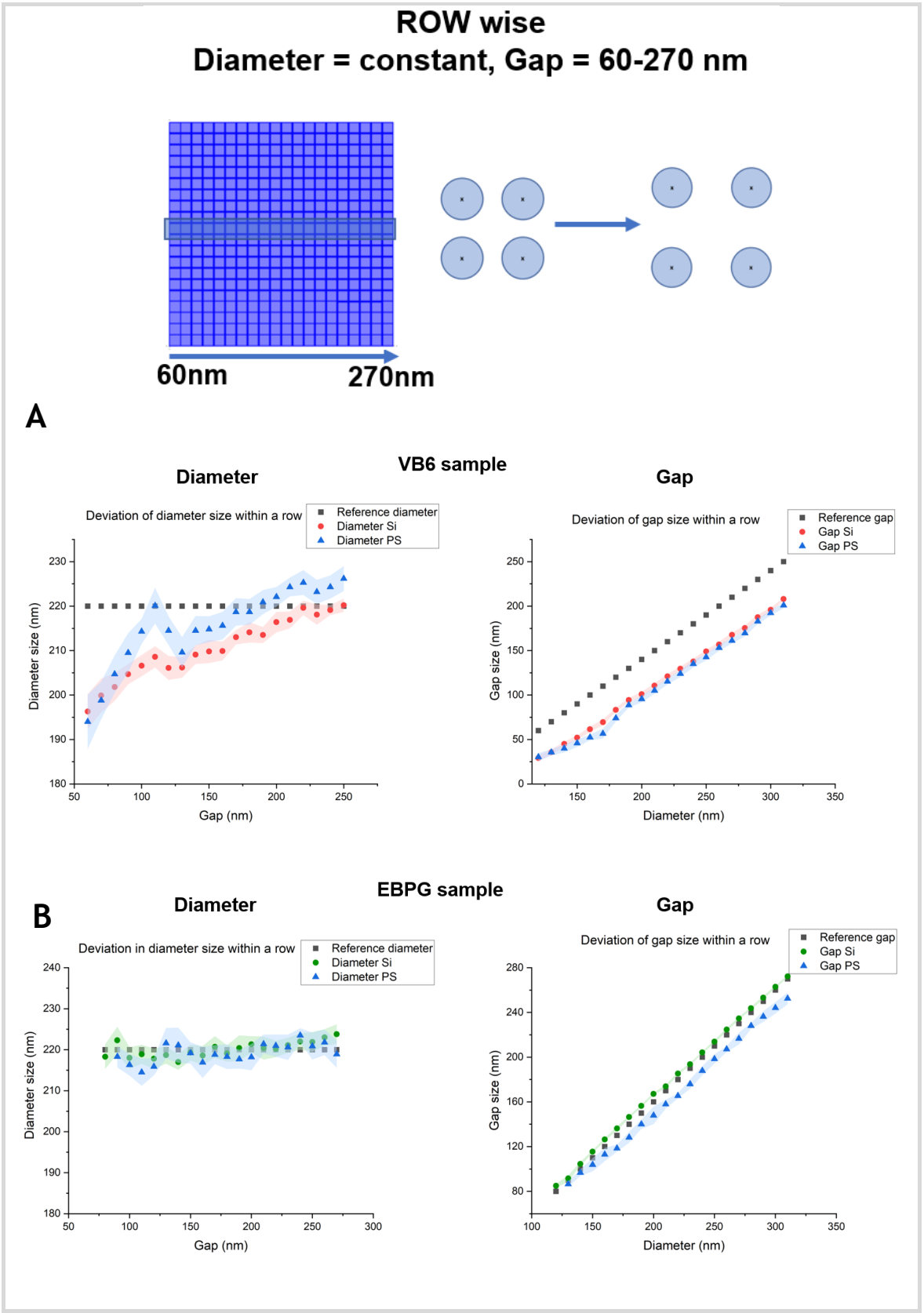

Figure 2.13 Row wise cross-sectional analysis comparison of Si master stamps VB6 sample and EBPG sample with their respective polystyrene (PS) replica. The comparison aims to systematically depicts the variations in quality after injection moulding process is used to replicate the metasurfaces from the Si master stamp. Within a given row, the outcomes of nanoarrays demonstrate constant diameter size while exhibiting an increasing interspacing between nanostructures, falling within the range of 60-270 nm (see top diagram). Panel A – scatter plots showing the outcome when assessing the VB6 sample Si to PS. Panel B – scatter plots showing the outcome when assessing the EBPG sample Si to PS.

Figure 2.14 presents a column cross sectional analysis that involves the comparative assessment of both silicon master stamps and their corresponding polystyrene (PS) replicas. Panel A is dedicated to the examination of how effectively the quality of VB6 sample is transferred to the PS replica.

The objective here is to maintain a consistent gap size, as indicated by a reference line representing the target dimension of 160 nm.

The graphical representation of VB6 sample in the scatter plot reveals substantial deviations from this specified reference point. Notably, these deviations exhibit a consistent decreasing trend in tandem with the expansion of diameter size.

This observation aligns with the earlier discussion in Figure 2.10, where we provided a comprehensive clarification of the limitations associated with the selected range of pitch values for the fabrication of the VB6 sample master stamp. This analysis highlighted how the imprecise range of pitch values negatively influence the resulting gap size.

In accordance with these findings, it is not unexpected that the polystyrene replica, being an exact duplicate of the Si master stamp, closely emulates these deviations, diverging far below from the reference gap size.

This alignment between the two substrates underscores the parallel trends observed in the nanofabrication process.

The second plot in Panel A is dedicated to evaluating diameter size within the assessed column, with the expected outcome being variations within the range 120-310 nm, as indicated by a reference line. The scatter plot evaluating the diameter size between the VB6 sample Si to PS transcription stage reveals that most of the data points aligns with the reference. There are few points within the range of 280 – 310 nm that result in larger diameter sizes.

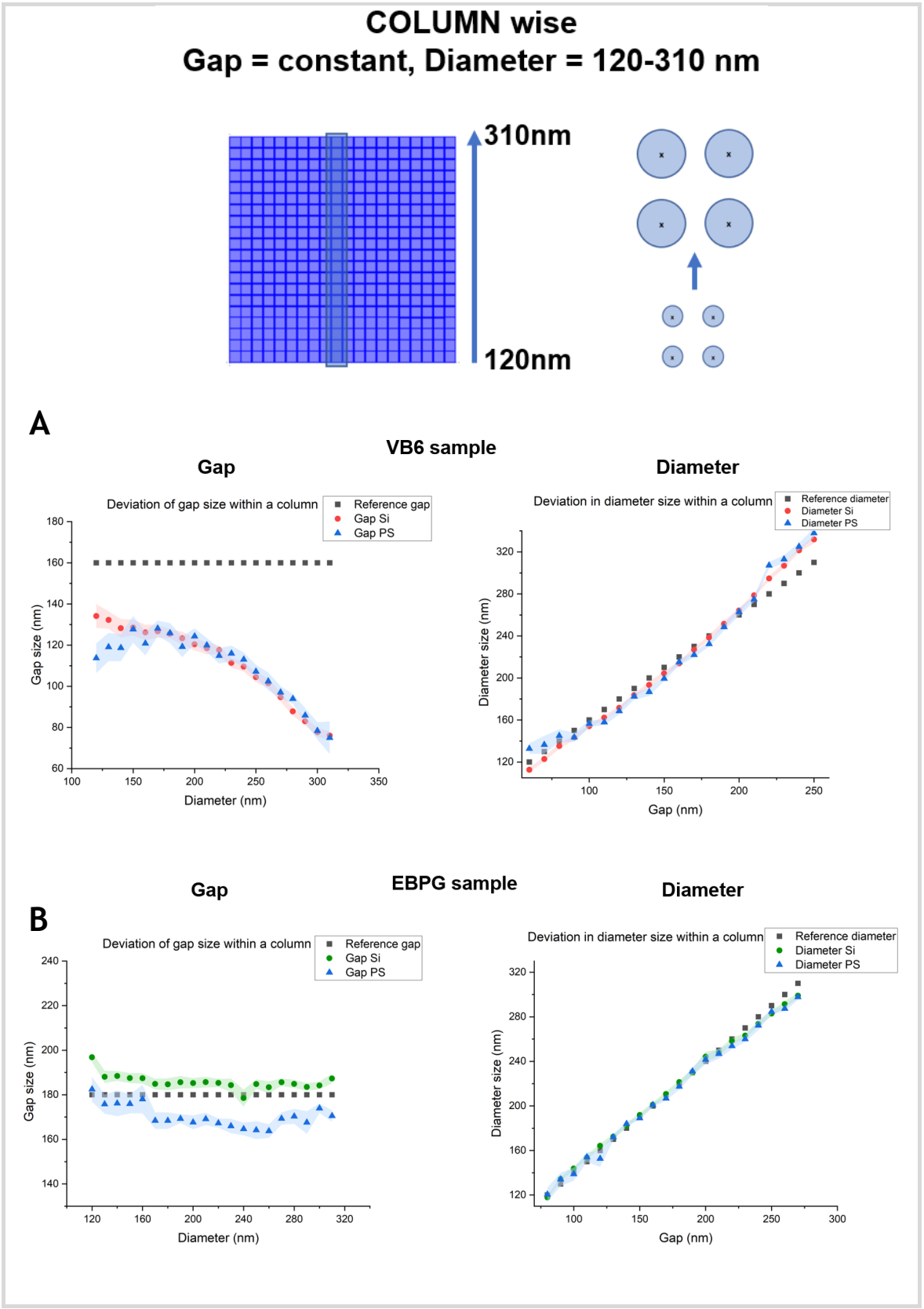

Figure 2.14 Column wise cross-sectional analysis comparison of Si master stamps VB6 sample and EBPG sample with their respective polystyrene (PS) replica. The comparison aims to systematically depicts the variations in quality after injection moulding process is used to replicate the metasurfaces from the Si master stamp. Within a given column, the outcomes of nanoarrays demonstrate constant gap size while exhibiting an increasing diameter size of nanostructures, falling within the range of 120-310 nm (see top diagram). Panel A – scatter plots showing the outcome when assessing the VB6 sample Si to PS. Panel B – scatter plots showing the outcome when assessing the EBPG sample Si to PS.

This observation aligns with the earlier discussion in Figure 2.10, where we provided a comprehensive clarification of the limitations associated with the selected range of exposure doses for the VB6 sample master stamp. This analysis highlighted how the imprecise exposure doses negatively influence the resulting diameter size in both evaluated substrates.

Panel B is dedicated to the examination of how effectively the quality of EBPG sample is transferred to the PS replica. The objectives here are identical, maintaining a consistent gap at 180 nm and varying diameter size within the range 120-310 nm.

In contrast, the scatter plot for EBPG sample demonstrates a desirable consistency, with values taken from both Si and PS substrates, with gap sizes closely aligning with the reference. The second plot also advocates for high quality achievement as the diameter size variations closely align with the baseline.

The final SEM analysis accessing the quality performance of the transcription from Si to PS of the VB6 sample and EBPG sample focus on the consistency within a single nanoarray. Up until now we have discussed the performance across the double gradient library, but it is equally important to identify any deviations within the 1 mm^2 unit of the plasmonic library.

In order to visualize the outcome, we have compared a cluster of 9 areas within a nanoarray where SEM images were obtained namely – corner 1 to 4 taken from all four corners, middle 1 to 4 taken from the middle area and centre which is the most important. A small diagram in the beginning of Figure 2.15 is depicting the map of the sampled zones.

The first piece of analysis in Panel A is showing if the expected consistency in diameter size is met. The VB6 sample bar plot with a reference dotted line at 220 nm perfectly demonstrates the proximity effect issues where on Si, diameter results in the periphery are roughly around 200 nm which is 20 nm below the baseline and the cluster sampled from the middle area and centre is around 230 nm, which is 30 nm larger than the periphery and 10 nm above the reference point. On the PS replica results from periphery are roughly around 190 nm which

is 30 nm below the baseline and the cluster sampled from the middle area and centre is around 220 nm aligning with the reference.

The second piece of analysis in Panel A is showing if the expected consistency in gap size is met in both Si and PS substrates. The VB6 sample bar plot with a reference dotted line at 200 nm perfectly demonstrates the diameter – gap interdependence. As the middle area and centre are with larger diameter size this render the size of gap to significantly diminish to about 140 nm which is 60 nm below the mark. All values for gap size taken from the corners are around 25 nm below the reference point. On the PS replica results from periphery are roughly around 190 nm which is 10 nm below the baseline and the cluster sampled from the middle area and centre is around 150 nm, which is 50 nm below the reference.

In contrast, EBPG sample bar plot in Panel B demonstrates perfectly executed proximity effect correction where all sampled areas within the nanoarray hit the mark. The reference dotted line at 220 nm is merging with diameter size measurements and gap size. When the consistency in diameter size is maintained that inevitably reflects into a consistent gap parameter.

The concluding graphic representation in Figure 2.15, Panel C, encapsulates two box plots visualising the distribution of data for diameter and gap size respectively.

In the case of VB6 sample, both diameter and gap are represented by broader boxes, where data points are divided in two distinct clusters representing the periphery and middle area respectively.

The results imply an inconsistency in both parameters within the evaluated nanoarray that was expected to adhere to constant values.

In contrast, the parameters of EBPG sample exhibit commendable uniformity, characterized by closely clustered data points for diameter and gap.

This outcome closely aligns with the objective of the design and demonstrate the desired quality necessary for subsequent experimentation.

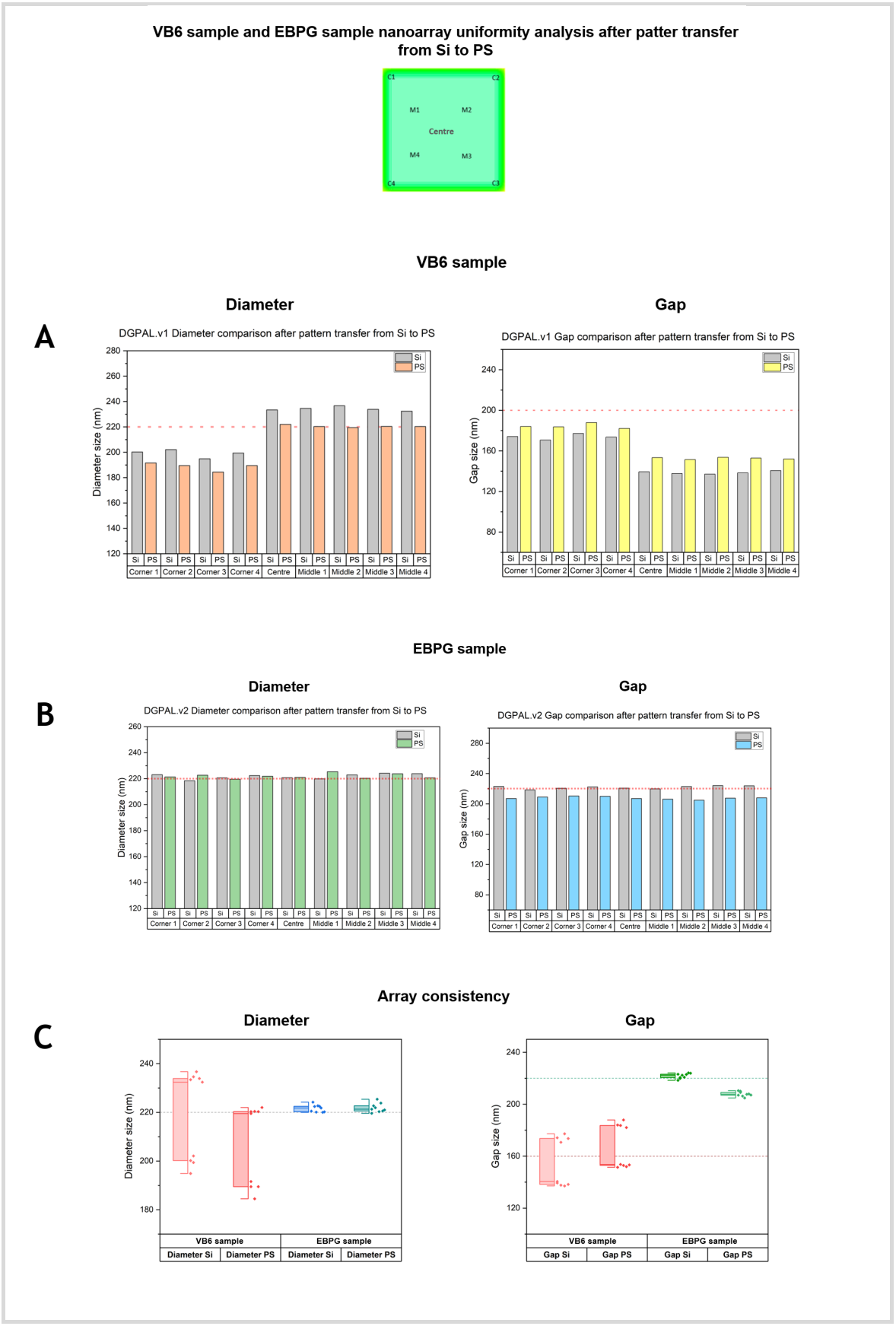

Figure 2.15 Uniformity within a nanoarray – comparison of Si master stamps VB6 sample and EBPG sample with their respective polystyrene (PS) replica. The comparison aims to systematically depicts the variations in quality within a given nanoarray. Design parameters of diameter and gap taken from all corners, middle area and centre are tested for consistency. Panel A – diameter and gap size of VB6 sample transcription. Panel B – diameter and gap size of EBPG sample transcription. Panel C – box plots summarizing the diameter and gap consistency.

In summary, the outcomes indicate a notably high degree of fidelity in replicating the nanoarray library from the silicon (Si) substrate onto the polystyrene replicas, without any discernible alteration to the nanoscale structures. This underscores that high-throughput template assisted nanofabrication via injection moulding provides a high efficiency in fabrication achieving regularly-arranged plasmonic nanostructure arrays across expansive areas.

Furthermore, it becomes evident that the imperfections accumulated during the fabrication of the Si master stamp will be transferred on the PS substrate during the replication process. This observation underscores the necessity of an extensive focus that must be invested into the fabrication of the Si master stamp and most importantly into the design and file preparation of it. This will ensure consistency, uniformity and accuracy of the design parameters and ultimately high quality replication onto the PS substrate.

The translation of VB6 sample and EBPG sample to its respective polystyrene replica is assessed for another parameter – height of nanopillar structures. The was made possible with a comprehensive AFM (atomic force microscopy) analysis performed on a few locations on the Si and PS substrates. To ensure high performance, improved quality and speed in measurements, the Bruker's Dimension Icon® (Bruker Nano GmbH, Germany) tip-scanning AFM technology was used.

The measurements were performed with a standard OTESPA AFM probe with < 7 nm tip radius for standard tapping mode imaging in air. The scan size of 1 µm, and a scan rate of 0.45 Hz ensured proper AFM tip tracking of the surface with overlapping height contours.

Figure 2.16 summarize the AFM feature height analysis of VB6 sample Si to PS replication. The Si master stamp is developed with a 300 nm nanopillar height as a result from the dry etch process. Notably, this height was consistently maintained across various locations within the library, even when the periodicity of the nanoarrays varied.
However, after the replication process, the nanopillar height exhibit a range of 140 nm to 160 nm, losing approximately half of the original height.

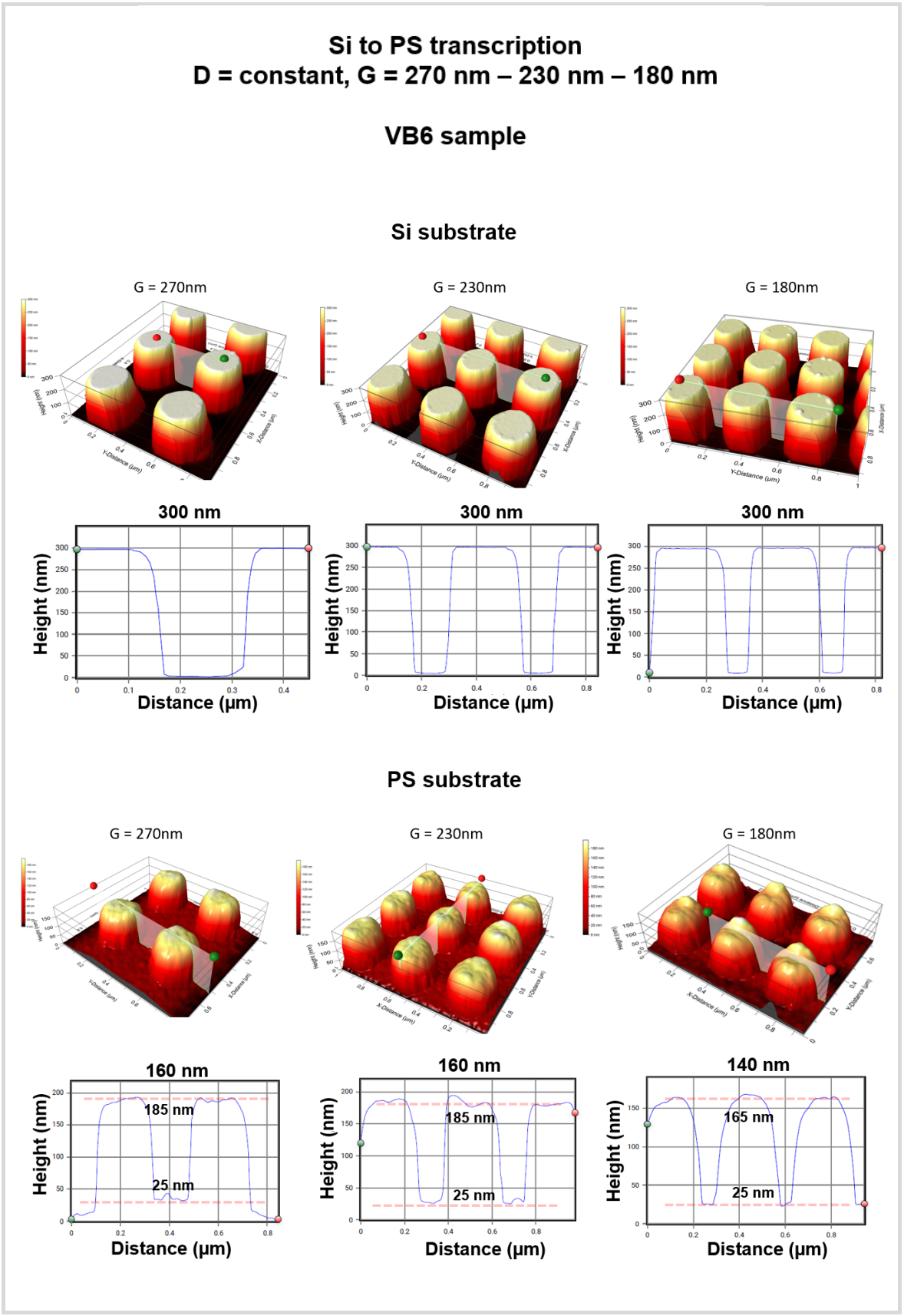

Figure 2.16 AFM feature height analysis of VB6 sample Si to PS transcription. The figure depicts the results of VB6 sample analysis where Si nanopillars from different locations with varying gap – 270nm, 230nm and 180nm, show consistency at 300 nm whereas the PS substrate demonstrate deviations in the outcome. The nanopillars after injection moulding are within the height range of 160 nm and 140 nm with a 25 nm surface roughness at the bottom of the substrate.

Furthermore, the analysis reveals an uneven bottom surface, deviating by approximately 25 nm from the baseline.

Figure 2.17 provides a concise overview of the AFM feature height analysis of EBPG sample Si to PS replication. In this instance, the Si master stamp was initially engineered with nanopillars standing at 280 nm, again derived from the dry etch process. This outcome is consistent throughout different locations in the library with changing periodicity of the nanoarrays. Post-replication, the nanopillar heights fall within a range of 210 nm to 218 nm, representing an approximately 22% reduction from the original height. The roughness of the bottom surface exhibits acceptable variation, deviating approximately 2 nm to 10 nm from the baseline.

The observed variations in the replication process quality may find a conclusive explanation through an investigation into the quality of the PET foil. However, certain constraints prevented such an analysis. Firstly, the soft and deformable nature of the PDMS layer makes surface measurements on PDMS with indentations challenging [151]. Secondly, the high-energy electron beam utilized in imaging may inflict permanent damage on the observed sample [152], leading to swelling and distortion, a phenomenon attributed to the interaction between the PDMS and the electron beam.

A third constraint arises from the material's transparency, making it difficult to focus on specific areas and maintain measurement consistency. To overcome this limitation, sputter-coating the PET foil was considered, but this would render it unsuitable for injection moulding.

Given the impracticality of analysing the PET foil, we offer plausible explanations for the observed differences in the quality of the replication process. These differences can be attributed to the characteristics of the inlay fabrication process. During replication, each polystyrene sample is moulded to mimic the morphology of the inlay.

As detailed in section A2 from the Appendix (describing the inlay fabrication) the nanoimprint lithography for VB6 sample and EBPG sample was executed with distinct soft stamp materials, known as SmartNIL.1 and SmartNIL.2, respectively. Both SmartNIL.1 and SmartNIL.2 are proprietary formulations commercially available from EV Group GmbH.

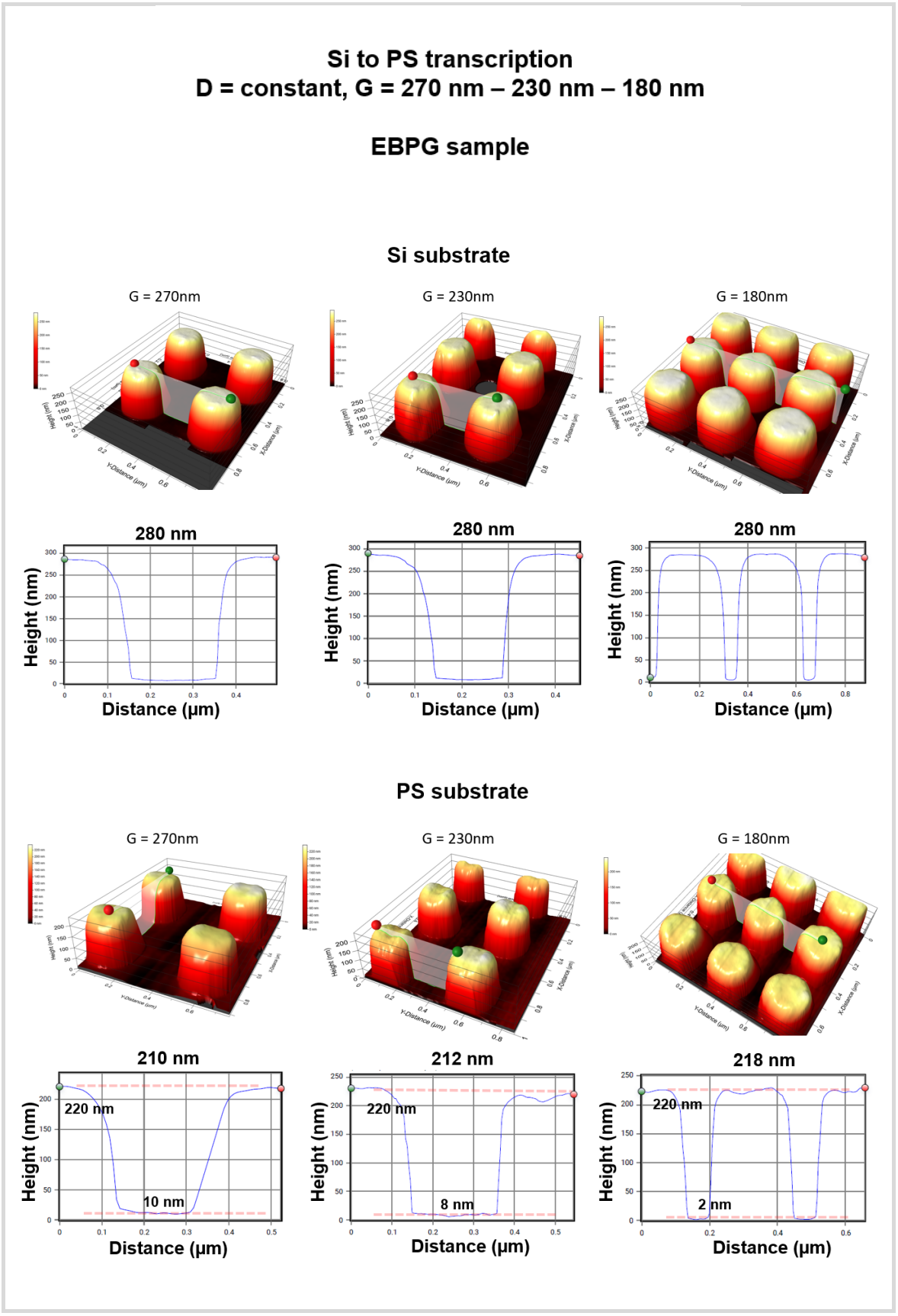

Figure 2.17 AFM feature height analysis of EBPG sample Si to PS transcription. The figure depicts the results of EBPG sample analysis where Si nanopillars from different locations with varying gap – 270nm, 230nm and 180nm, show consistency at 280 nm and the PS substrate demonstrate consistency in the outcome. The nanopillars after injection moulding are within the range of 210 nm and 218 nm with a bottom substrate surface roughness ranging from 2 nm to 10 nm.

SmartNIL.1 encountered challenges such as de-wetting issues and retraction following the spinning of the working stamp, leading to an uneven and higher thickness distribution across the Si master stamp [153]. These limitations led to its replacement by the more reliable and performance-optimized SmartNIL.2. Conversely, SmartNIL.2 represents an improved formulation designed for UV-NIL technology, offering enhanced accuracy in the process flow application. This enhancement significantly improved feature resolution and the quality of inlay fabrication.
This reason might influence the outcome after the exposure time finish and create a higher surface roughness at the bottom [154]. Conversely, SmartNIL.2 represents an improved formulation designed for UV-NIL technology, offering enhanced accuracy in the process flow application. This enhancement significantly improved feature resolution and the quality of inlay fabrication.

2.3 Summary/Conclusion

Within this chapter was discussed the nanofabrication of plasmonic nanostructures organized in a double gradient plasmonic array library.

The methodology adheres to a fast and cost-effective approach of nanofabrication allowing pattern transfer and mass-replication of high-resolution periodic arrays. In such manner, the fabrication of a plasmonic library containing hundreds of geometry combinations on a single chip becomes an achievable task and a vast number of characteristic properties of the plasmonic behaviour can be extracted systematically.

The nanofabrication multi-step process consists of three major milestones, namely – fabrication of the master stamp, fabrication of the inlay and injection moulding. The fabrication of nanoscale arrays involves high-resolution top-down EBL technique and always begins with a computer aided design and file preparation stage. A simplified and advanced CAD/file preparation approach was implemented to produce a double gradient plasmonic library referred to respectively as DGPAL version 1 (VB6 sample) and DGPAL version 2 (EBPG sample).

The simplified approach creates the design based on the exposure commands controlling the electron beam e.g., dose and VRU information known as “dot

writing". This would mean that the design stage does not include graphic data and thus cannot be optimised further with any data processing software.

The advanced approach was based on graphic data and represent the arrays with actual shapes. The generation of the graphic data file was automated via customised Python code and CNST toolbox. Data in GDS format is readable by various software programs such as TRACER and BEAMER lithography software. These provided highly efficient proximity effect correction by implementing a customized PSF simulated to be utilised in an absorbed energy distribution algorithm. Additionally, exposure fields placement was positioned automatically avoiding stitching to intersect nanoarrays. High-resolution shape detection facilitated electron beam shots filling with 10 nm BSS which achieving the desired circularity.

EBL patterning of the resist was carried out using two distinct generations of EBL systems. The old generation Vistec VB6 UHR EWF electron beam tool was employed to scan the VB6 sample, whereas the state-of-the-art EBL system Raith EBPG 5200 was used to pattern the EBPG sample.

The master stamps fabricated via the simplified and advanced approach strategies were comparatively analysed and results demonstrate enormous differences in quality.

Optical imaging has revealed several issues in the development of nanoarrays within the VB6 sample framework. These challenges have resulted in unsuccessfully developed areas reducing the nanoarray varieties of the VB6 sample and a vast area affected by stitching issues during the fracturing process of the patterns. Consequently, a significant portion of the surface bears missing nanopillars within the arrays. Furthermore, the use of a single-beam exposure method for defining dot contours has led to noticeable aspect ratio deformations in the features. In-depth SEM cross-sectional analysis has unveiled a range of discrepancies, notably affecting the interplay between diameter and gap parameters across the entire library and within each nanoarray. The post-replication SEM analysis reveals that all defects accumulated in the Si master stamp are translated onto the PS replica. Additionally, post-replication AFM

analysis indicates a noteworthy 50% reduction in the height of nanopillars, along with an uneven bottom surface.

These challenges have been systematically addressed in the development of EBPG sample. This iteration incorporates an improved shape-writing technique, accounting for the proximity effect and employing high-resolution e-beam exposure to create a library with nanoarrays characterized by enhanced accuracy. Optical images now display 400 meticulously developed arrays, all free from stitching issues and maintaining high aspect ratios. Detailed cross-sectional SEM analysis underscores the alignment of features with design parameters throughout the library and showcases high consistency within each individual nanoarray. Post-replication analysis attests to the superior quality of the PS replica, meeting the standards necessary for subsequent experimentation. Furthermore, post-replication AFM analysis reveals consistent nanopillar heights, primarily attributed to the utilization of the enhanced SmartNIL.2 formulation, specifically tailored for UV-NIL technology.

Based on the outcomes and conclusions presented in this chapter, all subsequent analyses and research experiments involving a double gradient plasmonic array library will exclusively utilize the EBPG sample device.

The subsequent chapter delves into an exploration of the resonance responses generated by the plasmonic nanoarrays within the double gradient library. It intricately examines the progressive tuning of resonance peaks observed through orthogonal adjustments of parameters, specifically the dimensions of diameter and periodicity.

Chapter 3 Resonance characterisation

3.1 Introduction

After a detailed description of the creation and morphology characterisation of the double gradient device, this chapter will be exclusively dedicated to the resonance performance of the plasmonic arrays.

While a plethora of literature has previously documented the plasmonic behaviour of nanoparticles with diverse shapes and properties, there remains a notable research gap in the investigation of injection-moulded nanopillars featuring a continuous gold film coating. Consequently, the resonance profile and the underlying mechanisms governing peak tuning in this specific context have yet to be fully elucidated. In order to provide a more comprehensive understanding of this concept, we have developed the double gradient platform, which enables a systematic exploration of the significance of design parameters in shaping resonance wavelengths.

Furthermore, subsequent to the identification of resonance characteristics within each nanoarray, a pivotal facet of this study involves the classification of their sensitivity performance. The data collected from this rigorous analysis will serve as a valuable resource in pinpointing the ideal combination of design parameters for optimal compatibility with the Nicoya OPEN SPR tool.

In this chapter, section 3.2 is dedicated to the spectroscopy analysis of the project. It involves a detailed description of the optical setup for resonance characterisation, followed by the data analysis algorithms used to process and organise the measurements. Consequently, the analysed data is presented and visualised in a comprehensive manner, where the discussion and argumentation are displayed in the resonance characterisation subsection. This includes segments focusing on peak tuning through variations in design parameters, revealing the significant potential of the library design, and plasmonic activation by adjusting the thickness of gold, adding further depth to the domain of peak engineering. The following segment reveals the regions on interest within the double gradient library and demonstrates the multifaceted capabilities of the device. Section 3.3 supplements the experimental results presented in section 3.2 with simulation

data. The simulation model was validated and refined through iterative adjustments and comparisons with experimental data, ensuring its accuracy and reliability. The refined model revealed deeper insight into the intricate interaction of light with periodically corrugated metal thin films. Lastly, section 3.4 explores the sensitivity performance of the double gradient library. A summary of the chapter and extracted conclusions are reported in section 3.5.

3.2 Spectroscopy

3.2.1 Optical setup for resonance characterisation

A decision was made to minimise the complexity of the experimental setup based on the fact that the majority of commercial SPR instruments operate at normal incidence.

Nanostructured metal films as the double gradient plasmonic array library can be excited by direct illumination and measured with conventional transmission-mode spectroscopy as depicted in Figure 3.1 (and Figure 1.7-B). The rationale behind adopting this approach for resonance characterisation lies in the significant simplification of the experimental setup. It does not require cumbersome optics or alignment to a specific contrast angle. It allows to be incorporated into microfluidic systems, well plates and can be easily reproduced as all components can be miniaturized in affordable, compact, and portable configuration.

Following the systematic investigation and signal acquisition, the results remain universally applicable particularly if any of the plasmonic configurations are integrated into a system with a similar spectroscopy design. Moreover, the nanoplasmonic biosensors explored in this study could be seamlessly developed into a point-of-care device, incorporating automated signal reading through a mobile device.

The resonance characterisation of the DGPA library was performed on a Nikon Diaphot microscope with a halogen light source coupled through an optical fibre to a CCS200 spectrometer with a detection range from 200 to 1000 nm (Thorlabs, USA). Figure 3.1 depicts a schematic of the optics and an image of the optical setup.

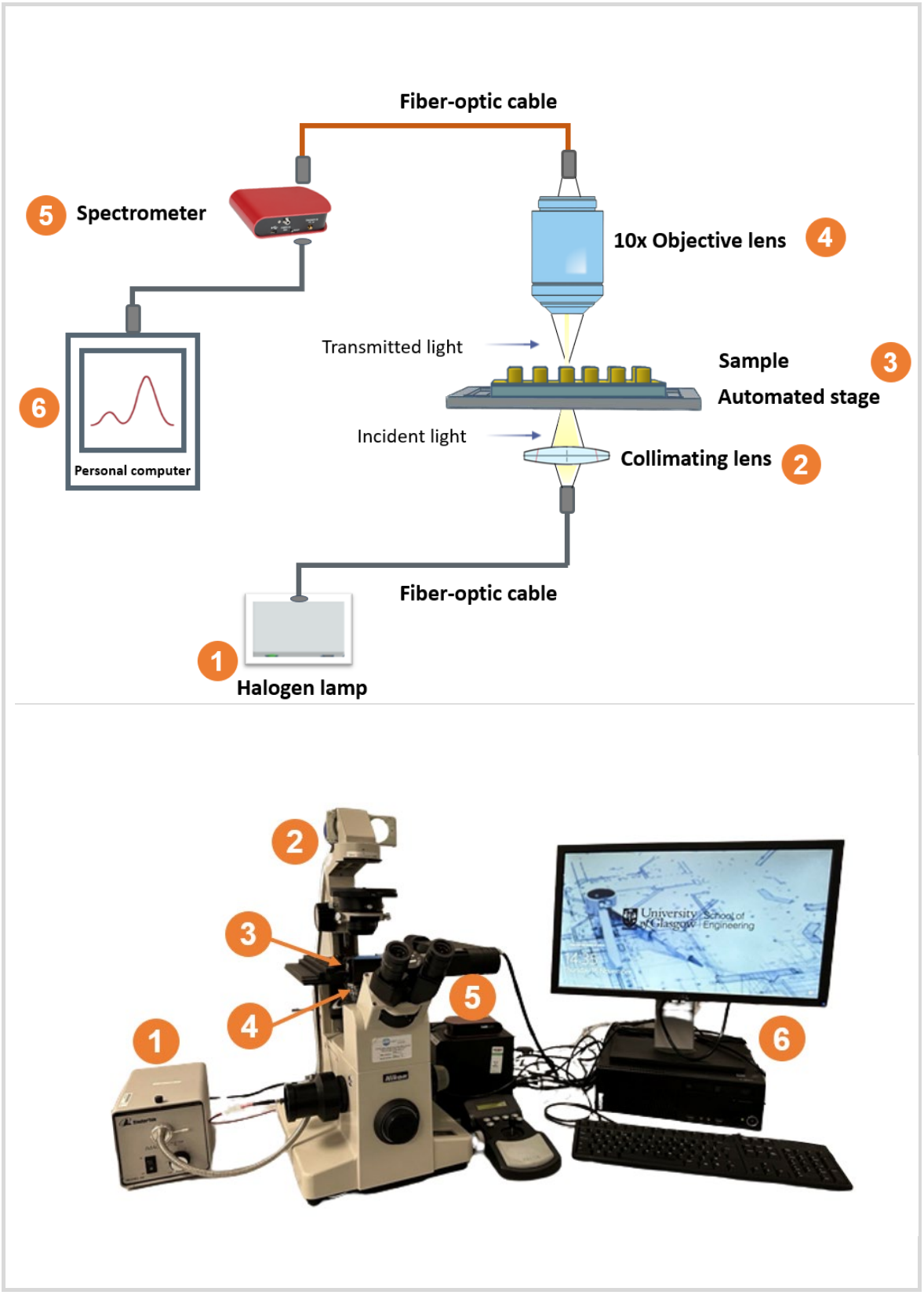

Figure 3.1 Diagram of the optical setup used for the resonance characterisation of the double gradient plasmonic array library. Fiber-optic cables and lenses are used to focus white light on a sample and measure the transmission of light through it using the CCS200 spectrometer (Thorlabs, USA). The output signal was visualized and recorded using the Thorlabs OSA software. The data acquisition process was advanced with an XY automated stage completing a full dataset within a few minutes.

Transmission measurements were taken after collimated beam from a white-light source probe the plasmonic device at normal incidence. A 10x objective was used to couple the transmitted light into an optical fibre attached to a CCS200 spectrometer with spectral resolution < 2nm. This resulted in a field of view size of approximately 0.5 mm covering sufficient middle area of the 1 mm^2 nanoarray. The output signal was visualised using the Thorlabs OSA software after 100 milliseconds integration time.

Transmission measurement from each plasmonic nanoarray was collected in all respective solutions used in the experiment evenly distributed on the surface by a coverglass. Reference measurements were taken on the flat area of the gold coated polystyrene slide away from the patterns matching the same experimental conditions.

In order to address the demanding task of recording 400 transmission measurements, completing a full scan of the double gradient library, an XY automated stage coupled with a controller was used (Figure 3.1 B). The automated stage performs all measurements by moving in an accurately pre-set grid of points within a few minutes.

As each acquisition point is aligned with the middle area of each nanoarray, the step size is set to be equal to the nanoarray pitch which is 1050 μm. All text files are automatically saved in a predefined directory and can be easily imported for analysis.

The integration of automated data acquisitions significantly advanced the project's progression, facilitating the recording of multiple datasets within a single day. Numerous experiments subsequent to the resonance characterization required comprehensive scan recordings in various media, a task that would have been otherwise impractical. The manual process is usually extremely laborious, time consuming (approximately 4 – 5 hours) and susceptible to errors due to the repetitive nature of the task.

3.2.2 Data analysis techniques

Transmission (T) is the fraction of incident light which is transmitted or successfully passes through the sample and comes out the other side.

The transmission measurements were analysed with MATLAB (The MathWorks Inc.) following the data operations presented in Figure 3.2.

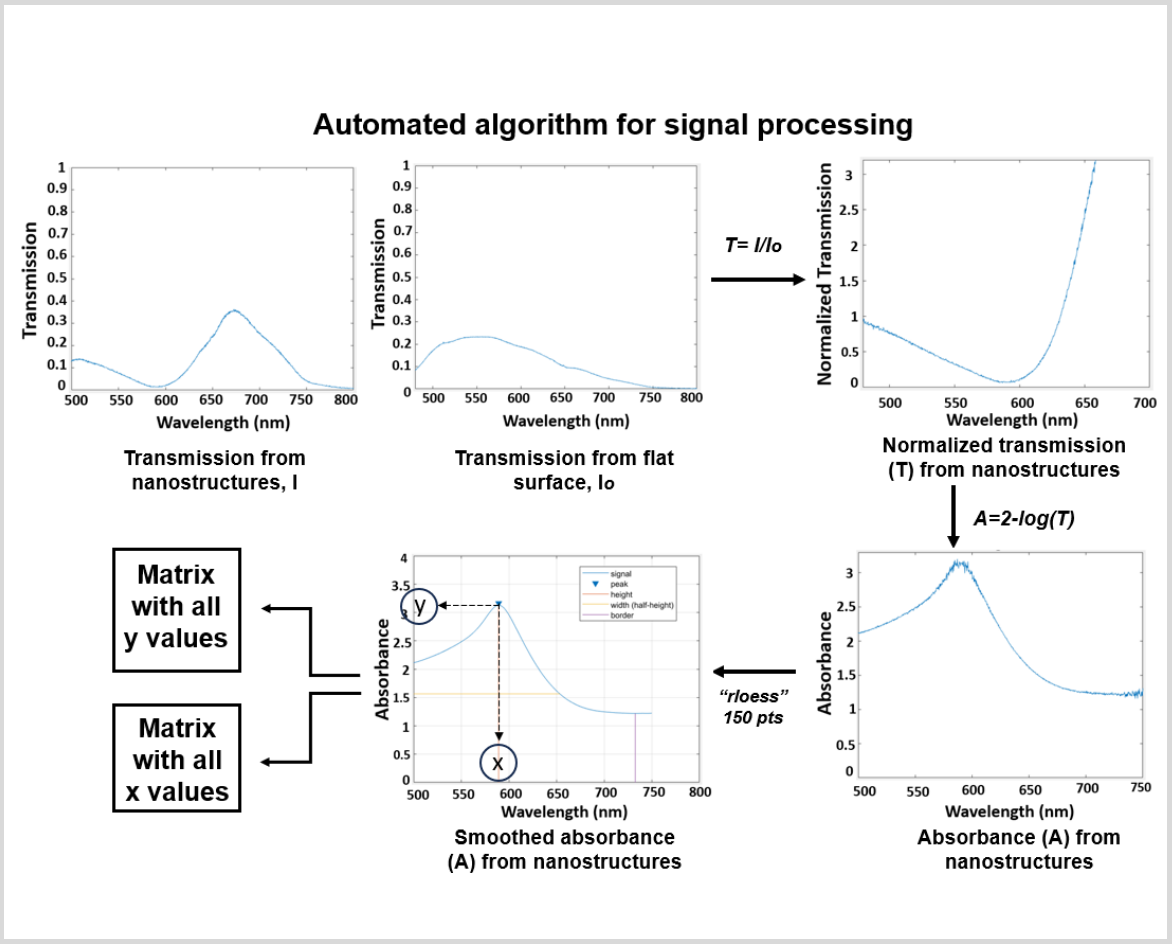

Figure 3.2 Schematic diagram visualizing the automated algorithm for signal processing. Transmission measurements from each nanoarray are obtained and it is normalized by the transmission taken from flat surface. The normalized transmittance is then converted to absorbance and further subjected to rloess function for denoising the signal with 150 points. The final output absorbance peak is screened for its wavelength peak position and intensity of the absorbance and further stored into two separate matrices.

The raw spectrum intensities obtained from all 400 nanoarrays (I – intensity at the gold coated nanopatterned location) was normalized by dividing it with the raw signal taken from outside the patterned area, i.e., surface of the flat gold film (I_o - intensity at gold coated flat surface). The division of the plasmonic data with the

reference from flat gold was performed to give the true value of the plasmonic transmission of the device.

The normalized transmission (T) from each nanoarray was converted to its absorbance expression (A). The absorbance states how much of the light is absorbed by the sample and is usually referred to as optical density O.D. The conversion is calculated with the formula where absorbance is a decimal logarithmic function of T.

The equation $A = 2 - \log(T)$ with a factor "2" is applied as an offset in spectroscopic analysis to rescale absorbance values, thereby enabling direct comparison across different datasets. Empirical evaluation has shown that using a factor of 2 provides a practical rescaling that effectively prevents the occurrence of negative data points. Negative absorbance values are generally considered non-physical and can complicate interpretation, and data visualization. In this context, negative values arise because the transmission signal is normalized against a reference taken from a flat gold film—which inherently has low transmittance—rather than the full intensity of the incident light. Consequently, when converting normalized transmission to absorbance, parts of the spectrum may falsely appear to exhibit negative absorbance.
Applying a uniform offset approach involves subtracting a constant value from all absorbance points in a spectrum, effectively achieving rescaling which does not result in any data loss but rather ensures compatibility and consistency across different measurement sets.

The resultant peak signal is smoothed with a filter function "rloess" which is the robust version of "loess" [155] and performs better at removing outliers without drastically influencing the signal profile. This method executes robust quadratic regression over a window which in this case is with a size of 150 points and is more computationally expensive than "loess" [156, 157].

The subsequent operations perform peak characterisation by determining the wavelength position on the x- axis and the intensity of the absorption on the y-axis. Both parameters are individually stored into a 20 x 20 matrix, constructing a graphic representation of the distinct resonances and intensity of optical density. This visualisation enabled us to systematically investigate the importance of the

design parameters on our knowledge in controlling the optical response of periodic nanoarrays and peak engineering. Furthermore, the analysis has unveiled insights into our understanding how design parameters impact the sensing performance of the plasmonic nanostructures.

The analysis of small cross-sectional data subsets was conducted using Origin Pro (OriginLab Corporation, US). The signal processing algorithm remained unchanged. Supplementary descriptors, such as FWHM, data point masking, and cross-sectional lines, were incorporated to enhance the detailed argumentation. Various visualization plots, including line graphs, scatter plots, stacked plots, contour maps, 3D waterfall, and 3D colour-map surfaces, were utilized.

In this research, reflection data is not utilized primarily because the experimental setup and sensor design are optimized for transmission-mode measurements, consistent with the working principles of most LSPR tools. LSPR-based biosensors typically operate by monitoring changes in absorbance spectra as a function of the local refractive index. These changes are most effectively captured in transmission mode, especially when using optically transparent substrates.
The devices developed in this project are fabricated on transparent polymer substrates and coated with a thin gold film (~40–80 nm). This configuration allows incident light to pass through the plasmonic nanostructures with minimal attenuation, enabling accurate measurement of plasmonic resonance shifts via transmitted light.
In contrast, reflectivity measurements become more relevant when devices are coated with thicker gold layers (typically ≥100 nm), where the film becomes opaque and significantly attenuates transmitted light. Such configurations are suitable for Kretschmann-type SPR setups or reflection-based LSPR but are not compatible with the current sensor architecture designed for high-throughput, real-time absorbance measurements.
Therefore, the choice to exclude reflection data aligns with both the optical properties of the fabricated devices and the standard detection approach employed by the majority of commercial LSPR instrumentation.

3.2.3 Resonance characterisation

An exceptional attribute of LSPR is its adjustability through modifications in nanostructure size, shape, composition, and the refractive index of the surrounding medium.

Rapid progress has been made in plasmon research with the introduction of 2D and 3D plasmonic nanoarrays. They can be fabricated on a large scale by using high-precision top-down EBL technology with consistent uniformity, reproducible in variety of shape, size, and periodicity. Some of the key aspects with research significance are the discovery of new plasmonic modes, better understanding of the existing plasmonic modes and ultra-high sensitivity due to the improved quality of the system [158].

However, significant challenges remain for the massive fabrication of nano-arrays at nanoscale-resolution and low-cost with excellent repeatability, controllability, and great flexibility in tuning optical properties [158]. Accordingly, this thesis is dedicated to overcoming these challenges and elucidating the engineering and development of a nanoplasmonic sensor that conforms to the aforementioned technological standards. The nanoscale-resolution of the template-assisted double gradient nanopillar arrays achieved outstanding design controllability and versatility, reproducible through a low-cost, high-throughput injection moulding process. The invested effort was undertaken to facilitate a robust experimental investigation into the flexibility of tuning optical properties in the gradient plasmonic platform.

The resonance characterisation in this chapter explores how the size, periodicity, and thickness of the gold film in 2D square nanoarrays influence the light-matter interaction resulting in the creation of a characteristic oscillation frequency in the metal electrons, spatially confined to the interface of the nanoscale object (Figure 3.3).

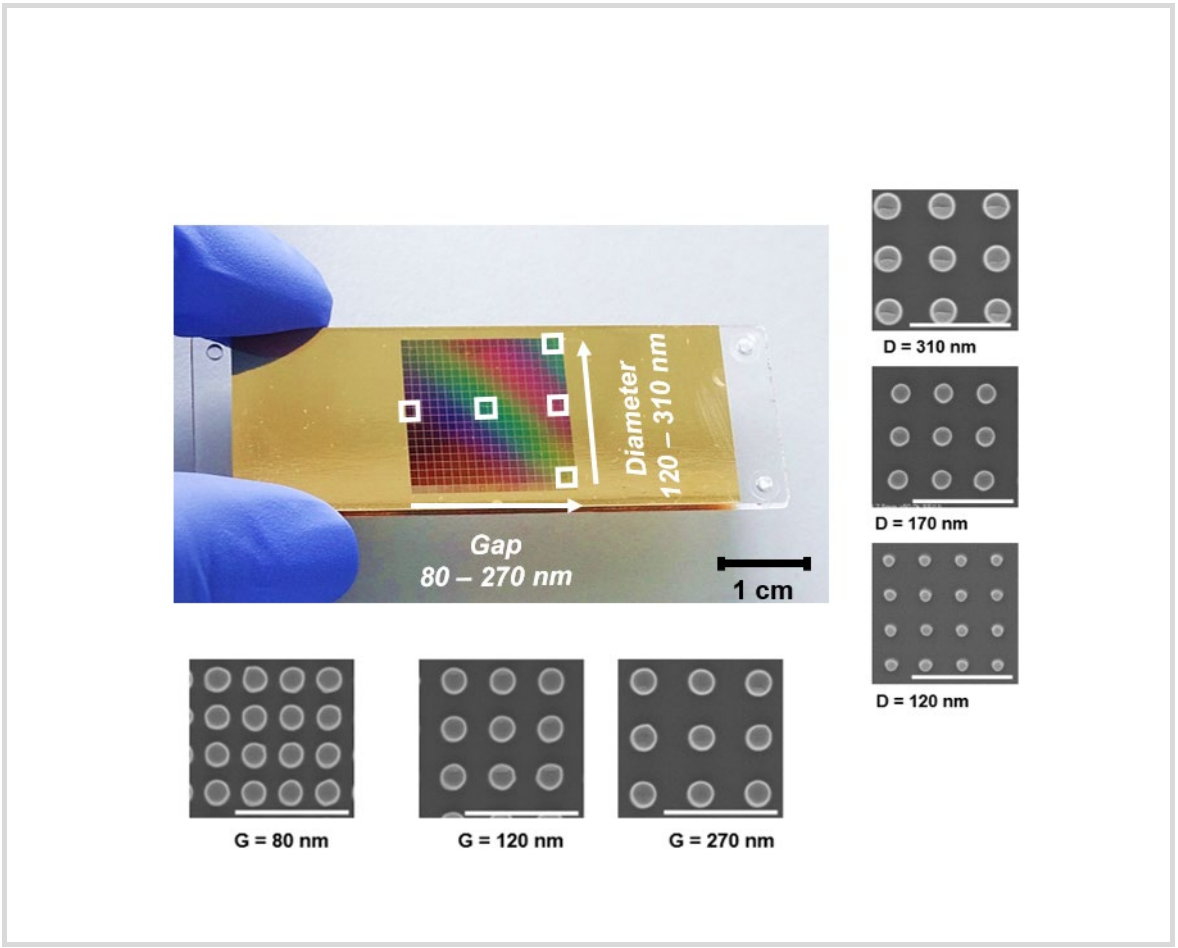

Figure 3.3 Double gradient plasmonic array library (DGPAL) consisting of 400 locations arranged in 20x20 columns and rows enabling the systematic investigation of the flexibility in tunning the optical properties of nanopillar arrays. Scale bar in DGPAL photo is 1 cm, scale bar in SEM inserts is 1 µm.

3.2.3.1 Peak tunning by varying design parameters

The data analysis algorithm workflow selects a peak for identification which is the highest in amplitude within the signal and disregards the other minor peaks.

This confirms with high certainty that only the pre-dominant resonance modes, which are also of most interest in this research, are outlined in the heat maps.

The peak tunning characterisation begins with a device coated with a thin film of 40 nm gold. This gold layer is sufficiently thick to induce plasmonic activation of the array nanostructures, making it a suitable platform for comprehensive investigation.

After scanning the surface of the plasmonic library in water with RI 1.333, Figure 3.4 illustrates the outcome with two heat maps. The first heat map collects all absorbance peak positions and each pixel within the map is represented with its corresponding colour from the visible spectrum. In the second heat map the amplitudes of all absorbance peaks are summarised and colour coded to accurately outline the strength of the plasmonic oscillation.

A vertical white arrow in Figure 3.4 shows the locations on the heat maps where we can systematically follow the peak tunning effect by changing the size of the nanopillars within the range 310 – 120 nm. The interspacing between pillars of all 20 nanoarrays is constant, equal to 130 nm.

The nanoarray configuration with largest diameter (310 nm) of nanopillars resonates at λ_{D310nm}=737 nm (see Figure 3.4), which is close to the end of the red region in the visible spectrum. Decreasing the size gradually up to 120 nm blueshifts the oscillation into higher frequencies. The nanoarray configuration with smallest diameter (130 nm) of nanopillars resonates at λ_{D130nm}=594 nm (see Figure 3.4). The blueshift is equal to $\Delta\lambda = \lambda_{D310nm} - \lambda_{D130nm}$ = 143 nm, which crosses the whole range of the red and orange band of the VIS, almost reaching the yellow band [159].

Another signature characteristic of plasmonic nanopillars that becomes evident from the scatter plot in Figure 3.4 is the change in extinction amplitude and spectral width of the peaks with diameter size.

As decreasing the size of diameter, linearly the oscillation shifts into higher frequencies, but also the amplitude of the resonance peaks is increasing in the same fashion. This demonstrates that the degree of highly confined plasmon energy from gold-coated nanopillars amplifies.

Diameters between the range 310 – 200 nm are presented with relatively low amplitude and those ranging from 190 – 120 nm develop efficient coupling and high absorption peaks. This correlates with the optical properties and the related decay time for arrays made from identical nanostructures. The decay time has been widely discussed in literature and is determined by the damping of the plasmon oscillation.

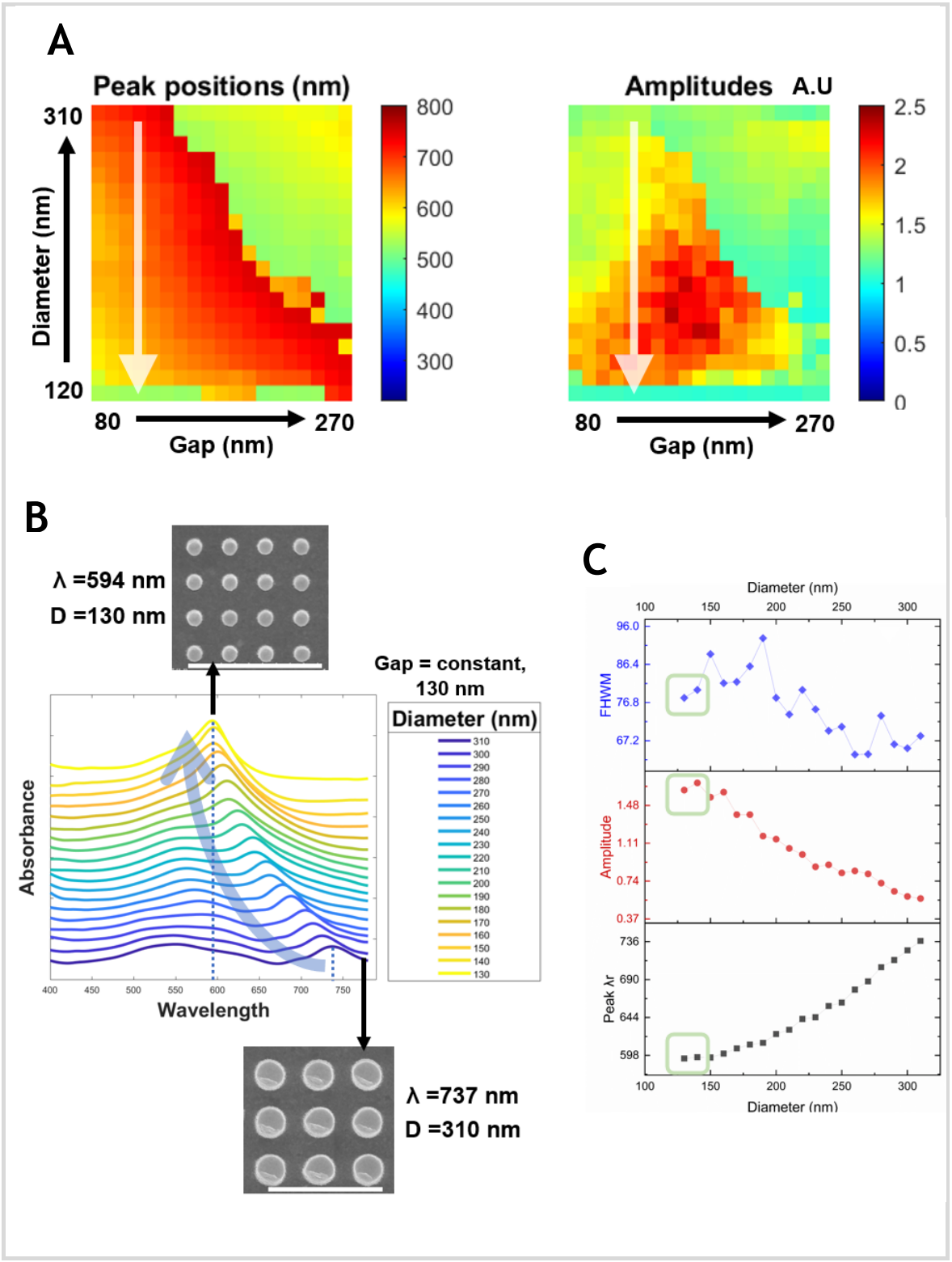

Figure 3.4 Plot A - absorbance maps of the double gradient plasmonic array library (DGPAL) with 40 nm thin gold film, displaying the absorbance peak positions (left) and absorbance amplitudes (right) obtained in RO water with RI 1.333. Plot B - the absorption spectra diameter-dependence is depicted through a y-stacked plot, representing 20 nanoarrays with constant gap (130nm) and varying diameters in the range 310-120nm. This plot is complemented by SEM inserts (scale bar = 1μm) showcasing the nanoarray with 310 nm diameter and λD310nm=737 nm, as well as the nanoarray with 130nm diameter and λD130nm=594 nm. Plot C - scatter plot demonstrates the linear relationship between resonant wavelengths and diameter parameter, along with the dynamics of peak amplitudes and full width half maximum (FWHM). The locations of the most efficient near-field plasmon enhancement are denoted by green squares.

There are two types of damping effect occurring - since LSPR can be excited by incident light, the plasmon can also re-radiate its energy into the far field named as scattering causing energy losses and the second type is non-radiative damping due to electron-electron or electron-phonon collisions called absorption. The relative contributions of absorption and scattering to the total extinction are changing as the size of diameter alter. Generally, as the size of diameter increases, the total extinction is pre-dominated by scattering [42] and the weaker repulsion of the oscillating electrons drives the resonance into lower energy wavelengths. On the contrary, when the diameter size decrease, the field will be concentrated like a lightning rod, increasing the field intensity further.

Finally, the third trend associated with nanoarrays with varying diameter size and constant interspacing between nanopillars is the changing full width half maximum (FWHM) descriptor.

Planar 2D plasmonic substrates support propagating Bloch-wave surface plasmon polaritons (BW-SPPs). The SPP cannot re-radiate the absorbed energy into free space due to the momentum mismatch, so thus can occur together with the LSPR mode. Since both SPP and LSPR have local fields, at a certain lattice periodicity the metal nanoarray can support coupling. The coupling leads to an enhanced local field and shift the spectral position due to hybridization between the modes. The SPP mode is dependent on the periodicity of the nanopillar array. For a non-periodic array, SPP mode disappears while LSPR mode still exists [160]. At Figure 3.4, the y-stacked plot perfectly demonstrates the gradual hybridisation of the SPP mode with the LSPR mode. The bottom dark blue resonance line corresponding to a nanoarray with diameter 310 nm consists of a very broad, low-amplitude peak at around 550 nm induced by the emergence of a SPP mode and a sharp LSPR mode creating a peak at 737 nm. By following the profiles of the next resonance signals we can easily understand how the nature of the oscillators, decreasing in size, drive the LSPR mode to shift closer to the SPP mode and eventually completely merge with one another. This phenomenon is gradually changing the FWHM descriptor to increase in value, starting from roughly 65 nm while the two modes exist separately to roughly 85 nm when the two modes merge. These experimental results are in good adherence with the work of Jiangtian Li, et al published in 2013, where the chip-based plasmonic metal nanostructures investigated, focus

on the origin of SPP and LSPR mode emergence and define the range of the optical band. The SPP leads to an enhanced transmission in the 300- to 500-nm range, whereas the LSPR mode induces an increased absorption in the 550- to 750-nm range.

At Figure 3.5 a horizontal white arrow shows the locations on the heat maps where we can systematically follow the peak tunning effect by changing the interspacing between nanopillars within the range 80 – 270 nm. The size of the pillars of all 20 nanoarrays is constant, equal to 160 nm.

The nanoarray configuration with the narrowest interspacing (80 nm) between nanopillars resonates at λ_{G80nm}=603 nm (see Figure 3.5), which denotes the beginning of the orange region in the visible spectrum. Increasing the interspacing gradually up to 270 nm redshifts the oscillation into lower frequencies. The nanoarray configuration with the widest interspacing (270 nm) between nanopillars resonates at λ_{G270nm}=753 nm (see Figure 3.4). The redshift is equal to $\Delta\lambda = \lambda_{G270nm} - \lambda_{G80nm}$ = 150 nm, which again encompasses the orange and red band of the VIS.

From the scatter plot on Figure 3.5, showing the resonance wavelengths, absorption amplitudes and FWHM of the peaks we can better understand the dynamics of gap-induced shifts. The first thing that becomes evident is the linear oscillation shifts into lower frequencies as gap increases in size. As mentioned above, the bandwidth window of peak tuning is 150 nm which is almost equal to diameter-induced shifts.

The second observation from the scatter plot is that the profile of peak amplitudes does not linearly change with the resonant wavelength shift. The amplitudes rather escalate to a critical point where the electromagnetic enhancement achieve a maximum and everything outside this gap-fulfilling size, reduce the absorption (Figure 3.5). This suggests that interspacing between nanopillars in ordered 2D square arrays clearly influence the LSPR band as interparticle coupling effects interfere. Gap size within the 270-240 nm range does not support the coupling of nanopillars with 160 nm size and thus the resonant peaks in these configurations reach low value amplitudes equal to 0.3-0.4.

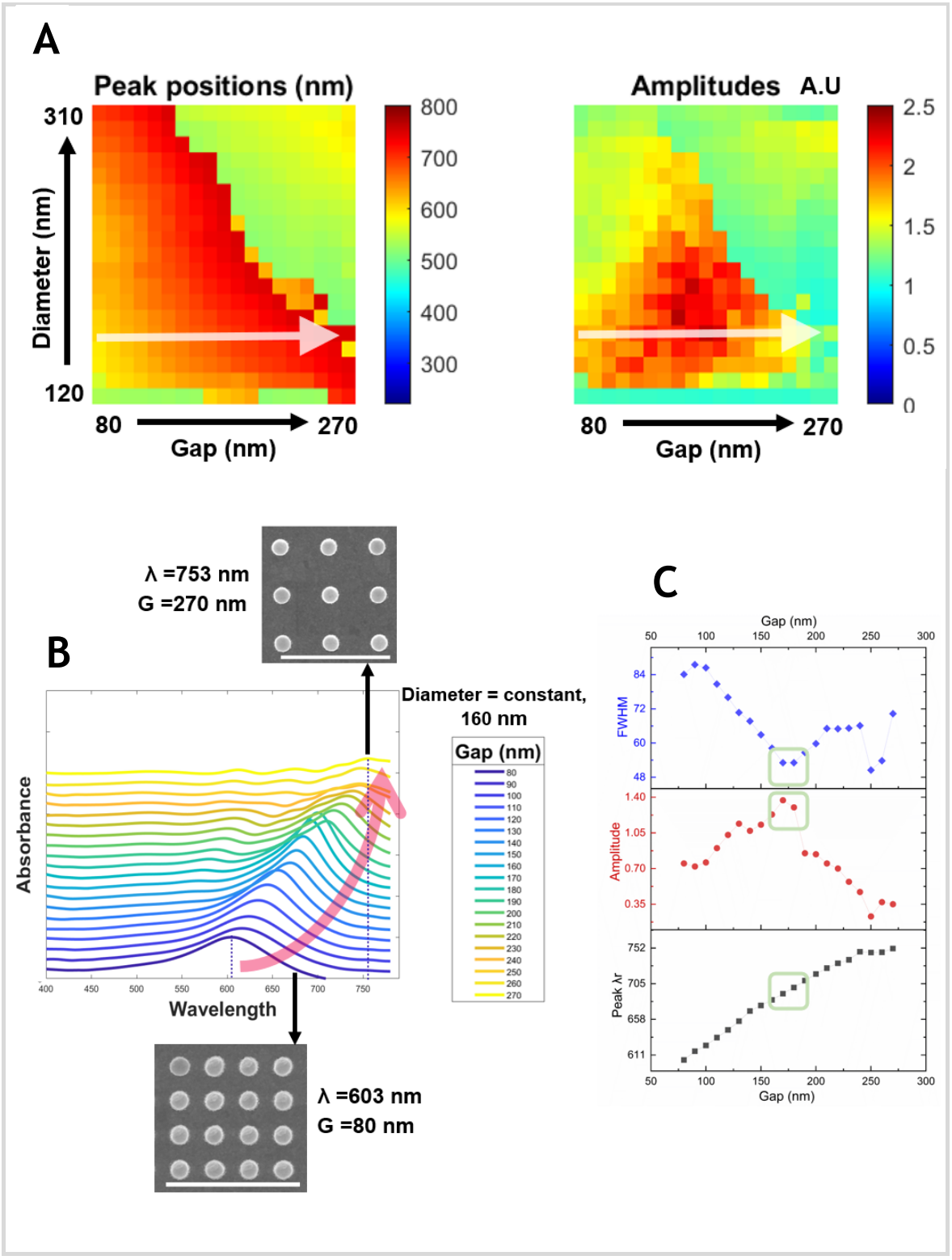

Figure 3.5 Plot A - absorbance maps of the double gradient plasmonic array library (DGPAL) with 40 nm thin gold film, displaying the absorbance peak positions (left) and absorbance amplitudes (right) obtained in RO water with RI 1.333. Plot B - the absorption spectra gap-dependence is depicted through a y-stacked plot, representing 20 nanoarrays with constant diameter (160nm) and varying gaps in the range 80-270nm. This plot is complemented by SEM inserts (scale bar = 1μm) showcasing the nanoarray with 80 nm gap and λG80nm=603 nm, as well as the nanoarray with 270nm gap and λG270nm=753 nm. Plot C - scatter plot demonstrates the linear relationship between resonant wavelengths and gap parameter, along with the dynamics of peak amplitudes and full width half maximum (FWHM). The locations of near-field plasmon enhancement are denoted by green squares.

However, the 160 nm size diameter can support the appearance of quadrupoles and higher-order multipole mode resonances at shorter wavelengths. This phenomenon is explained with the light-matter interaction. For nanostructures much smaller than the incident wavelengths (e.g. 10 – 80 nm), the electric field of the light can be taken as a constant and the interaction leads to a homogenous displacement of the conductive electrons, resulting in an oscillating dipole field. For large nanostructures, the external electric field does not achieve the same homogeneity, and not all conductive electrons sense the same phase in order to move in the same frequency. The electromagnetic wave retardation results in an increased dipolar LSPR wavelength and higher order resonances at shorter wavelengths. Consequently, as gap parameter decrease and coupling effect take place, the dominating LSPR peak at 753 nm move to shorter frequencies and merge with the higher-order modes observed at 665nm and 600 nm. This would gradually increase and broaden the amplitude of the LSPR peak (Figure 3.5) at first place while the merging is happening. But at gap size of 170 – 180 nm, the resonance achieves maximum enhancement as the superposition of the waves result in constructive interference. The reinforcement is a result of perfect overlap between the LSPR peak with both higher-order modes, accumulating to relatively low FWHM values. Beyond that critical gap size, the LSPR peak merge with the faint and broad SPP wave which introduces a destructive interference, affecting the electromagnetic performance which decreases and broadens the amplitude.

Figure 3.6 summarizes the contribution of altering diameter and gap parameters and explains how mixed LSPR modes occur achieving electromagnetic enhancement and narrow resonances.

Plot A demonstrates the condition when nanopillars in the arrays are interlocked with the same gap equal to 130 nm. The interspace is small enough to fulfil the coupling effect between nanostructures, and we can systematically follow how diameter size tunes the resonance.

Nanoarray with relatively large diameter (290nm) supports narrow LSPR peak with low amplitude due to the pre-dominant scattering effect and weak absorption capabilities. The large size nanostructures support weak repulsion for electrons at opposite surfaces and thus the resonance is positioned in the low-frequency deep-red region of the VIS [161].

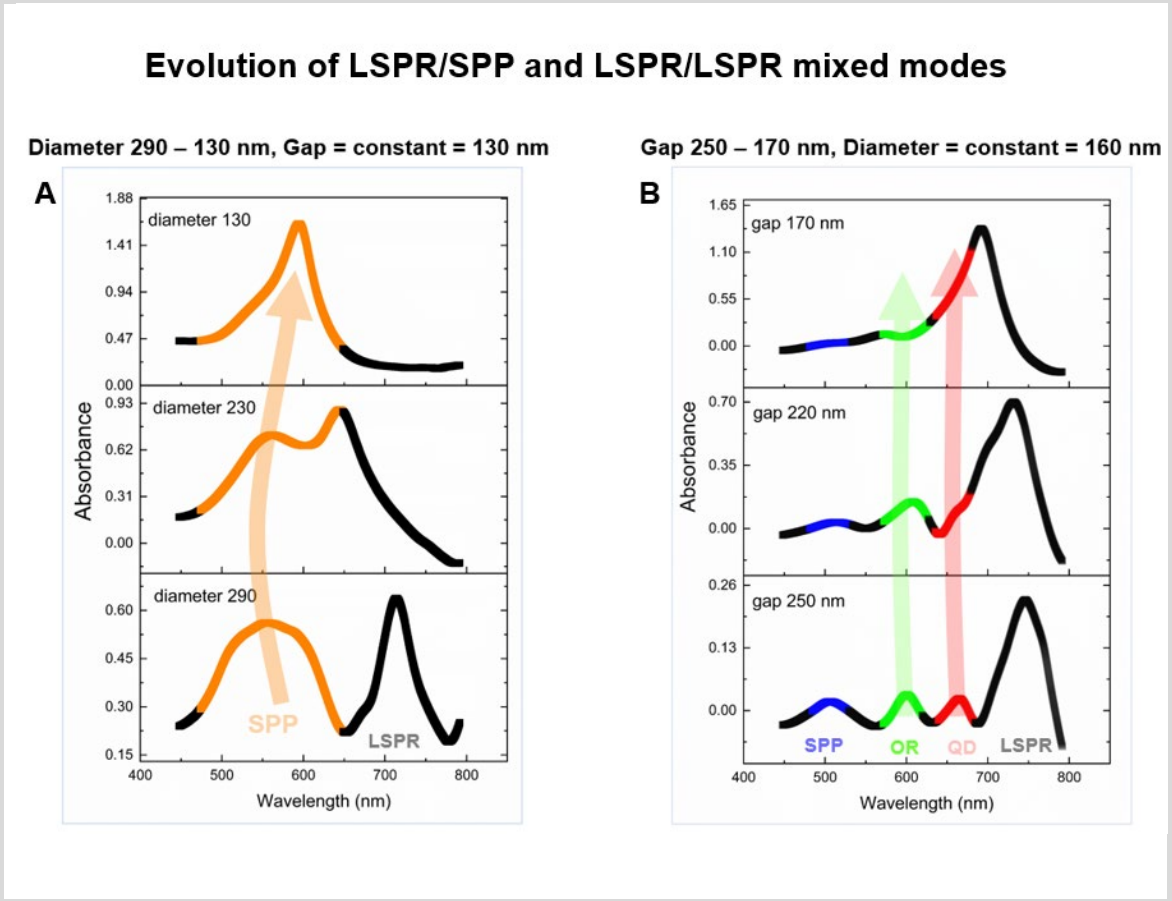

Figure 3.6 Plot A - demonstrates the effect of variations in diameter size and constant gap on the evolution of the LSPR/SPP mixed mode. Plot B - demonstrates the impact of gap size and constant diameter on the evolution of the LSPR/LSPR mixed mode as the predominant dipole LSPR mode merge with higher-order multipole mode resonances (QR – quadrupole and OR octupole resonance). Note that the colours on the plots are for visualization purposes and do not correspond to the colours on the VIS spectrum.

However, this configuration also supports almost equal in amplitude broad SPP mode. Diameter size <290nm, enhance the absorption amplitude but as the resonance shifts to shorter wavelengths, inevitably merges with the SPP-mode. The transition gives the rise of a narrow LSPR/SPP mixed mode.

Plot B demonstrates the condition when nanopillars in the arrays are constructed with the same diameter size equal to 160 nm. The nanopillar size is small enough so that the arrays exhibit strong absorption, and we can systematically follow how gap size tune the resonance. Nanoarray with relatively large gap (250nm) supports narrow LSPR peak with low amplitude due to the pre-dominant isolated localised electromagnetic (EM) fields, not being able to influence each other. However, when lacking coupling capabilities, the configurations express their other higher-order multipole mode resonances, positioned at shorter wavelengths. Gap size

<250nm, predisposes EM fields of nanopillars to influence the neighbouring EM fields. The coupling effect enhances the absorption amplitude but as the resonance shifts to shorter wavelengths, gradually interferes with the higher-order modes. The transition gives the rise of a narrow LSPR/LSPR mixed mode.

The resonances exhibit a linear blue-shift when the nanopillar diameter and gap interspace decrease. Moreover, the diameter-induced shifts and pitch-induced shifts can be considered as equally strong predictors, exerting significant control over the optical properties of gold-coated nanopillars. To validate this assumption, we have analysed the correlation between resonance amplitude and the ratio between diameter and gap. As we are focusing on the dataset where the LSPR effect is predominant we have included the arrays with strong absorption properties. The analysed subset consists of 210 data points covering more than 50% of the double gradient library. The remaining 190 data points predominantly demonstrate scattering effect and the ratio between diameter and gap express less correlation to enhancement.

As depicted in Figure 3.7-A, the anticipated outcome is the emergence of the "ideal square array" configuration, resulting in the maximum enhancement of the gold nanoantenna within each specified setup. This favourable configuration is attained when the square array maintains a diameter and gap that are nearly identical in size. Consequently, resonance peaks experience an increase in amplitude, highlighting the effectiveness of a square array with a diameter-to-gap ratio near 1 or equivalent to 1.

To enhance the visualisation of the "ideal square array" effect, three distinct subgroups are highlighted on the scatter plot in grey, red and blue. These subgroups represent array configurations with diameter-to-gap ratios above 1.5, near 1, and below 1, respectively. In Figure 3.7-B are plotted their resonance signals alongside with a SEM insert, underscoring the importance of geometric parameters. The nanoarray belonging to the grey subgroup, characterized by a diameter-to-gap ratio of 1.7, exhibits resonance at 569 nm, featuring a broad peak with relatively low amplitude. In this instance, the array comprises nanostructures with a diameter size of 310 nm spaced apart with 180 nm gaps.

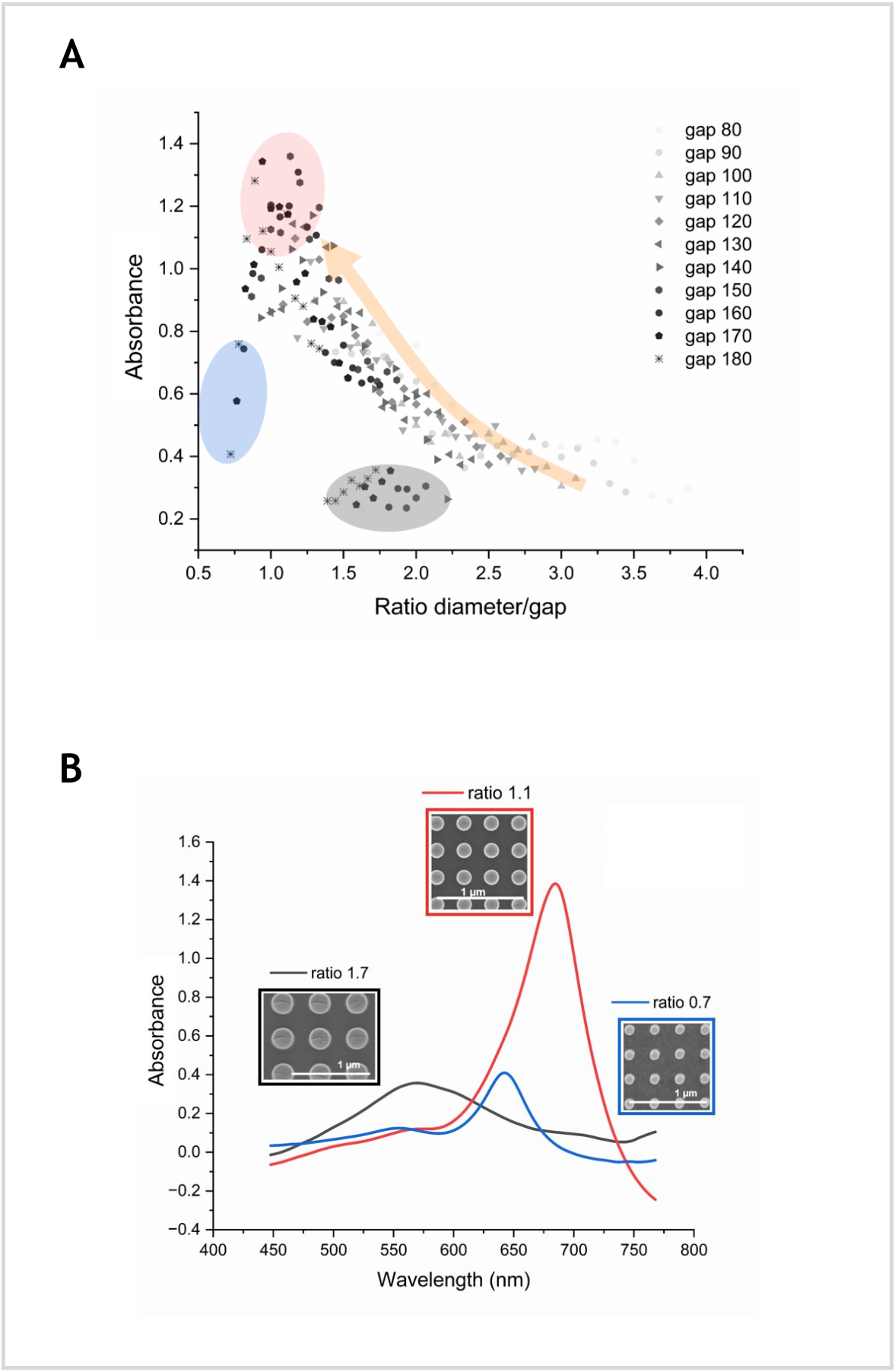

Figure 3.7 A-Scatter plot depicting the dependence of maximum resonance enhancement and geometry configuration of the square array. The peak amplitudes gradually increase when the ratio diameter/gap approach 1. Groups with significantly different ratio are outlined with grey, blue, and red ellipse. B- Representative resonance signals plotted from each outlined group supported with SEM inserts. Scale bar = 1 µm.

Large nanostructures like these tend to be inefficient absorbers, leading to weak localized resonances. The relatively narrow gap of 180 nm (gap << diameter) predisposes mode coupling, such as the SPP mode. However, the superposition of two broad waves results in interference with limited enhancement gain.

In contrast, the nanoarray in the blue subgroup, characterized by a diameter-to-gap ratio of 0.7, exhibits resonance at 642 nm, featuring a narrow peak with relatively low amplitude. This array comprises nanostructures with a diameter of 130 nm spaced apart with 180 nm gaps. Small nanostructures like these tend to be efficient absorbers, leading to distinct localized resonances. The relatively large gap of 180 nm (gap >> diameter) minimizes mode coupling. The strongly localised resonances remain isolated with little to no interference with other modes.

Lastly, the nanoarray in the red subgroup, characterized by a diameter-to-gap ratio of 1.1, exhibits resonance at 684 nm, featuring a narrow peak with 3.5 times higher amplitude. This configuration consists of nanostructures with a diameter size of 170 nm spaced apart with 150 nm gaps. Small nanostructures like these are efficient absorbers, leading to distinctive localized resonances with high electromagnetic distribution spread. The gap of 150 nm, slightly smaller than diameter size, promotes efficient coupling. The strongly localised resonances display positive interference with other modes resulting in significant gain in resonance enhancement.

In conclusion, the resonance oscillation of plasmonic nanoarrays is intricately influenced by the interplay of diameter, gap configurations, and their respective ratios. The observed reliance of resonances on these array parameters highlights the potential for fine-tuning oscillations to specific wavelengths, each characterized by tailored linewidths, bandwidth, and amplitude, making them well-suited for various applications. Specifically, these tailored nanoarray configurations can be harnessed to create highly sensitive and selective biosensors, paving the way for advancements in medical diagnostics and environmental monitoring Moreover, this precise control finds significant relevance and can be useful in the development of photonic and plasmonic/photonic hybrid devices such as higher-efficiency photovoltaic solar cells and enhanced optical emitters and detectors.

3.2.3.2 Plasmonic activation by varying the thickness of gold film (Au) - 40 nm, 60 nm, 80 nm data sets.

In the previous section a detailed overview on the dependence of resonance peaks and design configuration was provided. Apart from influencing the size and density of the nanopillar array, there is another parameter that can also be tunned providing more dimensionality on the double gradient library. This is the thickness of deposited gold film ensuring plasmonic activation.

Understanding of how the optical properties of metal films depend on thickness is important for the performance optimization of plasmonic devices. Films with thickness of more than 200 nm are guaranteed to behave as a bulk metal [162]. In bulk metal, free conduction electrons do not oscillate against a restoring force, eliminating the presence of a resonant frequency. Since we aim to avoid bulk metal behaviour, our research focused on film thicknesses well below 200 nm. Film thickness above 80 nm significantly limits the transmission of light and introduce more noise in data measurements. As this is our main technique of data acquisition (see section 3.2.1), the experimental devices were investigated within the range 40-60-80 nm gold deposition. Gold layers below 40 nm thickness have extremely low conductivity and demonstrate a drastic increase in the overall optical losses [163].

The imaginary part Im [ε”] of the dielectric function governing the optical losses in the Au film exhibits notable variations across different film thicknesses. As shown in Figure 3.8, ε” tends to decrease while the film thickness increases. Plot A (bottom part) demonstrates the relationship between ε” and film thickness within the range of 8.5 – 44.3 nm, revealing significant optical losses between 8.5 – 26.3 nm. Optical losses are minimal for 41.9 nm and 44.3 nm gold thickness, notably overlapping on the plot and within the VIS range values are fluctuating between 0 and 1. At the same time, there is no noticeable dependence of the real component of the dielectric function, Re [ε’], on the film thickness.

Figure 3.8 plot B further validates this observation and illustrates the increasing damping effect and reduced free electron relaxation time for gold film thicknesses bellow 40 nm.

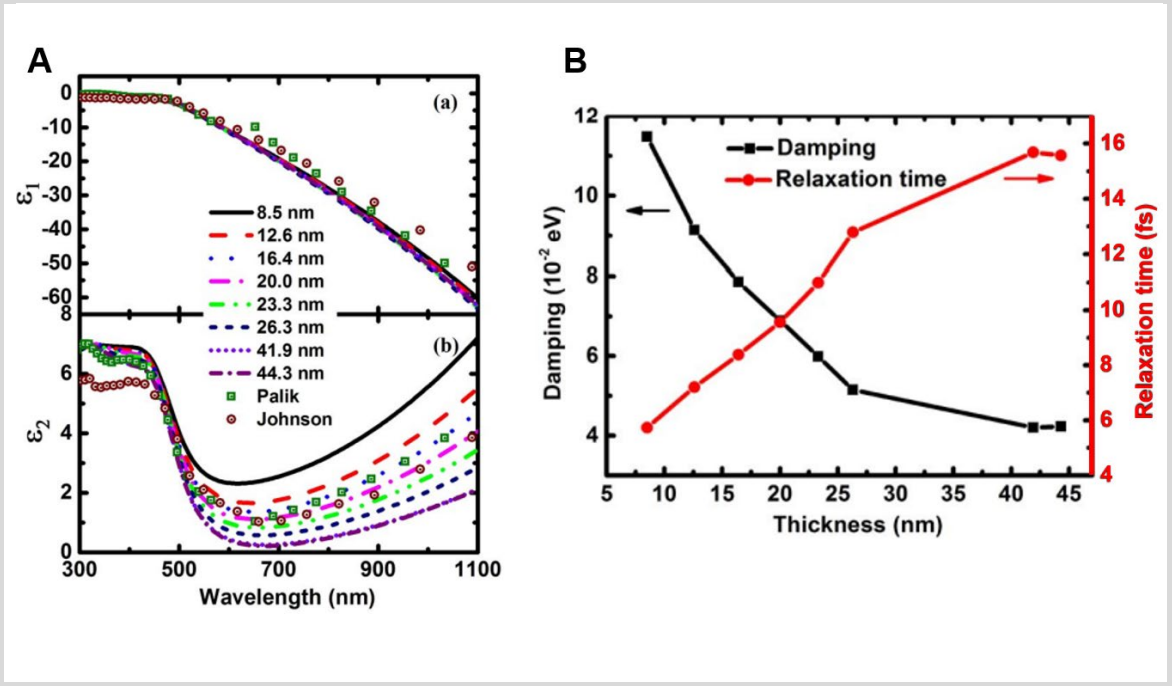

Figure 3.8 Plot A is showing the real and imaginary parts of the dielectric functions of nano-thin Au films at different thicknesses. Plot B is demonstrating damping and free electron relaxation time for the Au films. Adapted from E.-T. Hu et al. [163]

This phenomenon is attributed to increased scattering rates happening on the surface and specifically the larger contribution of the electron-grain boundaries scattering at smaller thicknesses. The enhanced scattering consequently amplifies optical losses and is quantified by the Drude damping factor (Γp). The Drude damping factor is directly proportional to ε" and inversely proportional to free electron relaxation time ($\tau = 1/\Gamma p$).

After establishing the optimal window of gold film thickness (40 nm, 60 nm, and 80 nm) our research focused on understanding how increasing metal deposition affects plasmon resonances. Uncertainty in the evaporated gold thickness with more than 10 nm can introduce errors such as resonance shifts, and changes in the absorption, all of which affect plasmonic performance and sensor reproducibility. However, the thickness control in the Plassys MEB 550S Electron Beam Evaporation System mitigate these issues providing total errors, including distribution and reproducibility, within tolerance limits of ±0.5% of the intended thickness [164, 165]. The precise control over the deposited gold thickness is ensured through:

Quartz Crystal Microbalance (QCM) Monitoring: The system employs QCM sensors that measure real-time mass deposition with nanometre precision, allowing precise control over the final film thickness.
Pre-Calibrated Deposition Rates: The evaporation rate is pre-calibrated based on material properties and chamber conditions, ensuring uniform film growth.
Substrate Rotation and Uniform Heating: The system includes a rotating stage and controlled substrate heating, minimizing thickness gradients and enhancing uniformity.
Weekly maintenance of the tool by the JWNC metallisation team involves performing thorough chamber cleaning, checking and replenishing source materials, calibrating the quartz crystal thickness monitor, and inspecting system components to ensure consistent deposition rates and film uniformity.
By leveraging these features, the Plassys MEB 550S achieves high precision and ensures a high degree of reproducibility and accuracy in gold film deposition, reducing errors in plasmonic device fabrication.

In the next figure (Figure 3.9), the experimental device with 400 nanoarrays is coated with a gold nanofilm of 40 nm, 60 nm, and 80 nm. Plot A illustrates the comparison of all absorption peak resonances and peak amplitudes within heat maps. The overall absorbance increases as the gold deposition increases.

This is demonstrated in the accompanying line plot (Figure 3.9 B) where resonance signals did not undergo normalisation to the intensity of the respective density of flat gold film. It illustrates that a nanoarray from the same location (outlined with a white box) in each dataset resonates with amplitudes of 1.2, 1.85, and 2.3 for gold film thicknesses of 40 nm, 60 nm, and 80 nm, respectively. Without normalizing the signals, the actual increase in absorption amplitude is revealed. Additionally, the augmentation of gold induces a resonance peak shift, transitioning through red, orange, and yellow bandwidths with peak positions at 645 nm, 596 nm, and 582 nm. It worth reminding that these results represent the continuity of the gold film, including the contribution of the flat gold surface.

As the objective of the research is to understand the true value of the plasmonic activation itself, it is important to note that the heat map plots in Figure 3.9 A and all subsequent cross-sectional analysis (Figure 3.9 C and D) are made after

absorbance measurements are normalized to the intensity of a flat gold film with its respective thickness. Thus, when evaluating the amplitude scale bar across all datasets, it might appear constant.

The next notable difference in the heat maps is that the total percentage of nanoarrays resonating within the red bandwidth is decreasing in the following order 40nm (66%) >60nm (45%) >80nm (32%). Furthermore, the general trend of diameter-induced shifts and gap-induced shifts is followed within each film-thickness dataset but the transition from red to yellow wavelengths is more pronounced. Lastly, notable differences are also seen when comparing the amplitude heat maps. Considerable shrinkage of the regions resonating with high amplitudes is observed in the same following order 40nm>60nm>80nm. The changes mentioned above happen due to modifications of the resonant profile influenced by the increasing gold deposition on the nano surface. In order to visualise all details, two cross-sectional analyses as three-dimensional waterfall plots are provided in Figure 3.9 C and D. The colour mapping applied in the Y-directions facilitates to easily follow the enhancement of each plasmon mode and their evolution with the gradually changing array geometry.

Figure 3.9, panel C illustrates the resonance signals along the vertical axes of the heat maps, following the variations in diameter size and constant gap. In all three plots, representing gold thicknesses – Au 40, Au 60, and Au 80, the dynamics between the SPP and LSPR mode are outlined. A common characteristic observed within all three plots is that a broad SPP and a narrow LSPR peaks are differentiated when diameter size is relatively large and as nanostructure size decrease the two waves merge. Supporting data visualizing the peak positions of SPP and LSPR are demonstrated in Figure 3.10 (Plot B, C and D). The SPP wave does not shifts its resonating wavelength while the LSPR peak is positioned more than 200 nm away from it. But the LSPR peak is strongly influenced from diameter size which makes it extremely prone to transition.

Smaller nanopillars become stronger absorbers and the localised electromagnetic field is enhanced, shifting the LSPR position to higher frequencies shortening the distance with the SPP wave. When close enough, the two waves reach a merging point where the SPP peak redshifts drastically, being overpowered by the enhanced LSPR (Figure 3.10 - Plot B, C and D).

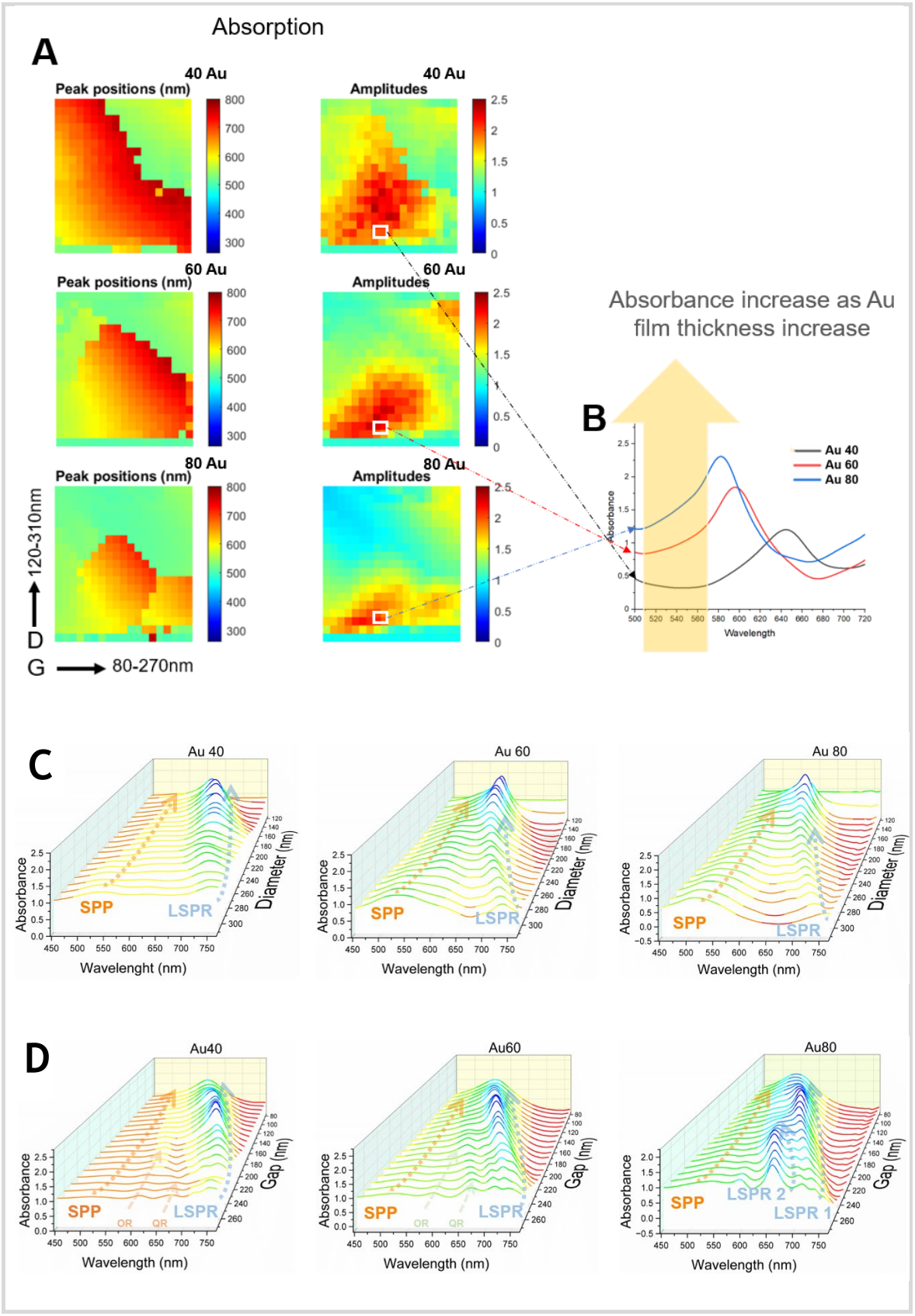

Figure 3.9 A - Heat maps representing the peak positions and amplitudes of the double gradient plasmonic array libraries when measuring absorption and varying the thickness of deposited gold film from 40 nm to 60 nm and 80 nm. B – explains the increasing absorption trend when normalizing is omitted. C - demonstrates the diameter-dependence variations and constant gap whit increasing gold thickness. D - demonstrates the gap-dependence variations and constant diameter whit increasing gold thickness.

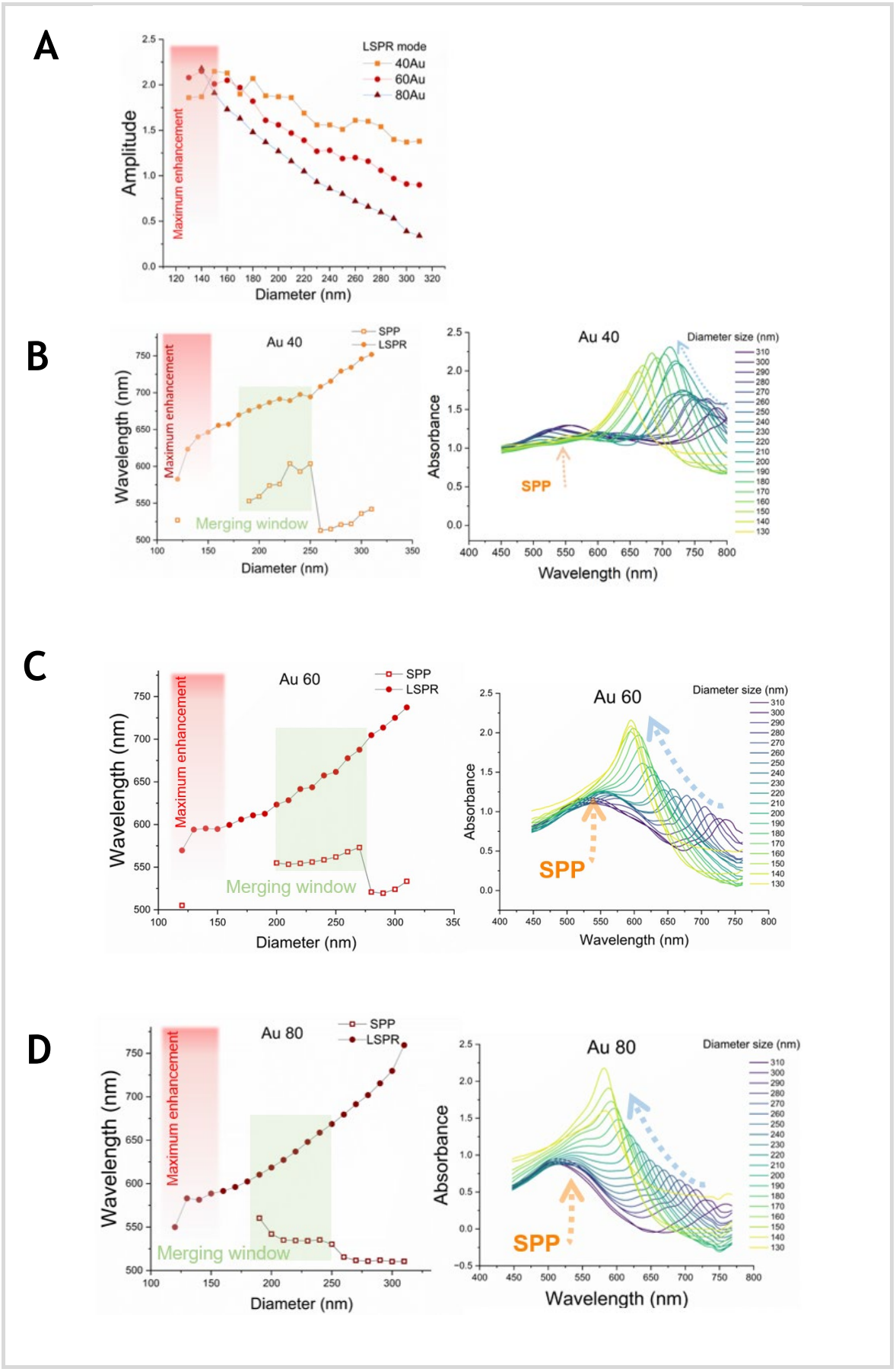

Figure 3.10 Demonstrates the SPP, LSPR dynamics within the cross-section with diameter-dependence variations and constant gap while increasing gold thickness. Plot A – illustrates the amplitude enhancement and a red stripe is locating the designs with maximum amplitude. Plot B, C and D – depict the SPP-LSPR merging dynamic and how the merging window (in green) is followed by a peak profile with maximum amplitude.

The merging point denotes the beginning of the merging window where the SPP wave becomes a shoulder peak of the LSPR mode. The subsequent evolution of the peak after this point is a complete overlap and merge into one. This kind of positive interference drives the SPP/LSPR mixed mode to quickly gain more energy. The design configurations achieving maximum enhancement are outlined in the red area. Figure 3.10-Plot A, represent the amplitude enhancement driven by diameter size variations, confirming that after the merging window, the resonance peaks exhibit maximum magnitude.

However, there are a few intricate differences which make the SPP/LSPR interplay modify as gold deposition increase. The first feature is the profile of the SPP mode. The influence of SPP mode increases as gold deposition increase (Figure 3.10 -B, C and D). In the Au 40 dataset the amplitude of the SPP mode is lower than the LSPR peak but within the Au 60 and 80 dataset the ratio is reversed. That would mean these two peaks influence each other differently. The combination of low amplitude SPP peaks in the Au 40 device leaves the narrow LSPR mode to dominate the resonance, oscillating in the red bandwidth. This interplay shapes the Au 40 resonance heat map to be predominantly red, having outspread regions with high amplitudes.

The configuration of high amplitude SPP peaks as in the Au 60 and 80 datasets dominating over the emerging LSPR peaks, shapes the heat maps differently, significantly reducing the red pixels on it. The amplitude of the SPP peak is 1.2 and 2.5 times higher than the LSPR peak for the Au 60 and Au 80 respectively. This suggests that as the amount of gold increase on the surface, the pure SPP wave becomes more pronounced and the pure LSPR mode more weakened.

Figure 3.9, panel D illustrates the resonance signals along the horizontal axes of the heat maps, following the variations in gap size and constant diameter. In all three plots, representing gold thicknesses – Au 40, Au 60, and Au 80, the dynamics between the SPP and LSPR dipole and higher modes are outlined. A common characteristic observed within all three plots is that the LSPR modes are with much more pronounced amplitude than the SPP wave. When we look at the 3D plots in Figure 3.9 D, the SPP peak is very discrete. This is because the horizontal cross-section is with default diameter size of 160 nm and nanopillar arrays from this calibre develop enhanced localized electromagnetic fields. The LSPR peak is also

accompanied with two higher mode resonances. All LSPR modes are differentiated when gap size is relatively large and as the interpillar space decrease the modes merge. Once again, the dipole LSPR mode is strongly influenced from gap size. Shorter gap implies smaller coupling distances allowing strong resonance hybridization between LSPR modes. The mixed LSPR/LSPR peak increase in amplitude and as it is gaining more energy, the resonance shifts to higher frequency. With the deposition of more gold all LSPR modes enhance their amplitudes. Within the 80 nm gold film it is even observed that two different LSPR modes lead the dominance for highest amplitude. This interplay can be also noticed on the heat map with peak positions, but the actual details are revealed on the 3D plot.

The differences occurring with gold augmentation is the enlarging window of resonance shift. The Au 40 device provide a bandwidth range of 147 nm which becomes wider within the Au 60 with 183 nm and reach 195 nm for the Au 80. The increase in gold deposition provides more variety of wavelengths and is a powerful tool for dynamic tunning. In Figure 3.11, plot A provides a histogram representation of the resonance wavelengths combined from the vertical and horizontal cross-sections for each gold film thickness within its characteristic resonance bandwidth 540 nm – 760 nm range. The Au 40 dataset represents a distribution predominantly skewed in the far red bandwidth. Nanoarrays whose resonances are tuned into the NIR spectral region where tissue is relatively transparent are especially valued for biomedical application [35]. Alternatively, the Au 60 and 80 datasets show normal distribution within the mention range with peaks of the distribution curve at 645 nm and 638 nm respectively.

Furthermore, the analysis of the resonance signals in Figure 3.11 – plots B and C, demonstrate that highest plasmonic enhancement is observed in the Au 40 and Au 60. These groups demonstrate the highest amplitudes and narrow peak profiles with no significant difference between them. Lastly, the analysis of their profile outlines the Au 60 gold film with the narrowest plasmonic peaks and average FWHM of 47.6 nm. This would have a huge impact on the Q-factor performance of the Au 60 device as the Q-factor is inversely proportional to its bandwidth.

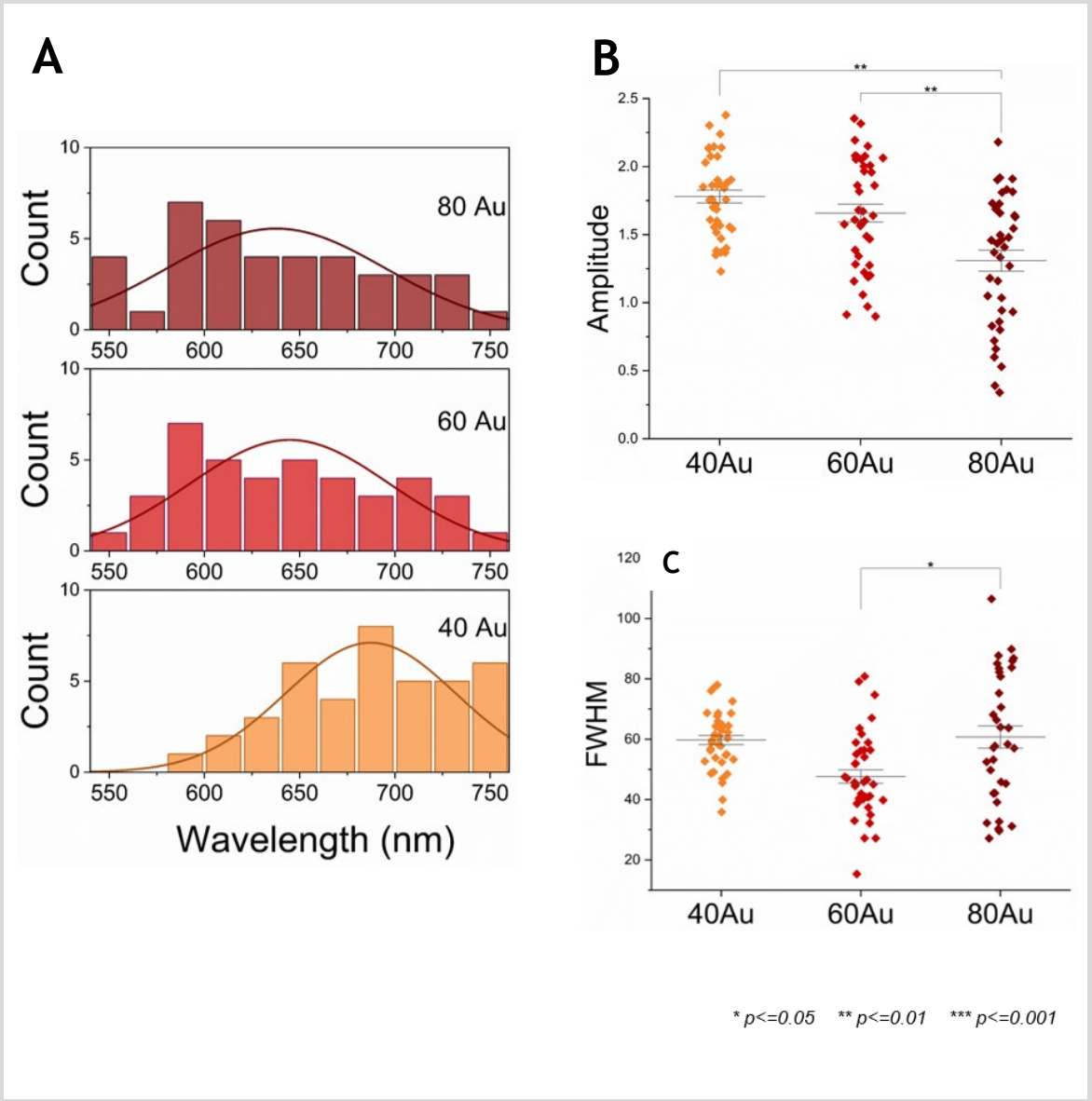

Figure 3.11 Summarized analysis of both horizontal and vertical cross-sectional datasets for each respective gold thickness 40 Au, 60 Au and 80 Au. Plot A – stacked histogram diagram illustrating the distribution of resonance wavelengths with a distribution curve. Plot B – scatter interval plot showing mean amplitude for each group. There is a significant difference between the groups except between 40Au and 60Au datasets. Plot C - scatter interval plot showing mean FWHM for each group. There is a significant difference only between the 60Au and 80Au datasets.

It is defined as the ratio between the spectral position of the resonance (λ) and the full width at half-maximum (FWHM) (Q = λ / FWHM). Additionally, when the FWMH is narrow enough the plasmonic nanoarray can achieve accurate detection of resonance wavelength changes. This correlation refers to the figure of merit (FOM) of the sensor.

In conclusion, if we compare the peak amplitudes, the wavelength range coverage and their full width half maximum, the results point out that the most beneficial and balanced interplay between SPP and LSPR is outlined in the Au 60 dataset (Figure 3.11).

This is the reasoning behind why in further experiments the preferred plasmonic platform is the double gradient library coated with 60 nm thick gold film.

In this section of the resonance characterisation chapter, we report the investigation of the transmission properties of the fabricated metallodielectric structures with strong surface corrugation of the gold film. We show that the diffractive scattering on a specific region from the double gradient library display unusual dispersion properties, compared to gold film on flat surface. More importantly, the transmission peak amplitudes increase very dramatically as the gold film thickness is increased. Figure 3.12 summarises the outcomes observed when transmission of resonant signals is analysed while increasing the thickness of the gold film. Plot A illustrates the heat maps for peak resonances and corresponding peak amplitudes after deposition of 40 nm, 60 nm, and 80 nm gold. In all heat maps the same region in the top right corner is outlined but anomalously high transmission features are observed when the gold film is 80 nm. This region is comprised of nanoarrays with diameter between 290 – 310 nm and nanopillar interspace between 270 – 200 nm. Relatively large structures like these exhibit weak LSPR properties as the radiative dampening and electron–electron scattering make the lifetime of the LSPR much shorter than that of the SPP [166]. This condition classifies them as predominantly strong scatterers [31].

The normalized transmission spectra of a single pixel taken from the heat map, shown in Figure 3.12 – B, demonstrates the critical threshold needed in terms of gold deposition to unlock enhanced optical transmission. The gold film thickness of 40 nm and 60 nm certainly begin to modify transmission signal, but the EOT activation is undoubtedly induced with the 80 nm gold where EOT peak reach an amplitude 20 times and 5 times higher than the thinner 40 nm and 60 nm gold films.

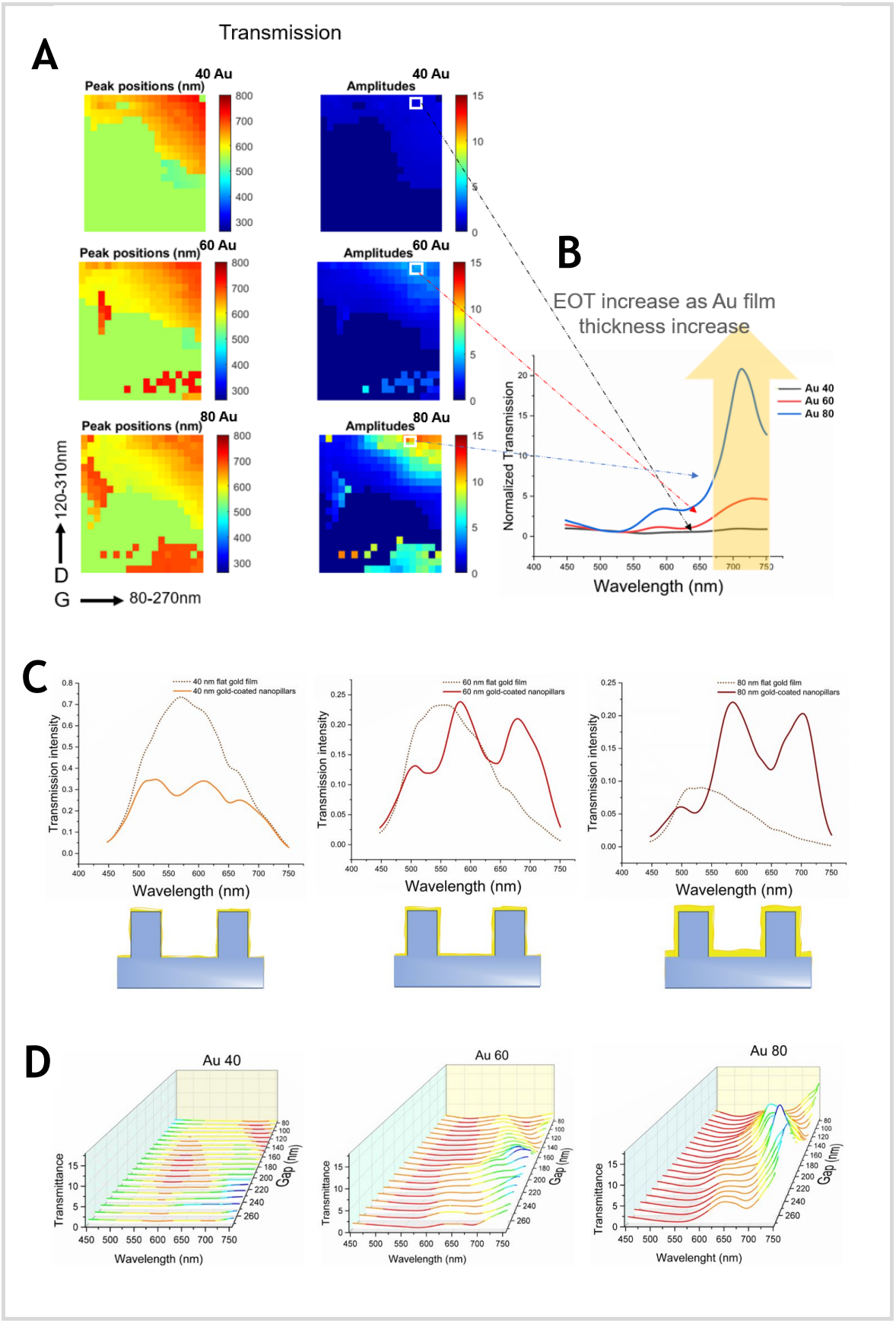

Figure 3.12 A - Heat maps representing the peak positions and amplitudes of the double gradient plasmonic array libraries when measuring transmission and varying the thickness of deposited gold film from 40 nm to 60 nm and 80 nm. B – visualize the increasing EOT trend with gold augmentation and a diagram with nanopillars cross-section depicting the metal network. C – demonstrates the intensity of transmitted light through flat and nanopatterned area with 40nm, 60nm and 80nm gold film. D - demonstrates the gap-dependence variations and constant diameter whit increasing gold thickness.

These findings align closely with the plots presented in Figure 3.12-C, where each transmission signal from the periodically patterned area is superimposed with the transmission from a flat gold substrate of the corresponding film thickness. A noticeable distinction is immediately apparent in the amplitude ratios for 40 nm and 80 nm.

The transmission signal from the 40 nm nanopatterned gold film is notably overpowered by the amplitude from the flat area signal, explaining the absence of transmission enhancement. In contrast, the intensity of transmitted light from the 80 nm gold is two times more when incident light wave impinges on gold coated periodic nanopillars than that from the respective flat substrate. This underscores the pronounced reliance on the quantity of gold coating the nanopillars to meet the conditions for diffractive coupling.

A plausible hypothesis to explain this dependence is the geometric alteration within the nanoarray with a higher thickness of gold deposited at the bottom. This outcome transforms the nanoarray into an interconnected periodic metal network, enabling extended surface plasmon polaritons propagation, leading to strong light transmission through the conversion of surface waves to light radiation, observed as peaks within the transmission spectra (Figure 3.12-C, 80 nm Au plot). In contrast, thinner gold films, with less gold deposited on their sidewalls and interpillar space, configure nanostructures in a more isolated manner, likely generating shorter or more localized SPPs (Figure 3.12-C, 40 nm Au plot). Figure 3.12, panel D illustrates the normalized transmission signals along the horizontal axes of the heat maps, following the variations in gap size and constant diameter. In all three plots, representing gold thicknesses – Au 40, Au 60, and Au 80, the dynamics between the SPP and EOT modes are outlined. A common characteristic observed within all three plots is that the EOT mode is significantly increasing in amplitude as gold metallization build up.

Additionally, as depicted in the heat maps, when we follow the 3D plots in Figure 3.12-D, the EOT maxima is shifting towards higher frequencies as lateral gaps becomes narrower and eventually dissipates.

The optical transmittance can exhibit resonances through various mechanisms. In this context, the EOT phenomenon is facilitated by the corrugations on the metal

surface, with the underlying mechanism termed surface-enhanced EOT (SEOT). Such anomalies represent abrupt dips and peaks on the spectrum as a function of wavelength namely Rayleigh-Wood anomaly. Peaks are usually presented in square arrays of subwavelength nanostructures, where an important length scale is the Rayleigh wavelength (RA) [167]. This wavelength is a fundamental feature in diffraction gratings, where incident light undergoes diffraction into grazing orders. This kind of diffraction anomaly surprisingly do not depend on the material of the nanostructure but instead strongly dependent on the grating parameters and on the environmental refractive indices. Thus, the $\lambda RAs = n_d p$, where n_d is the refractive index of the medium where the diffraction occurs, p is the minimum nanopillar interspace (i.e., the period). λRAs marks the minimum wavelength at which normal incident radiation coming from the air side is transmitted into only one diffraction order, all other diffraction orders being evanescent. The dips are called Wood's anomaly (WA) or surface anomaly, emerging from the excitation of the SPPs supported by the periodicity of the metallic nanoarray [168].

In the SEOT configuration, resonant transmission arises from the coupling of incident radiation to leaky surface modes residing in the interface between the substrate (or the superstrate) and the corrugated metal, occurring at a resonant wavelength λSEOT, where $\lambda SEOT > \lambda RAs$. This mechanism allows light that would typically be reflected by the metallic mirror to remain at the interface, thereby increasing the transmission efficiency.

To further elaborate on the intriguing research findings based on SEOT we utilized the cross-sectional data from Figure 3.12-D, focusing only on the 80 nm gold-coated nanoarrays. The subsequent analysis is summarized in Figure 3.13. Plot A is showcasing the correlation $\lambda SEOT > \lambda RAs$ on a transmission heat map.

The positions of RAs are predicted following the equation mentioned above and delineated on the heat map via a white dashed line.

Notably, all SEOT peaks are positioned to the right of the RA boundary, aligning with expectations for their resonant location at higher wavelengths. Another interesting observation worth noting is that the SEOT enhancement is not supported by the SPP wave but from the LSPR modes. The interference between LSPR/RAs and the occurrence of SLR has been previously discussed in literature.

It has been demonstrated that with shorter grating periods, where there is considerable spectral detuning between the LSPR wavelength and λRAs, the grating primarily displays localized plasmonic characteristics. When the lattice constant is chosen in way that its resonance wavelength is comparable to λRAs, the structures sustain the so called surface lattice resonances (SLRs), mixed modes sharing both plasmonic (LSPR) and photonic properties [169] [170].

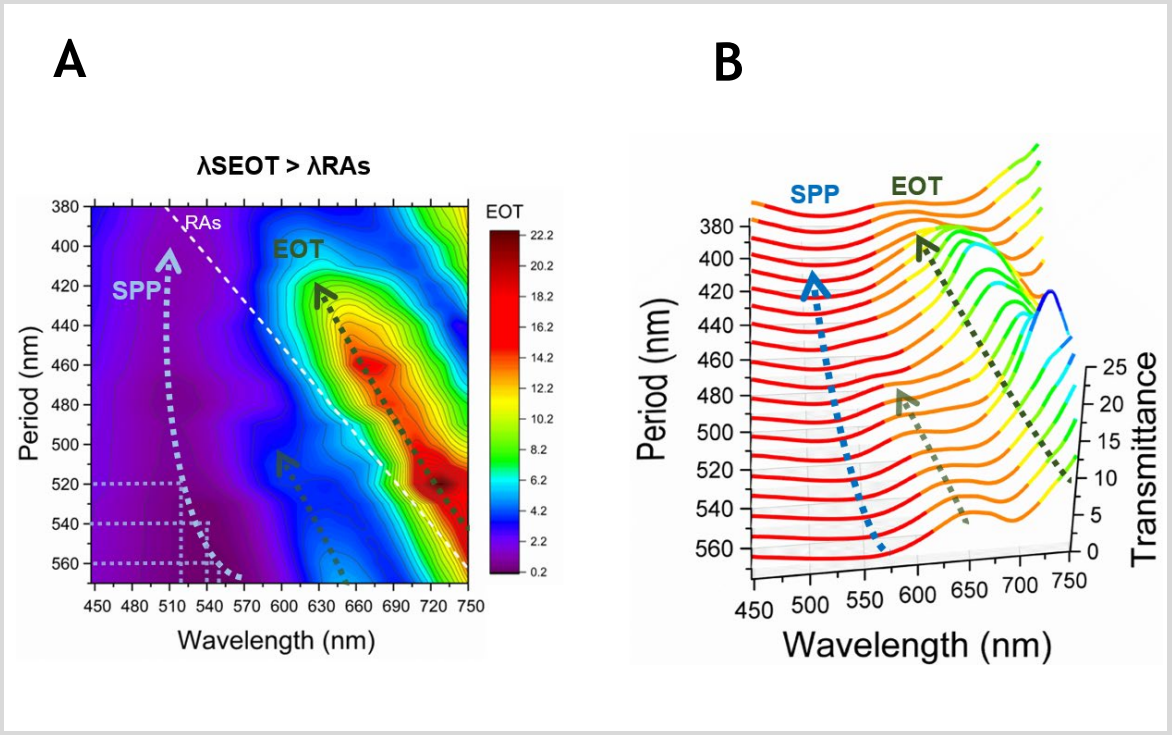

Figure 3.13 Plot A – Transmission heat map for 80 nm gold coated nanopillar arrays with a diameter of 300 nm as a function of the period, and the corresponding Rayleigh anomalies (RAs) in the media (deionized water with RI 1.333) depicted as a white dashed line. The colour bar on the right represents the EOT intensity. Plot B – 3D Y spectral plot of the same data showing the resonance signals. On both plots arrows are depicting the emerging EOT peaks and SPP wave.

These SLRs are long living modes, delocalized on several grating cells significantly increasing the extend of the nanopillar EM fields where energy is distributed in the plane of the array. In figure 3.13 the most pronounced SEOT peak amplitudes occur when scattering nanostructures are adequately spaced with wider gaps. The SEOT peak locations are also well tunned with RAs which is a necessary condition to excite SLRs. However, as the period narrows, the spectral detuning between RAs and SEOT maxima widens, resulting in a diminished effect and dissipation of the SLR mode. Figure 3.13, plot B depicts the SEOT signals as a function of period and the evolution of the peak from SLR to LSPR. In both scenarios, the interference

process may yield constructive interference, leading to arising resonance where the field intensifies, becomes confined and cannot escape from this region, except by absorption (LSPR modes) or radiation (SLR mixed modes) [111].

In square lattice the WA or SPP wave is predicted to occur at a transmission minimum (T=0) and wavelength approximately equal to period size [110] [171]. Remarkably, data in Figure 3.13-A, aligns closely with this prediction, particularly for nanoarrays finely tuned with the RAs border.

The phenomenon of SEOT has garnered significant interest in the research field and has been explored to develop sensor systems where the configuration of the periodic array is altered to enhance sensing performance. SEOT shows promising potential for refractometric sensing applications and particularly for detecting large analytes such as viruses, cells, and bacteria.

3.2.3.3 Regions of interest within the DGPAL

The gold coated nanopillar arrays in the double gradient device as reported exhibit complex optical responses. It can support the periodic analogue of SPPs namely Bragg plasmons, LSPRs and related diffractive effects such as Rayleigh-Wood anomalies (RWAs) and combinations of these resonant and diffractive phenomena.

It is worth noting that RAs, SPPs, SPPs/LSPRs and LSPRs have very different near-field distributions. More specifically, for RAs, the field enhancement extends far from the grating surface, whereas, for SPPs, plasmons propagate along a metal-dielectric interface with an electric field that decays exponentially over hundreds of nanometres into the dielectric. LSPRs are non-propagating resonances in which the mode intensity is confined near the nanoparticle. The hybrid SPPs/LSPRs are mixed modes of localized plasmons vibrations combined with diffracted grazing waves. The surface SPPs/LSPRs mode propagates over the structure resulting from a coherent scattering of light in the array [172]. As a result, the sensing performance of the nanoarrays exhibit either an impressive bulk refractive index sensitivity determined by the extended electric field enhancement or local refractive index sensitivity, which is a key figure of merit for label-free biological sensing, determined by the local confinement of the electric field [168].

The Rayleigh-Wood anomalies particularly depend on the angle of the incident wave, the index of the surrounding medium and the grating period. In this research, the angle of incidence is kept normal ($\theta = 0^{\circ}$) but due to the gradient nature of the plasmonic library, now we can systematically follow the resonance behaviour translating into their geometry configurations.

By observing the peak positions within the absorbance heat map in Figure 3.14-A, it becomes evident that two regions of interest emerge across the gradient library. Almost diagonally, a belt of near NIR peaks appears and expands all the way to the left, covering roughly 60% of the absorbance map and transitioning their oscillation within the red-orange-yellow bandwidth of the VIS. On the other hand, the top right corner of the same map resonates in higher frequencies outside the red region of the VIS. Within this investigation and for more clarity, both plasmonic oscillation modes would be named respectively, Mode 1 and Mode 2.

The collective plasmonic electron oscillation within Mode 1 and Mode 2 are significantly different. They cause extinction of incident light by two distinguished mechanisms. Generally, the predominant resonance in the regions of interest is absorption of the light to generate heat and Rayleigh scattering of the light into other directions.

Upon examination of their positions within the absorbance heat map depicted in Figure 3.14 -A, it becomes evident that the structural configurations manifesting the Mode 1 oscillation predominantly encompass nanopillars characterized by smaller diameters and shorter grating periods. It has been demonstrated that for short grating periods where the spectral detuning between the LSPR and the Rayleigh anomalies (λ_{RA}) is large, the array primarily exhibits purely plasmonic feature.

In such scenarios, the electromagnetic intensity is confined near the nanoparticle in a non-propagating regime (Figure 3.14 -B, Mode 1). Conversely, the Mode 2 type oscillation is dominating the configurations with large nanopillar diameters spaced apart with long grating periods (Figure 3.14 -A).

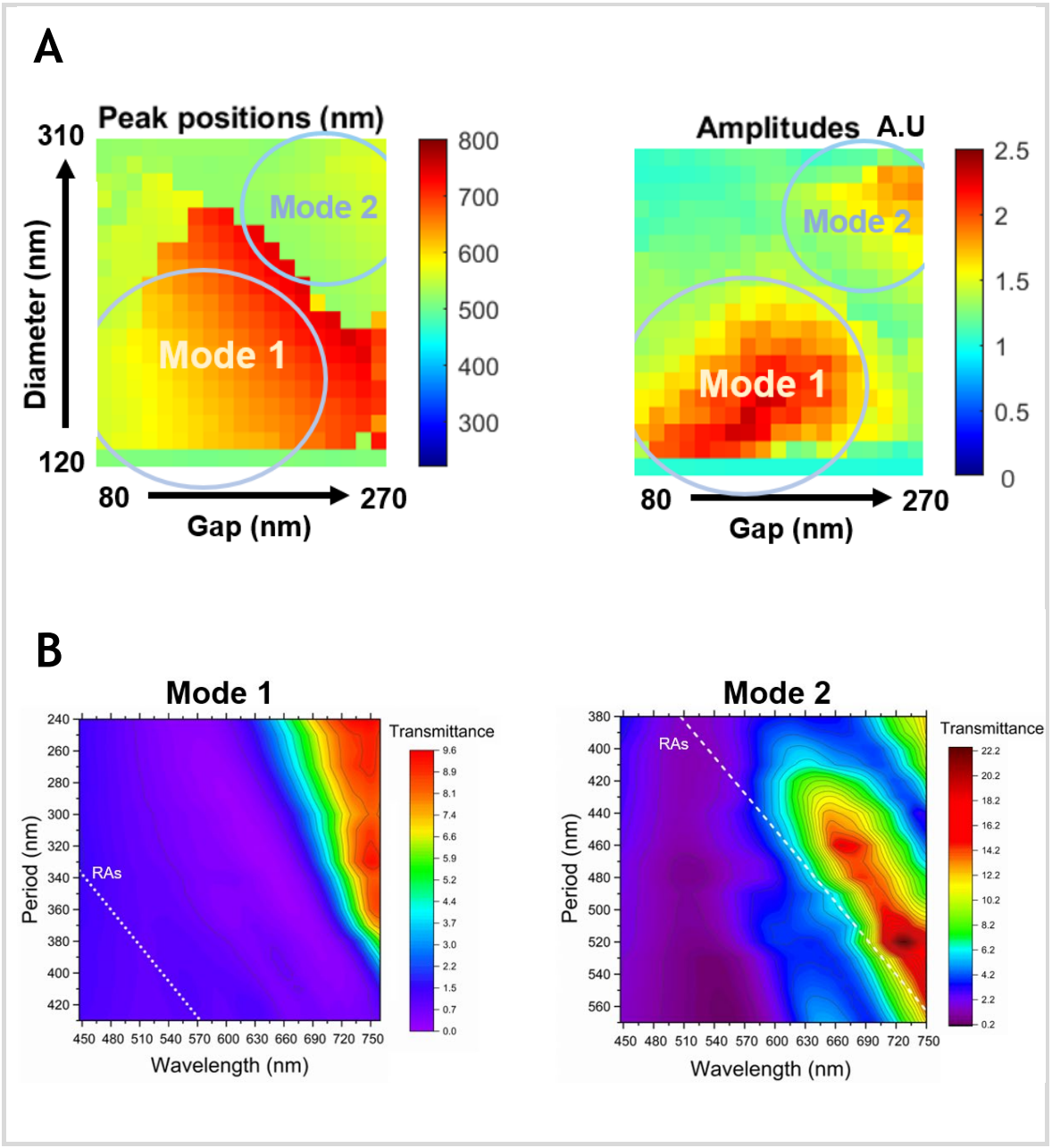

Figure 3.14 Panel A - Absorbance maps of the double gradient plasmonic array library (DGPAL) with 60 nm thin gold film, depicting the absorbance peak positions (left) and absorbance amplitudes (right). On both maps both distinguished modes of oscillation are outlined with a circle: the purely plasmonic LSPR mode is Mode 1 and the SPP mode exhibiting propagating far-field effects is Mode 2. Panel B – Contour heat maps representative for Mode 1 and Mode 2 depicting the tunning with Rayleigh anomalies (RAs). Mode 1 exhibits large spectral detuning with RAs, shaping its purely plasmonic character and Mode 2 well aligned with RAs which satisfies the conditions of diffractive coupling of light into propagating SPPs.

The anomalous transmission of light exemplifies their scattering properties generating Bragg plasmons or SPPs propagating across the periodic mesoscale surface (Figure 3.14 -B, Mode 2). The Bragg plasmons are bound to the surface and propagate only a short distance until their energy is dissipated, but this is

sufficient to transport light from one side of the coating to the other or generate some beneficial lateral enhancement of the electric field. Thus, when the lattice constant is chosen comparable to (λ_{RA}), the structures sustain the so called surface lattice resonances (SLR), mixed modes sharing both plasmonic (LSPR) and photonic properties.

The characteristic properties of resonant oscillations Mode 1 and 2 are further elucidated in the appendix of the thesis, section A4. Finite element modelling is employed to **qualitatively** illustrate and depict their electromagnetic field distribution alongside experimental assessments of refractive index sensing and biomolecular detection performance.

3.3 Demonstrating refractive index sensing and biomolecular detection

3.3.1 Refractive index sensing

The plasmonic resonant peaks are sensitive to the surrounding dielectric environment and show redshift when the refractive index (RI) of the surrounding medium is increased. This RI sensing property of plasmonic nanostructures is utilized in the development of LSPR-based refractometric sensors. The sensitivity to changes in RI is quantified as the shift in the SPR peak position per unit change in the RI of the surrounding medium.

3.3.1.1 Methodology

To measure the bulk RI sensitivity of the double gradient plasmonic library coated with 60 nm gold film, water, and aqueous solution of sucrose [0–30% (w/v)] with refractive index of 1.33 and 1.38 was utilized. Bulk RI sensitivity of all nanoarrays were calculated by evaluating the sensitivity factor. The refractive index sensitivity of all nanoarrays was determined by calculating the sensitivity factor ($S_f = \Delta\lambda_{SPR}/\Delta n$) expressed in units of nm per RIU, where $\Delta\lambda_{SPR}$ represents the change in plasmon frequency and Δn denotes the change in the refractive index of the surrounding medium. The results were visualized by evaluating ΔλSPR for each location and presenting them collectively with their respective sensitivity factor in a heatmap format.

3.3.1.2 RI sensitivity results and discussion

Figure 3.15 summarizes the RI sensitivity analysis depicting S_f of all nanoarrays as a function of their design parameters constructing a heat map. The importance of visualizing the results as a heatmap is to be able to outline a region of interest within the DGPAL where bulk sensitivity is exhibited predominantly. Additionally, it is easier to confirm the correlation of this region to resonance types of Mode 1 and Mode 2.

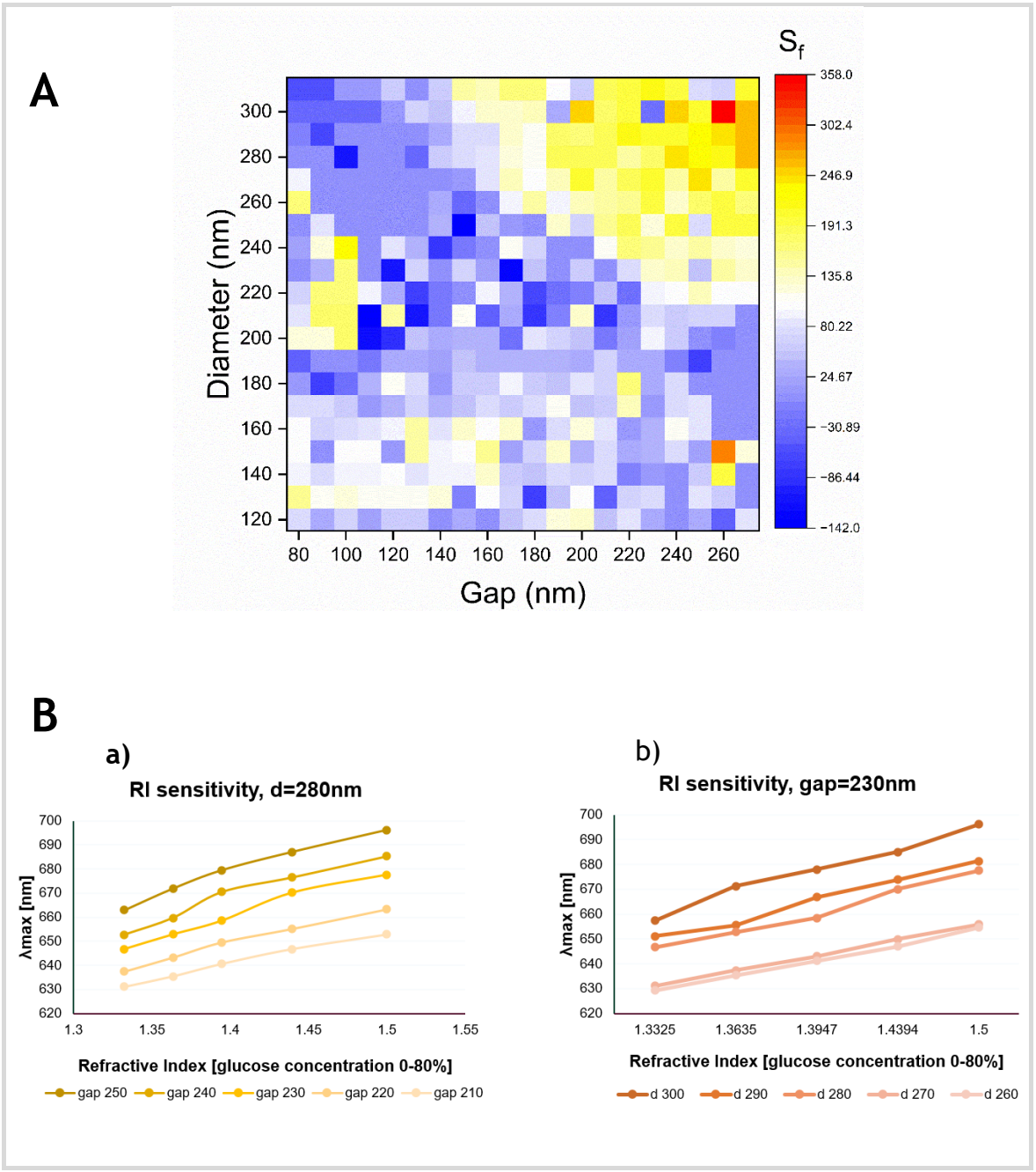

Figure 3.15 Panel A- Heatmap representing the S_f after RI of the surrounding medium is increased from RI 1.333 to RI 1.38. [0–30% (w/v), aqueous solution of sucrose]. Panel B – analysis of both horizontal and vertical cross-sectional datasets demonstrating the linearity in RI sensing of the nanoarrays located within Mode 2 area. The correlation coefficient (R-square) values for plot a) $R^2 > 0.96$ and plot b) $R^2 > 0.98$.

When observing the heatmap in figure 3.15 it becomes evident that RI sensitivity is extremely well outlined in the top right corner. The calculated S_f values are within the range of 120 nm/RIU to 358 nm/RIU. As discussed in previously (section 3.2.3.3) this specific region is identified with resonance Mode 2.

The screening analysis suggested that nanoarrays with the following design combinations – diameter size in the range 310 – 250 nm and gap size 270 – 190 nm hold the potential for bulk biosensing applications. After identifying the region of interest (ROI) with high sensitivity on the plasmonic library the experiment followed a further investigation by immersing these nanoarrays into a series of RI liquids with RI values from 1.33 – 1.5. After each measurement, the sensor is carefully cleaned with DI water and dried to remove the residual liquid until the spectrum returns to the initial status. Figure 3.15-B shows that shifts are proportional to the increasing RI of the analyte which confirms the linear dependence of the trend.

These observations are consistent with previously reported findings in the literature suggesting that the bulk sensitivity of the LSPR is increasing with the size of the nanostructures, which is in an agreement with theory [173]. Undoubtedly, the outcomes also align with the findings from the resonance characterization analysis reported in this chapter as we anticipated Mode 2 oscillation, characterized by large nanopillar diameters spaced apart with long grating periods to prevail in the configurations. Configurations like these generate SPPs propagating through the periodic mesoscale surface. The propagating plasmons are bound to the surface and travel only for a short distance until their energy is dissipated but this is sufficient to generate some useful lateral enhancement of the electric field. The COMSOL model also confirmed the extended EM distribution for nanoarrays with relatively large sizes and wide interspacing. EM fields was shown exceeding the distance of decay multiple times compared to nanoarrays with small features. Hence, the structures sustain the so called surface lattice resonances (SLR), mixed modes sharing both plasmonic (LSPR) and photonic properties.

The LSPR sensors with different material composition and different shape and size ensembled particles resonating in the VIS bandwidth exhibit RI sensitivity between 100 – 500 nm/RIU [68]. The LSPR sensors exploiting the geometry of nanoparticle

arrays and other planar nanostructures can be designed with higher refractive index sensitivities. The state of the art LSPR plasmonic sensors can achieve as high as 1900 nm/RIU at the NIR region [174]. However, working at IR range has prevented them from broader application with low-cost and common equipment to observe [175]. At visible spectrum, the sensitivity for LSPR nano-array sensor is about hundreds of nanometres per RIU. Examples reported in the literature have demonstrated that bowtie arrays achieve sensitivity of 577 nm/RIU [176] and the double-hole structure in a gold film improves the bulk refractive index sensitivity with 600 nm/RIU [177]. In comparison to our research findings, the sensitivity of 358 nm/RIU achieved with the nanopillar arrays is quite close to the reported accomplishments. The trend observed in the heatmap depicted in Figure 3.15-A indicates a gradual rise in sensitivity as both diameter and interspacing increase. This trend presents an opportunity for future optimization efforts, which may have the potential to surpass the performance of other nanoarrays.

3.3.2 Biomolecular detection

Biomolecular detection requires plasmonic resonant peaks to be sensitive to the surrounding dielectric environment and show redshift when the local refractive index of the surrounding medium is increased. Low protein concentrations suspended in water-based saline buffers matching the physiological conditions of biological entities does not change the RI of the buffer due to the small number of binding molecules. LSPR spectroscopy is a sensitive method for measuring the local refractive index changes surrounding the gold nanostructures. A main advantage of LSPR sensors is the very short decay length of the EM field at the nanopillar surface. The short decay length arises from the confined nature of the plasmons in a nanoscale material [178]. The inherent property of LSPR sensors is most sensitive to refractive index changes occurring within 5 - 15 nm of the nanostructure surface [71]. This highly localized sensitivity confers huge advantages when the analyte in question is on the nanoscale, or when refractive index changes occur very close to the nanoparticle surface.

3.3.2.1 Methodology

In this particular reaction we used a low concentration, small MW protein like bovine serum albumin (BSA) to activate the ROI with predominantly localised type of oscillation.

BSA is relatively small– 66.5 kDa, stable, moderately non-reactive protein, and it is often used as a blocking reagent in many biological assays. Its detection in small amounts and with high selectivity is of particular importance in medical and biological fields. The BSA protein (Sigma-Aldrich, A9418) was added in concentration 0.5 μM and incubated for 2 hours in RT during continuous mixing. After a mandatory washing step with PBS removing any unbound target protein, scan measurements of the surface finished the biomolecular detection experiment.

3.3.2.2. Biomolecular detection – results and discussion

The heat map in Figure 3.16 is a visual representation of the shift in LSPR peak positions for all 400 nanoarrays. It illustrates the changes on the electromagnetic metasurface after introducing a low-concentration of small protein and showcase the non-specific adsorption events. This shift is calculated relative to a reference scan, which comprises measurements of the DGPAL under operating buffer conditions in PBS and a intact gold nanopatterned layer. The detection of binding events is registered on the heat map as pixels in various shades of red. The colour palette of the heat map differentiates the unsuccessful LSPR shifts with shades in blue colour. The collective colours from all pixels in the DGPAL create a signature fingerprint indicative of the binding event. As anticipated, the most sensitive region of the plasmonic library corresponds to the area associated with Mode 1 oscillation. These nanoarrays are characterized by relatively small nanopillars and narrow lateral interspacing enabling a gradient of mixed LSPR/SPP and pure LSPR oscillations to exist.

The energy enveloping the nanopillars, with an electromagnetic distribution confined strictly around their dimensions and field attenuation extending over a few tens of nanometres, is extremely sensitive to subtle changes in the local refractive index induced by similar-sized proteins.

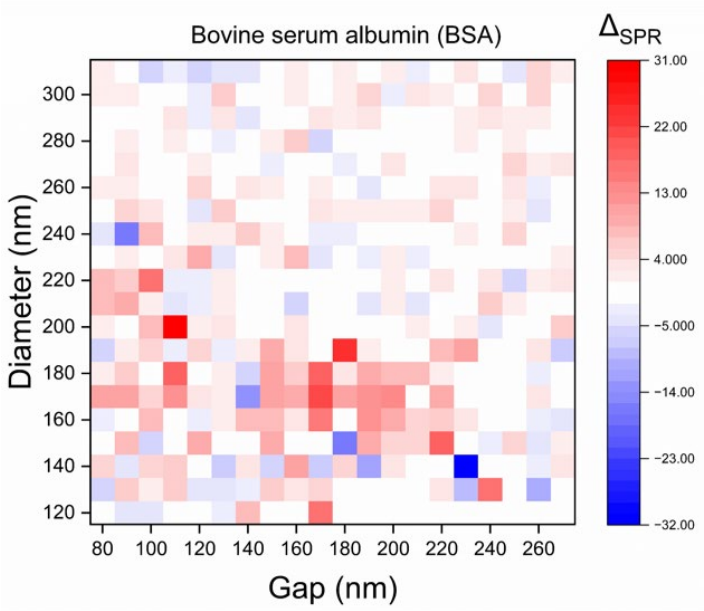

Figure 3.16 Heat map representation of a biomolecular detection process depicting the absorption of 0.5 µM bovine serum albumin (BSA).

3.4 Templet-assisted plasmonic array device for Nicoya OPEN SPR

The next level of exploration utilizing phase-coherent coupling of the localized electromagnetic fields is integrating the templet-assisted plasmonic array device to a commercially available SPR instrument to deliver repeatable, high quality, label-free interaction analysis. As the focus of the SPR instrument is to provide kinetic data, the biomolecular detection characterisation certainly outlined a cluster of nanoarrays that can be identified suitable for integration. To refine the geometry configuration for real-time kinetic analysis, the resonance profile must align with the operational detection window of the instrument. However, the detailed peak engineering characterisation with design parameters and thickness of gold provided sufficient data to address this adjustment.

Figure 3.17-A illustrates the absorbance peak of the default sensor installed in the instrument. The operational detection window spanning 450 -750 nm is corresponding precisely to the visible bandwidth which is focus of our research.

The centre position of the absorbance peak is expected to be around 550 nm. To achieve plasmonic oscillation similar to the 550 nm frequency, the plasmonic array design should feature small diameters and relatively narrow interspacing between nanopillars. Additionally, the enhancement factor was considered, with preference given to plasmonic configurations with the highest absorbance amplitude. This is demonstrated in Figure 3.17-B. Plot (a) – illustrates that if the interspacing between nanopillars is 120 nm, the oscillation is blue shifting as diameter size is decreasing. The most advantageous configuration, which oscillates near 550 nm, features a diameter of 130 nm.

The configuration featuring a diameter of 130 nm and a gap of 120 nm also maintains a diameter-to-gap ratio close to 1, exhibiting the highest absorbance amplitude, as indicated in the legend. Plot (b) – illustrates that if a diameter is 130 nm, the oscillation is shifting to even higher frequency as gap size is getting narrower. Specifically, the oscillation can reach up to 570 nm when the gap size is reduced to 90 nm. However, it is evident that the peak with the highest amplitude and sharpest FWHM profile, conforming to the "ideal square array" effect with a diameter-to-gap ratio near 1, oscillates at 590 nm. LSPR enhancement and a sharp peak profile are crucial characteristics, as they are considered more advantageous for biomolecular detection purposes.

Despite deviating by 40 nm from the expected 550 nm resonance, the 590 nm peak still falls within the operational detection window of the instrument. Consequently, this deviation was not deemed critical for the performance. This rationale led to the selection of the nanoarray configuration with a diameter of 130 nm and a gap of 120 nm for further investigation.

Figure 3.17-C presents the exact location on the resonance heat maps of the chosen configuration and a SEM image of the optoelectronic device additionally fabricated for real-time kinetic analysis, integrated into the Nicoya OpenSPR system. Detailed findings derived from experiments conducted with the Nicoya OpenSPR system are elaborated upon in Chapter 4.

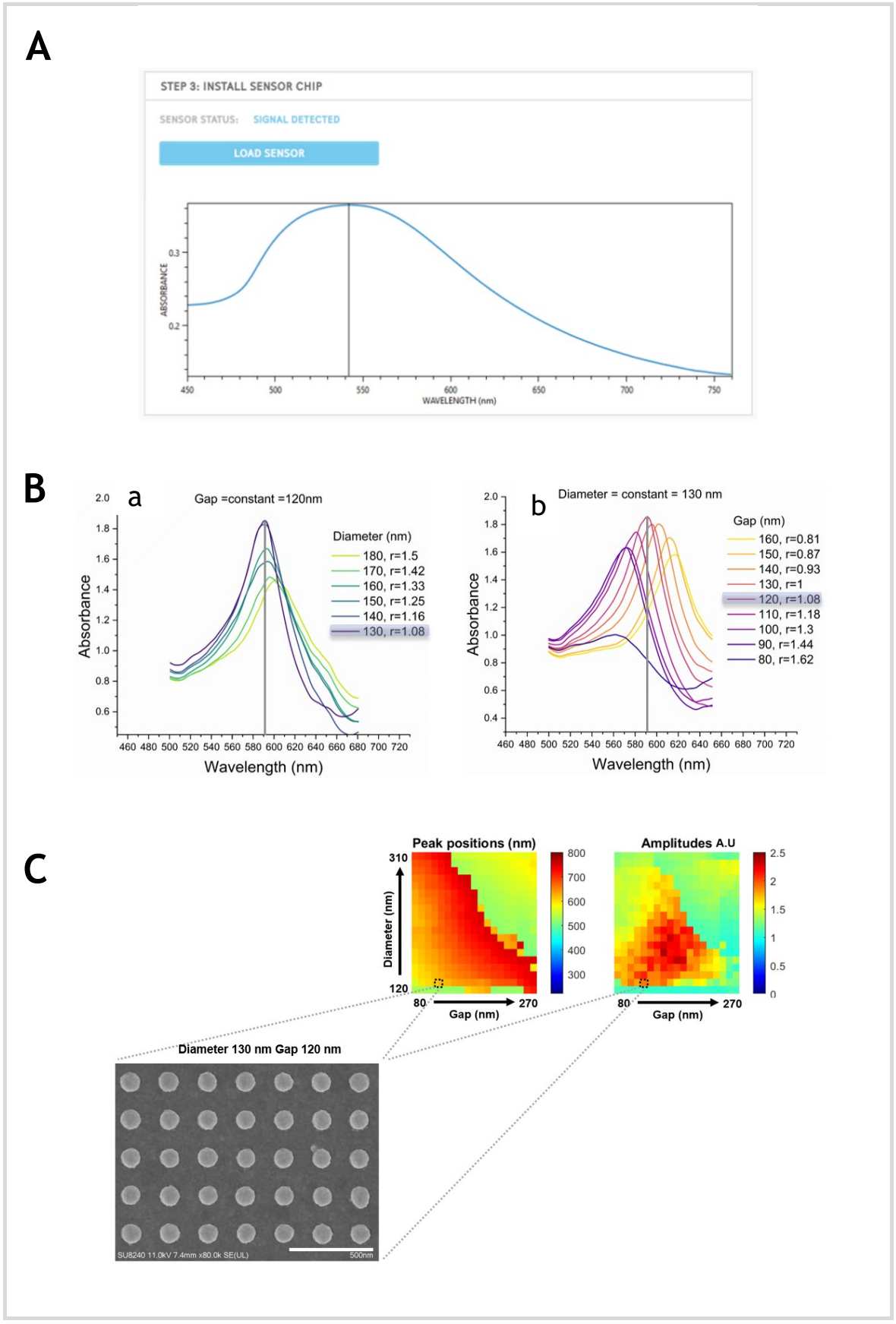

Figure 3.17 A - Absorbance graph of the default sensor installed into the Nicoya OpenSPR. B – Absorbance graph of nanoarray clusters from the DGPAL considered for integration as an optoelectronic device for real-time kinetic analysis in the Nicoya OpenSPR. C – SEM image illustrating the newly fabricated nanoarray configuration. The scale bar in the image is 500 nm. The location of this particular configuration is also shown on the resonance heat map.

3.5 Summary/Conclusion

While numerous studies explore randomly disordered nanoparticle arrangements as a cost-effective alternative, periodic arrays offer a controlled platform for investigating optical properties. This enables the investigation of near- and far-field interactions between adjacent nanostructures, which may lead to the controlled manipulation of optical signals and light-matter interactions. In this research we demonstrated the development of a library comprising injection-moulded nanopillars featuring a continuous gold film coating fabricated via high-throughput replication addressing high-quality, reproducibility and low production cost. The templet-assisted nanoarrays are composed of high-quality durable glass-clear polystyrene which is a widely adopted material for laboratory products. The high optical transparency allows maximum transmission of light. Additionally, the gold film providing plasmonic activation exhibits the characteristic properties of a noble metal including high biocompatibility, corrosion resistance preserving device sensitivity. These combined attributes position the injection-moulded nanopillar library as a SPR-based detector suitable for operation in various working conditions, including clinical and biomedical laboratory settings.

The characterisation of the DGPAL yields an insightful investigation over the various phenomena of light conservation generating valuable information for the optical properties of square nanoarrays. The investigation provided detailed information for peak engineering through the adjustment of geometry configurations and gold film thickness. Resonance oscillations can be manipulated towards higher frequencies by reducing the interspacing gap between nanopillars and decreasing the diameter size of the nanopillars, or a combination thereof. Conversely, alterations in the opposite direction result in oscillation shifts towards lower frequencies. Optimal plasmonic enhancement is achieved when the square nanoarray is constructed with dimensions where the diameter-to-gap ratio is close to 1. Varying the thickness of gold deposition offers a broader bandwidth of resonance wavelengths and serves as an effective means of dynamic tuning. The Au 40 device provide a bandwidth range of 147 nm, which widens to 183 nm for Au 60 and reaches 195 nm for Au 80. The peak profiles are also significantly different, exhibiting higher amplitudes with 40 nm and 60 nm gold film and best FWHM profile is obtained with 60 nm Au.

Array periodicity provides an additional dimension for improving the performance of optical and optoelectronic devices through phase-coherent coupling of the localized electromagnetic fields between adjacent nanoparticles or through multiple scattering or grating-diffraction effects. Activation of extraordinary optical transmission induced with the 80 nm gold film, exhibit strong emission of light as the intense fields of SPPs transition from nonradiative to radiative upon coupling with incident light. The gold coated nanopillar arrays in the double gradient device as reported exhibit complex optical responses. It can support the periodic analogue of SPPs namely Bragg plasmons, LSPRs and related diffractive effects such as RWAs and combinations of these resonant and diffractive phenomena which have very different near-field distributions. Bringing localized and propagating surface plasmons together in a single platform demonstrates the unique opportunity to investigate the mixed as well as the pure form of those phenomena. This distinction led to the identification and further exploration of oscillation types labelled as Mode 1 and Mode 2. Mode 2 was associated with refractive index sensitivity, while Mode 1 governed biomolecular detection. The sensitivity of both oscillation modes was experimentally assessed and further analysed through finite element modelling. The comprehensive characterisation of the DGPAL provided sufficient data to define the nanoarray configuration for additional fabrication as an optoelectronic device tailored for real-time kinetic analysis, integrated into the Nicoya OpenSPR system.

Chapter 4 Optoelectronic sensor for kinetic analysis via Nicoya OpenSPR

4.1 Introduction

4.1.1 Sensor technology

A biosensor is a device used to detect and/or quantify a biochemical molecule, such as a protein, strand of DNA, polymers, virus particles etc. Three essential components construct a biosensor device – the biointerface, the transducing mechanism, and the output system [179] [180]. The biointerface is the biorecognition element that selectively binds the target analyte known as a capture probe or receptor ligand. The biointerface is immobilised on the optical transducer component and determines the manner in which the target is recognized and the selectivity of the sensor [10]. As both components retain direct spatial contact, the produced signal from the biointerface-analyte interaction translates the capturing events into a measurable parameter [181]. Optical transduction utilizes the interaction of optical fields and provides readable change in signal which is quantified from the output system. The output system deals with all post-processing that must be done to the raw data provided by the transducer, including amplifying, filtering, reading, and transmitting [182].

In this work, we demonstrate a biosensor which transducer component is based on gold-coated nanopillar periodic array layout over a solid-state chip. Nanostructured materials have tunable physicochemical characteristics and understanding the fundamental optical properties has allowed significant growth in plasmonic nanostructure research and development in the fields of medicine, biosensing, imaging, solar energy, catalysis, and optoelectronics [183]. When the chip-based nano-array patterns are irradiated with light they generate collective behaviour of plasmons producing a coherent optical response, which leads to strong EM field and narrow spectral features [184]. When molecules bind to the nanopillars surface, a shift in the resonance peak position can be detected in absorption spectroscopy (Figure 4.1). The produced quantifiable signal is proportional to the amount of biological material present on the sensor surface.

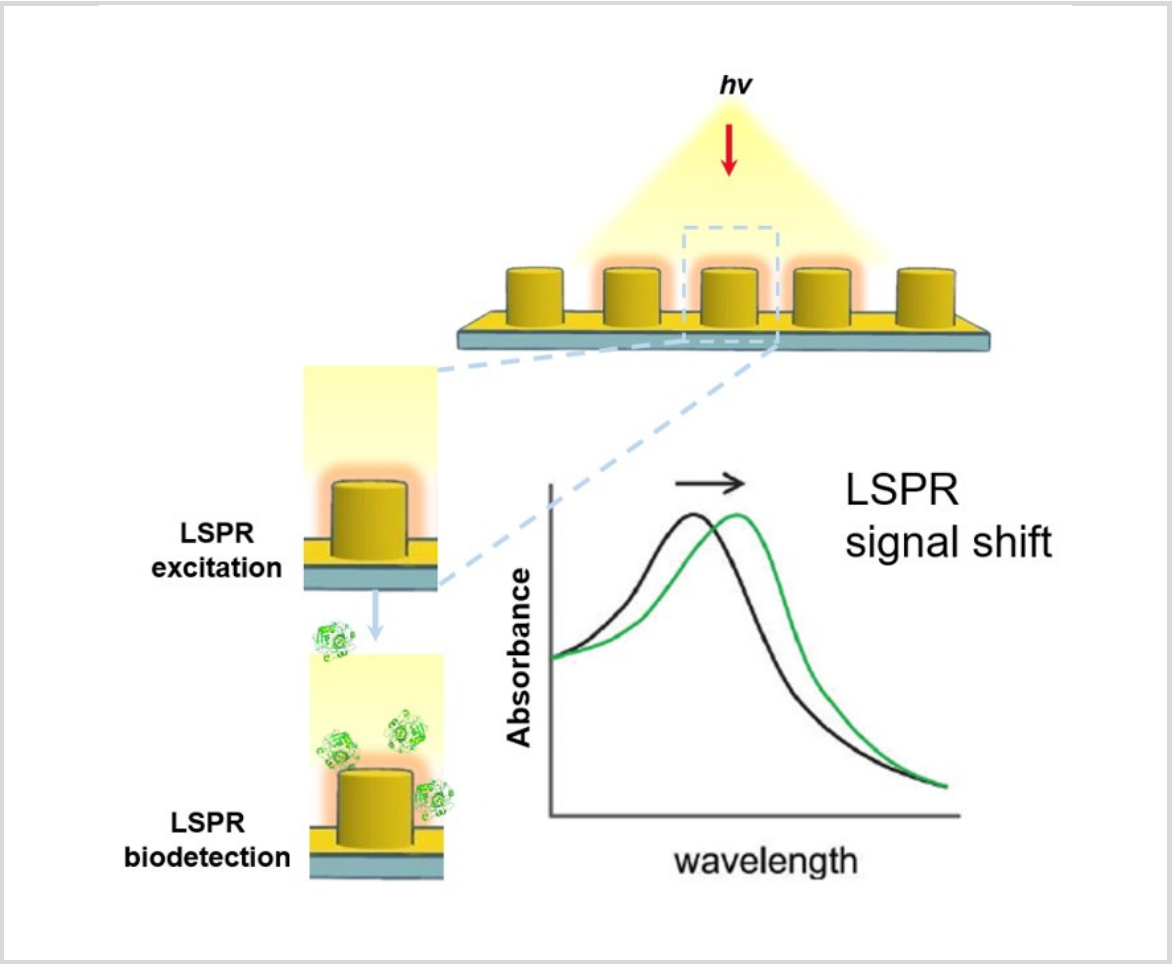

Figure 4.1 Schematic illustration outlining the fundamental principles of plasmonic metallic nanostructure-based biosensors. The sensing mechanism for an array of nanopillar structures relies on LSPR excitation, resulting in a shift in the peak position observed within the absorbance spectrum upon interaction with the analyte. Illustration of biomolecules are adapted from [185].

Biomolecular detection requires plasmonic resonant peaks to be sensitive to the surrounding dielectric environment and show redshift when the local refractive index of the surrounding medium is increased [124]. Low protein concentrations suspended in water-based saline buffers matching the physiological conditions of biological entities does not change the RI of the buffer due to the small number of binding molecules. However, LSPR spectroscopy is a sensitive method for measuring the local refractive index changes surrounding the gold nanostructures. A main advantage of LSPR sensors is the very short decay length of the EM field at the nanopillar surface. The short decay length arises from the confined nature of the plasmons in a nanoscale material [186]. The inherent property of LSPR sensors is most sensitive to refractive index changes occurring within 5 - 15 nm of the nanostructure surface [187, 188]. This highly localized sensitivity confers huge

advantages when the analyte in question is on the nanoscale, or when refractive index changes occur very close to the nanoparticle surface. Thus, SPR spectroscopy has emerged as a valuable technique for studying protein-protein interactions in real-time [189].

In sensor technology, specificity and sensitivity are two fundamental parameters that define the sensor's performance in detecting a target analyte.

1. Sensitivity: Measuring the Sensor’s Detection Capability

Sensitivity refers to the ability of a sensor to detect a target analyte and to produce a measurable response. It is often expressed as the change in output signal per unit change in analyte concentration [190] [191].

Key Aspects of Sensitivity:

Limit of Detection (LOD): The smallest concentration of the analyte that the sensor can reliably detect. A lower LOD indicates higher sensitivity.

Dynamic Range: The range of analyte concentrations over which the sensor provides a proportional and reliable response.

Signal-to-Noise Ratio (SNR): The ratio of the sensor's response to the target analyte relative to background noise. A high SNR means better sensitivity.

2. Specificity: Distinguishing the Target Analyte from Others

Specificity refers to the sensor's ability to identify and measure the intended analyte while minimizing interference from non-target substances. High specificity ensures that the sensor does not produce false positives or cross-react with structurally similar compounds [192].

Key Aspects of Specificity:

Selectivity Towards Target Molecule: The sensor must be designed to recognize only the desired analyte using specific biorecognition elements (e.g., antibodies, enzymes, or aptamers in biosensors).

Minimal Cross-Sensitivity: The sensor should not respond to similar but unrelated compounds in the sample matrix.

Robustness in Complex Environments: A highly specific sensor should perform well even in complex samples such as blood, wastewater, or air, where multiple interfering substances may be present.

For instance, in COVID-19 diagnostic testing, a highly specific sensor should only detect SARS-CoV-2 viral proteins and not cross-react with proteins from other coronaviruses to avoid false positives.
Optimizing both parameters is crucial for developing effective and reliable sensors tailored to specific applications.
In LSPR sensors, sensitivity is primarily governed by the localized electromagnetic field enhancement generated by the plasmonic nanostructures. The magnitude of this enhancement depends on the size, shape, periodicity, and material composition of the nanostructures, as well as the refractive index contrast between the sensing environment and the nanostructure surface. The specificity, on the other hand, is largely dictated by the biorecognition elements immobilized on the sensor surface, ensuring selective interaction with the target analyte. However, factors such as surface chemistry, non-specific binding, and matrix effects can influence specificity and should be carefully optimized to achieve reliable detection.

As the optical biosensors in our research exert detection based on the intrinsic property of mass of the biological target, the detection type is considered – label-free. Historically, biological research relied upon attachment of some sort of "label" e.g. a tag or fluorophore to make detection possible. However, the procedures of introducing a label tag can affect the integrity or functionality of the target leading to inaccurate assessment. The above considerations have driven the curiosity in the research field towards label-free detection, reducing the assay complexity and cost while providing more reliable quantitative information. Label-free detection removes experimental uncertainty induced by the effect of the label on molecular conformation, steric hindrance, blocking of binding epitopes and artefacts as quenching, background fluorescence and shelf-life [193].

The optical biosensor is also a passive optical component from the standpoint that the light needed for the LSPR excitation is supplied externally [181]. This is an advantageous feature as the sensor itself does not consume any power. Additionally, the illumination level required for the proper functioning of the biosensor to generate measurable response is generally very low.

4.1.2 Surface functionalization

The transducer alone however intricately designed is not sufficiently intelligent to identify the investigate biological target. The surface of the transducer should be modified to selectively attach specific material from a mixed test sample while not allowing undesired materials to attach. Selective detection capability is provided through the biointerface [194]. The biointerface is the biorecognition surface coating realized through surface chemistry procedures used to immobilize the receptor ligand with covalent bond linkages so that they are not easily washed away while maintain their biological activity. Biomolecular detection methods in this research obtain specificity from nanopillar functionalisation with biorecognition elements like antibodies.

A suitable surface technique that is widely used with metal surfaces and particularly gold layer is that of self-assembled monolayers (SAMs) (Figure 4.2-A). SAMs are organic polymers forming highly organized compact monolayers on the surface of solids after adsorption, usually from solution. The SAMs of thiols are prepared by immersing a clean gold substrate into a dilute solution of the thiol. Although self-assembly takes place rapidly, good experimental procedures require the duration of the incubation to be around 24-48 hours. Longer assembly times tend to result in better monolayer packing. These monolayers exhibit molecular order and are relatively stable in ambient conditions. The application of SAMs is generally for either passivating the surface or/and functionalizing the nanosized objects with active functional groups [195].

The incorporation of monolayer components containing different functional head and tail groups allows for the chemical control and tailoring of metal-surface properties. The bifunctional alkanethiol utilized in the biomolecular detection reaction in this project is a biotinylated SAM. A tail group that exhibits strong affinity to bond with inert gold is the thiol group. The sulfhydryl group forms a reactive sulfhydryl radical which covalently chemisorbs to the gold surface. The body of the organothiol consists of repeated PEG units which is modified to attain the desired choice of surface functional groups as required for a particular set of bio-affinitive reactions. The biotinylated functional head utilized in the investigation is to create streptavidin sandwiches and ensure the strong immobilisation of the biorecognition ligand.

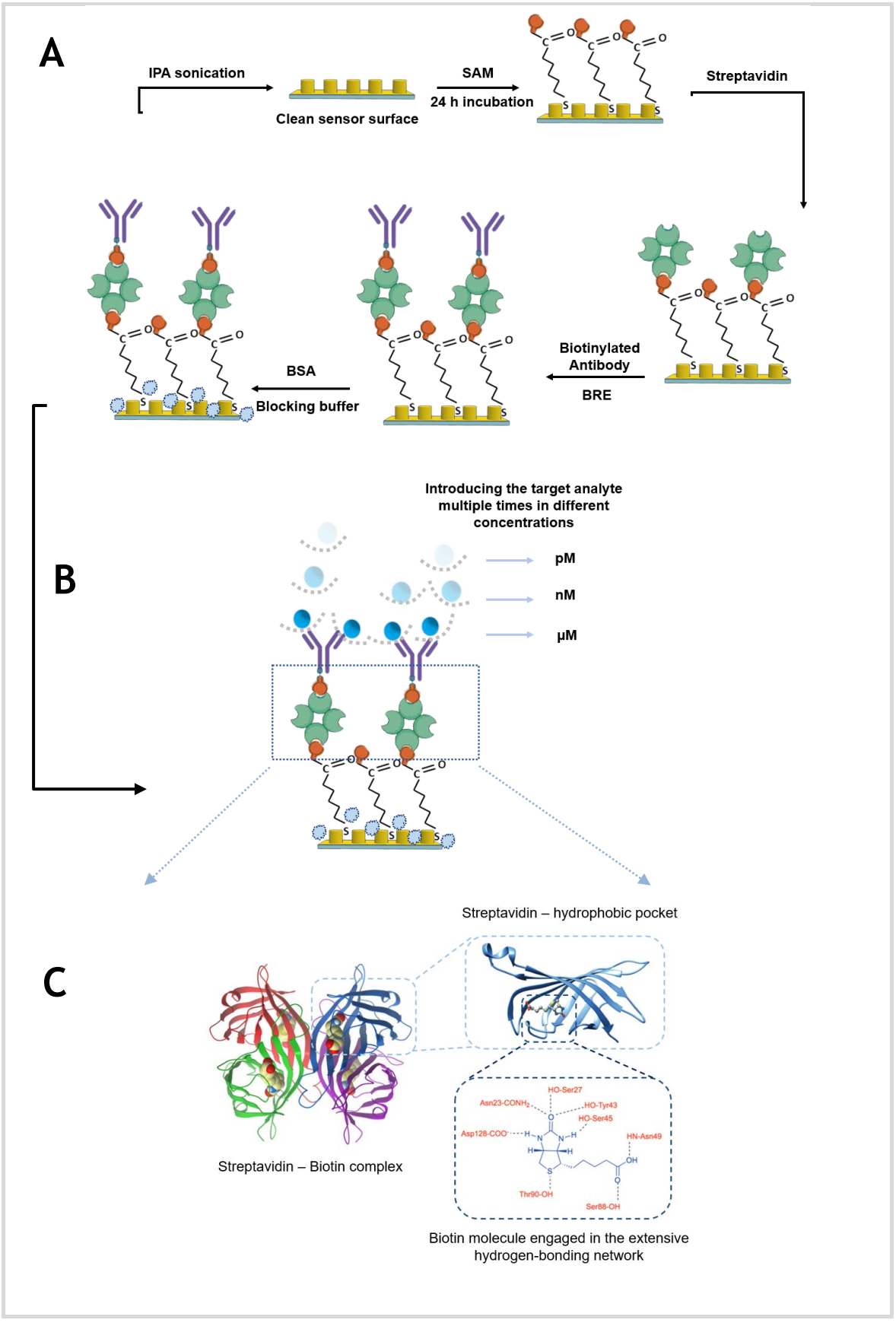

Figure 4.2 A-Schematic illustration of the biointerface of a sensor surface. Nanopillar array is functionalised with bifunctional self-assembled monolayer of biotinylated alkanethiol, sandwiched streptavidin with biotinylated biorecognition elements e.g. IgG antibody. The gold film is blocked with BSA protein. B- the biointerface configuration can withhold multiple detection reactions when varying the analyte concentration. C – illustrating the extensive bonding network of the biotin-streptavidin complex securing the antibodies anchored on the surface adapted with permission from [196] [197] [198].

Streptavidin (SA) is a 55 kDa tetramer featuring four hydrophobic binding pockets with high shape complementarity for biotin and biotinylated biomolecules [199]. This interaction ranks among the strongest known noncovalent biological interactions, characterized by femtomolar affinity constants [200] (Figure 4.2-C). Given the symmetrical structure of streptavidin, the protein's orientation is not crucial, as it is likely to bind to only 1 or 2 biotin sites, leaving 2 or more pockets available. This vacant biotin binding capacity presents an opportunity for the introduction of additional biotinylated molecules, such as antibodies, acting as highly specific biorecognition elements (BREs) to selectively target the analyte under investigation.

Class immunoglobulin (IgG) antibody type is a relatively large size globular protein - 150 kDa, consisting of two fragment antigen binding (Fab) arms connected to a Fc tail (fragment crystalline) forming the trunk of the “Y”-shape [201]. The MAbs are laboratory-produced molecules, derived from a monoclonal cell line, engineered to exert a defined immunological activity based on binding to a specific ligand or antigen [202]. MAbs have strong affinity to only one particular sequence, an epitope (typically 4-6 amino acids in length) and their tailored specificity make them widely used in research to identify and detect target proteins of interest. By adding the biotinylated MAb on the surface of the DGPAL, the functionalisation process of the plasmonically active nanopillars is finalized as it is designed to only capture the target of investigation while everything else would be washed away during the rinsing steps in between measurements.

Minimisation of non-specific binding events is usually achieved by blocking the uncoated parts of the gold with abundance of BSA protein [203]. The BSA protein is a small globular protein sticking easily on the gold surface. The high adsorption of BSA on the gold nanopillar arrays was discussed in Chapter 3, section 3.4.5 and section 3.4.6, demonstrating significant resonance shift. The inert character of BSA makes it a compulsory step before each biosensing evaluation providing high accuracy of the immunoreaction.

4.1.3 LSPR response curve

The output system of a real-time binding kinetic analysis presents the results of a LSPR biosensor experiment as a series of sensograms. The sensorgram visualise the

LSPR binding signal in response units (RU) as a function of time and allows binding constants to be derived (Figure 4.3) [204] [205]. The binding stages of any investigated analyte shape the response curve of the sensogram with more or less the following signature profile.

A reference baseline is initially established by buffer flow and while it is running the response curve remains unchanged as the resonance peak does not shift (Figure 4.3). In the second stage, the target analyte is injected over the surface and immediately with the start of the analyte flow the response increases. The binding of the analyte to the biorecognition antibodies (Abs) is monitored by changes in the LSPR signal. With sufficient time, a steady-state plateau is reached. This stage signifies the established equilibrium between association and dissociation rates of the analyte.

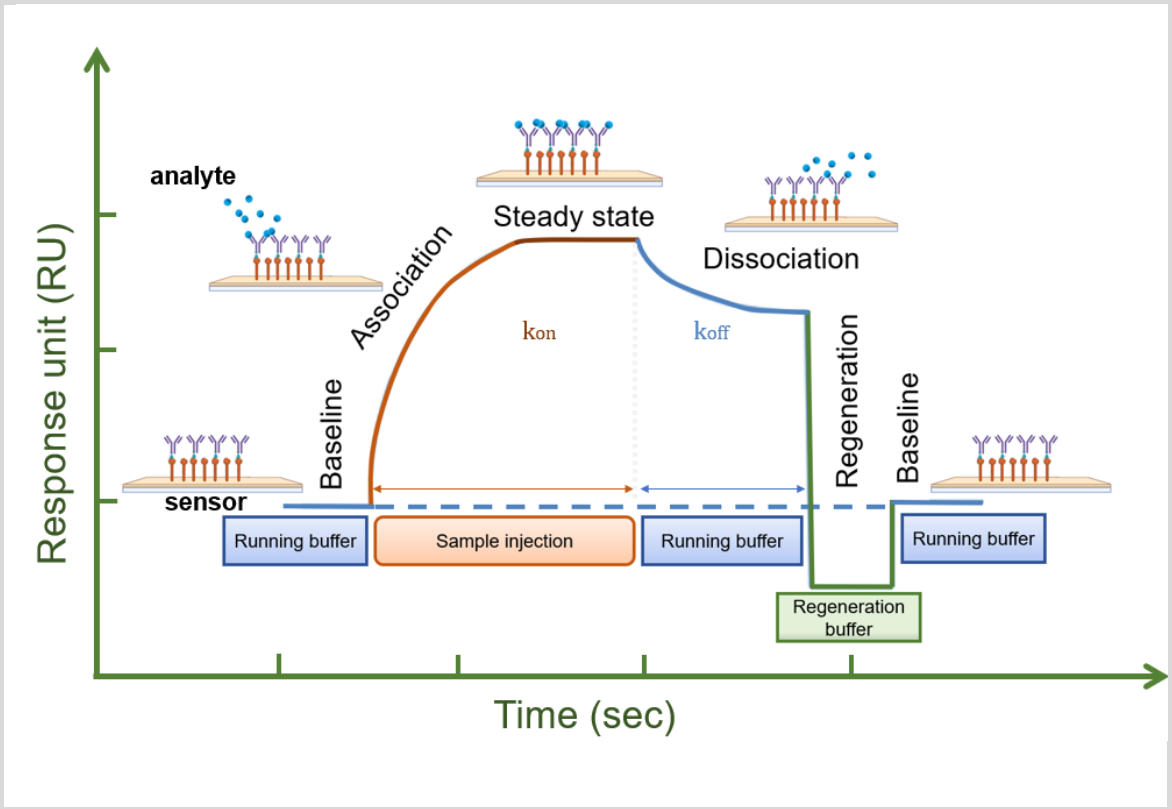

Figure 4.3 LSPR sensorgram and its components described in steps. 1) Running buffer was injected to stabilize the baseline of the sensor surface; 2) Association: analyte is injected over the immobilized antibodies and there is a rise in RU as they bind to their recognition sites; 3) Bound and unbound analyte in equilibrium at the steady state; 4) Dissociation: the running buffer flow after the end of analyte injection remove it and determine the dissociation constant; 5) Injection of regeneration buffer to remove any remaining ligand on the sensor chip and 6) followed by the running buffer flow to stabilize the baseline for the next ligand injection.

Subsequently, as the volume of the sample injection finishes, the flow reinitiates with the running buffer and the response curve gradually drops. In this stage the dissociation of the complex is monitored as a function of time. The remaining analyte traces are removed from the surface of the sensor by injecting regeneration buffer disrupting the bonds between the analyte epitope and the binding pockets of the antibody. This stage regenerates the sensor to its initial state bringing the response signal back to baseline. The above steps are repeated with a series of analyte concentrations and the resulting sensograms are fitted to an appropriate binding model as described below.

The binding of an analyte (A) to a capture probe (B) and forming a complex (AB), is described by the Langmuir adsorption isotherm (assuming a 1:1 interaction) [206]. The interaction describing the basic transfer function is the following equation:

$$A + B \underset{k_{off}}{\overset{k_{on}}{\rightleftharpoons}} AB \qquad (1)$$

The equilibrium constants:

$$K_A = \frac{k_{on}}{k_{off}} = \frac{[AB]}{[A].[B]} = \frac{1}{K_D} \text{ the equilibrium association constant } [M^{-1}] \quad (2)$$

$$K_D = \frac{k_{off}}{k_{on}} = \frac{[A].[B]}{[AB]} = \frac{1}{K_A} \text{ the equilibrium dissociation constant } [M] \quad (3)$$

Where [A] is the concentration of injected analyte, [B] is the concentration of the capture probe, and [AB] is the concentration of the complex; K_A is the equilibrium binding constant, expressing the affinity; Kon - association rate constant, is the rate at which the complex forms; K_D is the equilibrium dissociation constant; Koff - dissociation rate constant, is the rate at which the complex falls apart.

A direct equilibrium analysis examines the binding of two entities yielding an interaction affinity. The analyte [A] is injected over a surface containing the receptor [B] and monitors [AB] complex formation in real time to produce a binding response, R. The fraction of analyte θ bound to the probe, is described

with the following equation which is the basic transfer function for many biosensors:

$$\theta = \frac{R}{Rmax} = \frac{[AB]}{[B] + [AB]} = \frac{[A]}{[A] + K_D} \qquad (4)$$

R is the response of the sensor induced by the formation of the complex AB. Rmax is the response observed when all receptor sites are occupied. By generating a plot of R (at equilibrium) versus [A] and fitting to an isotherm, Rmax and K_D can be found. The affinity of the probe significantly affects sensor performance. Higher affinity towards the analyte results in lower detection limit and faster detection times with less background interference.

4.2 Detection instrumentation

4.2.1 Nicoya OpenSPR – hardware and software

OpenSPR™ is the world's only benchtop surface plasmon resonance (SPR) instrument. It provides high quality, label-free interaction analysis for a fraction of the cost of existing solutions. With the specifically designed cost-effective optoelectronic sensor in this research, utilizing localized SPR it can deliver repeatable, highly sensitive kinetic data [207].

The OpenSPR instrument consists of an optical detection system, fluidics system, two temperature sensors (Section A5, Figure S9 in the Appendix).

The optical detection system comprises the cool light LED board, illuminating the sensor and a spectrometer on the other side of the optical path. The scanned spectrum bandwidth is between 350 nm – 800 nm where the absorbance peak from the LSPR nanogold film should be operating.

Optical references are important to be able to measure the absorbance of the nanogold sensor chip to receive an accurate response signal. For the purposes of this research the optical reference is taken from a blank polystyrene chip.

After the completion of the priming and reference processes, the subsequent step involves navigating through the sensor setup screen, as illustrated in Figure S10 from the Appendix-B. Upon ensuring the proper installation of the sensor and sensor holder is in docked position, and the flow cell has been filled an absorbance peak should become visible on the main screen graph. As discussed earlier in Chapter 3, the peak position is expected to be approximately near 590 nm.

4.2.2 Loading the sensor chip

The plasmonic device intended for integration into the Nicoya OpenSPR system was recognized successfully as its design was tailored to ensure full compatibility with both the hardware and software components.

The injection-moulded polystyrene samples, resembling the shape of a mini-SIM (2FF) card with dimensions of 25 x 18.5 mm, were precision laser-cut using the Full Spectrum laser cutting instrument (USA). Subsequently, the batch of devices underwent thorough cleaning procedures before being subjected to the thermal evaporation process. A 60 nm thin layer of gold film was precisely deposited onto the nanopillar arrays to render them plasmonically active, employing the Plassys MEB 550S electron beam evaporator.

Upon evaluation the thickness of the polystyrene substrate was determined to be 1 mm, which is twice the thickness of the glass sensor. To facilitate seamless docking of the sensor to the flow cell, a new sensor holder was fabricated. The newly developed sensor holder was 3D printed from UV black printer resin via the Formlabs Form3 3D Printer (Figure 4.4). The modifications primarily involved designing a wider slot to accommodate the sensor chip while maintaining all other dimensions as closely as possible to the original component. However, the original sensor holder is fabricated from metal while the newly developed one is plastic which results in distinct physical properties, such as elasticity. It was observed that during the undocking process, when the sensor separates from the flow cell, elastic deformation occurs in the sensor holder. As the stage moves backward, the sensor remains tightly sealed to the flow cell, pulling the sensor holder along with it. As the motion of the stage proceeds to move in the opposite direction this cause the plastic component to bend and retract rapidly. To mitigate this issue,

an additional piece was incorporated at the back of the sensor holder to firmly anchor it to the stage. Careful consideration was given to the design of this anchor to ensure it does not obstruct the passage of transmitted light through the sensor holder window (Figure 4.4). The design, optimisation and printing of the sensor holder component was successfully executed with the expertise of our PhD colleague in the group, Pedro Duarte Carvalhal Calhau De Menezes. Subsequent experiments conducted with the adapted sensor and sensor holder revealed no faults or issues with liquid flow.

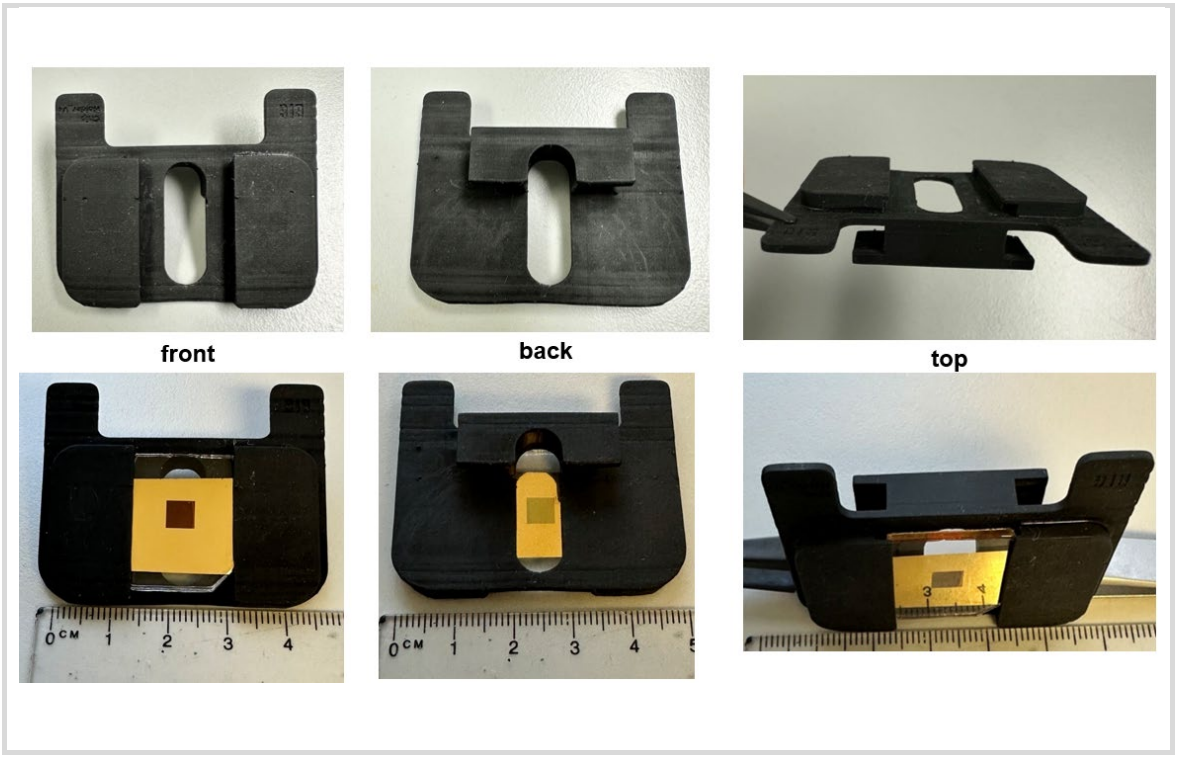

Figure 4.4 A – 3D printed sensor holder. Slot designed above 1 mm without affecting the total thickness of the component. Top row – 3D print of the sensor holder Bottom row - sensor holder accommodating the polystyrene chip.

The comparison between the optical references of glass and polystyrene in the OpenSPR software is depicted in Figure 4.5-A. Both substrates exhibit similar levels of transparency and similar refractive indices: n_{glass} = 1.5168 and $n_{polystyrene}$ = 1.5916 [208]. Consequently, the profiles of the optical reference signals show minimal deviation. The comparison between the sensor absorbance peak is depicted in Figure 4.5-B. The default sensor resonates at around 550 nm with an amplitude of 0.36. The newly fabricated sensor device resonates at 577 nm, aligning with the absorbance window of the default sensor.

A

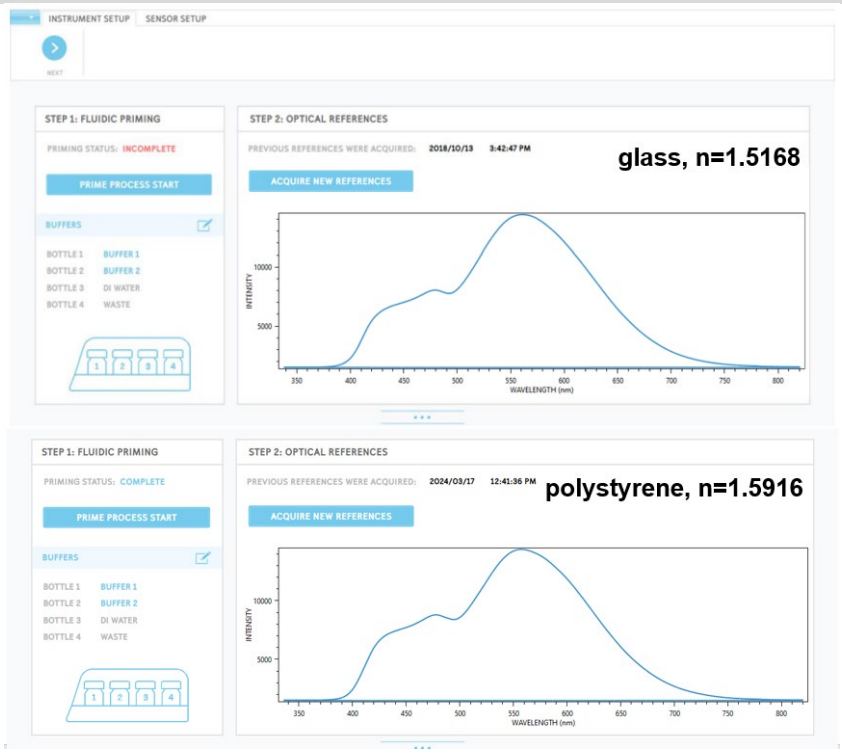

B

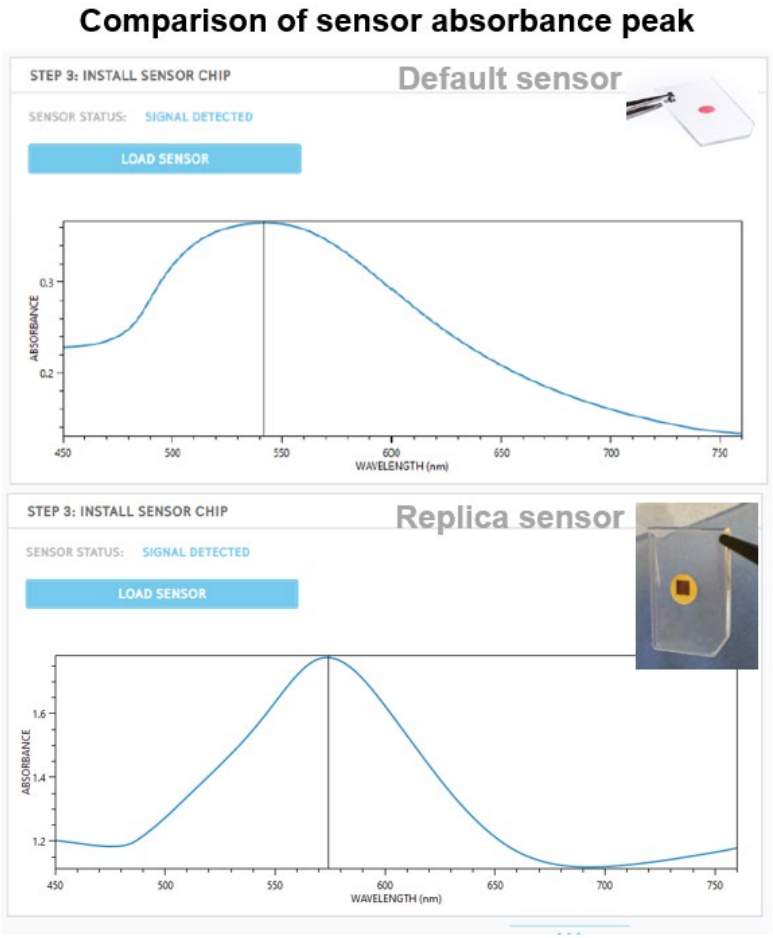

Figure 4.5 A - Comparison of the optical references. The profiles of both signals exhibit remarkable similarity due to the similar refractive indices of the substrates. B - Comparison of the sensor output is depicted, where the default sensor's peak position resides close to 550 nm, while the newly designed sensor is adjusted to 577 nm for enhanced sensitivity.

The peak amplitude exhibits five times higher values compared to the default sensor, which indicates higher optical density [O.D]. Despite of demonstrating a stronger signal, the absorbance measurement signifies that a less percent of the transmitted light would reach the detector. However, the sophisticated OpenSPR instrument indicates the sensor signal is reliably detected and during a test accurately performs peak tracking. The noise associated with the entire sensor system is typically quantified by allowing the sensor to reach a steady state and measuring the standard deviation, **σ,** of the signal over a period of time. In order to evaluate the noise, the signal was recorder over 1 hour and 45 minutes where the **σ = 0.01 nm**.

4.3 Experimental design

4.3.1 RI evaluation, repeatability, LOD evaluation, and dynamic range

The optical properties of the sensor were investigated with the UV-Vis spectroscopy system in transmission mode. The LSPR peak is resonating at 557 nm in air, red shifting to 577 nm (+/-2nm) in water (Figure 4.6-A). This confirms responsiveness of the sensor to bulk refractive index changes. However, a comprehensive investigation of the refractive index sensitivity (RIS) was performed, tested with real-time measurements via the Nicoya OPEN SPR system. This was determined by using various water-glycerol solutions (0%, 5%, 10%, 15%, 20%, 25%, 30%, and 35%) injected inside the flow cell with constant flow rate of 200 µl/min and measuring the response signal for each solution.

The real-time plot is depicted in Figure 4.6-B where all seven concentrations are gradually increasing the response proportional to their refractive index. The 0% solution is the negative control in the experiment and as shown it does not elicit any response. The refractive index sensitivity is plotted in Figure 4.6-C where the y-axis illustrates the signal response as the peak shifts from the 577 nm baseline. Through linear regression fit, the sensitivity factor (Sf) was determined to be 112.16 nm/RIU. The results reported by other researchers when evaluating RIS of a LSPR based sensor within the visible bandwidth of the spectrum observe a typical value of around 200 nm/RIU. Also as reported in the previous chapter the result is

consistent with expectations for nanopillars predominantly exhibiting localized resonance nanopillars to perform with an Sf around that range.

The full width half maximum (FWHM) evaluated from the OPEN SPR instrument peak detection is 54.5 which gives an overall LSPR figure of merit (FOM = Sf/FWHM) of 2.05. This performance aligns favourably with reports in the literature which suggest that a desirable device performance is achieved. The last section of Figure 4.6 is panel D which is a table summarising the standard deviation between two independent experiments.

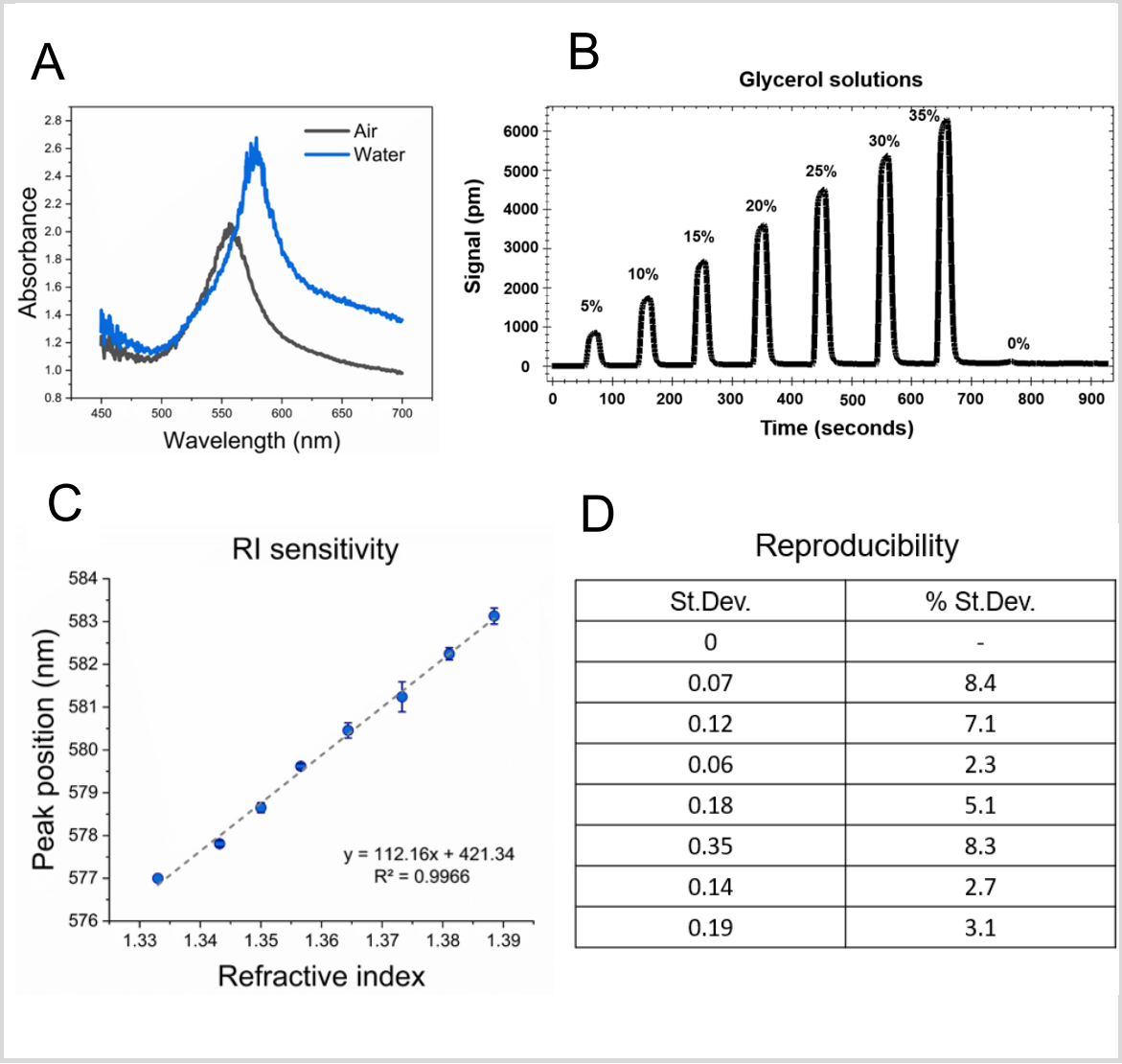

St.Dev.	% St.Dev.
0	-
0.07	8.4
0.12	7.1
0.06	2.3
0.18	5.1
0.35	8.3
0.14	2.7
0.19	3.1

Figure 4.6 A - Spectra from the LSPR biosensor captured using a UV-Vis spectrometer in transmission mode, both in air and water. The LSPR peak is observed at 557 nm in air and shifts to 577 nm in water. B - Real time LSPR peak shift induced by solutions of different RI made of glycerol and water. C- Sensitivity of the LSPR peak position to changes in the bulk refractive index. The Sf was found to be 112.16 nm/RIU by using linear regression. D - illustrates the reproducibility of the real-time LSPR peak shift measurements conducted using the Nicoya Open SPR system, demonstrating consistent results across independent measurements.

The values, all below the 10% threshold, underscore the good reproducibility of the results obtained, thus reinforcing the reliability of the sensor's performance.

The limit of detection (LOD), and dynamic range of the LSPR sensor are tested using the biotin–streptavidin system. The LSPR peak position was monitored in real time during the binding of SA to the surface of the nanopillars. The preliminary formation of the Biotin-$(PEG)_{10}$-Thiol SAM capture layer allowed the subsequent detection of the SA protein.

The LSPR sensor was tested for seven different SA concentrations, ranging from 10ng/ml to 500,000 ng/ml depicted in Figure 4.7-A and in a table-format shown in Table 1.

The LSPR peak shifts from each concentration run are summarized below. For the smallest concentration (10ng/ml), the peak shifts an average of 0.016 nm, and for the highest concentration (500,000ng/ml), the peak shifts an average of 3.014 nm. These results demonstrate successful operation of the real-time LSPR immunosensor and validate its ability to detect and quantify SA.

After flushing the system, the binding of SA to the sensor surface results in a peak shift proportional to the concentration of the SA protein (Figure 4.7-A). Binding curves demonstrate stable steady state with no drop in peak position, which is expected due to the very strong bond between biotin and SA.

Using this data, a dose-response curve can be generated and fit with the Langmuir isotherm to determine the maximum peak shift, Rmax, and the association/dissociation constant, KD. Using Trace Drawer and the least squares curve fitting function, this curve is generated and shown in Figure 4.7-B, along with the experimental peak shifts. When plotted logarithmically, the signal-vs-concentration curve should be S-shaped, with signs of target saturation at the higher ligand concentrations. A wide concentration span, consisting of at least five concentrations and covering at least two orders of magnitude, is often needed to ensure this.

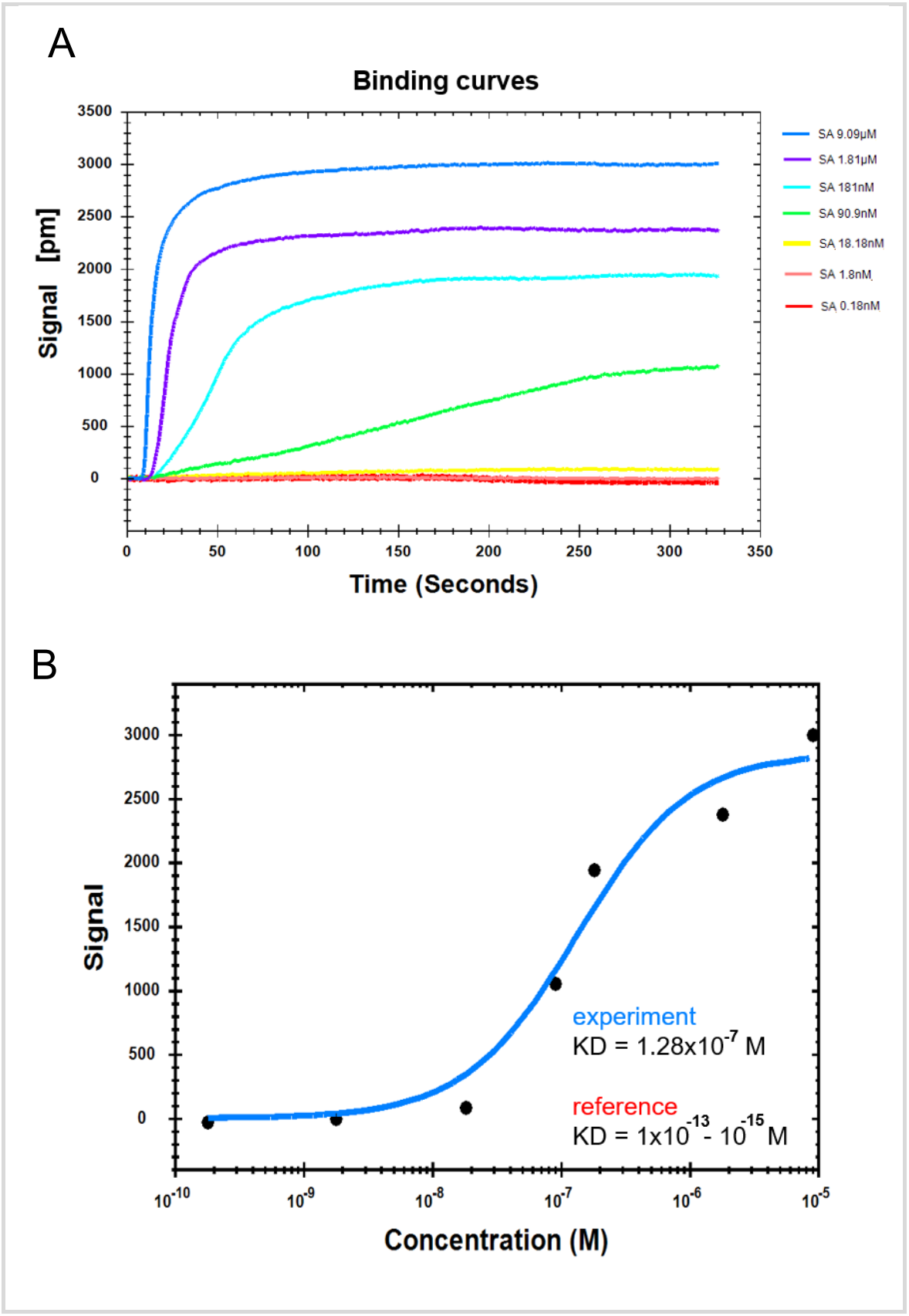

Figure 4.7 A – Real-time binding curves of various Streptavidin [SA] concentrations attaching to the biotinylated gold nanopillar surface. B – LSPR sensor response curve generated from the affinity evaluation with TraceDrawer software. After generating the response curve, the dissociation constant KD was evaluated as $1.28x10^{-7}$ M. Compared to the reference value reported in literature the applied affinity evaluation model does not reflect the true binding strength between biotin and SA (reference value KD=$1x10^{-13}$ -10^{-15} M) [209].

Table 1 Presenting various Streptavidin [SA] concentrations presented as mass concentration in ng/ml and molar concentration in nM; Experimental results from the detection with LSPR biosensor and the fitted LSPR peak shifts evaluated with equation (6)

[SA] ng/ml	[SA] nM	LSPR peak shift nm	Fitted LSPR peak shift nm
10	0.18	0.016	0.004
100	1.8	0.022	0.042
1000	18.18	0.092	0.375
5000	90.9	1.065	1.252
10 000	181.8	1.953	1.769
100 000	1800	2.398	2.814
500 000	9090	3.014	2.972

From the fitting analysis, KD was estimated as 128 nM, and Rmax was found to be 2.97 nm. This gives the following transfer function for the SA sensor:

$$R = \frac{Rmax * [SA]}{KD + [SA]} = \frac{2.97nm * [SA]}{128nM + [SA]} \qquad (6)$$

The limit of detection (LOD) is the minimum detectable difference in mass density or analyte concentration that can be measured reliably [22]. The LOD depends on the noise associated with the entire sensor system and the sensitivity. The noise is typically quantified by allowing the sensor to reach a steady state and measuring the standard deviation, σ, of the signal over a period of time. Typically, the minimal detectable signal is defined as three times the standard deviation σ, which means LOD = 3σ/sensitivity. The peak to peak wavelength shift noise of the baseline in repetitive experiments was found to be +/- 0.01nm over 1 hour 40 min.

The sensitivity of the biosensor is defined as the response in nm when probed with 1 µg/ml concentration of the analyte. From Table 1 it is seen that the sensitivity is 0.375 nm. Based on the formula the LOD for the system was determined to be 3.5 nM or approximately 192 ng/ml. This results in a wide dynamic detection range, from 192 ng/ml to 500,000 ng/ml, which is almost four orders of magnitude. A lower LOD is usually preferred in order to detect analytes at the low concentrations typically found in the blood.

$$LOD = \frac{3 * 0.01}{0.375} = 0.08\ nm$$

$$R = 0.08 = \frac{2.97 * [SA]}{128 + [SA]} = 3.5\ nM$$

$$(nM) * (MW\ kDa) = 3.5\ nM * 55\ kDa = 192\ ng/ml$$

The applied affinity evaluation is also known as steady-state evaluation that characterizes an interaction based on signal height at equilibrium, extracted at the horizontal equilibrium part of the curve. As not all concentration curves reach steady state over the injection period the KD-value of $1.28x10^{-7}$ M is thus an underestimation of the binding strength.

Kinetic evaluation, i.e. fitting a kinetic model to a real-time binding curve, is one of the best ways of extracting information from the binding curve. Interaction kinetics are determined from the change in response as a function of time, as represented in the sensograms (Figure 4.8-A). Sensograms are recorded for a series of analyte concentrations and evaluated together as one data set, and a mathematical model of 1:1 binding interaction model is fitted to the experimental data. The result is a set of parameters that describes the interaction, such as the affinity (KD), the association rate constant (K_{on}) and the dissociation rate constant (K_{off}). These are summarised in Figure 4.8-B.

The affinity constant KD = $1.12x10^{-14}$ M extracted with the kinetic evaluation model is in a good alignment with the true value of what is reported in the literature about the strongest known non-covalent interaction between a protein and ligand, biotin-streptavidin (KD = 10^{-13}-10^{-15} M) [209-211].

A

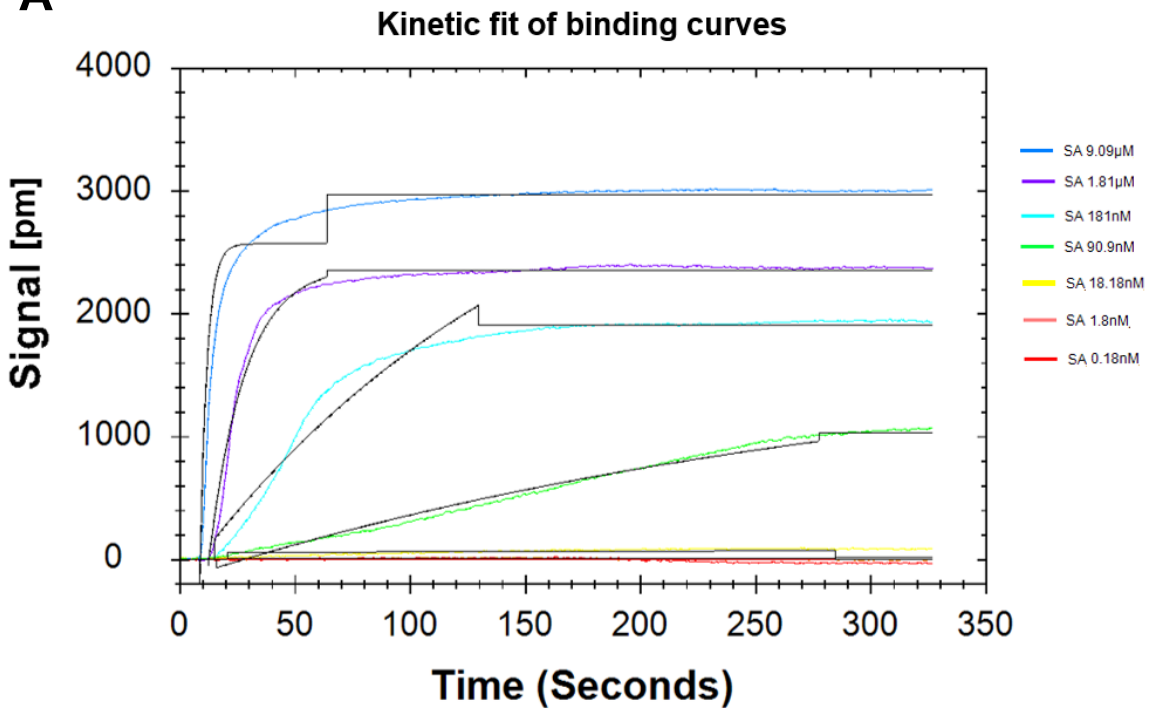

B

	Experiment	Reference	Reference M88 oxidized SA
KD [M]	1.12×10^{-14}	4×10^{-14} [212-214]	2.6×10^{-15} [214]
Kon [$M^{-1}s^{-1}$]	3.53×10^{4}	5.4×10^{7} wild type [214]	4.6×10^{5} [214]
Koff [s^{-1}]	3.96×10^{-10}	2.7×10^{-7} wild type [214]	1.2×10^{-9} [214]

Figure 4.8 A - Kinetic analysis of the binding between SA and biotin on the OpenSPR instrument. Analysis performed in TraceDrawer using a 1:1 binding interaction model. Concentrations (from bottom to top): 0.18 nM, 1.8 nM, 18.18 nM, 90.9 nM, 181 nM, 1.81 µM, and 9.09 µM. B – The experimental affinity (KD), the association rate constant (Kon) and the dissociation rate constant (Koff) summarised in a table and compared with reference values published in literature for the wild type and M88 oxidized form of SA.

In more recent studies the affinity constant is even specified as KD = 4×10^{-14} M [212-214]. The differences between the experimental and reference association/dissociation rates might suggest that the SA molecule oxidized. J. M.

Marangoni et al. [214] have published data where the M88 oxidized form of SA has values resembling the experimental values obtained in this assay (see Figure 4.8-B)

The M88 disulfide bond during oxidation forms rapidly and stabilizes the closed conformation, which explains why it is decreasing the rate of biotin dissociation and have a slower rate of association compared to the wild type of SA. The torsion angles of the disulfide bond formed in M88 are closer to the angles seen in natural disulfide bonds and thus it is expected to form more favourably [214].

4.3.2 Optimisation of the surface functionalisation process

Proteins adsorb nonspecifically to gold surfaces through electrostatic and hydrophobic interactions [215] [216]. However, these interactions are weak, causing proteins to easily desorb after a washing step or exposure to the running buffer. Figure 4.9 illustrates this effect using streptavidin (SA) deposited on a bare gold film. The pink trace represents nonspecifically bound SA, which exhibits low saturation signal values (1400 pm shift) followed by a rapid decrease (23 pm/min), indicating weak and inconsistent immobilization. In contrast, the blue trace, where SA is immobilized via a biotinylated organothiol polymer, shows significantly higher and more stable signal values (1920 pm shift) over time (4 pm/min).

This experiment demonstrates that simply depositing the analyte on the sensor surface leads to weak and inconsistent interactions, making it unsuitable for reliable biosensing assays. To ensure specific and stable interactions, the sensor surface must be functionalized with a biointerface designed to capture the target molecules effectively.

The biointerface of the sensor accounts for the accurate target detection and provides high selectivity. An important step in the immobilization process is to achieve well-organized monolayers of all constituent elements. High concentrations of the immobilized components create surface defects and the formation of aggregates compromising the integrity of the monolayer compactness. Additionally, high concentration of high molecular weight proteins reduces the performance of the sensor due to steric hindrance effect.

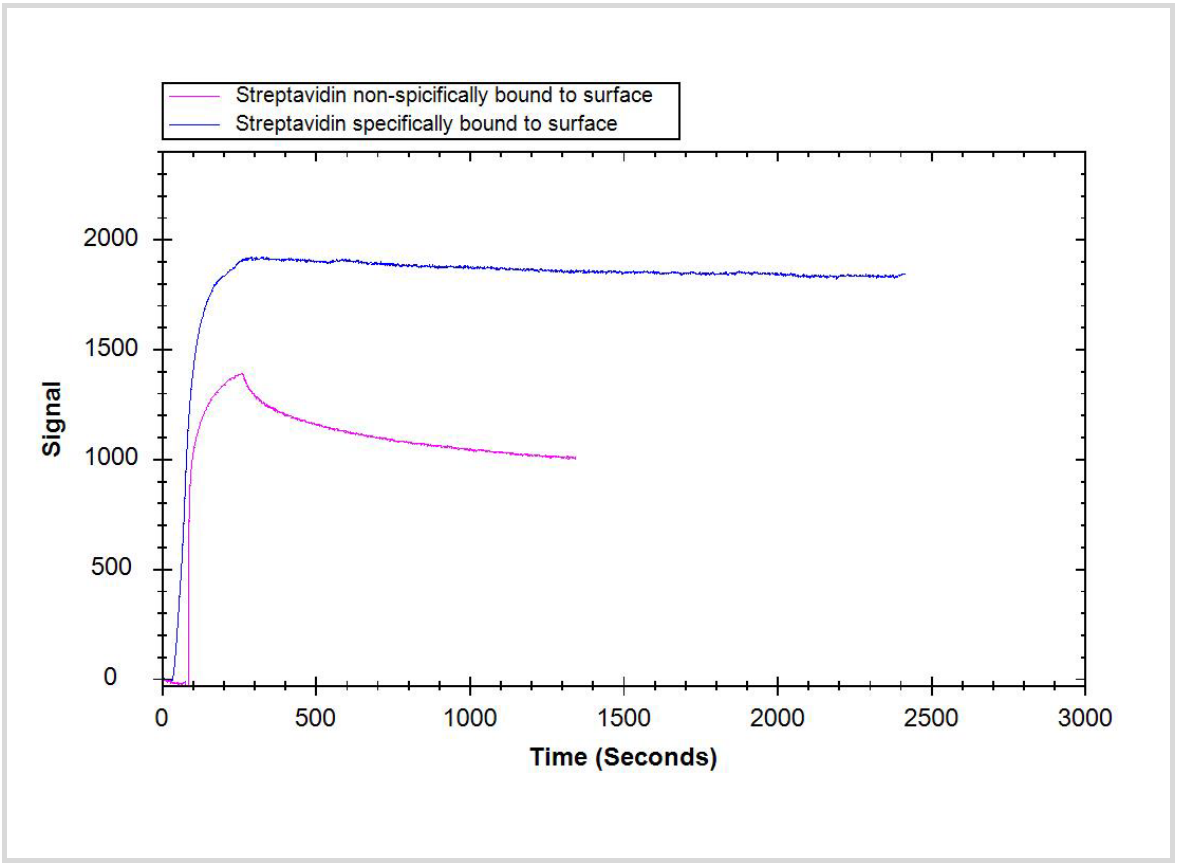

Figure 4.9 Sensorgram traces of 0.5 µM Streptavidin demonstrating different binding profiles. The pink trace is non-specifically bound Streptavidin directly on the gold surface, showing lower signal values and desorption with time. The blue trace with higher signal is the specifically bound Streptavidin via biotinylated organothiol. After saturating the surface, the amount of immobilized protein remains constant.

On the other hand, low concentrations of the components do not provide suitable surface coverage of the sensor rendering its performance prone to high non-specific binding events. This would also leave the surface insufficiently saturated with biorecognition elements which would result in a very weak response during the target detection. As explained in section 1.1.2 the structure of the sensor biointerface consist of organothiol polymer with a biotin functional group, streptavidin, and biotinylated monoclonal antibody. The surface immobilization of the last two proteins is monitored in real-time as the process take place within the Open SPR instrument. This confirms not only the binding events are taking place but also the level of saturation and steady-state. As the immobilization of the organothiol polymer happens in a petri dish outside the instrument without the process being monitored, this creates uncertainty over its binding rate. In order to evaluate the successful SAM formation over the 12 hour incubation time

and get an idea of the effectiveness, three PEG polymer concentrations were tested on the surface - 5 µM, 20 µM, and 60 µM.

After finishing the immobilization step, each sensor was loaded in the Open SPR instrument, and the subsequent binding steps were evaluated in real-time. The sensograms are illustrated and summarized in Figure 4.10.

The concentrations used for the rest of the components comprising the biointerface are as recommended in the Open SPR Biotin-streptavidin Tech Guide protocols [217].

The first graph in Figure 4.10 demonstrates the response of the sensors functionalized with 5 µM, 20 µM, and 60 µM biotinylated PEG (b-PEG) to blocking buffer (running buffer (RB) with 0.1% BSA). All three binding traces fluctuate within the level of the background noise which demonstrate that the sensor surface is adequately passivated and the small sized BSA protein cannot non-specifically bind.

After confirming the successful coverage of the SAM, 0.5 µM SA protein was injected into the instrument with a flow rate of 20 µl/min. The binding traces are shown in Figure 4.10-B, where the response of the sensor incubated in 60 µM b-PEG significantly differs from the response of sensors with lower concentration b-PEG. This is expected due to the higher density of biotin functional groups generating higher capacity of binding SA protein. The binding trace commences with extremely high association rate and within 25 to 30 seconds has reached full saturation and steady-state. The typical straight lines in the trace also suggest mass transport limitation (MTL). The initial part of the curve should not be a straight line, instead the association should follow a single exponential and have at least some curvature before the analyte injection ends [218]. Mass transport limitations occur when the binding rate of an analyte to the ligand is faster than its diffusion rate to the surface [219]. Lowering surface density of the ligand helps reduce mass transport limited effects as less analyte needs to diffuse for the interaction to occur. Another benefit of avoiding MTL is the improvement in the Rmax (max signal at saturation) which is higher for sensors incubated in 5 µM and 20 µM b-PEG. The subsequent element in the biointerface is the immobilization of the BRE or namely the biotinylated monoclonal antibody (MAb).

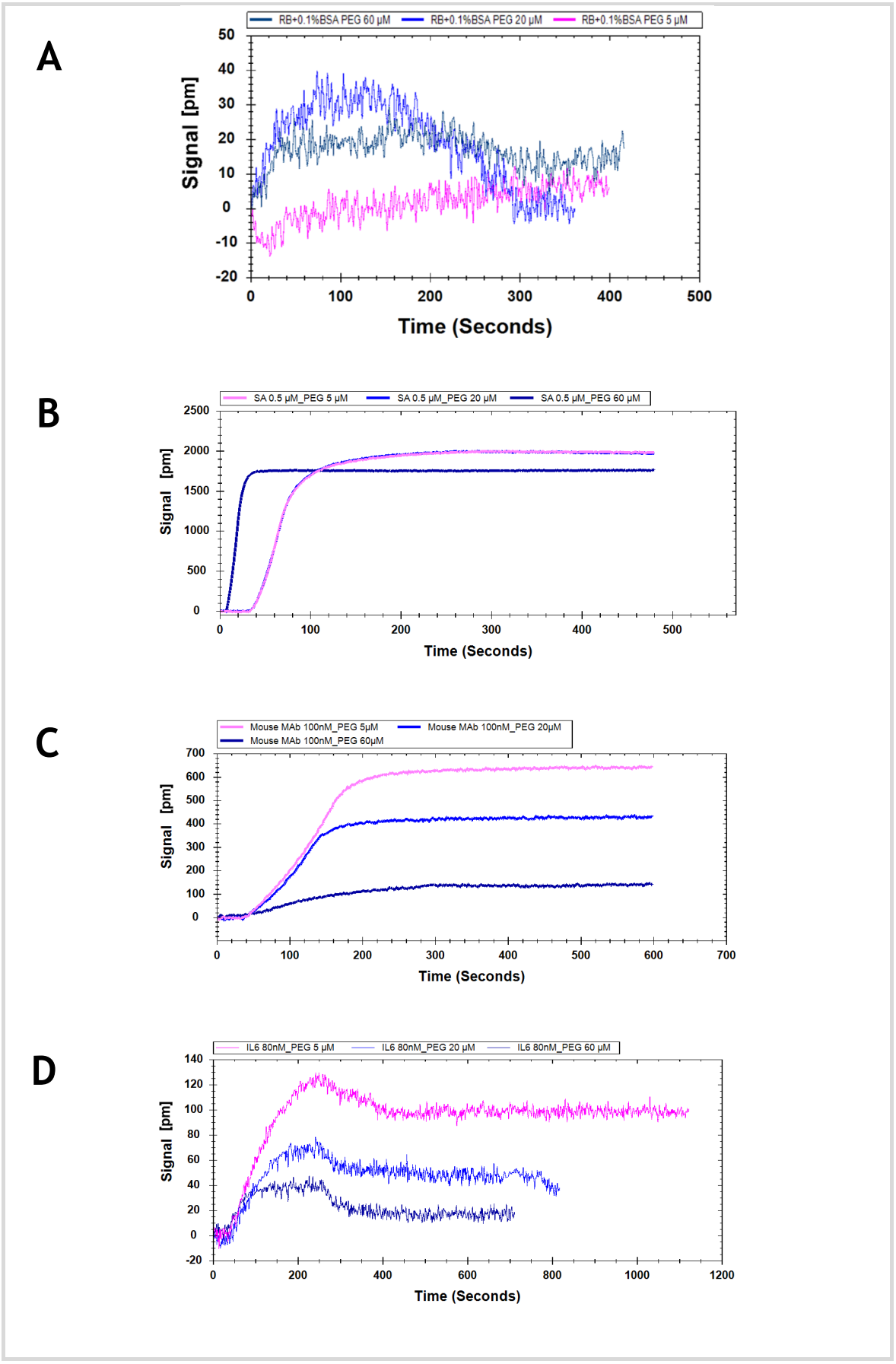

Figure 4.10 Sensograms evaluating the optimal concentration of the biotinylated organothiol forming high quality self-assembled monolayer (SAM). 5 µM, 20 µM, and 60 µM PEG polymer was incubated for 12h on the sensor surface. Panel A – demonstrating the lack of NSB events; Panel B – evaluating binding of 0.5 µM SA; Panel C - evaluating binding of 100 nM MAb; Panel D – evaluating binding of 80 nM IL6.

The built-in ligand immobilization wizard calculates based on the relative molecular weights of the ligand and analyte the theoretical minimum of ligand immobilization target to obtain sufficient analyte signal for analysis. The estimated target minimum for the chosen reaction is 357 RU.

Figure 4.10-C depicts the MAb binding traces of the investigated sensors. At this stage the significance of the b-PEG concentration can be clearly observed. The sensor with 60 µM b-PEG provides 145 RU which is way below the minimum target mark. The sensors with 20 µM provide 436 RU which is slightly above the minimum target mark whereas the sensor with 5 µM b-PEG reaches 648 RU satisfying the conditions for analyte detection. The results suggest that the decreasing concentration of b-PEG improves the immobilization conditions for the following components within the biointerface. Another observation worth mentioning is that even though the 5 µM and 20 µM b-PEG sensors elicit identical response during the SA immobilization step this further resulted in significantly different Rmax when evaluating the MAb binding trace. Plausible explanation could be the variations in SA distribution over the sensor surface. The 20 µM b-PEG sensor having four times higher saturation of biotin functional groups than the 5 µM b-PEG sensor, potentially binds the SA protein in a clustered fashion without leaving any interspacing between them. This arrangement is a prerequisite for steric hindrance rendering the massive 150 kDa antibodies to cluster ineffectively causing less protein to bind on the surface [220] (Figure 4.11).

The final Figure 4.10-D demonstrates the bioanalyte detection where 80nM IL-6 is specifically recognised by Anti-IL-6 MAb. The result observed on the graph follows a similar trend to the preceding immobilization step. The highest response units (110 RU) are achieved with the 5 µM b-PEG sensor. The result meets our expectations as the 5 µM b-PEG sensor demonstrated the highest immobilization level of SA and MAb.

The IL-6 response produced by the 20 µM and 60 µM b-PEG sensor is respectively 64 RU and 25 RU. The poor performance as a result of the insufficient BRE on the surface provided weak response. Figure 4.11 illustrating the steric hindrance effect while functionalizing the sensor surface contributes to less binding sites for the investigated analyte and thus significantly lower response.

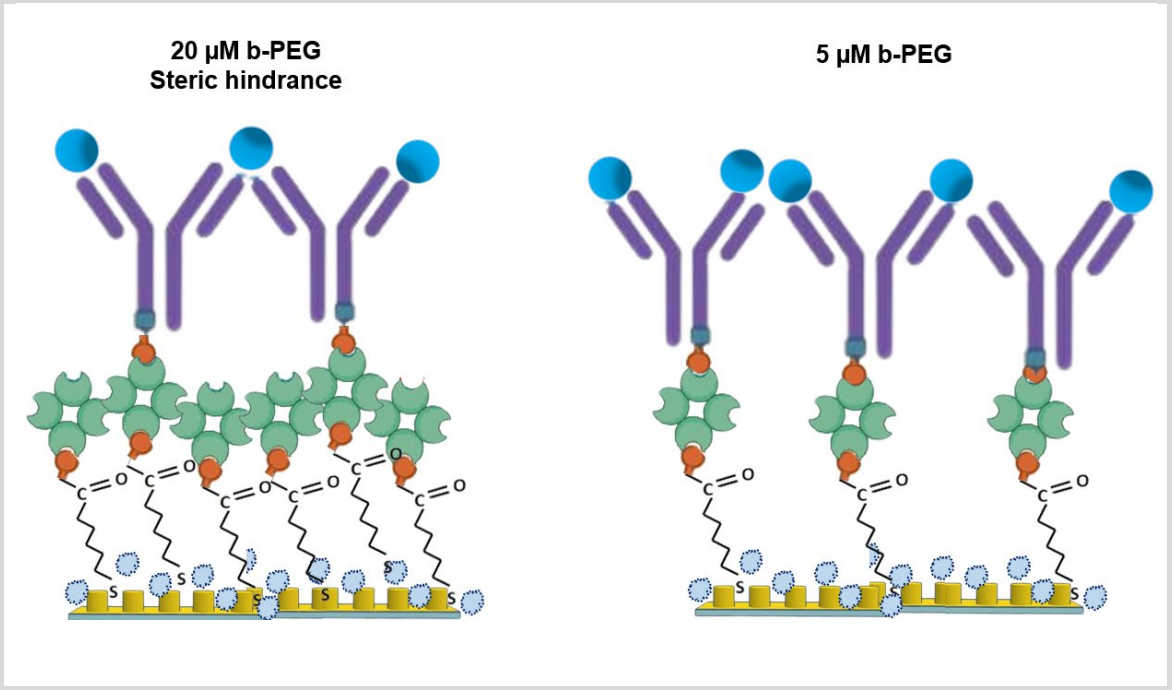

Figure 4.11 Illustration depicting the limitations of steric hindrance not allowing even distribution of BRE over the surface. The overall result of this effect lowers the sensitivity of the sensor and hampering the full performance potential.

4.3.3 Analyte detection - methodology, results, and discussion

Validation that the LSPR sensor could detect small proteins crucial in controlling immune system cell signalling called cytokines is detailed below. The data acquisition is then analysed, and affinity profile of the investigated analyte is extracted. Experiments to determine whether or not the antibody capture layer could be regenerated using a regeneration buffer were also conducted. Lastly, the selectivity and specificity of the LSPR sensor is also demonstrated.

The bifunctional alkanethiol utilized in the biomolecular detection is Biotin-(PEG)10-Thiol (Polypure 41156-1095). The biotin PEG thiol holding 10 PEG units is with MW 788 and is not more than 3-4 nm in length [221]. It is water soluble and the solution for functionalisation was prepared in concentration 5 µM in PBS buffer.

The sensor sample was thoroughly cleaned three times with IPA solution during 3x2 min sonication and rinsed with DI water. The pristine surface is of utmost

importance for SAM formation as any small impurities would disrupt the integrity of the monolayer. The sample was immersed in the SAM solution for 24 hours in room temperature (RT) during continuous mixing on an orbital shaker. Low-concentration thiol SAMs require long incubation periods to allow enough time for the polymer units to densely pack on the surface spontaneously forming ordered molecular assemblies. The process was followed by rinsing with PBS to remove the excess molecules and wash away the chemically unabsorbed polymers.

Following this, the sensor was loaded into the Open SPR instrument, and all subsequent binding events were monitored in real-time. The immobilization of 0.5 µM Streptavidin (Merck KGaA, SA101) was performed at a flow rate 20 µl/min, preceded by the injection of 10 mM HCl (pH 2-3, flow rate 150 µl/min) to precondition the sensor surface. Immediately after that the ligand immobilization followed with 0.1 µM biotinylated Anti-IL6 Mouse Monoclonal Antibody (MAb) (SinoBiological, 10395-MM72-B) again at a 20 µl/min flow rate allowing 5 min interaction time.

In this particular reaction the tailored specificity of the MAb is designed to recognise and bind the investigated target – human interleukin-6 (IL-6). IL-6 is a multifunctional α-helical cytokine, relatively small in size – 19.7 kDa, with important role as a biomarker and its detection in small amounts and with high selectivity is of particular importance in medical and biological fields. It is produced in response to infections and tissue injuries. Thus, IL-6 is a reliable predictor of sepsis diagnosis [222]. Sepsis as a life-threatening organ dysfunction caused by a dysregulated host response to infection. The mortality rate in patients with sepsis is still high and early identification and diagnosis are crucial, as timely intervention and treatment can improve prognosis [223].

The interaction between IL-6 and IL-6 receptor (IL6-R) forms a low affinity complex with a KD = $5.5x10^{-9}$ M [224]. The complex subsequently recruits a third molecule stabilizing the IL-6 and IL-6-R to form a high affinity complex with a KD = $5x10^{-11}$ M [225]. To investigate the interaction in our experiment the recombinant human IL-6 glycoprotein (SinoBiological, 10395-HNAE) was added in a gradient of concentrations ranging between 2 nM and 900 nM.

Sensograms are recorded for a series of analyte concentrations and evaluated together as one data set, and a mathematical model of 1:1 binding interaction model is fitted to the experimental data (Figure 4.12-A).

A

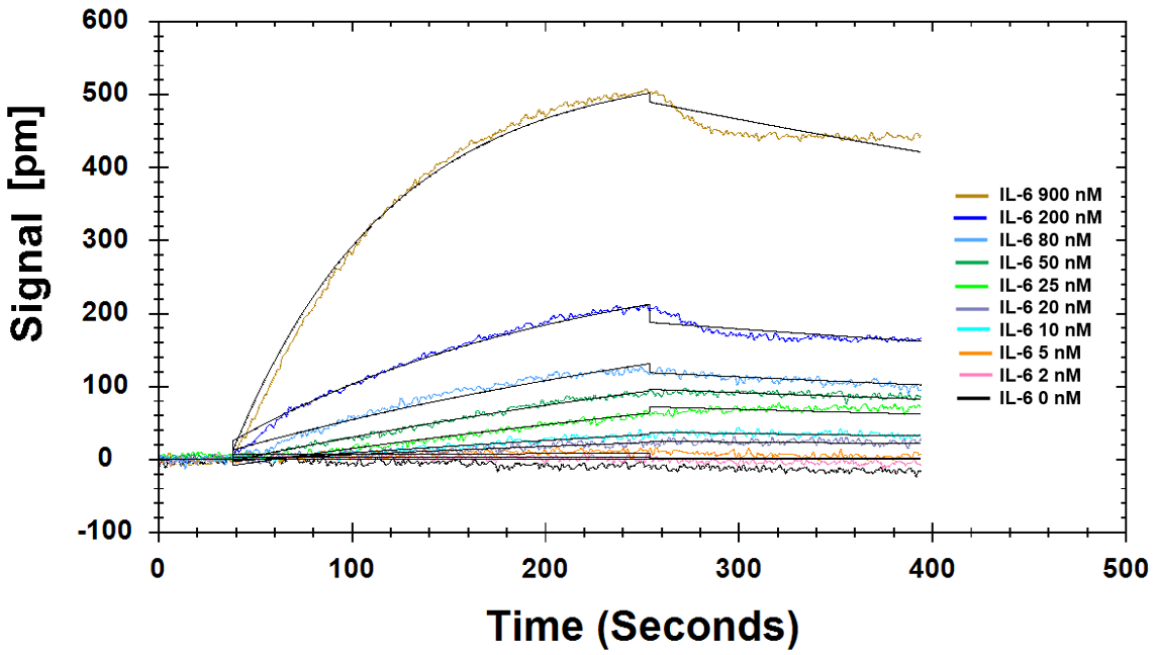

B

	Experiment MAb	Reference IL6-R	Reference Aptamer
KD [M]	1.67×10^{-9}	5.5×10^{-9} [224]	2.3×10^{-10} [226]
Kon [$M^{-1}s^{-1}$]	1.36×10^{4}	18.8×10^{4} [227]	1.2×10^{5} [226]
Koff [s^{-1}]	2.25×10^{-5}	64×10^{-4} [227]	2.8×10^{-5} [226]

Figure 4.12 A - Kinetic analysis of the binding between MAb and IL6 on the OpenSPR instrument. Analysis performed in TraceDrawer using a 1:1 binding interaction model. Concentrations (from bottom to top): 2 nM, 5 nM, 10 nM, 20 nM, 25 nM, 50 nM, 80 nM, 200 nM, and 900 nM. B – table summarising the kinetic evaluation results. The experimental affinity (KD), the association rate constant (Kon) and the dissociation rate constant (Koff) summarised in a table and compared with reference values published in literature for IL6-R and slow off-rate modified aptamers (SOMAmers).

This peak shift is much smaller than the typical peak shift seen with SA and the antibody capture layer binding at a similar concentration. It is most likely due to the very large size of these proteins compared to IL-6. The LSPR sensor demonstrates adequate response at each level of the biointerface. This highlights the importance of optimal nanostructure design providing efficient decay length of the nanopillars.

The affinity (KD), the association rate constant (K_{on}) and the dissociation rate constant (K_{off}) are summarised in Figure 4.12-B. The affinity constant KD = 1.67×10^{-9} M extracted with the kinetic evaluation model closely aligns with the values reported in the literature for IL6-R and other binding proteins, such as chemically modified slow-off rate aptamers (SOMAmers). Additionally, when looking into the dynamic of the binding process, the results obtained for the association rate constant also closely match the reported values. However, the dissociation rate constant for IL6-R is observed to be an order of magnitude higher than that of MAb and SOMAmers.

This outcome is anticipated, as MAbs and aptamers are specifically engineered to slowly release their targets, making them effective IL6 inhibitors with potential therapeutic applications for treating inflammatory diseases.

Discontinuities in Biosensor Kinetic Curve Fitting:

In surface-based biosensing experiments, such as those using surface plasmon resonance (SPR), kinetic binding data are typically analysed by fitting the sensorgram (response vs. time) to a mathematical model, most often representing a 1:1 Langmuir binding interaction (Equation 1 and Equation 2).

$$One\ to\ one\ reaction:$$

$$A + B \Leftrightarrow AB$$

$$\frac{dR}{dt} = Ka * CA * (Rmax - R) - Kd * R \qquad (1)$$

$$One\ to\ one\ reaction\ including\ mass\ transfer:$$

$$\frac{dCs}{dt} = Kt * (CA - CS) - Ka * CS * (Rmax - R) + Kd * R$$

$$\frac{dR}{dt} = Ka * CS * (Rmax - R) - Kd * R \qquad (2)$$

A and B – molecular species involved
AB – molecular complexes formed during the binding processes
R - is the sensor response (in resonance units, RU) at time (t)
CA - concentrations of the analyte A
Cs - used in the mass transfer equations, is the concentration of analyte at the sensor surface.
Rmax - total concentration of the immobilised biorecognition element or the maximum binding capacity of the sensor surface.

Explanation of Terms
The first term $Ka \cdot CA \cdot (Rmax - R(t))$ describes the **association phase**, where analyte binds to available sites on the surface.

The second term $-Kd \cdot R(t)$ represents the **dissociation phase**, where the analyte-ligand complex breaks down over time.

Equation (2) is solved numerically by TraceDrawer during curve fitting. The software uses nonlinear least-squares regression to estimate the kinetic constants Ka and Kd, and calculate the equilibrium dissociation constant:

$$KD = \frac{Kd}{Ka}$$

This fitting is performed on the **association and dissociation phases** of the experimental SPR sensorgram.

Ideally, the fitted curve should closely match the experimental data across both the association and dissociation phases, maintaining smooth continuity. However, in some cases, a jump or discontinuity appears in the fitted curve, most commonly at the transition point between these two phases.

Causes of Jumps in Fitted Curves

Such discontinuities are generally artifacts of the fitting process, rather than real physical phenomena. Several factors may contribute:

Incorrect Baseline Correction: Inaccurate reference subtraction or baseline drift correction can result in a vertical shift in the fitted curve. This misalignment forces the fitting algorithm to introduce a jump to compensate for the baseline discrepancy [228].

Model Inadequacy: Fitting a complex or multi-site interaction using an oversimplified model (e.g., assuming 1:1 kinetics when the system exhibits mass transport limitation or conformational changes) can lead to poor curve representation, especially at the association-dissociation boundary [229].

Buffer Injection Artifacts: Mechanical effects during buffer exchange—such as bulk refractive index changes or pressure shifts—can introduce real, rapid signal changes. If these are not properly corrected (e.g., by double referencing), the model will interpret them as binding-related and fit them with a jump [230].

Numerical Fitting Artifacts: Nonlinear least-squares fitting is sensitive to noise and initial parameter estimates. If the optimizer converges on a local minimum that numerically reduces the residuals, a jump may result—even if it lacks physical meaning.

A visible discontinuity in the fitted kinetic curves at the highest analyte concentrations in Figures 4.8 and 4.12 suggests that the software incorporated a bulk refractive index shift into the fit, resulting in a noticeable jump in the continuity of the curve. This effect likely stems from the absence of a parallel reference channel in the SPR system used for the experiments. In single-channel configurations, the reference and sample signals are recorded sequentially rather than simultaneously, which can introduce temporal inconsistencies and compromise the accuracy of bulk shift correction.

These issues could be effectively mitigated by using the dual-channel systems of Nicoya SPR. In this manner, bulk shift correction is performed in real time by simultaneously recording both the reference and sample signals significantly improving the quality of the data. Unfortunately, due to equipment constraints, a dual-channel setup was not available for this study, limiting our ability to implement real-time correction.

4.3.4 Surface regeneration, selectivity, and specificity

A regeneration buffer was developed to allow in-situ regeneration of the capture layer, so that the protein could be removed without compromising the activity of the antibody. It is quite challenging to find the right experimental conditions and get optimal binding kinetics. One of the most important steps to consider is the regeneration step, or more specifically, the regeneration buffer.

To determine accurate binding constants (kon, koff and KD) for an interaction using SPR, 3-5 binding curves of analyte at different concentrations are needed. The indication of a regeneration step becomes evident by the value of the off rate of the ligand-analyte complex. If the off rate is high, the analyte will dissociate from the surface in a short amount of time (approximately 5 minutes), so a regeneration step is not needed in order to have multiple analyte injections. If the off rate is low, the analyte will take a very long time to dissociate (hours), so in order to get multiple analyte injections in a reasonable amount of time, you need to regenerate.

It is critical to choose a regeneration buffer that is harsh enough to remove all of the analyte, but mild enough that it does not severely damage the functionality of the ligand. The ligand activity should be preserved even after multiple regeneration cycles, otherwise the analyte response will decrease significantly during future injections.

The regeneration buffer appropriate for an antibody-protein interaction is a weak acidic buffer with a pH > 2.5. A commonly used buffer is the 10 mM Glycine/HCl. The results of using this buffer to regenerate the surface are shown in Figure 4.13-A. IL-6 was injected at 8.4 µg/ml concentration, causing the peak to shift up by 250 pm. After the binding is complete, the Glycine/HCl buffer was injected at a flow rate of 150 µl/min flow rate.

The peak position dropped almost immediately but as shown in the graph the interaction time was short, and the signal remained above the baseline. The accuracy of the regeneration injection was improved by testing lower flow rates allowing longer interaction and recovering all binding sites of the ligand. In Figure 4.13-A are demonstrated four successful regeneration cycles.

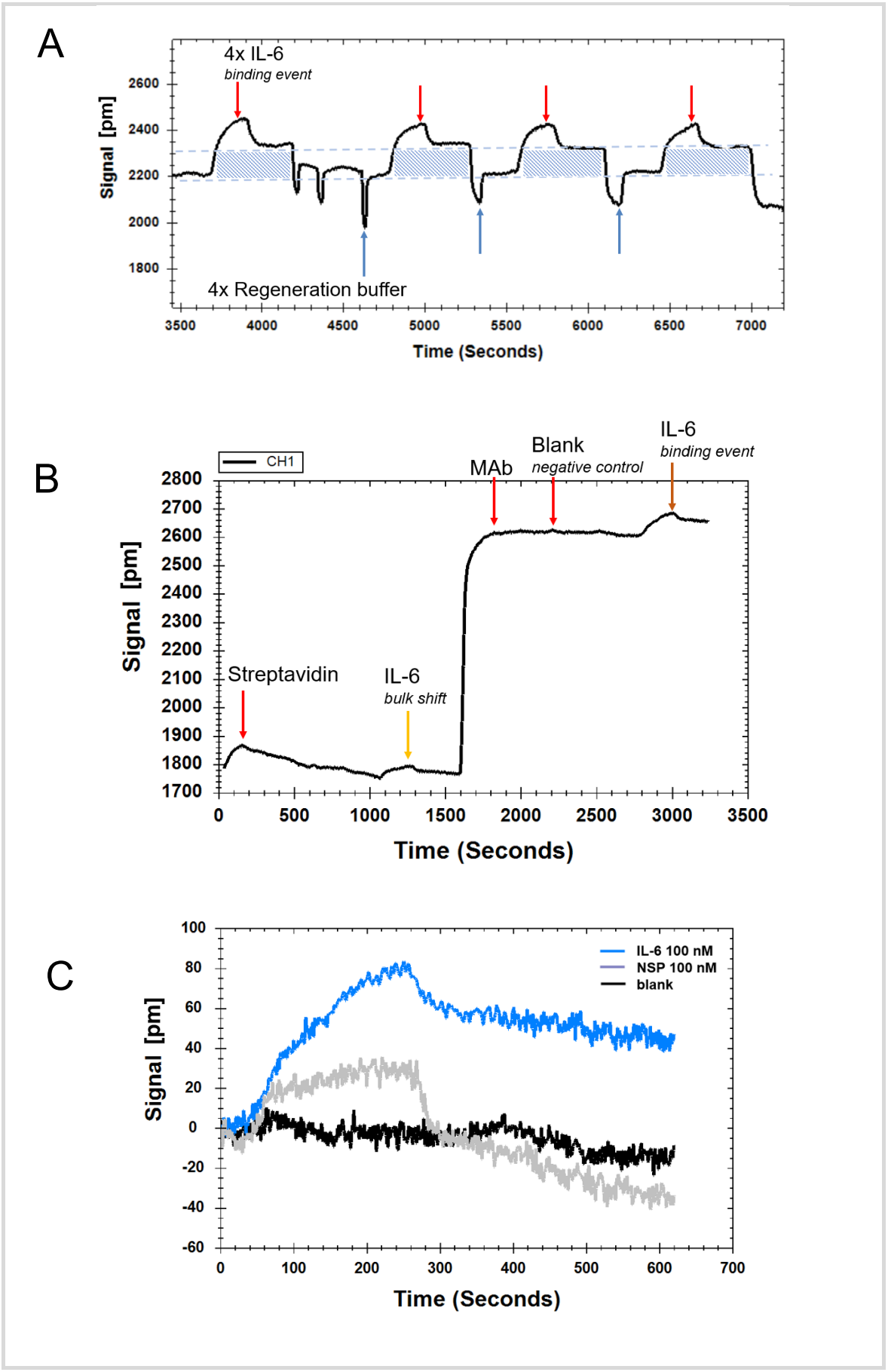

Figure 4.13 A – Regeneration of the IL-6 LSPR sensor using Glycine/HCl buffer which results in removal of the protein from the capture probe. Subsequent injection provides similar binding level indicating the capture layer is still active. B – experiment demonstrating the specificity of the sensor. C - experiment demonstrating the selectivity of the sensor.

By being able to regenerate the ligand-analyte complex, researchers can reuse the same sensor chip many times, making SPR a cost-effective technique.

The specificity of the sensor is demonstrated in the next graph. The investigated analyte IL-6 is introduced before and after immobilizing the capture layer. The sensorgram in plot B in Figure 4.13 shows the real-time trace after covering the surface with SA. Injecting 100 nM IL-6 would introduce the protein on the sensor surface but as it would not bind specifically, it was washed away. This leaves the peak position unchanged after the end of the injection. In the next part of the experiment, the sensor surface becomes specifically sensitive to IL-6 as the anti-IL-6 MAb is introduced.

As shown in the plot the peak position shifts with 800 pm. Injecting a blank sample as a negative control does not affect the LSPR peak position in the absence of the analyte. Injecting the same concentration of 100 nM IL-6 again elicit a response with a typical association and dissociation curve indicating the expected specificity.

The selectivity of the LSPR sensor was presented in plot C in Figure 4.13. An injection with 100 nM protein, non-specific to the sensor biointerface. As the capture layer does not recognize it, the trace shapes a typical square bulk shift and remain the peak position unchanged as no binding event occurs. In order to visualise the difference between the traces, plot C overlays a signal from a blank sample, IL-6, and a non-specific protein (NSP). The negative control demonstrates the fluctuations of the background noise, compared to a signal intensity of binding occurrence and a bulk shift.

4.4 Biomolecular detection with DGPAL

4.4.1 Methodology

The DGPAL sample was thoroughly cleaned three time with IPA solution during 3x2 min sonication and rinsed with DI water. The pristine surface is of utmost importance for SAM formation as any small impurities would disrupt the integrity of the monolayer. The DGPAL sample was immersed in the 5 µM Biotin-$(PEG)_{10}$-Thiol (Polypure 41156-1095) solution for 24 hours in room temperature (RT) during

continuous mixing on an orbital shaker. Low-concentration thiol SAMs require long incubation periods to allow enough time for the polymer units to densely pack on the surface spontaneously forming ordered molecular assemblies. The process was followed by rinsing with PBS to remove the excess molecules and wash away the chemically unabsorbed polymers. Optical measurements of the device are taken in PBS after the rinsing step of each functionalisation stage so that the scanned map after adding any biological entity can be compared with the blank reference where gold film is just covered with blank PBS buffer.

The next protein added on top of the biotin functional head of the SAM is 0.5 μM Streptavidin (Merck KGaA, SA101) in PBS and incubated for 1 hour during continuous mixing. The subsequent step in the process involves a washing step removing excess and unbound Streptavidin and incubating the DGPAL for 1h in RT with 0.1 μM biotinylated Anti-IL6 Mouse Monoclonal Antibody (MAb) (SinoBiological, 10395-MM72-B).

The biodetection reaction with the double gradient plasmonic array library was also tailored to recognise and bind the investigated target – human interleukin-6 (IL-6). Recombinant human IL-6 protein (SinoBiological, 10395-HNAE) was added in concentration 0.2 μM and incubated for an hour in RT during continuous mixing. After a mandatory washing step with PBS removing any unbound target protein, scan measurements of the surface finished the biomolecular detection experiment.

4.4.2 Biomolecular detection – results and discussion

Figure 4.14 illustrates the changes on the electromagnetic metasurfaces after each functionalisation event and showcase the target binding event. Each generated heat map is a visual representation of the shift in LSPR peak position after adding a low-concentration biomolecular entity. This shift is calculated relative to a reference scan, which comprises measurements of the DGPAL under operating buffer conditions in PBS and a clean gold nanopatterned layer. The detection of total binding events is registered on the heat map as pixels in various shades of red. The colour palette of the heat map differentiates the unsuccessful LSPR shifts with shades in blue colour.

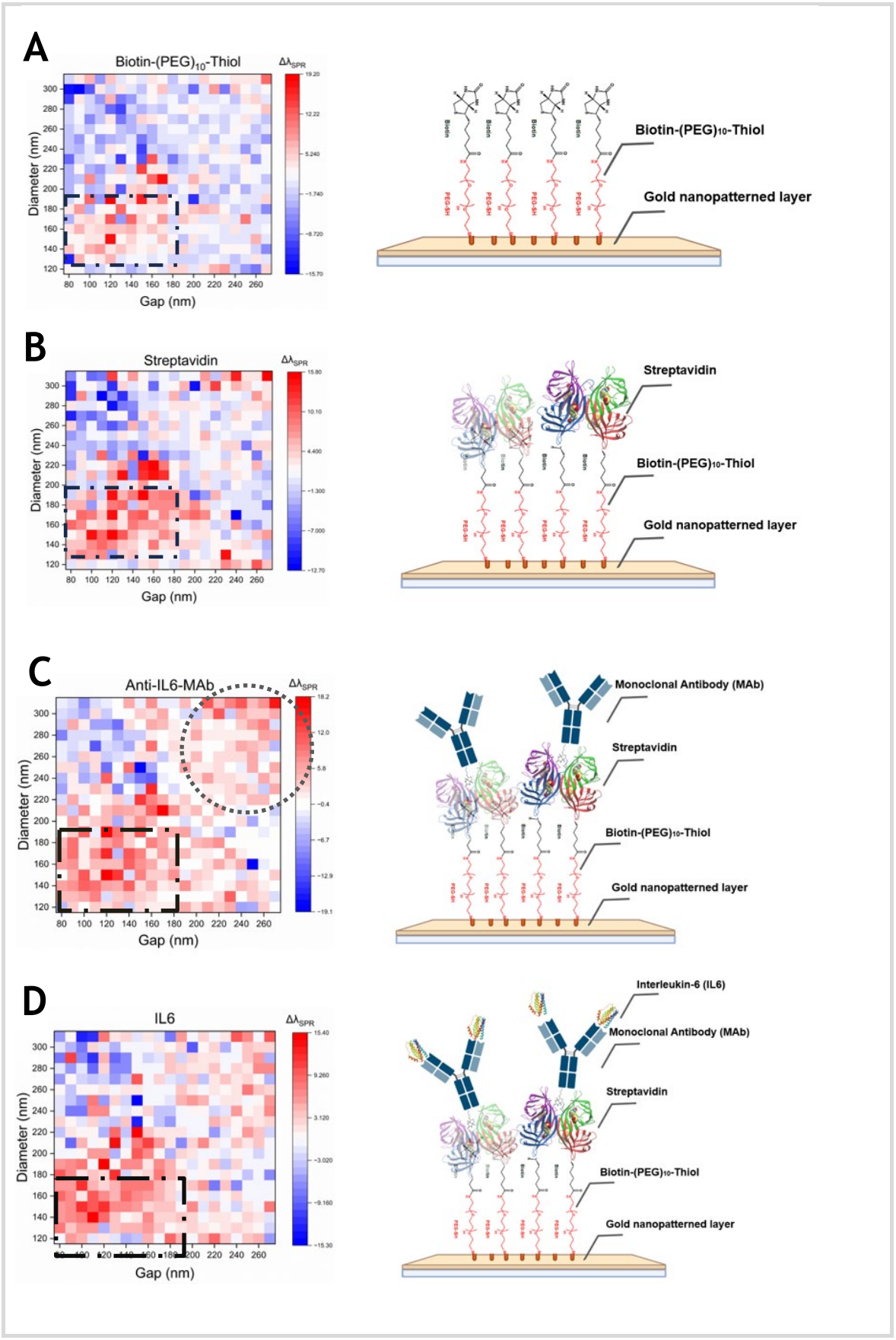

Figure 4.14 Heat map representation of a biomolecular detection process complemented with a diagram of the nanopatterned device illustrating each functionalization step. Illustration of biomolecules are adapted from [196] [198] [185]. Plot A – depicts the absorption of SAM; Plot B – adding Streptavidin; Plot C – adding biotinylated IgG antibody; Plot D – introducing the investigated target, IL-6. The progression of all 400 reactions can be followed simultaneously by the increasing intensity of red pixels.

The collective colours from all pixels in the DGPAL create a signature fingerprint indicative of the binding event. Thus, we can follow the progression of 400 biomolecular detection reactions simultaneously.

As anticipated, the most sensitive region of the plasmonic library corresponds to the area associated with Mode 1 oscillation. These nanoarrays are characterized by relatively small nanopillars and narrow lateral interspacing enabling a gradient of mixed LSPR/SPP and pure LSPR oscillations to exist. The confined energy surrounding the nanopillars, with an electromagnetic distribution limited strictly around their size and field decay spanning a few tens of nanometres, is demonstrated in the initial functionalization event. The low molecular weight (MW) and low-concentration SAM polymer allows for detection with a similar-sized electromagnetic field sensitive to minor changes in the local refractive index. As depicted in Figure 4.14-A, the heatmap corresponding to the SAM assembly illustrates a cluster of red pixels outlined with a dash-dotted line, aligning with the location of Mode 1 oscillation. Upon the addition of Streptavidin, the intensity of Mode 1 cluster increases (Figure 4.14-B) as subsequent binding events occurs. The aggregation of the polymer arm with Streptavidin and an IgG antibody collectively forms a complex with MW slightly above 205 kDa.

The size of the aggregate can be detected from nanoarrays with large nanostructures as its size is comparable to their EM field distribution. This is evident in Figure 4.14-C, where binding events are registered in the region of both Mode 1 and Mode 2 (outline with dash-dotted square and dotted circle respectively). The IL-6 is introduced in the end of the biomolecular detection process on a pretty much saturated with red pixels heat map. The findings presented in Figure 4.14-D suggest that the occurrence of binding events does not visually change the intensity of red pixels in the heat map.

This observation is typically attributed to the small MW of the investigated target. High MW proteins induce a redshift in the LSPR peaks with higher values compared to small proteins, thereby the changes induced by small proteins like IL-6 in the heatmap appear insignificant. However, if we evaluate the pure LSPR region on the heat map where it is more likely for the shifts to be successfully detected, the higher intensity of red pixels confirms the presence of the target analyte.

The LSPR regions being the most sensitive area on the heat map are additionally analysed. Regions are outlined with a dash-dotted line in Plot A, B, C and D in Figure 4.14 and the resultant bar plot is depicted in Figure 4.15. Apart from visualizing the increasing intensity of red pixels on the heat maps as more binding events occur a quantitative analysis is also performed. All peak position shifts within the outlined region are summed and depicted as a bar plot. This suggest that the shown differences in peak positions are quantified as a total shift of all accumulated binding events after each functionalisation step.

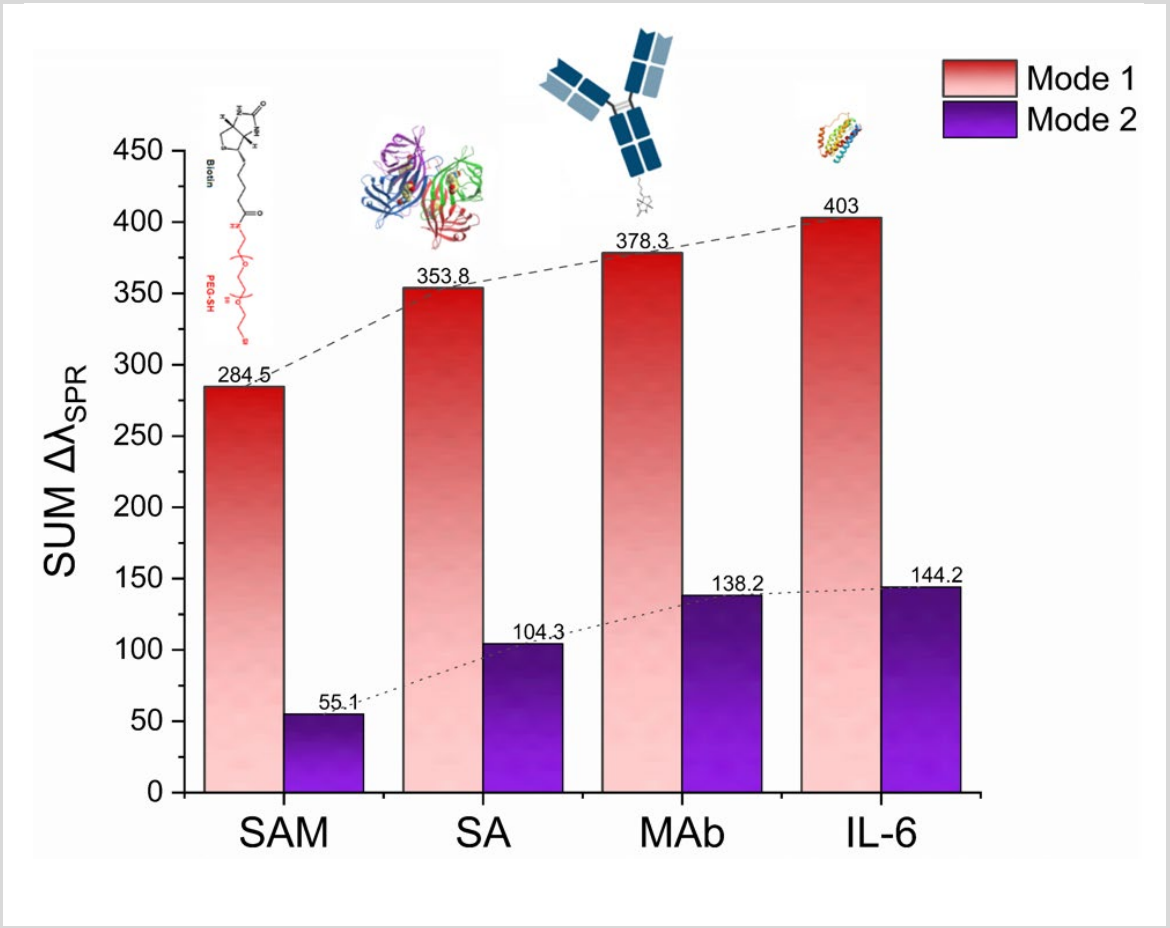

Figure 4.15 Bar plot representation of the biomolecular detection process for Mode 1 and Mode 2 at each stage. The values are presented as the sum of the shift within the outlined area of the respective resonance mode. Illustration of biomolecules are adapted from [196] [198] [185]

4.5 Conclusion

In this work, a label-free IL-6 sensor based on the LSPR of gold nanopillars was designed and tested. The design was specifically accommodated to be compatible

with the Open SPR instrument from Nicoya for real-time measurements. A 3D printed sensor holder was developed hosting the chip and seamlessly dock with the flow cell. Optical references and absorption peaks for the default and replica sensor demonstrate full compatibility with the software.

The bulk sensitivity was characterized using glycerol-water solutions and found to be 112.16 nm/RIU, with an LSPR peak position at 577 nm in water with a FWHM of 54.5 nm, giving a FOM of 2.05.

A surface functionalization protocol was developed using alkanethiols of 10 (PEG) units long finishing with biotin functional group. Experimental trials demonstrated that variability in the density of antibody binding sites caused a proportional variation in the LSPR sensor response. Thus, the optimum concentration of alkanethiols was verified at 5 μM allowing enhanced binding of streptavidin and capture antibody on the sensor surface minimizing steric hindrance.

The LSPR biosensor was experimentally tested using both the model protein system of biotin-streptavidin and human IL-6 and its synthetic antibody.

The response of the sensor to streptavidin was investigated. Detection of purified streptavidin in real time over the range 55-500,000 ng/ml was demonstrated from 200 μl samples, which resulted in peaks shifts from 0.016 - 3.014 nm. Using these results an equilibrium binding constant of $1.28x10^{-7}$ M was determined. These results demonstrate the ability of the LSPR sensor to detect and quantify streptavidin over a wide range (over 4 orders of magnitude) with a low detection limit of 192 ng/ml. This binding constant is comparable to some studies but is much lower than the reported in literature ($KD = 10^{-15}$). By using the more accurate kinetic evaluation model the affinity constant was estimated at $KD = 1.12x10^{-14}$ M.

Detection of purified human IL-6 was shown through attaching its synthetic antibody to the nanopillar surface. Real time detection of IL-6 was shown for concentrations of 2 nM to 900 nM, which resulted in a LSPR peak shift of 0.5 nm to 0.07 nm +/- 0.03 nm. The estimated affinity constant $KD = 1.67x10^{-9}$ M extracted with the kinetic evaluation model is in a good alignment with the true value of what is reported in the literature of $KD = 5.5x10^{-9}$ M.

The IL-6 sensor could be regenerated by a pH 2.0 10 mM glycine-HCl buffer. The protein could be removed without adversely affecting the antibody capture layer, so that the sensor could be easily reused. The specificity of the sensor was demonstrated when the investigated analyte IL-6 is introduced before and after immobilizing the capture layer. Induced peak shift was observed only after introducing the capture probe. The selectivity of the LSPR sensor was presented by comparing the response signal from a non-specific protein, the target protein IL-6, and a blank reference. Induced peak shift was observed only by the target analyte IL-6.

Finally, the same biodetection process was demonstrated simultaneously including all 400 structures from the double gradient plasmonic array library. The heat map representation of the binding events provides a visual reproduction of the sensitivity of the surface outlining Mode 1 and Mode 2 resonance. Each stage of the biodetection is illustrated with a fingerprint plot which upon evaluating the sum of peak shift within the sensitive areas, provides an accurate dynamic of the binding events.

In summary, an optimized LSPR sensor was designed to meet the performance specifications needed for label-free detection of human IL-6 in point-of-care and remote applications. A proof of concept LSPR sensor was experimentally shown to recognise IL-6 in real time and as a fingerprint detection. The many benefits of LSPR sensors, including high sensitivity, ease of use, simple and low cost hardware, and low noise make it an excellent technique for the development of point-of-care IL-6 biosensors.

Chapter 5 Summary and Outlook

5.1 Summary

In this thesis, a scalable platform based on injection-moulded periodic nanopillar arrays coated with thin gold films was developed and rigorously evaluated for its plasmonic and biosensing performance. This work represents a significant step toward advancing LSPR-based biosensors from proof-of-concept research to commercially viable diagnostic technologies.

It is evident from the recent pandemic that early sensor diagnosis is the key to rapid and effective treatment. Furthermore, research and development efforts focused on vaccines and medicines, combined with robust monitoring systems for tracking environmental pollution and contaminants, emphasize the importance of accessible and efficient healthcare services to improve global health outcomes. Novel biosensors, which offer portable, in-situ applications in real-time and act as cost-effective analytical tools, are emerging as the future of diagnostic systems. Among the various biosensing techniques, optical biosensors based on LSPR offer great advantages over conventional analytical techniques.

The expectations for an optical sensor include reliability, speed, sensitivity, and simplicity, without the necessity of expensive equipment. These features must be achieved at ultralow fabrication costs. To meet these requirements, and after carefully reviewing the chip-based sensor configurations, in this project we focused on the coupling between LSPR and SPP of periodic nanostructures on a metal film, operating under normal light incidence. This hybridization model offers significant sensitivity improvements and requires careful investigation of its full coupling potential.

Hundreds of periodic nanostructures with varying sizes and periodicities were fabricated on a single platform, allowing for experimental study of their plasmonic resonance. This platform, known as the double gradient plasmonic array library (DGPAL), systematically demonstrates how the geometry of the arrays transitions from predominantly SPP mode exhibiting photonic Rayleigh anomalies (RA) to hybrid SPP-LSPR combinations, and finally to predominantly LSPR properties. The

intriguing results extracted from the DGPAL analysis show improvements in high bulk RI sensitivity and biomolecular detection.

The multi-step nanofabrication process was approached with two different methods in order to compare and outline the most efficient strategy. The simplified approach relies on exposure commands that control the electron beam, such as dose and VRU information, known as "dot writing." This method does not involve graphic data, thus lacking optimization potential through data processing software. The advanced approach uses graphic data to represent arrays with actual shapes. The generation of the graphic data file was automated using customized Python code and the CNST toolbox, producing data in GDS format compatible with various software programs like TRACER and BEAMER. This advanced method includes proximity effect correction and automated exposure field placement, avoiding stitching intersections in nanoarrays, with 10 nm BSS ensuring the desired circularity.

EBL patterning of the resist was performed using two generations of EBL systems: the older Vistec VB6 UHR EWF electron beam tool for the VB6 sample and the state-of-the-art Raith EBPG 5200 for the EBPG sample. Detailed comparative analysis of the master stamps and final devices fabricated using both approaches revealed significant quality differences. Based on the results, the advanced nanofabrication approach using the EBPG system was deemed advantageous. Consequently, all subsequent analyses and research experiments involving the double gradient plasmonic array library will exclusively utilize the EBPG sample device.

A major improvement in the nanofabrication of plasmonic architectures is that the methodology adheres to a fast and cost-effective approach allowing pattern transfer and mass-replication of high-resolution periodic arrays. Nanoimprint lithography followed by injection moulding enables the replication of large-area periodic nanostructures with high fidelity and minimal cost per device—essential attributes for widespread PoC diagnostics.

In such manner, the fabrication of a plasmonic library containing hundreds of geometry combinations on a single chip becomes an achievable task and a vast number of characteristic properties of the plasmonic behaviour can be extracted systematically. Additionally, every final custom designed chip-based array validated for sensing purposes is readily optimized for a manufacturing production line.

After a detailed description of the creation and morphology characterisation of the double gradient device, the next focus is on systematically describing the resonance profile and the underlying mechanisms governing peak tuning. This analysis encompasses the resonance performance of the plasmonic arrays. Furthermore, a pivotal facet of the study involves the classification of their sensitivity performance.

The periodic arrays within the library offer a controlled platform for investigating optical properties. This enables the investigation of near- and far-field interactions between adjacent nanostructures, which may lead to the controlled manipulation of optical signals and light-matter interactions. Resonance oscillations can be manipulated towards higher frequencies by reducing the interspacing gap between nanopillars and decreasing the diameter size of the nanopillars, or a combination thereof. Conversely, alterations in the opposite direction result in oscillation shifts towards lower frequencies. Optimal plasmonic enhancement is achieved when the square nanoarray is constructed with dimensions where the diameter-to-gap ratio is close to 1. Varying the thickness of gold deposition offers a broader bandwidth of resonance wavelengths and serves as an effective means of dynamic tuning. The most advantageous bandwidth range for peak tuning in combination with a favourable FWHM profile is obtained with film thickness of 60 nm gold. The gold coated nanopillar arrays in the double gradient device as reported, exhibit complex optical responses. It can support the periodic analogue of SPPs namely Bragg plasmons, LSPRs and related diffractive effects such as Rayleigh-Wood anomalies (RWAs) and combinations of these resonant and diffractive phenomena which have very different near-field distributions. Bringing localized and propagating surface plasmons together in a single platform demonstrates the unique opportunity to investigate the mixed as well as the pure form of those phenomena. This distinction led to the identification and further exploration of oscillation types labelled as Mode 1 and Mode 2. Mode 2 was associated with refractive index sensitivity, while Mode 1 governed biomolecular detection. The data collected from this rigorous analysis served as a valuable resource in pinpointing the ideal combination of design parameters for optimal compatibility with the Nicoya OPEN SPR tool.

A label-free IL-6 immunosensor based on the LSPR of gold nanopillars was additionally fabricated and tested to meet the performance specifications needed

for label-free detection of human IL-6 in point-of-care and remote applications. A proof of concept LSPR sensor was experimentally shown to recognise IL-6 in real time and as a fingerprint detection. The many benefits of LSPR sensors, including high sensitivity, ease of use, simple and low cost hardware, and low noise make it an excellent technique for the development of point-of-care device.

A surface functionalization protocol was developed using bifunctional alkanethiols with a biotin functional group. Experimental trials demonstrated that variability in the density of antibody binding sites caused a proportional variation in the LSPR sensor response. Thus, the optimum concentration of alkanethiols was verified at 5 μM allowing enhanced binding of streptavidin and capture antibody on the sensor surface, minimizing steric hindrance.

Detection of purified human IL-6 was shown through attaching its synthetic antibody to the nanopillar surface. Real time detection of IL-6 was shown for concentrations of 2 nM to 900 nM, which resulted in a LSPR peak shift of 0.07 nm to 0.5 nm +/- 0.03 nm. The estimated affinity constant KD = 1.67x10-9 M extracted with the kinetic evaluation model is in a good alignment with the true value of what is reported in the literature of KD = 5.5x10-9 M. Importantly, the IL-6 sensor capturing sites can be regenerated with a pH 2.0, 10 mM glycine-HCl buffer. The protein could be removed without negatively impacting the antibody capture layer, allowing the sensor to be easily reused. This reusability enhances the cost-effectiveness of the experiments.

Finally, the same biodetection process was demonstrated simultaneously including all 400 structures from the double gradient plasmonic array library. A heat map representation of the binding events provides a visual reproduction of the sensitivity of the surface outlining Mode 1 and Mode 2 resonance. Each stage of the biodetection is illustrated with a fingerprint plot which nicely illustrates the responsiveness of all SPP, LSPR and SPP-LSPR hybrid combinations.

The LSPR sensors with different material composition and different shape and size ensembled particles resonating in the VIS bandwidth exhibit RI sensitivity between 100 – 500 nm/RIU. The LSPR sensors exploiting the geometry of nanoparticle arrays and other planar nanostructures can be designed with higher refractive index sensitivities. The state of the art LSPR plasmonic sensors can achieve as high as 1900 nm/RIU at the NIR region. However, their applicability is limited due to the

requirement for low-cost and widely available equipment, which is typically suited for the visible spectrum. At visible spectrum, the sensitivity for LSPR nano-array sensor is about hundreds of nanometres per RIU. Examples reported in the literature have demonstrated that bowtie arrays achieve sensitivity of 577 nm/RIU and the double-hole structure in a gold film improves the bulk refractive index sensitivity with 600 nm/RIU. In comparison to our research findings, the sensitivity of 358 nm/RIU achieved with the nanopillar arrays is quite close to the reported accomplishments. A notable trend outlined in the results indicates a gradual rise in sensitivity as both diameter and interspacing increase. This trend presents an opportunity for future optimization efforts, which may have the potential to surpass the performance of the investigated nanoarrays.

Today, SPR sensors are widely utilized in fields ranging from biomedical diagnostics to environmental monitoring. The COVID-19 pandemic underscored the importance of rapid and reliable diagnostic tools, leading to increased interest in SPR-based point-of-care testing. Ongoing research aims to improve SPR sensor performance through machine learning algorithms, advanced nanomaterial engineering, and integration with portable electronic devices for real-time and on-site analysis. Beyond passive detection, the integration of light-generating materials, including quantum dots and hybrid metal-semiconductor systems, suggests the possibility of creating biosensors with self-contained light sources, thus eliminating the dependence on external illumination and advancing the development of compact, electrically addressable platforms.

Another emerging area involves chiral sensing. Recent efforts have focused on engineering metasurfaces capable of generating strong electric and magnetic dipole moments, producing superchiral near-fields to detect and separate enantiomers of biomolecules with high specificity [231] [232]. Such advancements are critical for fields like pharmaceutical development, where the chirality of a molecule can dramatically alter its biological function. Importantly, increasing the information gathered through optical degrees of freedom — including spectral, temporal, spatial, and polarization domains — is pivotal. When combined with machine learning and artificial intelligence (AI) methodologies, such comprehensive data acquisition can significantly enhance the interpretability and predictive power of biosensor outputs [233]. Future intelligent biosensors, autonomously operated and connected via the Internet of Things (IoT), are

envisioned as integral components of digital healthcare ecosystems, enabling real-time health monitoring and predictive diagnostics [234].

Despite the remarkable sensitivity achieved by contemporary nanophotonic biosensors — down to the observation of single molecular binding events [235] [236]— significant challenges remain in translating these laboratory successes into commercially viable, everyday diagnostic tools. Progress in fundamental optical physics at the nanoscale is expected to yield new sensing mechanisms, broadening the capabilities of biosensors beyond current limits. Equally important is the coupling of nanophotonic biochips with microfluidic systems to facilitate sample pre-treatment and delivery. Traditional fabrication methods for SPR sensors often involve complex and costly processes, limiting their widespread application. Recent advancements in nanoimprinting and injection moulding techniques offer promising avenues to overcome these challenges, enabling the production of SPR sensors that are both cost-effective and high-performing. Addressing these challenges is essential to unlock new possibilities for SPR sensors, especially in portable and high-throughput applications. This doctoral thesis aims to explore these challenges by focusing on two innovative fabrication techniques: nanoimprinting and injection moulding.

5.2 Outlook

Beyond biosensing, the LSPR nanoarrays developed in this thesis offer significant potential for broader photonic applications. If more time were available, one promising direction we would explore further is their role in enhancing fluorescence signals, specifically through Metal-Enhanced Fluorescence (MEF), leveraging the strong near-field interactions generated by the plasmonic nanostructures. In the Outlook section, we have presented compelling preliminary evidence that our injection-moulded plasmonic nanoarrays can support MEF, expanding their functional versatility beyond label-free biosensing. These results demonstrate that the same nanoarrays can be adapted for fluorescence-based detection platforms, broadening the scope of applications in bioimaging, diagnostics, and multiplexed sensing.

Within life sciences, fluorescence microscopy is used for variety of applications where measurements could benefit greatly from the improvements of fluorophore’s quantum yield [237]. It is most effectively utilised in biomedical

sensing and fluorescence microscopy imaging. Biological analytes can be detected to ultra-low concentrations and fluorescently labelled markers can enhance the reporting of molecular events in the microenvironment [238].

Metallic nanopatterned surfaces supporting LSPR can modify favourably the brightness and photostability of fluorophores in the near-field, a phenomenon introduced as Metal-Enhanced Fluorescence (MEF) [239]. MEF occurs when a fluorophore is excited near a plasmonic surface, typically around 5 - 90 nm, under certain conditions [240]. This near-field effect is strongly distant dependent and decreases exponentially with the distance from the plasmonic surface. It is characterised by an increased fluorescence intensity and a decreased fluorescence lifetime. This usually leads to enhanced fluorophore photostability, as the fluorophores spend less time “on average”, in an excited state, prior to their return to the ground state, and are subsequently less prone to photodestruction [241].

The high-throughput injection moulded plasmonic arrays created in this project can be customed designed and easily integrated within variety of liquid-handling platforms applicable for fluorophore labelled sensing similar to an ELISA test. Thus, we have decided to explore and evaluate their MEF response and expand the applicability further.

As mentioned previously the near-field LSPR interaction with the fluorophore is governing the fluorescence enhancement. Other influencing factors include the size, shape, periodicity of the plasmonic nanostructures and nature of the metal. In this case the DGPAL platform can serve as an ideal platform for MEF evaluation as a function of array geometry.

A significant spectral overlapping between the plasmonic band of the metallic nanostructure with absorption and emission band of the fluorophore is required to have a reasonable overall fluorescent enhancement [242]. The plasmonic band of the DGPAL was evaluated between 550 – 750 nm with predominantly arrays resonating within the 600 – 680 nm range governed by the properties of gold metallic film. The fluorophore chosen for the experiment is the commercially available Alexa Fluor 647 (AF 647) with excitation peak at 650 nm and emission at 671 nm. To facilitate the fluorophore proximity to the plasmonic surface, a

monolayer of alkanethiols was established using the optimized protocols for functionalisation. Subsequently 100 nM Streptavidin labelled protein with AF 647 was incubated for 2 hours in room temperature. It is then washed three times with PBS buffer and Tween20 solution to remove the excess. This type of biotin-streptavidin conjugation system acts as a spacer providing sufficient separation distance of 7-8 nm ensuring less quenching effect (Figure 5.1-A). As the functionalisation treatment was applied to the whole slide, the flat gold film around the patterns was also labelled with the fluorophore. This provides an opportunity to first compare the MEF intensity between flat film of gold and plasmonic architectures coated with gold film.

Shown in Figure 5.1-B are the scan fluorescent images taken with an EVOS™ M7000 Imaging System, using the 10X objective and the Cy5 LED light cube whose spectra best match the excitation/emission of AF 647. The scan images provide sufficient context of the MEF dynamic. In all images the flat gold film around the patterned area is dark and demonstrates close to zero enhancement. This control confirms that the MEF phenomena is exhibited only when the fluorophore is proximal to plasmonically active structures.

Secondly, the comparison between all three images is emphasizing on the increasing fluorescent intensity as gold deposition increase – 80 nm Au < 120 nm Au < 160 nm Au. A green arrow starting from bottom right corner diagonally across the double gradient library of arrays to top left corner depicts the direction of the sampled cross-section in order to be evaluated.
Figure 5.1-C1 presents the overlayed fluorescent intensity profiles where all arrays despite their location and plasmonic performance increase their MEF score when more gold is added. Lastly, the gradient of design parameters creates a gradient of fluorescent enhancement. In order to reveal this trend, the fluorescent intensities of a vertical and horizontal cross-sections encompassing the diameter and gap variations are plotted in Figure 5.1-C2. Likewise, the direction of both profiles is depicted with dashed yellow arrows on the 120 nm Au image. Analysis demonstrates that when decreasing the size of the nanopillars and expanding their periodicity fluorescent intensity enhancement improves. In comparison with flat gold film, the fluorescent plasmonic arrays achieve 56-, 92- and 102-fold higher MEF, respectively with 80 nm, 120 nm and 160 nm gold film.

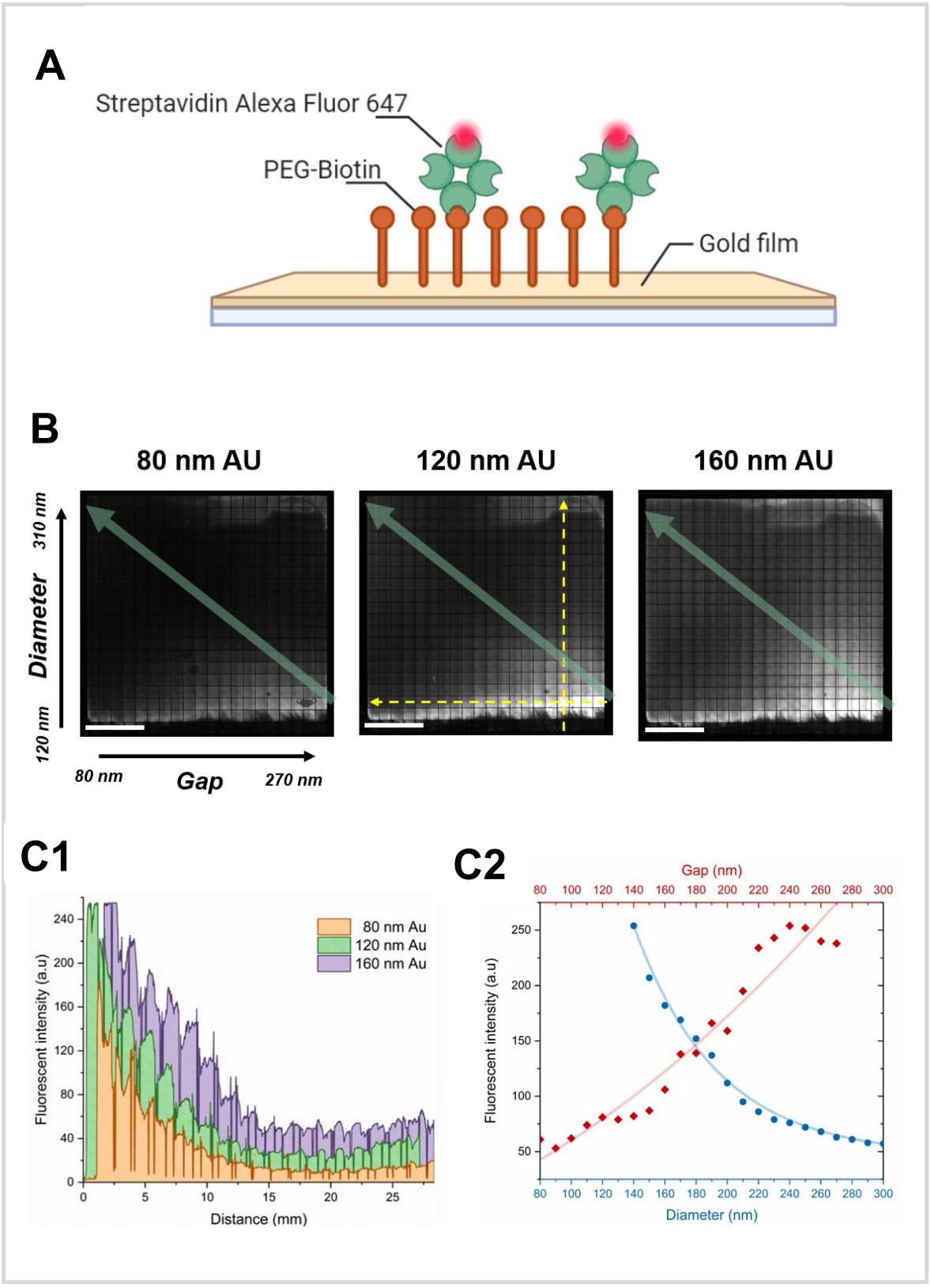

Figure 5.1. A – diagram representing the attachment of the AF 647 facilitated by a monolayer of alkanethiols creating uniform distribution on the plasmonic surface and the biotin-Streptavidin conjugation system acting as a spacer. B – Scan fluorescent images of the DGPAL coated with increasing thickness of gold film – 80 nm, 120 nm, and 160 nm. Scale bar 5 mm. C1 – Comparison of the fluorescent intensity of 80 nm, 120 nm, and 160 nm taken diagonally across the surface as shown with green arrow in their respective image. C2 – Scatter plot showing the fluorescent intensity as a function of design parameters (diameter and gap). The cross sections used for the analysis are depicted as dashed yellow arrows on the 120 nm Au image.

From Figure 5.1-B, it is obvious that maximum enhancement is always observed at the bottom right region of the double gradient library irrespective of the Au thickness. To understand the reason behind this interesting observation we have explored further with 160 nm thickness sample. Three plasmonic arrays were chosen for further investigation and their position is following the gradient of fluorescent enhancement. The exact location is shown on Figure 5.2 and for more simplicity are named as Region 1 (R1), Region 2 (R2) and Region 3 (R3).

The SPR spectra collected from the three different nanostructure regions have been compared with the excitation and emission spectra of AF 647. The plots showcasing the spectral overlap are shown in Figure 5.2 (a), (b) and (c).

As we move in the nanostructured regions from R1 to R2 to R3, the SPR absorption spectra red shift and its magnitude increases. As a result of this a gradual increase in spectral overlapping between SPR, excitation and emission spectra of AF 647 is observed from R1 to R2 to R3. Among different regions R3 is having the highest spectral overlapping with the SPR spectra. This spectral overlapping is a crucial factor in MEF to obtain better excitation and emission enhancement. As a next step, the reflectivity nature of different nanostructured regions is investigated.

Figure 5.2 (d) shows the relative reflectance spectra collected from R1, R2 and R3 and compared the same with the emission band of Alexa Fluor 647. Moving from R1 to R2 to R3, reflectivity of the nanostructured regions for emission band of the dye molecule increases and more than 90% reflectance is observed for R3 region. Thus, the R3 region assists in directing emitted photons to the detector, minimizing losses from other optical processes.

Due to its high spectral overlap and sufficient reflectance, the R3 region of the fabricated nanopillar library provides significant enhancement in fluorescence (FL) intensity.

The spectroscopic investigation of the MEF properties within the plasmonic nanopillar arrays has captured the interest of other researchers. Collaborating with Dr Gordon Hedley and Dr Saptarshi Mandal from the University of Glasgow, School of Chemistry, we conducted an advanced spectroscopic exploration.

Utilizing a home-built confocal microscope setup with a piezo stage, connected to PicoQuant's HydraHarp-400 time-correlated single photon counting (TCSPC) unit, we performed time-resolved measurements.

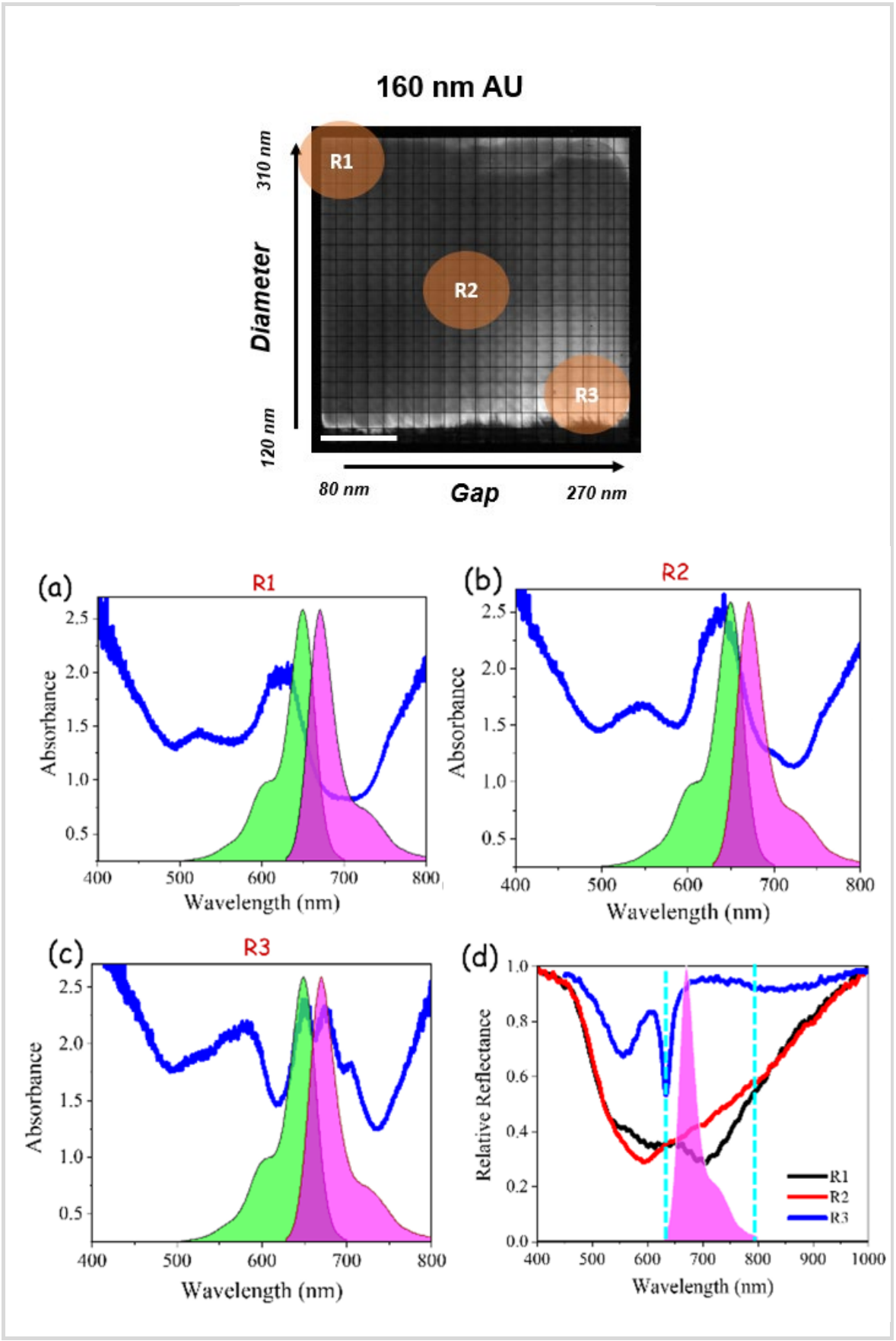

Figure 5.2. The top image diagram outlines the location of the three arrays chosen for spectral investigation. (a), (b), and (c) depict the spectral overlap between the absorption resonance of R1, R2, and R3 and the excitation/emission peaks of AF647. (d) depicts the spectral overlap between the reflectance of R1, R2, and R3 and the excitation/emission peaks of AF647.

By scanning the fluorescent intensity image and measuring the fluorescent decay from different regions of interest, our results demonstrated that the enhancement in fluorescent intensity is correlated with faster fluorescent decay (results not shown). Specifically, fluorescent decay in the nanostructured region is approximately four times faster than in the flat gold region, indicating a significant enhancement in the radiative decay rate of the fluorophore.
The concept of integrating high-throughput injection-moulded plasmonic MEF platforms with fluorophores offers promising opportunities. This combination can create ultra-bright fluorescent probes, significantly enhancing sensitivity beyond the limitations of conventional organic fluorophores.

In conclusion, this research introduces an innovative method for creating high-performance optical biosensors based on plasmonic nanostructures. The nanofabrication of plasmonic architectures uses a methodology adhering to a fast and cost-effective approach allowing pattern transfer and mass-replication of high-resolution periodic arrays. The resulting plasmonic library serves as a powerful screening tool, providing diverse characteristics that deepen our understanding of controlling the optical response of periodic nanoarrays. These advancements offer substantial potential for applications in medical diagnostics and biotechnology, paving the way for significant improvements.

Future Outlook

The integration of injection-moulded plasmonic biosensors into portable diagnostic devices presents significant opportunities for improving healthcare accessibility, particularly in resource-limited environments. Future research directions should prioritize the following areas:

Multiplexed Detection: Enhancing the biosensor's capacity to simultaneously detect multiple biomarkers, enabling more comprehensive and informative diagnostic outcomes [243].

Microfluidic Integration: Coupling the biosensor with microfluidic platforms to facilitate automated sample processing, minimize reagent consumption, and improve assay precision.

Advanced Surface Functionalization: Investigating robust surface chemistries to increase sensitivity and specificity, while reducing nonspecific adsorption and biofouling.

Clinical Validation: Undertaking extensive clinical studies to establish the biosensor's reliability, reproducibility, and diagnostic accuracy in real-world healthcare settings.

Furthermore, quantum-enhanced biosensing platforms hold considerable promise for pushing the boundaries of detection sensitivity. By leveraging quantum phenomena such as entanglement, coherence, and superposition, these systems may enable detection of single-molecule interactions with unprecedented precision. Recent advances in quantum plasmonics—which explore the coupling between quantum emitters and plasmonic nanostructures—have shown potential to integrate quantum light sources and detectors within biosensor designs, improving signal-to-noise ratios and enabling ultra-sensitive diagnostics.

In conclusion, the injection-moulded, gold-coated nanopillar arrays developed in this thesis demonstrate a pivotal advancement in the development of scalable plasmonic biosensors. Their demonstrated high sensitivity, structural reproducibility, and compatibility with mass production techniques directly address long-standing challenges in translating nanophotonic sensing technologies from laboratory prototypes to commercially viable diagnostic tools. When paired with nanoimprinting—capable of producing high-resolution nanoscale features—this approach offers a robust and cost-effective pathway for fabricating sophisticated biosensor platforms at scale. The convergence of these fabrication strategies not only enhances manufacturing efficiency but also ensures device uniformity, which is critical for clinical reproducibility. As global healthcare systems increasingly pivot towards decentralized and point-of-care testing, such plasmonic devices stand poised to meet the demand for rapid, accurate, and accessible diagnostics. The integration of these platforms into portable instrumentation, coupled with innovations in quantum plasmonics and functional surface engineering, is expected to usher in a new generation of biosensors capable of operating with single-molecule sensitivity and unprecedented precision. Collectively, these developments position the presented plasmonic platform at the forefront of next-generation biosensing technologies, with wide-

ranging implications for biomedical diagnostics, environmental monitoring, and global health.

Appendix

A1 Fabrication of the master stamp

The high-resolution top-down EBL nanofabrication process of the DGPAL is a multi-step process that requires working in a clean room environment and was carried out in the James Watt Nanofabrication Centre at the University of Glasgow.

A1.1 Device cleaning

The substrate chosen for the fabrication of the master stamp is a 4-inch silicon wafer obtained from PI-KEM Limited, UK. Prior to wafer's entry into the fabrication process, its surface must be cleaned to remove any adhering particles and organic/inorganic contaminants. Substrate was ultrasonically cleaned for 5 minutes in the following cleaning sequence: acetone, methanol and isopropyl alcohol (IPA). Ultrasonication was followed by a 5 minute rinse with reverse osmosis (RO) purified water to remove ionic contaminations and blow dried with nitrogen gun. Wafer was then oxygen plasma cleaned in a (GaLa, PlasmaPrep5) barrel asher at 150 W and $3x10^{-1}$ mbar for 5 minutes. In order to further improve adhesion properties needed for the spin-coating of photoresist layer, wafer was dehydrated for an hour in 180 °C oven.

A1.2 Resist spin-coating

The electron beam photoresist used throughout for writing the nanopillar structures was a bi-layer of positive tone polymethyl-methacrylate (PMMA). The combined thickness of both layers was measured to be 250 nm.

Bottom layer was anisole based with 9% solids content PMMA (AP-R 632.09) and molecular weight (MW) of 50K, spun at 5000 rpm for 60 sec, creating a 180 nm thick coating.

The top layer was ethyl lactate based with 2% solids content PMMA (AP-R 679.02) and MW 950K, spun at 4000 rpm for 60 sec, creating a 70 nm thick coating.

The primary objective of the 50K/950K system is to ensure highest level of structural resolution with moderate e-beam exposure doses. The thinner but high in MW resist is the imaging layer providing high resolution. The thicker but low in MW resist is the supportive layer providing the desired undercut profile that facilitates lift-off [244]. The latter is more sensitive to chain scission caused by the incident electron beam, resulting in a larger area of the resist receiving the necessary clearing dose through electron scattering.

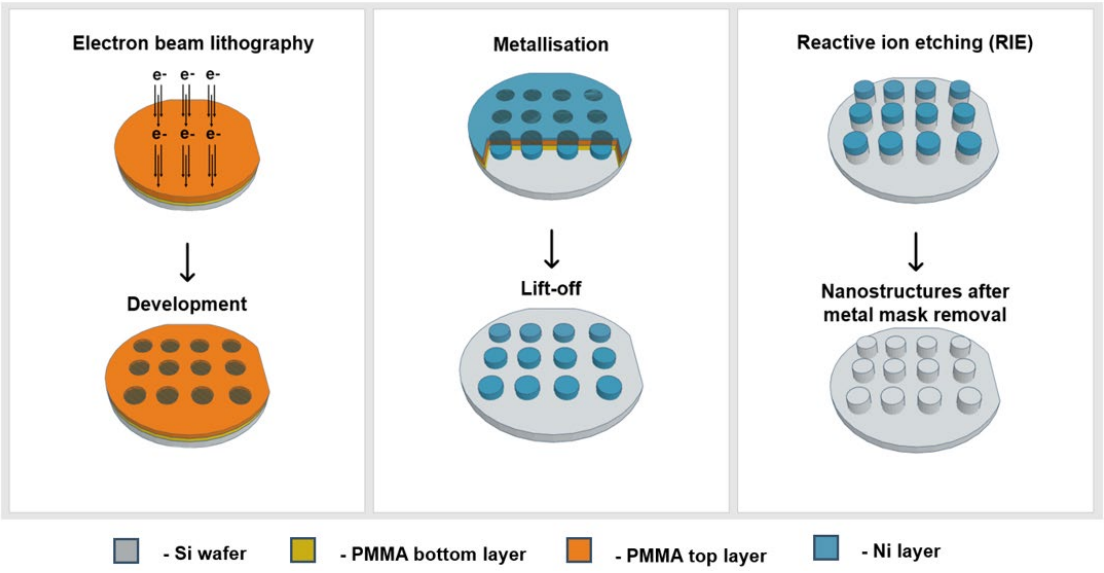

Figure S1 Illustrative diagram summarizing the key steps involved in the fabrication of the master stamp. The process commences with EBL on a positive tone bilayer resist previously spin-coated on a 4 inch Si wafer. A solvent developer is employed to remove the exposed resist material. Thermal evaporation of Ni metalizes the surface and the sample is subjected to a standard lift off process. The remaining Ni mask on the surface facilitates the application of reactive ion etching (RIE) technique to effectively transfer the desired pattern into the bulk Si material. Lastly, the Ni mask is removed in the final stage, completing the master stamp fabrication process.

The thickness of the bottom layer was estimated to be slightly over 3 times the depth of the intended subsequent metal deposition in the succeeding

nanofabrication steps. The thickness of the top layer was aimed to achieve thin profile within a reasonable acceleration speed.

The process of spin coating included covering the wafer with pre-filtered photoresist and spinning it at a pre-defined speed and duration by using a vacuum spinner. After each spinning phase, the back of the wafer was inspected for spill over stains from the resist and carefully cleaned with acetone. This was followed by a 5 minute bake on a 180 °C hotplate to evaporate the resist solvent.

Resist spin-coating signifies the beginning of the multistage process of the master stamp fabrication and a diagram depicting each step of the process is summarized in Figure S1 followed by a detailed description in the following sections.

A1.3 Patterning the resist using EBL

Electron beam lithography is a direct writing technique that uses an accelerated beam of electrons to pattern nanostructures with dimensions down to sub-10 nm size (Figure S2). The pattern is recorded in an electron sensitive film (photoresist) deposited by spin coating prior to exposure. Custom patterns created directly from CAD designs are scanned on the substrate as the highly focussed electron beam induces changes in the structure and solubility of the resist film upon irradiation.

The electron beam column presented in Figure S2-B consists of an electron source or gun at the top, with the most common thermal field emitter ZrO/W. The tip consists of sharpened crystalline tungsten tip with surface coating of zirconia. The electrons generated by the emitter are then focused by electrostatic lens and steer the beam down the axis of the column. Next, we find the blanker that can rapidly turn the beam off and on, zoom condenser lens to allow changes in the current and corresponding beam diameter. The stigmator helps make the beam round, hence producing equal linewidths along various scanned directions. Further down the column are the objective lens to focus the beam on the wafer every time the sample moves, and a deflector to scan the e-beam around within the field.

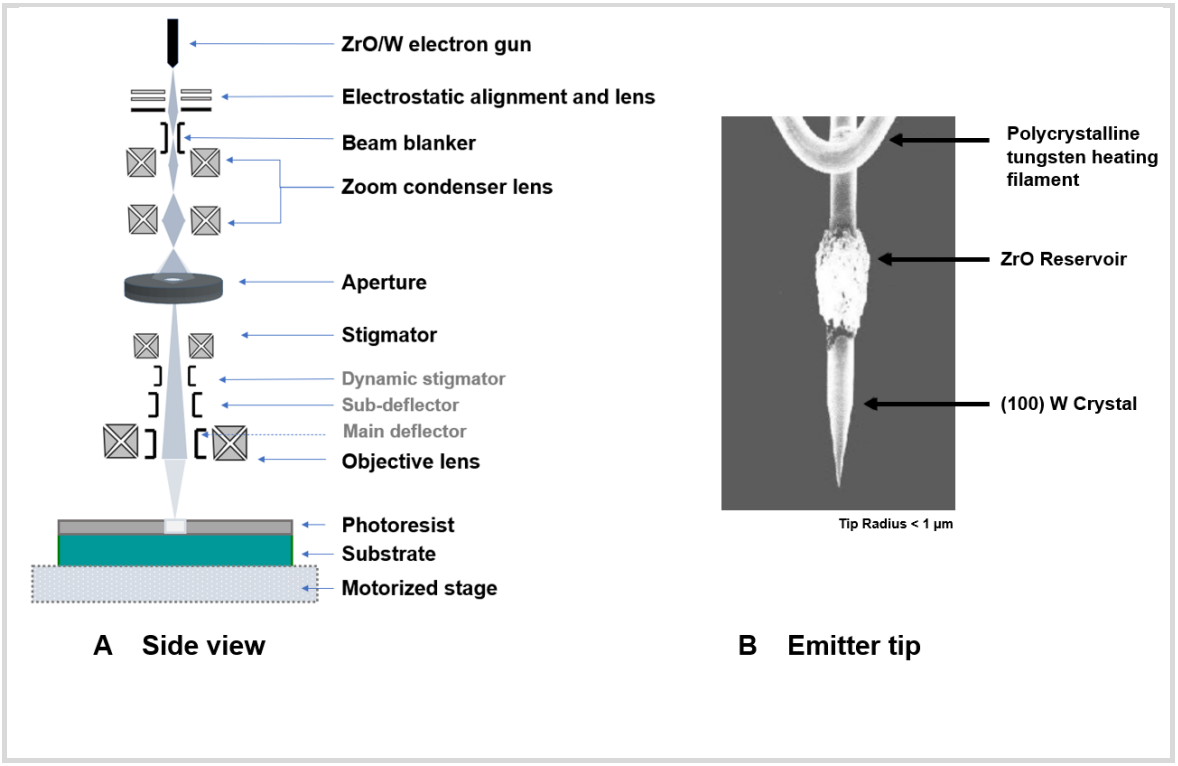

Figure S2 Schematic illustration of electron beam lithography. Electron beam is focused on a resist film to create a pattern by exposing dot by dot: (A) side view of the lithography setup (adapted from [245]); (B) Electron source assembly [245].

The substrate is placed below on a motorized stage preforming accurate positioning and various calibrations. A hight sensor corrects the focus and deflection gain after each stage movement and a laser interferometer measure the position of the stage with an accuracy below one nanometre. The entire optical system is held under vacuum.

EBL patterning of the resist was carried out using two distinct generations of EBL systems. The Vistec VB6 UHR EWF electron beam tool was employed to scan the VB6 sample, whereas the Raith EBPG 5200 was used to pattern the EBPG sample. The Raith EBPG 5200, being a state-of-the-art EBL system, is equipped with advanced calibration capabilities, precise electron optics with minimal errors, and a high-precision electron deflection system. This system produces small spot beams, ensuring excellent beam placement accuracy and pattern fidelity.

A1.4 Pattern development

Upon removal from the beam-writer, the substrate was developed for 75 seconds in a 2.5:1 mix of isopropyl alcohol (IPA) : methyl isobutyl ketone (MIBK) at a

controlled temperature of 23°C. The exposed areas of the positive tone PMMA resist, having undergone polymer scission, are now soluble in the MIBK developer and being washed away. Immersing the substrate in IPA solution for 30 seconds stops development process (Figure S1). Sample is further dried with nitrogen gun and treated with oxygen plasma for 15 seconds at 80 W and $3x10^{-1}$ mbar in a Gala Plasma Prep 5 oxygen barrel asher. This step etches away any undeveloped resist residue at the bottom of the patterned arrays.

A1.5 Metallisation and lift-off

The specimen was coated with a 50 nm layer of nickel (Ni) using either the Plassys MEB 400S or Plassys MEB 550S electron beam evaporation systems (Figure S1). The coating process involved placing the sample in a load-lock chamber, where a powerful 10 keV electron beam vaporized the nickel source material under high-vacuum conditions, allowing precise control over the deposition rate. The rate of evaporation and the thickness of the resulting film were monitored using a quartz crystal's oscillation frequency.

To ensure successful removal of excess material, the thickness of the nickel film was intentionally chosen to be three times smaller than that of the supportive PMMA layer. This approach facilitated a clean lift-off process by soaking the sample in acetone for 3 hours at a temperature of 50 °C in a water bath. When executed correctly, the nickel was selectively deposited in the recessed areas of the patterned features, without interfering with the metal on top. As a result, when the sample was immersed in acetone, the unexposed PMMA layer dissolved, causing the nickel film covering it to detach and wash away easily. Consequently, only the Ni mask deposited directly on the silicon wafer remained on the sample. Conversely, if the lift-off process was not performed accurately and the nickel film was too thick, it would fill the recessed areas and create unwanted connections with the metal on the side walls and top surface. This could lead to protruding metal remnants or unsuccessful removal of the excess material.

A1.6 Reactive-Ion Etching (RIE) of silicon

Reactive ion etching (RIE) is a plasma-based process in which species (radicals, ions) generated by a radiofrequency (RF) discharge are used to remove material

from a substrate. RIE, often called "dry etching," involves the use of plasma generated from gases to chemically react with and physically eliminate material in a controlled manner [246]. This process is employed to transfer a pattern on the surface of a sample into the bulk of the substrate material.

RF power is utilized to excite the plasma, while the substrate being processed is placed on a powered electrode. The powered electrode increases the negative charge on the substrate, promoting ion acceleration and bombardment of its surface.

RIE can achieve highly anisotropic etching by subjecting the substrate to energetic ion bombardment during the plasma-based chemical etching. This results in ions bombarding the substrate surface in a directional manner as they are accelerated towards the negatively biased substrate. Additionally, the chemical activity of reactive species further contributes to high etch rates by simultaneously acting on the substrate surfaces (Figure S1).

In this project, dry etching was performed on a silicon master stamp with a nickel (Ni) mask using the STS ICP (Inductive Charged Plasma) tool. The specific etch conditions were as follows: pressure = 9 mtorr, RF power = 12 W, ICP Power = 450 W, C_4F_8 flow rate = 50 sccm, SF_6 flow rate = 40 sccm.

The etch gases used in this process exhibit a material selectivity, resulting in an etch rate of 80 nm/min on silicon (Si) while showing almost negligible etching towards the Ni mask.

A1.7 Nanostrip process

Nano-Strip® solution is a stabilized formulation of sulfuric acid and hydrogen peroxide compounds. It is a strong oxidizing solution with the capability to remove metals like Ni from surfaces (Figure S1). This solution is highly corrosive to the skin and eyes, and it must be handled with utmost care while wearing appropriate personal protective equipment (PPE).

After being taken out of the STS ICP tool, the substrate was submerged in 100 ml of RO water. Gradually, 10 sets of 10 ml of Nano-Strip® solution were added at intervals of 5 minutes. The nature of the reaction is exothermic, generating heat, and thus the temperature was continuously monitored to ensure it did not exceed 65 °C. The end of the reaction was determined by the absence of bubbles forming on the surface, indicating that the oxidation process was complete. Subsequently, the sample was rinsed in RO water for 5 minutes and dried using a nitrogen gun.

The completion of the nanostrip process signifies the end of the nanofabrication procedure for the master stamp. The next step involves transferring the pattern from the master stamp to a (polyethylene terephthalate) PET foil. This PET foil will be utilized as an inlay during the injection moulding technique, making the successful fabrication of the inlay critically important.

However, before proceeding with a detailed description of the pattern transfer process it is critically important to focus our attention on the outcome of the master stamp fabrication. A thorough morphological comparison is created in section 2.2.2 summarizing the output from the VB6 master stamp nanofabrication and the much more optimized EBPG sample.

A2 Fabrication of the inlay

The fabrication of the inlay process from a DGPAL master stamp is done via UV nanoimprint lithography (UV-NIL) that requires working in a clean room environment and was carried out in the James Watt Nanofabrication Centre at the University of Glasgow.

Nanoimprint lithography (NIL) is a technique [247] based on surface structuring with a template consisting of topographic patterns. The UV-based approach relies on photo-curable resist, wherein UV-light exposure initiates cross-linking. The typical procedure for soft UV-NIL entails coating the master stamp with a UV-curable resist through spin coating, subsequently bringing it into contact with a PET foil and UV-curing the assembly (Figure S3). The UV exposure-induced curing is feasible due to the transparent nature of both the soft working stamp and the PET film, facilitating the penetration of UV light and activation of cross-linking

reactions [248]. Ultimately, the working stamp and PET foil are separated from the master stamp, resulting in a negative replica of the topography preserved on the master stamp surface.

To ensure the successful and uniform implementation of the UV-NIL process, the EVG®6200 (EV Group GmbH, Austria) tool was employed.

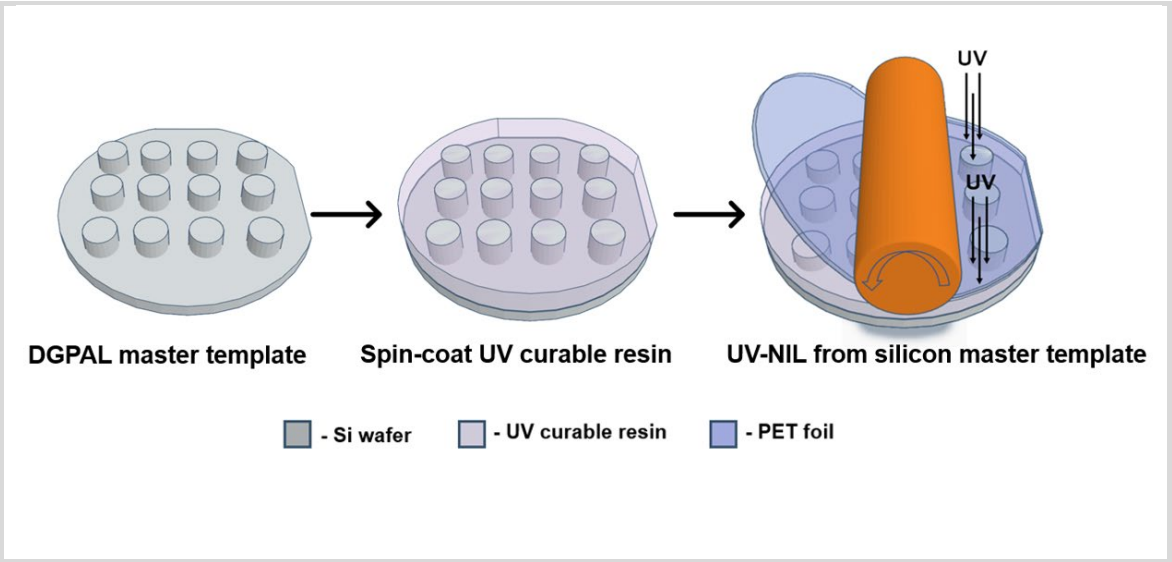

Figure S3 Schematic diagram of the UV-nanoimprint lithography process (UV-NIL) commencing with a clean nanopatterned template, followed by spin-coating of the SmartNIL material set and finishing the process by ensuring perfect alignment and adhesion with the PET foil as well as uniform parallel UV light curing of the working stamp.

A2.1 Master stamp cleaning

Before the master stamp can undergo the pattern transfer process, its surface needs to be cleaned thoroughly to eliminate any particles and organic/inorganic contaminants. The substrate was subjected to ultrasonic cleaning for 5 minutes using the following sequence of cleaning solutions: acetone, methanol, and isopropyl alcohol (IPA). After ultrasonication, the substrate was rinsed for 5 minutes with reverse osmosis (RO) purified water to remove any ionic contaminants and then dried with a nitrogen gun. Next, the wafer underwent oxygen plasma cleaning in a (GaLa, PlasmaPrep5) barrel asher, operating at 150 W and 3x10-1 mbar for 3 minutes. To enhance the adhesion properties necessary for the spin-coating of the soft stamp material, the wafer was dehydrated in a 180 °C oven for 15 minutes.

A2.2 Spinning soft stamp material

The soft stamp material comprises a triad of solutions collectively known as EVG SmartNIL technology. The SmartNIL is a full-field imprint technology providing a powerful next-generation lithography capability. The technology incorporates multiple-use soft stamp processing of the master template which extends its operational lifespan and positions UV-NIL as advanced, high-performance, cost-efficient approach enabling nano-scale patterns on large areas.

The initial solution applied on the master template after cleaning is the Anti-Sticking Layer (ASL). Cleaning the surface would greatly improve the adhesion of the resist to the wafer surface while the adhesion of the cured resist to the stamp surface must be as low as possible. The ASL is a fluorinated chemical acting as a surface release agent which ensures remarkably effortless detachment of the cured resist from the patterned template.

The second solution in this set serves the dual purpose of rinsing off excess ASL from the surface while achieving quickly surface hydrophobicity and acting as an edge bead removal (EBR) agent. Edge bead phenomenon appears during spin-coating when material tends to accumulate along the edges of the substrate, forming a ridge or bead also referred to as the “coffee ring effect”. To achieve high resolution and high aspect ratio features in contact lithography it is necessary to have both interfacing substrates in uniform proximity throughout the full area. However, the presence of edge beads on the wafer's edge impedes this uniformity and can measure multiples of the nominal resist thickness. Chemically wiping off the edge bead can be reliably achieved by an EBR solvent.

The third solution in the set is the soft stamp material used for casting and curing. Among the most commonly used materials is polydimethylsiloxane (PDMS), which exhibits excellent optical transparency to UV-NIL wavelengths with a low surface energy facilitating easy separation from the stamp template.

The nanoimprint lithography for VB6 sample and EBPG sample was performed with soft stamp material set SmartNIL.1 and SmartNIL.2 respectively. The following section describes the process flow for the spin-coat application of each material set.

The process flow for spin-coating SmartNIL.1 onto the VB6 sample master stamp involves several sequential steps. The cleaned master stamp wafer is positioned in a spinner, and the Anti-Sticking Layer 1 (ASL1) solution is statically dispensed as a puddle, completely covering the surface. Following a brief delay of 30 seconds, the ASL1 solution is spun at a speed of 2000 rpm for 30 seconds. Subsequently, a rinse with HFE solvent is performed at the same speed for 30 seconds. Finally, the working stamp is applied and spun for an extended duration of 300 seconds at a speed of 3000 rpm to ensure proper coating.

As for the process flow for spin-coating SmartNIL.2 on the EBPG sample master stamp, it comprises the following steps: The cleaned master stamp wafer is placed in a spinner followed by static dispense of ASL2 (2-Methoxy-1-Methylethyl Acetate) as a puddle covering the surface and immediately spun for 60 seconds at 800 rpm. The back of the wafer is carefully cleaned to remove any potential contamination and then placed on a hotplate at 200 °C for 75 seconds. Following this, the wafer is allowed to cool for 60 seconds before being reloaded into the spinner. For edge bead removal, the propylene glycol monomethyl ether acetate (PGMEA) solution is continuously dispensed through the spinner's lid opening while the spinner rotates at 500 rpm for 30 seconds. Once the duration time elapses, the spinner accelerates to 3000 rpm for an additional 20 seconds to achieve surface spin drying. Subsequently, the soft stamp material is applied for a duration of 300 seconds at a speed of 4000 rpm, ensuring a thin and uniform spread of the material.

Several significant distinctions were observed between the two sets of SmartNIL materials. In order to achieve repetitive UV-NIL using a single master template, it is necessary to repeat the spin-coating process with each run when employing SmartNIL.1. Furthermore, following the predetermined duration and timing of the spin-coating procedure, the film often experiences tearing and reveals patches on the surface devoid of coverage, a phenomenon known as "de-wetting." Lastly, upon completion of the curing process, cross-linked stamp material is frequently found on the surface, indicating the requirement for further template cleaning.

Conversely, the enhanced formulation of SmartNIL.2 necessitates only a single application of the ASL2 for the surface to be prepared for multiple UV-NIL processes. The thin film of the working stamp exhibits commendable resilience

even during prolonged spinning runs, even at higher speeds. The occurrence of film retraction from the edges, or "de-wetting," is not observed in this case.

The improved SmartNIL.2 formulation and the accuracy of the process flow application significantly improved the feature resolution and the inlay fabrication process.

A2.3 EVG 6200 Nanoimprint lithography tool

After the application of the working stamp on the surface, the next important step is to ensure full field contact of the wafer and the PET foil in a controlled way avoiding air encapsulation prior UV exposure. This becomes possible with the EVG6200NT semi-automated contact photolithographic alignment and exposure tool with a 1000 Watt light source ideal for thin and thick resist exposure (Figure S4-A). The tool utilizes a robust, high-power lamp house that ensures consistency of parallel and uniform UV light across the substrate surface which underpins the reliability and accuracy of the lithographic process, enabling precise replication of the nanopatterned arrays.

A detailed illustration of the lamp house operation is presented in Figure S4-A, where:

4. Following ignition, the ellipsoid mirror redirects the UV radiation towards a dielectric mirror.

5. Infrared (IR) radiation passes through, with heated air remaining confined within the exhaust.

6. The dielectric mirror then reflects the specified wavelengths of the UV towards the fly eye. This component, the fly eye, transforms the UV light from a non-uniform to a uniform irradiance distribution.

7. A deflection mirror then redirects the UV radiation toward the front lens. Apertures installed within the path light serve to reduce stray light in the lamp house.

Finally, a plan convex lens collimates the UV radiation onto the substrate, delivering parallel and uniform light.

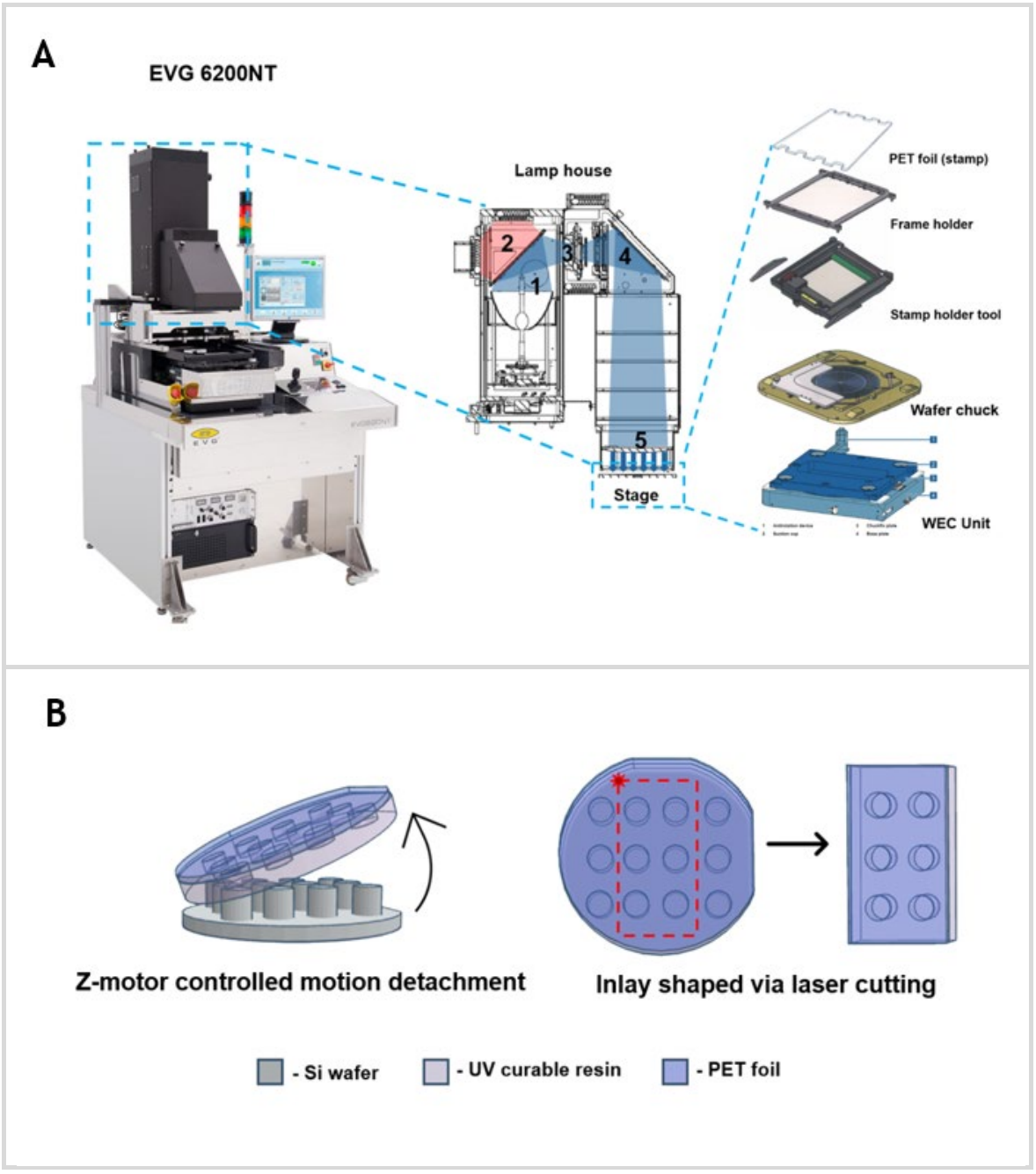

Figure S4 Panel A - Schematic diagram of EVG 6200NT key components. From left to right are shown an image of the tool installed in JWNC, the location of the lamp house and a schematic diagram of the UV light path creating a uniform parallel exposure over the stage, following are the stage components holding the stamp, the master template (wafer) and the WEC (wedge error compensation) unit. Panel B – unloading the stamp and the wafer after motor controlled detachment is creating a separation gap and laser cutting the inlay.

The evenly distributed UV light floods the stage encompassing several integral components. As depicted in Figure S4-A, a PET foil previously shaped via laser

cutting into a 16 x 20.8 cm sheet with ridged edges is screwed onto a frame holder to attain perfectly flat position.

The frame holder is installed in the stamp holder tool which is electrically powered and navigates a roller across the foil subsequent to the wedge error compensation process. This ensures comprehensive field contact and impeccable adherence between the stamp and the template (Figure S4-A).

Below this arrangement, there lies a vacuum-based wafer chuck, which securely holds the 4-inch wafer that has previously undergone treatment with working stamp materials. Subjacent to the wafer chuck, one finds the Wedge Error Compensation (WEC) unit, a vital component in improving the alignment between the substrate and the imprinting mold. This system assures a parallel contact between the mold and the substrate, thereby guaranteeing consistent imprinting across the entire substrate surface.

The exposure routines can be pre-written and saved as recipes by a user-friendly software interface. The intuitive graphical interface supports swift navigation through process sequences, with real-time monitoring and control capabilities.

The operational conditions, as outlined in the recipe employed for the UV-NIL process, adhere to the recommendations specified in the user manual. The process commences with a UV pre-exposure duration of 10 seconds targeting the PET sheet. Following this pre-exposure, the protective foil located at the back of the sheet is detached, and the contact with the resin-coated wafer is initiated.

The full field contact of the wafer and the PET sheet uses 1250 mbar contact force for the process, 500 mbar during the WEC phase and maintains 1250 mbar during the 300 seconds UV light exposure. The contact force is used to support the cover unit which houses the stamp holder tool, utilizing air pressure. A lower pressure during the WEC sequence is recommended. This increases the contact force. Conversely, a higher pressure during the exposure phase is advised, as this minimizes the contact force between the mask and the substrate. The separation parameter, set at 1000 µm with a proximity of 995 µm, is implemented for a wafer substrate thickness of 0.5 mm. Herein, the separation parameter signifies the

distance maintained during the alignment process step, while proximity characterize the distance during the exposure sequence.

After the exposure duration is over, a Z-motor moves the cover unit up allowing a predefined separation distance between the stamp and the wafer to be reached (Figure S4-B). This would enable for the stamp and wafer to be unloaded. The stamp is then shaped as a 25 x 75 mm inlay resembling the dimensions of a standard microscope slide via the Full Spectrum laser cutting instrument (USA) (Figure S4-B). The lase cutter has a 40 W CO_2 laser emitting a powerful beam of light. Thus, the cutting was performed with power of 18 and speed of the laser head fixed to 95 which ensured cutting the inlay within a single pass.

A3 Injection moulding

The nanofabrication process of the DGPAL was adapted to a high-throughput replication approach i.e., injection moulding.

Injection moulding is one of the most efficient technologies in modern manufacturing due to its unique combination of precision, scalability, and versatility [249]. This process involves the injection of molten plastic into a mold, which upon cooling, takes the shape of the desired product. The method's efficacy lies in its ability to produce large quantities of complex shapes with remarkable repeatability, minimizing variances and wastage. Further, its adaptability to a wide range of thermoplastic polymers and composites has enabled its broad application across industries, including medical devices, automotive components, and consumer electronics [250]. Critical to the moulding process's success is the careful control of temperature, pressure, and cooling time, each playing a pivotal role in the final product's mechanical properties, dimensional accuracy, and aesthetic quality. Consequently, injection moulding is not only a sophisticated industrial practice, but it also plays an integral role in scientific research, advancing our understanding of materials science, nanostructured surfaces, cell and tissue engineering, microfluidic devices, sophisticated robotic systems, etc. This underpins its status as an indispensable technology in the realm of modern manufacturing, driving innovation and efficiency on a global scale [251].

A3.1 Injection moulding process

Within the context of the injection moulding procedure, a specific thermoplastic polymer is heated, generally around 100°C above its designated glass transition temperature (Tg) before it is injected into the mould cavity. The low viscosity of the molten polymer allows complete filling of the mould until the material is cooled below the freezing point. Subsequently, the polymer undergoes a cooling phase until it solidifies. Upon solidification, the mold is uncoupled, and the fully formed component is ejected. As a result, the procedure is reiterated to manufacture subsequent parts, functioning in an entirely autonomous and unsupervised manner. This high degree of automation and lack of necessary supervision culminate in a cost-effective methodology for mass production.

To ensure the successful and uniform implementation of the injection moulding process, the Engel Victory 28 (ENGEL GmbH, Austria) tool was employed.

The essential mechanisms of injection moulding are heat transfer and pressure flow [252]. It all happens in the 2 main components of the injection moulding machine and an image with a schematic diagram of the Engel Victory 28 are depicted in Figure S5:

1. Injection unit – generate a uniform and homogeneous melt by heating the plastic material and inject it into the mold under controlled conditions of pressure and flow rate. Its functionality extends to the consistent and precise feeding, preparation, and dosing of the material, subsequently facilitating the injection of a predetermined volume of the material into the mold tool under high pressure.

   The injection unit consists of several integral segments: the hopper and feed throat section, the screw mechanism, and the injection nozzle. A typical operating sequence starts with the feeding of the material channelled from a hopper, usually in the form of pellets, transitions the throat section and advanced towards the screw section. This is where the material gets homogenously mixed with the screw oriented in a forward stance. The screw's rotation induces plasticization of the material, propelling it along the screw barrel. The consequent accumulation of

molten material at the screw's forefront triggers its backward motion. Once the injection command is issued, the screw propels forwards, pushing the material from the unit through the nozzle and into the mold.

Several operational parameters are intrinsically tied to the injection unit's functions. These encompass the regulation of melt temperature, the accurate definition of the shot volume, modulation of the injection velocity, and the screw's mixing speed, denoted by its back pressure. Upon the harmonization of these parameters at their predetermined thresholds, the plastic substrate is navigated through the injection nozzle. In terms of flexibility, the injection unit's carriage can either be positioned directly atop the sprue during the injection phase or be retracted during processes like dosing or purging when required necessary.

2. Clamping unit - The clamping mechanism is one of the most critical factors when producing high-quality products through injection moulding. The function of the clamp unit is the methodical opening and closing of the mold halves, and most critically, ensuring the mold securely retains closed during the infusion of the molten plastic. Due to the intrinsic high viscosity of plastic melts, there's a requirement for substantial injection pressures.

   Consequently, the force necessary to keep the mold closed under such conditions is considerable. It is the task of clamping mechanisms to counterbalance the internal pressures generated during the injection of the molten plastic, ensuring the mold remains tightly sealed. Thus, it is imperative for the clamping pressure to be strategically configured to exceed the injection pressure, mitigating the risk of the mold inadvertently opening during the process.

Regardless of specific design variations, clamping units universally comprise a stationary, or fixed, platen and its counterpart, the moving platen. The fixed platen is mounted rigidly on the machine base and is positioned proximal to the nozzle of the injection unit. The injection half of the mold is attached to the fixed platen while the moving platen is associated with the ejection half of the mold. Hence, the components of the clamping unit are commonly denoted as the "fixed and moving mold halves" as generic descriptors.

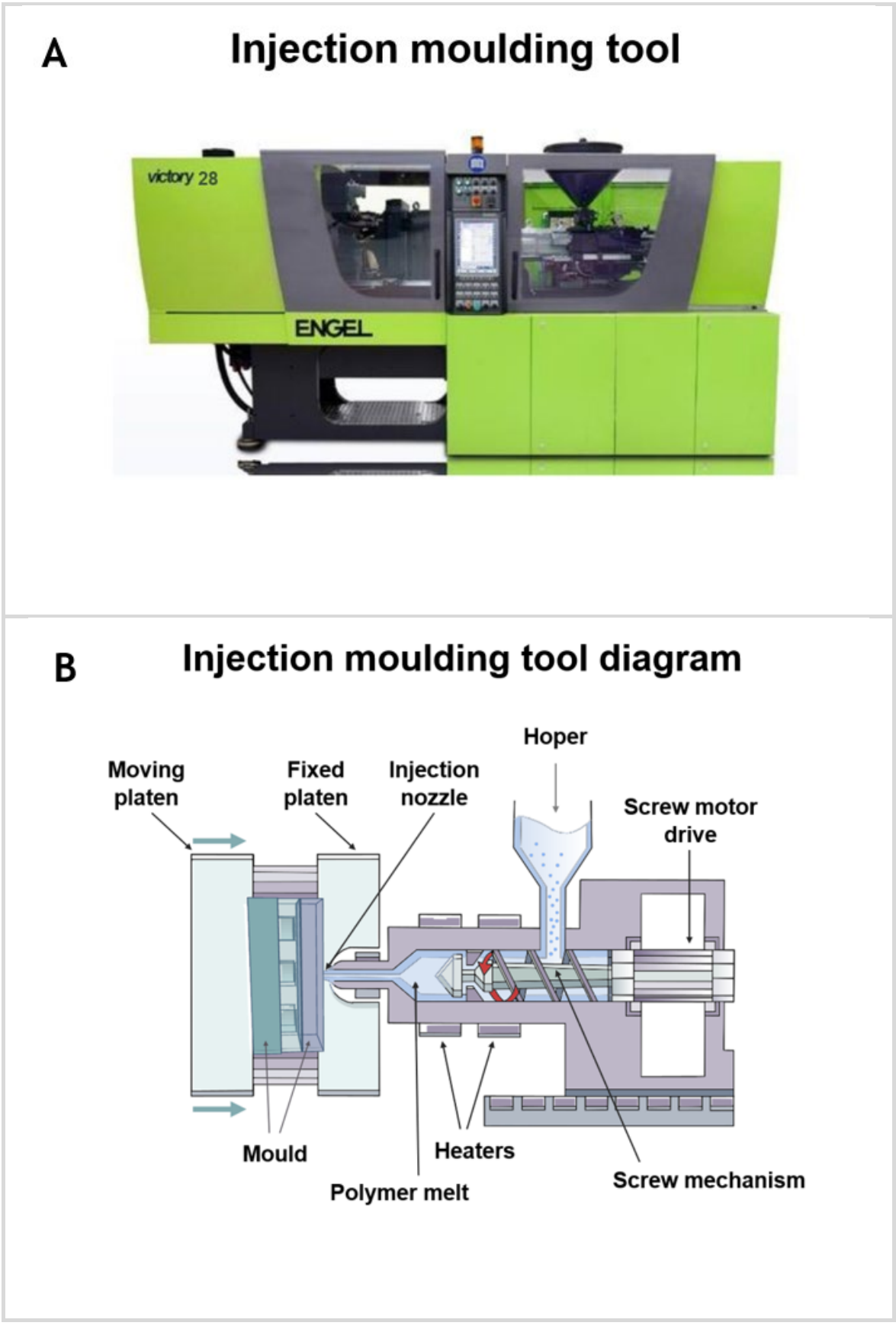

Figure S5 Panel A - presents the Engel Victory 28 injection moulding tool, while Panel B - illustrates a schematic diagram of the instrument, highlighting its principal components. The injection unit encompasses the hopper, screw mechanism with heaters, and the injection nozzle. The clamping unit, on the other hand, consists of the fixed and moving platens, as well as the frame tool that secures the inlay where the moulding process takes place.

The mold assembly happens when the "fixed and moving mold halves" are in their closed position comprising the mold which is a hollow metal block into which molten plastic is injected to from a certain fixed shape. To maintain precise temperature control, the block is perforated with various channels that accommodate hot water, oil, or distinct heating mechanisms.

The interface where the fixed and moving plates meet is referred to as the parting line. Liquefied plastic is introduced into the mold via a sprue, progressing to fill the cavities through the utilization of runners and gates. Post the cooling phase, the mold is separated. The ejector rod of the injection moulding machine pushes the ejector plate of the mold ensuring the effective ejection of mouldings.

In this project, injection moulding was performed on the Engel Victory 28 using polystyrene (PS) polymer. PS is a low cost, low density thermoplastic with high transparency and mechanical strength that also holds biocompatibility grade.

The specific injection moulding conditions were as follows: melt temperature = 260°C, tool temperature 30°C, injection speed = 10 cm^3, injection pressure = 1500 bar, holding pressure = 400 bar, holding time = 6 seconds, cooling time = 25 seconds.

A4 Finite Element Modelling (FEM)

The content presented in section 3.3 is carried out and generously shared by Dr Ramesh Ghosh, who was engaged to support the progress of the project and is affiliated with the North-West Centre for Advanced Manufacturing (NWCAM) supercluster.

A4.1 COMSOL model

Utilizing the power of computational modelling and simulation tools can reveal significant information over the intricate electromagnetic distribution of

nanoarrays with different geometries. A 3D frequency domain model in COMSOL 4.3b was employed for the finite element analysis (FEA). Implementing the finite element method begins with constructing the geometry of the simulation domain. The PS nanopillar cell unit with the corresponding gold layer domain boundaries are defined. The periodic conditions are also applied assuming the nanopillar array system is in ordered, periodic array that extends infinitely in the x and y direction. This step also includes defining the properties of the present materials - gold, water, and polystyrene. Material properties are assigned with their characteristic permittivity, permeability, refractive indices.

As the accuracy of the FEM depends on the number of discrete elements over which equations are solved, suitable mesh sizes were required to efficiently simulate the optical behaviour within the system. Different mesh sizes were chosen for each media, with a maximum mesh size of 15 nm for the Au as well as PS NP region. Maxwell's equations are then applied to each element, with the material properties considered. Maxwell's differential EM equations are further transformed into simpler to solve approximate solutions. A piecewise interpolation is employed to combine the integral equations with shape functions. The contribution of all elements is assembled to obtain a linear system of equations for the whole simulation domain and after analysing results information for the EM field strength is revealed.

The system consists of a unit cell as schematically shown in Figure S6-A. Transverse Electric (TE) - polarised light (wavelength 520-850 nm) enters normally through a port condition from the bottom (port 1) to the top (port 2) of the cell as shown in Figure S6-A(a). Periodic Floquet-Bloch boundary conditions were used at the sides of the unit cell. This condition assumes that the model is infinitely large, and the designed unit cell is repeating periodically in the plane of the gold thin film.

Transmission (T) through the setup is measured using port parameters of the unit cell and the extinction (E) spectra are determined through the relation:

$E = -\log_{10}(T)$.

Typically, above the nanostructure and within the nanopillar the domains are simulated as water and polystyrene with RI and permittivity values chosen accordingly. After probe measurement, the transmitted light is absorbed through a perfectly matched layer (PML) to prevent reflections back into the system. The top and bottom Au layer on PS NP were chosen as 60 nm, while the sidewall thickness was 6 nm, respectively, as shown in Figure S6-A(b).

The approximation estimate for the sidewall thickness of gold is presented in the subsequent section.

A4.2 Gold deposition on nanopillar sidewalls approximation

The gold deposition on the PS NPs is the plasmonically active layer providing the nanostructures with their characteristic resonance. As discussed previously, the gold thermal evaporation process is directional and facilitated by a rotating holder to ensure uniformity.

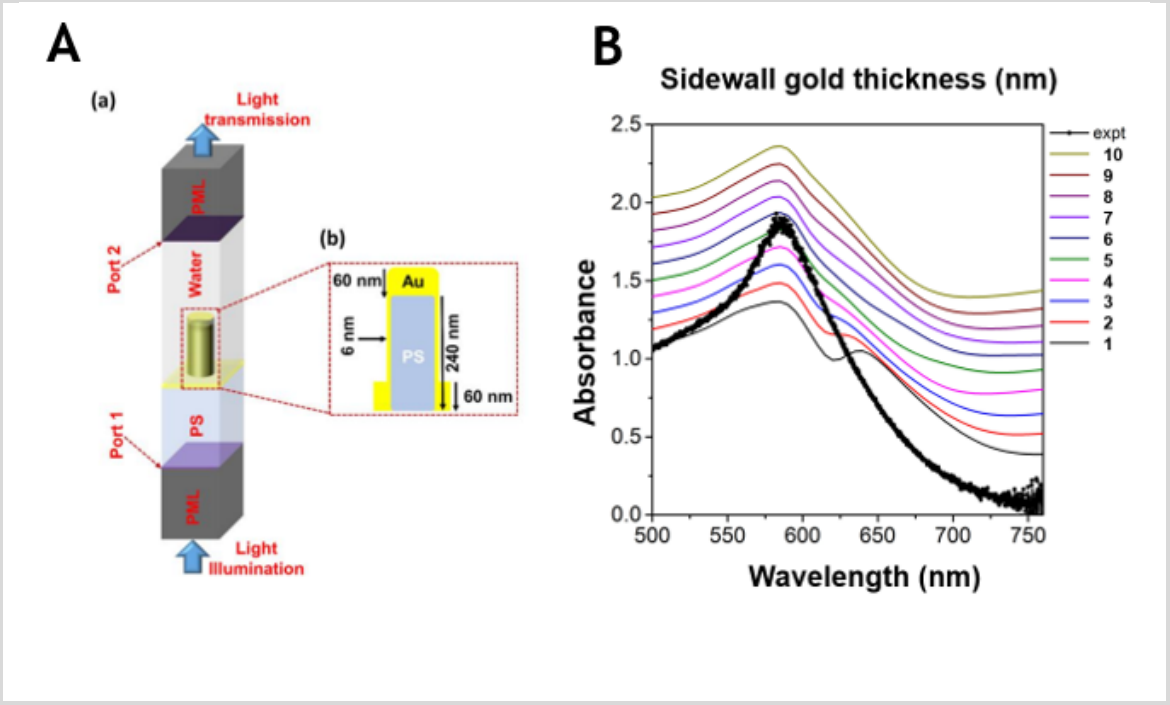

Figure S6 Panel A - (a) Schematic of the geometrical configuration of a unit cell constructed in the COMSOL model. (b) The enlarged view of the selected region showing the 60 nm Au-coated PS NP in YZ plane. Panel B - resonance simulations of gold-coated NP arrays with a unit cell of a nanopillar with diameter 160 nm, height of 240 nm and spaced with a period of 280 nm. Gold deposition is specified as 60 nm on top and bottom of the structure with varying thickness of the sidewall thickness within the range of 1-10 nm. To verify the model, simulated resonances are overlayed with the experimental result. Sidewall thickness of 6 nm is taken as the most appropriate fit for the unit cell.

However, this methodology leads to a thicker deposition of gold on the top and bottom surfaces of the nanopillars compared to their sidewalls. Consequently, the thickness of gold on the NP sidewalls is notably less than the intended coating but was not empirically examined.

To emulate the simulation conditions accurately, the uniformity of metal thickness around all sides of the nanopillar unit cell is crucial for model precision. Utilizing extensive experimental resonance data obtained from NP arrays, we validated the simulation outcomes by adjusting the sidewall thickness within a range of 1 nm to 10 nm of gold coating and compared it against empirical findings (Figure S6-B).

The simulation outcomes confirm that a nanopillar array, characterized by a NP unit cell featuring dimensions of 160 nm in diameter, 240 nm in height, spaced with a 280 nm period, and a 60 nm gold coating on the top and bottom surfaces, resonates comparably with the experimental nanoarray when the sidewall gold thickness is 6 nm.

A4.3 COMSOL model validation

To determine the validity of the COMSOL model a cross-sectional data encompassing both gradients within the DGPAL was simulated and compared with the experimental results taken in water medium (Figure S7).

The first gradient investigates nanopillars with same size but varying interspacing between them resulting in simulated nanoarrays featuring a consistent diameter of 160 nm and a range of lateral gap sizes between 80-270 nm presented in Figure S7-A.

Conversely, the second gradient investigated the impact of varying diameters while maintaining a constant gap size, resulting in simulated nanoarrays with diameters ranging from 120 nm to 310 nm and a consistent gap size of 190 nm (depicted in Figure S7-B).

The comparative analysis demonstrates precise predictions of the emergent LSPR and SPP modes, indicating a robust correlation between the simulation model and experimental findings.

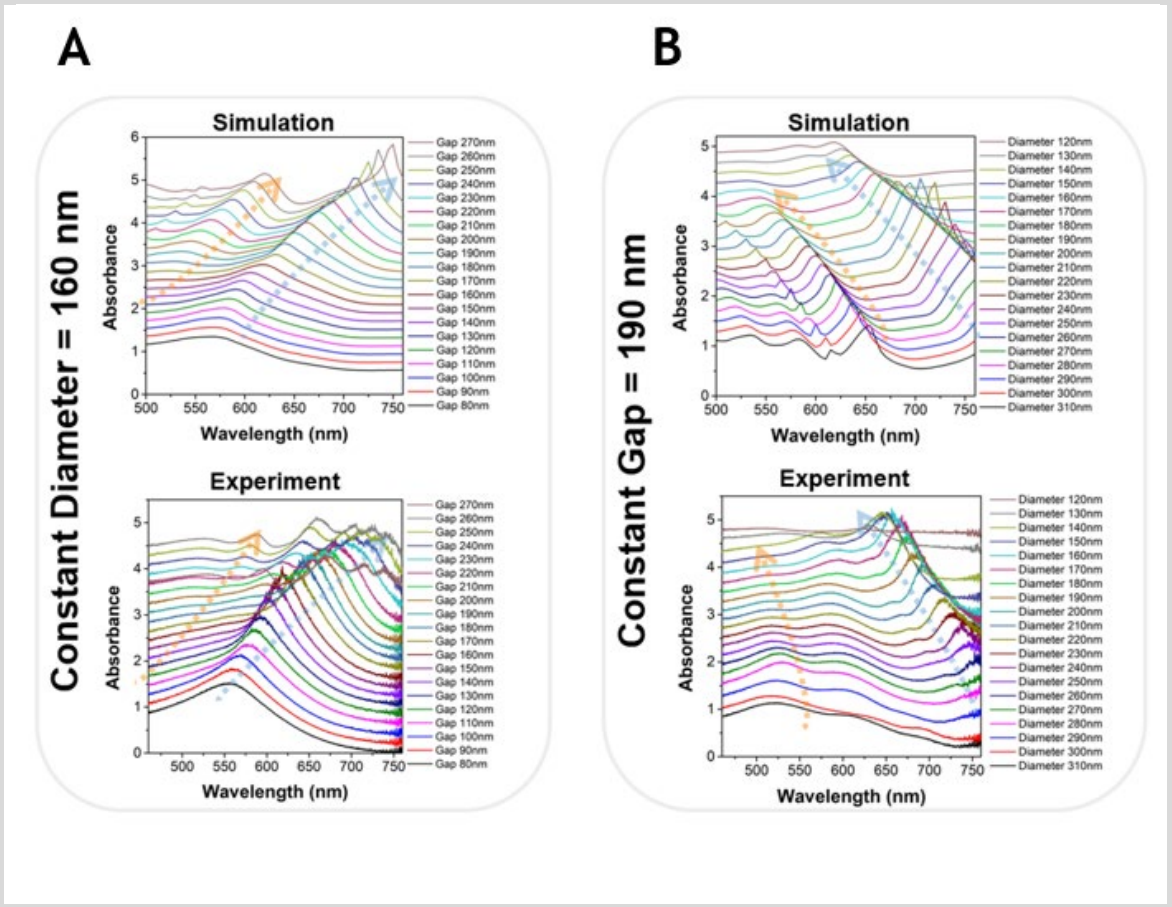

Figure S7 Comparison between simulated data and experimental data of resonance signals in water RI 1.333. Panel A – compare datasets when nanoarrays feature constant diameter and varying gap size. Panel B – compare datasets when nanoarrays feature constant gap and varying diameter size. Blue arrows display the resonance shifts of LSPR mode, while orange arrows depict SPP mode.

A4.4 Electromagnetic field dissipation

Consequently, after validating the simulation model the electromagnetic field decay was investigated, with particular interest over the nanoarrays representative for Mode 1 and Mode 2 type of oscillations. In order to demonstrate the diverse optical responses of the double gradient plasmonic library, simulation models were provided for both orthogonal gradients. Figure S8-A(a) illustrates the electromagnetic field dissipation for nanoarrays with constant gap size and varying diameter sizes within the range 120 nm – 280 nm. From the simulation results it becomes evident that the lateral enhancement of the electric field is dependent on the size of the plasmonic optical antenna. There is a significant difference

between the electric field coverage of 280 nm wide nanopillar and a 120 nm wide one. The large diameters reach more than 100 nm extended electric fields where the small sizes operate with less than 20 nm field decay. Additionally, the diameter size also influences the amplitude of the electric field enhancement. The electric field power of the 280 nm diameter is six times higher than the 120 nm diameter nanopillar. The simulation results for 280 nm diameter strictly aligns with the definition of coupled SPPs leading to longitudinal surface charge density oscillations that propagate along the surface and to an electromagnetic field with an amplitude that decays evanescently away from the interface. On the other hand, the electric field decay of the 120 nm diameter depicts the non-propagating electric confinement of light creating intense local fields.

Figure S8-A(b) illustrates the other orthogonal gradient where nanoarrays are with constant diameter and varying gap sizes within the range 100 nm – 220 nm. In this case the amplitude is not influenced much but the lateral enhancement is significantly higher for wider interspacing than the narrow ones.

The narrow lateral gap on the other hand predisposes coupling of the electric fields with neighbouring nanopillars leading to constructive interferences. This increases the extinction cross-section of a nanopillar and ultimately increase the sensitivity efficiency of the nanoarray.
Apart from the predominant SPP and pure LSPR modes, different array configurations in between the gradient exhibit the mixed SPP/LSPR optical resonances. Utilization of SPP and LSPR in plasmonic nanostructures is the key to overcoming the scattering/absorption trade-off.

Figure S8-B illustrates the XZ-plane cross-section of nanopillars exhibiting absorbance maxima due to the constructive interference between the SPP and the LSPR modes. Figure S8-B-a), illustrates the total resonance enhancement and the matching simulated signal and its deconvoluted peaks, visualizing the harmonic coupling between the SPP and LSPR. The resulting normalized EM field distribution in Figure S8-B-b shows that at wavelength 530 nm, the incident light is coupling with the SPP, which subsequently launches a propagating optical mode in the gold nanopillar.

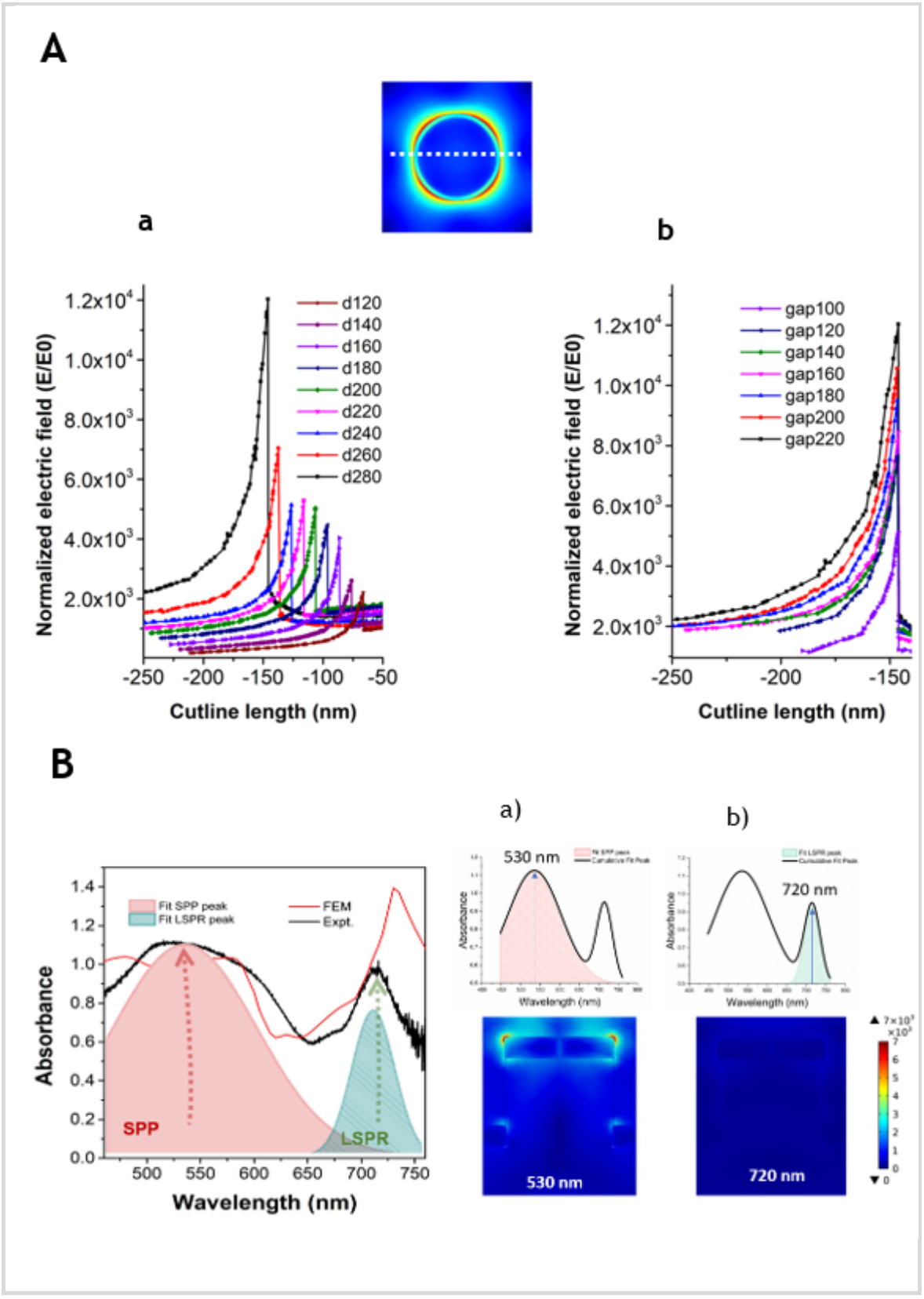

Figure S8 – Panel A illustrates the electric field distribution at the upper rim of the unit cell in multiple nanoarray geometries, coated with 80 nm gold layer. Panel B - by comparing the graphs shown in (a) and in (b), it can be observed that SPP occurs throughout the continues thin film, while LSPR occurs at film discontinuity boundaries with sharp edges. Plot B - (c) demonstrates the deconvoluted resonance signal depicting the interference between the SPP and LSPR modes.

The propagating resonance is turning the cylindrical nanostructure into a miniature ‘optical fibre’ increasing the light absorption. At 720 nm wavelength the model illustrates the emerging hotspots of highly confined energy around the outer rim of the nanopillar top.

A5 Nicoya OpenSPR -hardware and software

The system will first take a dark spectrum with the LED off. Immediately after the dark reference is taken, the LED will automatically switch on and the software will capture the bright reference. On the screen the bright reference is the peak signal while the dark reference is the flat line at the bottom.

Once the sensor is successfully loaded and a test is initiated, the software introduces the user to the experiment data interface facilitating data acquisition Figure S10-C. The real-time data will begin streaming into the graph as a line representing the data collected from the flow channel. During a test, the flow rate controls the interaction time of a sample injection with the sensor surface and the speed can be adapted within the range 5-200 µl/min. The interaction time can be calculated with the following formula:

$$Sample\ interaction\ time\ (min) = \frac{Sample\ loop\ volume\ (\mu l)}{\text{Flow rate}\ (\mu l/\text{min})} \qquad (5)$$

The standard sample loop of the OpenSPR instrument is 100 µl in volume. The minimum injection volume for a 100 µl sample loop is 150 µl. When an injection is made through the injection port, the sample name and the concentration of the liquid is entered. By doing so, the labels of all samples interfacing the sensor surface will be indicated in the sensogram and after test completion can be easily identified during the data analysis. The exact time when the injection content start interacting with the sensor within the flow cell and exact time when it finishes are outlined on the response curve. After the injection is complete, the sample will be replaced with running buffer. A build-in immobilization wizard facilitating ligand immobilization on the surface ensure the recommended procedures for surface conditioning and surface activation are followed in order to achieve optimal immobilization target level.

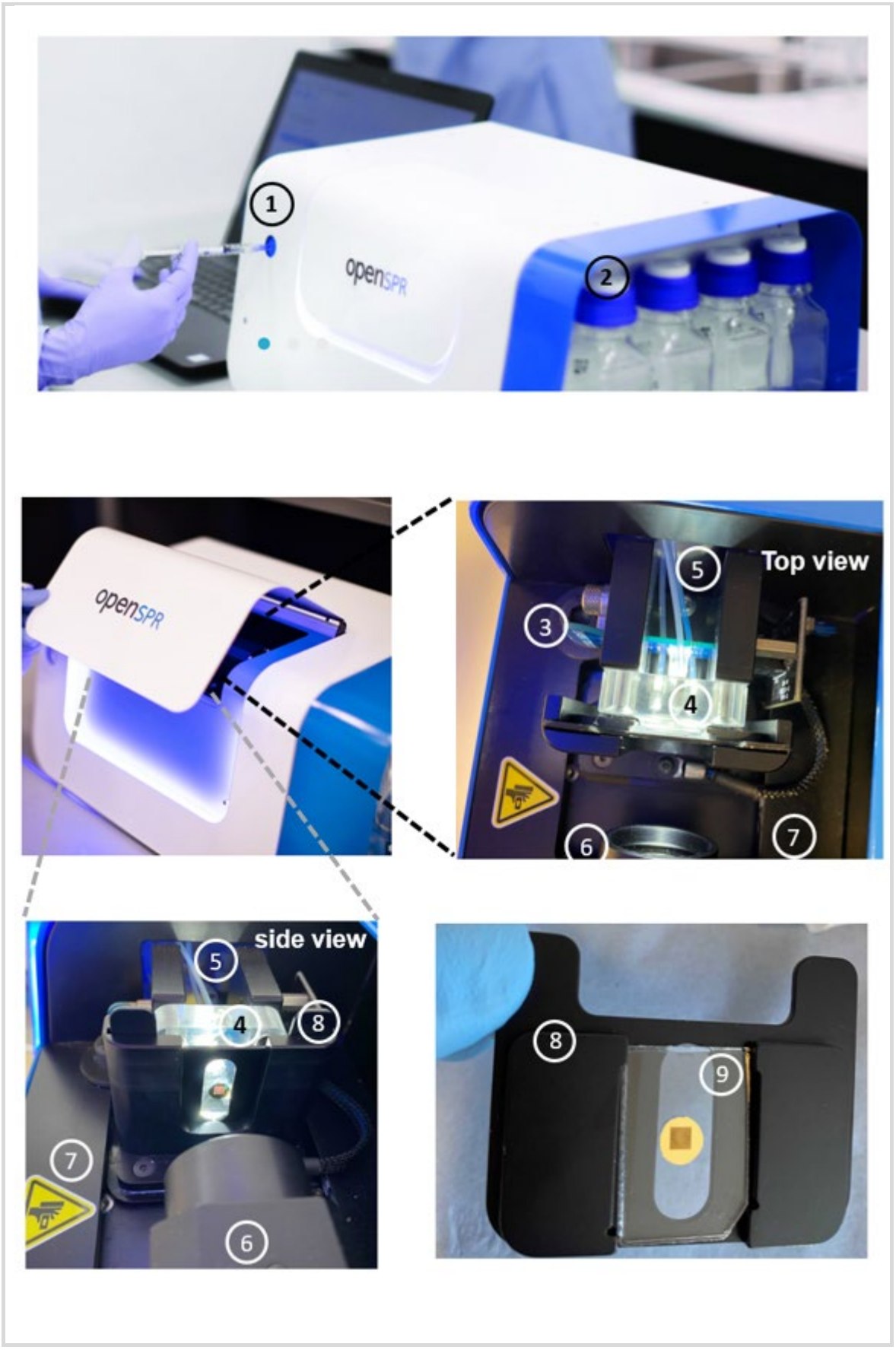

Figure S9 Nicoya Open SPR benchtop instrument and internal hardware. 1. Injection port; 2. Buffer bottles and a bottle for waste; 3. LED board; 4. Flow cell; 4. Sensor holder; 5. Tubing; 6. Detector; 7. Motorized stage; 8. Sensor holder; 9. Sensor device.

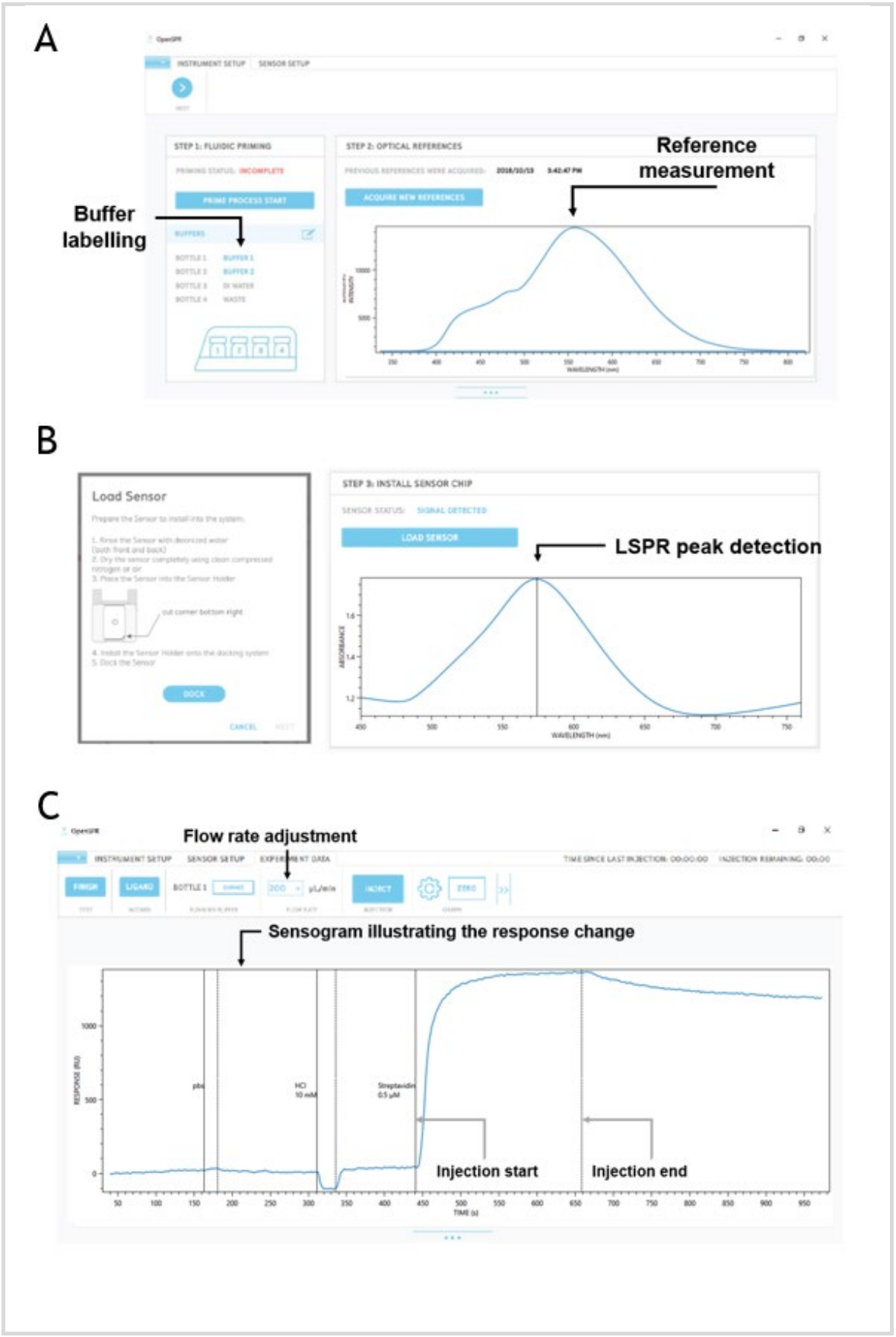

Figure S10 Nicoya OpenSPR software interface. A – the instrument setup screen will allow to indicate the running buffers and setup optical references. The optical reference shown is taken from polystyrene substrate matching the sensor design. B - Absorbance graph of the nanopillar array sensor installed into the OpenSPR. The software automatically indicates and tracks the LSPR peak position. C – Response graph (sensogram) illustrating the change in response units (picometers) with time (seconds).

References

[1] T. Ohashi and L. Dai, "Chapter 15 - C60 and carbon nanotube sensors," in *Carbon Nanotechnology*, L. Dai Ed. Amsterdam: Elsevier, 2006, pp. 525-575.

[2] D. R. Thévenot, K. Toth, R. A. Durst, and G. S. Wilson, "Electrochemical biosensors: recommended definitions and classification1International Union of Pure and Applied Chemistry: Physical Chemistry Division, Commission I.7 (Biophysical Chemistry); Analytical Chemistry Division, Commission V.5 (Electroanalytical Chemistry).1," *Biosensors and Bioelectronics,* vol. 16, no. 1, pp. 121-131, 2001/01/01/ 2001, doi: https://doi.org/10.1016/S0956-5663(01)00115-4.

[3] B. R. Eggins, "Biosensors: an Introduction," *Teubner Studienbücher Chemie,* 1996, doi: 10.1007/978-3-663-05664-5.

[4] P. K. Robinson, "Enzymes: principles and biotechnological applications," *Essays in Biochemistry,* vol. 59, no. 0, pp. 1-41, 2015, doi: 10.1042/bse0590001.

[5] G. M. Cooper, "The Cell: A Molecular Approach. 2nd edition.," in *The Cell: A Molecular Approach. 2nd edition.*, 2nd edition. ed.: Sunderland (MA): Sinauer Associates;, 2000, ch. The Central Role of Enzymes as Biological Catalysts.

[6] T. Vo-Dinh and B. Cullum, "Biosensors and biochips: advances in biological and medical diagnostics," *Fresenius' Journal of Analytical Chemistry,* vol. 366, no. 6-7, pp. 540-551, 2000, doi: 10.1007/s002160051549.

[7] M. Aizawa, "Principles and applications of electrochemical and optical biosensors," *Analytica Chimica Acta,* vol. 250, pp. 249-256, 1991/10/01/ 1991, doi: https://doi.org/10.1016/0003-2670(91)85073-2.

[8] M. Maidorn, S. O. Rizzoli, and F. Opazo, "Tools and limitations to study the molecular composition of synapses by fluorescence microscopy," *Biochemical Journal,* vol. 473, no. 20, pp. 3385-3399, 2016, doi: 10.1042/bcj20160366.

[9] F. S. Felix and L. Angnes, "Electrochemical immunosensors – A powerful tool for analytical applications," *Biosensors and Bioelectronics,* vol. 102, pp. 470-478, 2018/04/15/ 2018, doi: https://doi.org/10.1016/j.bios.2017.11.029.
[10] N. Bhalla, P. Jolly, N. Formisano, and P. Estrela, "Introduction to biosensors," *Essays in Biochemistry,* vol. 60, no. 1, pp. 1-8, 2016, doi: 10.1042/ebc20150001.
[11] P. Cordell, G. Carrington, A. Curd, F. Parker, D. Tomlinson, and M. Peckham, "Affimers and nanobodies as molecular probes and their applications in imaging," *Journal of Cell Science,* vol. 135, no. 14, 2022, doi: 10.1242/jcs.259168.
[12] P. Dauphin-Ducharme and K. W. Plaxco, "Maximizing the Signal Gain of Electrochemical-DNA Sensors," *Analytical Chemistry,* vol. 88, no. 23, pp. 11654-11662, 2016/12/06 2016, doi: 10.1021/acs.analchem.6b03227.
[13] J. A. Alberts B, Lewis J, et al., "DNA Replication Mechanisms.," in *Molecular Biology of the Cell. 4th edition.*, 4th ed.: New York: Garland Science, 2002, ch. Chapter 5. DNA Replication, Repair, and Recombination.
[14] I. Bazin, S. A. Tria, A. Hayat, and J.-L. Marty, "New biorecognition molecules in biosensors for the detection of toxins," *Biosensors and Bioelectronics,* vol. 87, pp. 285-298, 2017, doi: 10.1016/j.bios.2016.06.083.
[15] T. Hermann and D. J. Patel, "Adaptive Recognition by Nucleic Acid Aptamers," *Science,* vol. 287, no. 5454, pp. 820-825, 2000, doi: 10.1126/science.287.5454.820.
[16] W. Zhou, P.-J. Jimmy Huang, J. Ding, and J. Liu, "Aptamer-based biosensors for biomedical diagnostics," *The Analyst,* vol. 139, no. 11, p. 2627, 2014, doi: 10.1039/c4an00132j.
[17] H. Gu *et al.*, "Graphene oxide-assisted non-immobilized SELEX of okdaic acid aptamer and the analytical application of aptasensor," *Scientific Reports,* vol. 6, no. 1, p. 21665, 2016, doi: 10.1038/srep21665.
[18] J. H. Lee, "Interaction of C5 protein with RNA aptamers selected by SELEX," *Nucleic Acids Research,* vol. 30, no. 24, pp. 5360-5368, 2002, doi: 10.1093/nar/gkf694.

[19] K. Sefah, D. Shangguan, X. Xiong, M. B. O'Donoghue, and W. Tan, "Development of DNA aptamers using Cell-SELEX," *Nature Protocols,* vol. 5, no. 6, pp. 1169-1185, 2010, doi: 10.1038/nprot.2010.66.

[20] K. Baryeh, S. Takalkar, M. Lund, and G. Liu, "1 - Introduction to medical biosensors for point of care applications," in *Medical Biosensors for Point of Care (POC) Applications*, R. J. Narayan Ed.: Woodhead Publishing, 2017, pp. 3-25.

[21] V. V. Demidov, "PNA and LNA throw light on DNA," *Trends in Biotechnology,* vol. 21, no. 1, pp. 4-7, 2003/01/01/ 2003, doi: https://doi.org/10.1016/S0167-7799(02)00008-2.

[22] V. Viglasky and T. Hianik, "Potential uses of G-quadruplex-forming aptamers," *General physiology and biophysics,* vol. 32, no. 02, pp. 149-172, 2013, doi: 10.4149/gpb_2013019.

[23] L. Gong *et al.*, "DNAzyme-based biosensors and nanodevices," *Chemical Communications,* vol. 51, no. 6, pp. 979-995, 2015, doi: 10.1039/c4cc06855f.

[24] S. Chen, X. Chen, H. Su, M. Guo, and H. Liu, "Advances in Synthetic-Biology-Based Whole-Cell Biosensors: Principles, Genetic Modules, and Applications in Food Safety," *International Journal of Molecular Sciences,* vol. 24, no. 9, p. 7989, 2023, doi: 10.3390/ijms24097989.

[25] L. Bousse, "Whole cell biosensors," *Sensors and Actuators B: Chemical,* vol. 34, no. 1, pp. 270-275, 1996/08/01/ 1996, doi: https://doi.org/10.1016/S0925-4005(96)01906-5.

[26] K. Kalantar-Zadeh, "Introduction," Springer US, 2013, pp. 1-9.

[27] S. M. Borisov and O. S. Wolfbeis, "Optical Biosensors," *Chemical Reviews,* vol. 108, no. 2, pp. 423-461, 2008/02/01 2008, doi: 10.1021/cr068105t.

[28] P. Damborský, J. Švitel, and J. Katrlík, "Optical biosensors," *Essays in Biochemistry,* vol. 60, no. 1, pp. 91-100, 2016, doi: 10.1042/ebc20150010.

[29] M. Pirzada and Z. Altintas, "Recent Progress in Optical Sensors for Biomedical Diagnostics," *Micromachines,* vol. 11, no. 4, p. 356, 2020, doi: 10.3390/mi11040356.

[30] X. Fan, S. I. White Im Fau - Shopova, H. Shopova Si Fau - Zhu, J. D. Zhu H Fau - Suter, Y. Suter Jd Fau - Sun, and Y. Sun, "Sensitive optical biosensors for unlabeled targets: a review," (in eng), no. 1873-4324 (Electronic).

[31] M. Li, S. K. Cushing, and N. Wu, "Plasmon-enhanced optical sensors: a review," *Analyst,* 10.1039/C4AN01079E vol. 140, no. 2, pp. 386-406, 2015, doi: 10.1039/C4AN01079E.

[32] V. E. Babicheva, "Optical Processes behind Plasmonic Applications," *Nanomaterials*, vol. 13, no. 7*,* doi: 10.3390/nano13071270.

[33] R. W. Wood, "On a Remarkable Case of Uneven Distribution of Light in a Diffraction Grating Spectrum," *Proceedings of the Physical Society of London,* vol. 18, no. 1, p. 269, 1902/06/01 1902, doi: 10.1088/1478-7814/18/1/325.

[34] L. Rayleigh, "On the dynamical theory of gratings," *Proceedings of the Royal Society of London. Series A, Containing Papers of a Mathematical and Physical Character,* vol. 79, no. 532, pp. 399-416, 1907, doi: 10.1098/rspa.1907.0051.

[35] U. Fano, "The Theory of Anomalous Diffraction Gratings and of Quasi-Stationary Waves on Metallic Surfaces (Sommerfeld's Waves)," *Journal of the Optical Society of America,* vol. 31, no. 3, pp. 213-222, 1941/03/01 1941, doi: 10.1364/JOSA.31.000213.

[36] R. H. Ritchie, "Plasma Losses by Fast Electrons in Thin Films," *Physical Review,* vol. 106, no. 5, pp. 874-881, 06/01/ 1957, doi: 10.1103/PhysRev.106.874.

[37] A. Otto, "Excitation of nonradiative surface plasma waves in silver by the method of frustrated total reflection," *Zeitschrift für Physik A Hadrons and nuclei,* vol. 216, no. 4, pp. 398-410, 1968/08/01 1968, doi: 10.1007/BF01391532.

[38] E. Kretschmann and H. Raether, "Notizen: Radiative Decay of Non Radiative Surface Plasmons Excited by Light," *Zeitschrift für Naturforschung A,* vol. 23, no. 12, pp. 2135-2136, 1968, doi: 10.1515/zna-1968-1247.

[39] B. Liedberg, C. Nylander, and I. Lunström, "Surface plasmon resonance for gas detection and biosensing," *Sensors and Actuators,* vol. 4, pp. 299-304, 1983/01/01/ 1983, doi: https://doi.org/10.1016/0250-6874(83)85036-7.

[40] S. Löfås and B. Johnsson, "A novel hydrogel matrix on gold surfaces in surface plasmon resonance sensors for fast and efficient covalent immobilization of ligands," *J. Chem. Soc., Chem. Commun.,* no. 21, pp. 1526-1528, 1990, doi: 10.1039/c39900001526.

[41] M. E. Stewart *et al.*, "Nanostructured Plasmonic Sensors," *Chemical Reviews,* vol. 108, no. 2, pp. 494-521, 2008/02/01 2008, doi: 10.1021/cr068126n.

[42] E. A. Coronado, E. R. Encina, and F. D. Stefani, "Optical properties of metallic nanoparticles: manipulating light, heat and forces at the nanoscale," *Nanoscale,* vol. 3, no. 10, p. 4042, 2011, doi: 10.1039/c1nr10788g.

[43] S. S. Hinman, K. S. McKeating, and Q. Cheng, "Surface Plasmon Resonance: Material and Interface Design for Universal Accessibility," *Analytical Chemistry,* vol. 90, no. 1, pp. 19-39, 2018, doi: 10.1021/acs.analchem.7b04251.

[44] J. R. Lakowicz, "Plasmonics in Biology and Plasmon-Controlled Fluorescence," *Plasmonics,* vol. 1, no. 1, pp. 5-33, 2006, doi: 10.1007/s11468-005-9002-3.

[45] "Surface plasmons," in *Principles of Nano-Optics*, L. Novotny and B. Hecht Eds., 2 ed. Cambridge: Cambridge University Press, 2012, pp. 369-413.

[46] E. Kretschmann, ""“Die Bestimmung optischer Konstanten von Metallen durch Anregung von Oberflachenplasmaschuingungen”," *Z. Phys.,* vol. 241, pp. 313–324, 1971.

[47] J. Dostálek and W. Knoll, "Biosensors based on surface plasmon-enhanced fluorescence spectroscopy (Review)," *Biointerphases,* vol. 3, no. 3, pp. FD12-FD22, 2008, doi: 10.1116/1.2994688.

[48] A. V. Zayats, I. I. Smolyaninov, and A. A. Maradudin, "Nano-optics of surface plasmon polaritons," *Physics Reports,* vol. 408, no. 3, pp. 131-314, 2005/03/01/ 2005, doi: https://doi.org/10.1016/j.physrep.2004.11.001.

[49] N. L. a. N. Tao. "Technical Note 102: SPR Sensitivity and Detection Limit." Biosensing Instrument. https://biosensingusa.com/technical-notes/technical-note-102-spr-sensitivity-detection-limit/ (accessed.
[50] J. Homola, S. S. Yee, and G. Gauglitz, "Surface plasmon resonance sensors: review," *Sensors and Actuators B: Chemical,* vol. 54, no. 1, pp. 3-15, 1999/01/25/ 1999, doi: https://doi.org/10.1016/S0925-4005(98)00321-9.
[51] J. A. Jackman, A. Rahim Ferhan, and N.-J. Cho, "Nanoplasmonic sensors for biointerfacial science," *Chemical Society Reviews,* 10.1039/C6CS00494F vol. 46, no. 12, pp. 3615-3660, 2017, doi: 10.1039/C6CS00494F.
[52] H. Kurt *et al.*, "Nanoplasmonic biosensors: Theory, structure, design, and review of recent applications," *Analytica Chimica Acta,* vol. 1185, p. 338842, 2021/11/15/ 2021, doi: https://doi.org/10.1016/j.aca.2021.338842.
[53] K. L. Kelly, E. Coronado, L. L. Zhao, and G. C. Schatz, "The Optical Properties of Metal Nanoparticles: The Influence of Size, Shape, and Dielectric Environment," *The Journal of Physical Chemistry B,* vol. 107, no. 3, pp. 668-677, 2003/01/01 2003, doi: 10.1021/jp026731y.
[54] W. L. Barnes, "Particle plasmons: Why shape matters," *American Journal of Physics,* vol. 84, pp. 593-601, 2016.
[55] K. Yao and Y. Zheng, "Fundamentals of Nanophotonics," Springer International Publishing, 2023, pp. 1-33.
[56] P. P. Hari, S. Alireza, and N. L. Michael, "Nanoplasmonics in Metallic Nanostructures and Dirac Systems," in *Nanoplasmonics*, B. Gregory Ed. Rijeka: IntechOpen, 2017, p. Ch. 3.
[57] A. Ott, "Synthesis and application of hybrid materials based on plasmonic nanoparticles," 2016.
[58] U. Hohenester and A. Trügler, "MNPBEM – A Matlab toolbox for the simulation of plasmonic nanoparticles," *Computer Physics Communications,* vol. 183, no. 2, pp. 370-381, 2012, doi: 10.1016/j.cpc.2011.09.009.
[59] A. R. Shafiqa, A. Abdul Aziz, and B. Mehrdel, "Nanoparticle Optical Properties: Size Dependence of a

Single Gold Spherical Nanoparticle," *Journal of Physics: Conference Series,* vol. 1083, no. 1, p. 012040, 2018/08/01 2018, doi: 10.1088/1742-6596/1083/1/012040.

[60] W. Chen, H. Hu, W. Jiang, Y. Xu, S. Zhang, and H. Xu, "Ultrasensitive nanosensors based on localized surface plasmon resonances: From theory to applications*," *Chinese Physics B,* vol. 27, no. 10, p. 107403, 2018/10/01 2018, doi: 10.1088/1674-1056/27/10/107403.

[61] M. S. Bin-Alam *et al.*, "Ultra-high-Q resonances in plasmonic metasurfaces," *Nature Communications,* vol. 12, no. 1, p. 974, 2021/02/12 2021, doi: 10.1038/s41467-021-21196-2.

[62] P. K. Jain and M. A. El-Sayed, "Surface Plasmon Resonance Sensitivity of Metal Nanostructures: Physical Basis and Universal Scaling in Metal Nanoshells," *The Journal of Physical Chemistry C,* vol. 111, no. 47, pp. 17451-17454, 2007/11/01 2007, doi: 10.1021/jp0773177.

[63] P. K. Jain, X. Huang, I. H. El-Sayed, and M. A. El-Sayed, "Noble Metals on the Nanoscale: Optical and Photothermal Properties and Some Applications in Imaging, Sensing, Biology, and Medicine," *Accounts of Chemical Research,* vol. 41, no. 12, pp. 1578-1586, 2008/12/16 2008, doi: 10.1021/ar7002804.

[64] I. L. Violi *et al.*, "Challenges on optical printing of colloidal nanoparticles," *The Journal of Chemical Physics,* vol. 156, no. 3, 2022, doi: 10.1063/5.0078454.

[65] V. Nocerino *et al.*, "Plasmonic Nanosensors: Design, Fabrication, and Applications in Biomedicine," *Chemosensors*, vol. 10, no. 5*,* doi: 10.3390/chemosensors10050150.

[66] A. Holm *et al.*, "Nanoscale Spatial Distribution of Supported Nanoparticles Controls Activity and Stability in Powder Catalysts for CO Oxidation and Photocatalytic H2 Evolution," *Journal of the American Chemical Society,* vol. 142, no. 34, pp. 14481-14494, 2020/08/26 2020, doi: 10.1021/jacs.0c03842.

[67] A. Ahmadivand, "Analysis of the arm spacing effect on symmetric and asymmetric Y-shape optical power splitters: plasmonic interactions between gold nanorings," (in Eng), *Optica Applicata,* vol. 44, no. 1, pp. 123-133, // 2014.

[68] K. M. Mayer and J. H. Hafner, "Localized Surface Plasmon Resonance Sensors," *Chemical Reviews,* vol. 111, no. 6, pp. 3828-3857, 2011/06/08 2011, doi: 10.1021/cr100313v.

[69] Y. Xiao, Z. Zhang, S. Yin, and X. Ma, "Nanoplasmonic biosensors for precision medicine," *Frontiers in Chemistry,* vol. 11, 07/06 2023, doi: 10.3389/fchem.2023.1209744.

[70] H. Altug, S.-H. Oh, S. A. Maier, and J. Homola, "Advances and applications of nanophotonic biosensors," *Nature Nanotechnology,* vol. 17, no. 1, pp. 5-16, 2022, doi: 10.1038/s41565-021-01045-5.

[71] A. J. Haes, S. Zou, G. C. Schatz, and R. P. Van Duyne, "A Nanoscale Optical Biosensor: The Long Range Distance Dependence of the Localized Surface Plasmon Resonance of Noble Metal Nanoparticles," *The Journal of Physical Chemistry B,* vol. 108, no. 1, pp. 109-116, 2004/01/01 2004, doi: 10.1021/jp0361327.

[72] B. Luk'yanchuk *et al.*, "The Fano resonance in plasmonic nanostructures and metamaterials," *Nature Materials,* vol. 9, no. 9, pp. 707-715, 2010/09/01 2010, doi: 10.1038/nmat2810.

[73] E. Prodan, C. Radloff, N. J. Halas, and P. Nordlander, "A Hybridization Model for the Plasmon Response of Complex Nanostructures," *Science,* vol. 302, no. 5644, pp. 419-422, 2003, doi: 10.1126/science.1089171.

[74] M. A. Basyooni, A. M. Ahmed, and M. Shaban, "Plasmonic hybridization between two metallic nanorods," *Optik,* vol. 172, pp. 1069-1078, 2018/11/01/ 2018, doi: https://doi.org/10.1016/j.ijleo.2018.07.135.

[75] S. Ramadurgam and C. Yang, "Semiconductor-Metal-Semiconductor Core-Multishell Nanowires as Negative-Index Metamaterial in Visible Domain," *Scientific Reports,* vol. 4, no. 1, 2014, doi: 10.1038/srep04931.

[76] W. Huang, W. Qian, P. K. Jain, and M. A. El-Sayed, "The Effect of Plasmon Field on the Coherent Lattice Phonon Oscillation in Electron-Beam Fabricated Gold Nanoparticle Pairs," *Nano Letters,* vol. 7, no. 10, pp. 3227-3234, 2007/10/01 2007, doi: 10.1021/nl071813p.

[77] K. C. Woo, L. Shao, H. Chen, Y. Liang, J. Wang, and H.-Q. Lin, "Universal Scaling and Fano Resonance in the Plasmon Coupling between Gold Nanorods," *ACS Nano,* vol. 5, no. 7, pp. 5976-5986, 2011/07/26 2011, doi: 10.1021/nn2017588.

[78] N. Halas, "Playing with Plasmons: Tuning the Optical Resonant Properties of Metallic Nanoshells," *MRS Bulletin,* vol. 30, no. 5, pp. 362-367, 2005, doi: 10.1557/mrs2005.99.

[79] P. B. Johnson and R. W. Christy, "Optical Constants of the Noble Metals," *Physical Review B,* vol. 6, no. 12, pp. 4370-4379, 12/15/ 1972, doi: 10.1103/PhysRevB.6.4370.

[80] H. Raether, *Surface Plasmons on Smooth and Rough Surfaces and on Gratings*. 1988.

[81] S. A. Maier, *Plasmonics: fundamentals and applications*. Springer, 2007.

[82] V. G. Kravets, A. A.-O. Kabashin, W. A.-O. Barnes, and A. A.-O. Grigorenko, "Plasmonic Surface Lattice Resonances: A Review of Properties and Applications," (in eng), no. 1520-6890 (Electronic).

[83] W. L. Barnes, T. W. Dereux A Fau - Ebbesen, and T. W. Ebbesen, "Surface plasmon subwavelength optics," (in eng), no. 1476-4687 (Electronic).

[84] J. Homola, "Surface Plasmon Resonance Sensors for Detection of Chemical and Biological Species," *Chemical Reviews,* vol. 108, no. 2, pp. 462-493, 2008/02/01 2008, doi: 10.1021/cr068107d.

[85] K. Kneipp *et al.*, "Single Molecule Detection Using Surface-Enhanced Raman Scattering (SERS)," *Physical Review Letters,* vol. 78, no. 9, pp. 1667-1670, 03/03/ 1997, doi: 10.1103/PhysRevLett.78.1667.

[86] S. Schlücker, "Surface-Enhanced Raman Spectroscopy: Concepts and Chemical Applications," *Angewandte*

Chemie International Edition, vol. 53, no. 19, pp. 4756-4795, 2014, doi: 10.1002/anie.201205748.

[87] D. L. Jeanmaire and R. P. Van Duyne, "Surface raman spectroelectrochemistry: Part I. Heterocyclic, aromatic, and aliphatic amines adsorbed on the anodized silver electrode," *Journal of Electroanalytical Chemistry and Interfacial Electrochemistry,* vol. 84, no. 1, pp. 1-20, 1977/11/10/ 1977, doi: https://doi.org/10.1016/S0022-0728(77)80224-6.

[88] L. Liu, W. Ma, X. Wang, and S. Li, "Recent Progress of Surface-Enhanced Raman Spectroscopy for Bacteria Detection," *Biosensors,* vol. 13, no. 3, p. 350, 2023. [Online]. Available: https://www.mdpi.com/2079-6374/13/3/350.

[89] R. R. Jones, D. C. Hooper, L. Zhang, D. Wolverson, and V. K. Valev, "Raman Techniques: Fundamentals and Frontiers," (in eng), no. 1931-7573 (Print).

[90] M. Moskovits, "Surface-enhanced spectroscopy," *Reviews of Modern Physics,* vol. 57, no. 3, pp. 783-826, 07/01/ 1985, doi: 10.1103/RevModPhys.57.783.

[91] S. Nie and S. R. Emory, "Probing Single Molecules and Single Nanoparticles by Surface-Enhanced Raman Scattering," (in eng), no. 1095-9203 (Electronic).

[92] M. Fleischmann, P. J. Hendra, and A. J. McQuillan, "Raman spectra of pyridine adsorbed at a silver electrode," *Chemical Physics Letters,* vol. 26, no. 2, pp. 163-166, 1974/05/15/ 1974, doi: https://doi.org/10.1016/0009-2614(74)85388-1.

[93] M. G. Albrecht and J. A. Creighton, "Anomalously intense Raman spectra of pyridine at a silver electrode," *Journal of the American Chemical Society,* vol. 99, no. 15, pp. 5215-5217, 1977/06/01 1977, doi: 10.1021/ja00457a071.

[94] K. Srivastava, H. Le-The, J. J. A. Lozeman, A. van den Berg, W. van der Stam, and M. Odijk, "Prospects of nano-lithographic tools for the fabrication of surface-enhanced Raman spectroscopy (SERS) substrates," *Micro and Nano Engineering,* vol. 23, p. 100267, 2024/06/01/ 2024, doi: https://doi.org/10.1016/j.mne.2024.100267.

[95] T. R. Jensen, M. D. Malinsky, C. L. Haynes, and R. P. Van Duyne, "Nanosphere Lithography: Tunable Localized Surface Plasmon Resonance Spectra of Silver Nanoparticles," *The Journal of Physical Chemistry B,* vol. 104, no. 45, pp. 10549-10556, 2000/11/01 2000, doi: 10.1021/jp002435e.

[96] C. Ji *et al.*, "Recent Advances and Perspective in Electrically Regulated Surface-Enhanced Raman Spectroscopy," *Advanced Photonics Research,* vol. 4, no. 11, p. 2300171, 2023/11/01 2023, doi: https://doi.org/10.1002/adpr.202300171.

[97] J. R. Lombardi and R. L. Birke, "A Unified View of Surface-Enhanced Raman Scattering," *Accounts of Chemical Research,* vol. 42, no. 6, pp. 734-742, 2009/06/16 2009, doi: 10.1021/ar800249y.

[98] D. Cialla *et al.*, "Surface-enhanced Raman spectroscopy (SERS): progress and trends," *Analytical and Bioanalytical Chemistry,* vol. 403, no. 1, pp. 27-54, 2012, doi: 10.1007/s00216-011-5631-x.

[99] A. Otto, I. Mrozek, H. Grabhorn, and W. Akemann, "Surface-enhanced Raman scattering," *Journal of Physics: Condensed Matter,* vol. 4, no. 5, p. 1143, 1992/02/03 1992, doi: 10.1088/0953-8984/4/5/001.

[100] Q. D. Mai *et al.*, "Silver Nanoparticles-Based SERS Platform towards Detecting Chloramphenicol and Amoxicillin: An Experimental Insight into the Role of HOMO–LUMO Energy Levels of the Analyte in the SERS Signal and Charge Transfer Process," *The Journal of Physical Chemistry C,* vol. 126, no. 17, pp. 7778-7790, 2022/05/05 2022, doi: 10.1021/acs.jpcc.2c01818.

[101] J. P. Camden *et al.*, "Probing the Structure of Single-Molecule Surface-Enhanced Raman Scattering Hot Spots," *Journal of the American Chemical Society,* vol. 130, no. 38, pp. 12616-12617, 2008/09/24 2008, doi: 10.1021/ja8051427.

[102] R. Shi, X. Liu, and Y. Ying, "Facing Challenges in Real-Life Application of Surface-Enhanced Raman Scattering: Design and Nanofabrication of Surface-Enhanced Raman Scattering Substrates for Rapid Field Test of

Food Contaminants," *Journal of Agricultural and Food Chemistry,* vol. 66, no. 26, pp. 6525-6543, 2018/07/05 2018, doi: 10.1021/acs.jafc.7b03075.

[103] Y. Lv, Y. Qin, F. Svec, and T. Tan, "Molecularly imprinted plasmonic nanosensor for selective SERS detection of protein biomarkers," *Biosensors and Bioelectronics,* vol. 80, pp. 433-441, 2016/06/15/ 2016, doi: https://doi.org/10.1016/j.bios.2016.01.092.

[104] D. Cialla-May *et al.*, "Biomedical SERS – the current state and future trends," *Chemical Society Reviews,* vol. 53, no. 18, pp. 8957-8979, 2024, doi: 10.1039/d4cs00090k.

[105] R. R. Frontiera, A.-I. Henry, N. L. Gruenke, and R. P. Van Duyne, "Surface-Enhanced Femtosecond Stimulated Raman Spectroscopy," *The Journal of Physical Chemistry Letters,* vol. 2, no. 10, pp. 1199-1203, 2011/05/19 2011, doi: 10.1021/jz200498z.

[106] S. Berweger and M. B. Raschke, "Signal limitations in tip-enhanced Raman scattering: the challenge to become a routine analytical technique," *Analytical and Bioanalytical Chemistry,* vol. 396, no. 1, pp. 115-123, 2010/01/01 2010, doi: 10.1007/s00216-009-3085-1.

[107] T. W. W. Ebbesen, "Extraordinary optical transmission through sub-wavelength hole arrays," *Nature.,* vol. 391, no. 6668, pp. 667-669, 1998, doi: info:doi/.

[108] J. Lee *et al.*, "Extraordinary optical transmission and second harmonic generation in sub–10-nm plasmonic coaxial aperture," *Nanophotonics,* vol. 9, no. 10, pp. 3295-3302, 2020, doi: 10.1515/nanoph-2020-0066.

[109] S. G. Rodrigo, F. d. León-Pérez, and L. Martín-Moreno, "Extraordinary Optical Transmission: Fundamentals and Applications," *Proceedings of the IEEE,* vol. 104, no. 12, pp. 2288-2306, 2016, doi: 10.1109/JPROC.2016.2580664.

[110] A. Peer and R. Biswas, "Extraordinary optical transmission in nanopatterned ultrathin metal films without holes," *Nanoscale,* 10.1039/C5NR07903A vol. 8, no. 8, pp. 4657-4666, 2016, doi: 10.1039/C5NR07903A.

[111] D. Maystre, "Survey of Surface Plasmon Polariton History," in *Plasmonics: From Basics to Advanced*

Topics, S. Enoch and N. Bonod Eds. Berlin, Heidelberg: Springer Berlin Heidelberg, 2012, pp. 3-37.

[112]P. Zhan *et al.*, "The Anomalous Infrared Transmission of Gold Films on Two-Dimensional Colloidal Crystals," *Advanced Materials,* vol. 18, no. 12, pp. 1612-1616, 2006/06/19 2006, doi: https://doi.org/10.1002/adma.200502588.

[113]N.-M. Tran *et al.*, "Observation of the nonlinear Wood's anomaly on periodic arrays of nickel nanodimers," *Physical Review B,* vol. 98, no. 24, p. 245425, 12/28/ 2018, doi: 10.1103/PhysRevB.98.245425.

[114]Y. Kim, R. C. Johnson, and J. T. Hupp, "Gold Nanoparticle-Based Sensing of “Spectroscopically Silent” Heavy Metal Ions," *Nano Letters,* vol. 1, no. 4, pp. 165-167, 2001/04/01 2001, doi: 10.1021/nl0100116.

[115]H. Xu, X. Mao, Q. Zeng, S. Wang, A.-N. Kawde, and G. Liu, "Aptamer-Functionalized Gold Nanoparticles as Probes in a Dry-Reagent Strip Biosensor for Protein Analysis," *Analytical Chemistry,* vol. 81, no. 2, pp. 669-675, 2009/01/15 2009, doi: 10.1021/ac8020592.

[116]J. Liu, D. Mazumdar, and Y. Lu, "A Simple and Sensitive “Dipstick” Test in Serum Based on Lateral Flow Separation of Aptamer-Linked Nanostructures," *Angewandte Chemie International Edition,* vol. 45, no. 47, pp. 7955-7959, 2006, doi: 10.1002/anie.200603106.

[117]B. G. Andryukov, "Six decades of lateral flow immunoassay: from determining metabolic markers to diagnosing COVID-19," (in eng), no. 2471-1888 (Electronic).

[118]B. O’Farrell, "Evolution in Lateral Flow–Based Immunoassay Systems," Humana Press, 2009, pp. 1-33.

[119]Katarzyna and A. Gallotta, "Lateral flow assays," *Essays in Biochemistry,* vol. 60, no. 1, pp. 111-120, 2016, doi: 10.1042/ebc20150012.

[120] and P. Karen Steward, "An Introduction to the Lateral Flow Test: Strengths, Limitations and Applications," in *DIagnostics*, T. Networks, Ed., ed, 2023.

[121]Z. Ye, C. Li, Q. Chen, Y. Xu, and S. E. J. Bell, "Self-assembly of colloidal nanoparticles into 2D arrays at water–oil interfaces: rational construction of stable SERS

substrates with accessible enhancing surfaces and tailored plasmonic response," *Nanoscale,* vol. 13, no. 12, pp. 5937-5953, 2021, doi: 10.1039/d0nr08803j.
[122]K. A. Altammar, "A review on nanoparticles: characteristics, synthesis, applications, and challenges," (in eng), no. 1664-302X (Print).
[123]P. Baptista *et al.*, "Gold nanoparticles for the development of clinical diagnosis methods," *Analytical and Bioanalytical Chemistry,* vol. 391, no. 3, pp. 943-950, 2008, doi: 10.1007/s00216-007-1768-z.
[124]E. Petryayeva and U. J. Krull, "Localized surface plasmon resonance: Nanostructures, bioassays and biosensing—A review," *Analytica Chimica Acta,* vol. 706, no. 1, pp. 8-24, 2011/11/07/ 2011, doi: https://doi.org/10.1016/j.aca.2011.08.020.
[125]C. M. Das *et al.*, "Computational Modeling for Intelligent Surface Plasmon Resonance Sensor Design and Experimental Schemes for Real-Time Plasmonic Biosensing: A Review," *Advanced Theory and Simulations,* vol. 6, no. 9, 2023, doi: 10.1002/adts.202200886.
[126]S. Sarkar and T. A. F. König, "Engineering Plasmonic Hybridization toward Advanced Optical Sensors," *Advanced Sensor Research,* vol. 3, no. 1, 2024, doi: 10.1002/adsr.202300054.
[127]S. M. Kandil, I. A. Eshrah, I. S. El Babli, and A. H. Badawi, "Plasmon hybridization in split ring nanosandwich for refractive index sensing– Numerical Investigation," *Opt. Express,* vol. 24, no. 26, pp. 30201-30214, 2016/12/26 2016, doi: 10.1364/OE.24.030201.
[128]W. Zhou and T. W. Odom, "Tunable subradiant lattice plasmons by out-of-plane dipolar interactions," *Nature Nanotechnology,* vol. 6, no. 7, pp. 423-427, 2011, doi: 10.1038/nnano.2011.72.
[129]L. Wang, T. Sang, J. Gao, X. Yin, and H. Qi, "High-performance sensor achieved by hybrid guide-mode resonance/surface plasmon resonance platform," *Appl. Opt.,* vol. 57, no. 25, pp. 7338-7343, 2018/09/01 2018, doi: 10.1364/AO.57.007338.

[130]S. Sarkar *et al.*, "Hybridized Guided-Mode Resonances via Colloidal Plasmonic Self-Assembled Grating," *ACS Applied Materials & Interfaces,* vol. 11, no. 14, pp. 13752-13760, 2019, doi: 10.1021/acsami.8b20535.

[131]P. Säfsten, S. L. Klakamp, A. W. Drake, R. Karlsson, and D. G. Myszka, "Screening antibody–antigen interactions in parallel using Biacore A100," *Analytical Biochemistry,* vol. 353, no. 2, pp. 181-190, 2006/06/15/ 2006, doi: https://doi.org/10.1016/j.ab.2006.01.041.

[132]J. Segervald, N. Boulanger, R. Salh, X. Jia, and T. Wågberg, "Plasmonic metasurface assisted by thermally imprinted polymer nano-well array for surface enhanced Raman scattering," *Nano Select,* vol. 3, no. 9, pp. 1344-1353, 2022/09/01 2022, doi: https://doi.org/10.1002/nano.202200010.

[133]Y. Zhao, Y.-L. Zhang, J.-A. Huang, Z. Zhang, X. Chen, and W. Zhang, "Plasmonic nanopillar array embedded microfluidic chips: an in situ SERS monitoring platform," *Journal of Materials Chemistry A,* 10.1039/C4TA07076C vol. 3, no. 12, pp. 6408-6413, 2015, doi: 10.1039/C4TA07076C.

[134]S. E. Seo *et al.*, "Plasmon-Driven Gold Nanopillar Multiarrayed Gene Amplification Methodology for the High-Throughput Discrimination of Pathogens," *Advanced Science,* vol. 12, no. 9, 2025, doi: 10.1002/advs.202411849.

[135]T. Lednický and A. Bonyár, "Large Scale Fabrication of Ordered Gold Nanoparticle–Epoxy Surface Nanocomposites and Their Application as Label-Free Plasmonic DNA Biosensors," *ACS Applied Materials & Interfaces,* vol. 12, no. 4, pp. 4804-4814, 2020/01/29 2020, doi: 10.1021/acsami.9b20907.

[136]Y. Zheng, L. Li, X. Zong, Z. Geng, W. Li, and Y. Liu, "Large-scale plasmonic nanodisk array as a biosensing platform fabricated by transfer nanoprinting," *Appl. Opt.,* vol. 62, no. 29, pp. 7706-7712, 2023/10/10 2023, doi: 10.1364/AO.499639.

[137]S. Chu, Y. Liang, H. Yuan, L. Yu, Q. Liu, and W. Peng, "Ultranarrow Linewidth Coupling Resonance in Flexible Plasmonic Nanopillar Array for Enhanced Biomolecule

Detection," *Advanced Materials Interfaces,* vol. 9, no. 27, p. 2201011, 2022, doi: 10.1002/admi.202201011.
[138] S. Mohapatra, S. Kumari, and R. S. Moirangthem, "Fabrication of a cost-effective polymer nanograting as a disposable plasmonic biosensor using nanoimprint lithography," *Materials Research Express,* vol. 4, no. 7, p. 076202, 2017, doi: 10.1088/2053-1591/aa764e.
[139] A. Minopoli, A. Acunzo, B. Della Ventura, and R. Velotta, "Nanostructured Surfaces as Plasmonic Biosensors: A Review," *Advanced Materials Interfaces,* vol. 9, no. 2, p. 2101133, 2022/01/01 2022, doi: https://doi.org/10.1002/admi.202101133.
[140] K.-L. Lee *et al.*, "Injection compression molding of transmission-type Fano resonance biochips for multiplex sensing applications," *Applied Materials Today,* vol. 16, pp. 72-82, 2019/09/01/ 2019, doi: https://doi.org/10.1016/j.apmt.2019.05.003.
[141] C. Farcau, D. Marconi, A. Colniță, I. Brezeștean, and L. Barbu-Tudoran, "Gold Nanopost-Shell Arrays Fabricated by Nanoimprint Lithography as a Flexible Plasmonic Sensing Platform," *Nanomaterials,* vol. 9, no. 11, p. 1519, 2019, doi: 10.3390/nano9111519.
[142] K. E. Docherty, "Improvements to the alignment process in electron-beam lithography.," Doctoral PhD Thesis, Department of Electronics and Electrical Engineering, University of Glasgow, College of Science and Engineering; School of Engineering, Glasgow, glathesis:2010-1663, 2010. [Online]. Available: http://theses.gla.ac.uk/id/eprint/1663
[143] V. Lacatena, M. Haras, J. F. Robillard, S. Monfray, T. Skotnicki, and E. Dubois, "Phononic engineering of silicon using “dots on the fly” e-beam lithography and plasma etching," *Microelectronic Engineering,* vol. 121, pp. 131-134, 2014/06/01/ 2014, doi: https://doi.org/10.1016/j.mee.2014.04.034.
[144] J. M. Stormonth-Darling, "Fabrication of difficult nanostructures by injection moulding," Doctoral PhD Thesis, Biomedical Engineering, University of Glasgow, College of Science and Engineering, School of

Engineering, Glasgow, glathesis:2013-4456, 2013. [Online]. Available: http://theses.gla.ac.uk/id/eprint/4456

[145] D. A. W. K. C. Balram, M. Davanco, K. E. Grutter, Q. Li, T. Michels, C. H. Ray, L. Yu, R. J. Kasica, C. B. Wallin, I. J. Gilbert, B. A. Bryce, G. Simelgor, J. Topolancik, N. Lobontiu , Y. Liu, P. Neuzil, V. Svatos, K. A. Dill, N. A. Bertrand, M. G. Metzler, G. Lopez, D. A. Czaplewski, L. Ocola, K. A. Srinivasan, S. M. Stavis, V. A. Aksyuk, J. A. Liddle, S. Krylov and B. R. Ilic, "The Nanolithography Toolbox," *Journal of Research of the National Institute of Standards and Technology,* vol. Volume 121 (2016), pp. pp. 464-475, 2016. [Online]. Available: http://dx.doi.org/10.6028/jres.121.024.

[146] *BEAMER, GenISys GmbH*. Munich, Germany. [Online]. Available: https://www.genisys-gmbh.com/beamer.html

[147] N. Pala and M. Karabiyik, "Electron Beam Lithography (EBL)," in *Encyclopedia of Nanotechnology*, B. Bhushan Ed. Dordrecht: Springer Netherlands, 2012, pp. 718-740.

[148] Z.-J. Ding and R. Shimizu, "A Monte Carlo modeling of electron interaction with solids including cascade secondary electron production," *Scanning,* vol. 18, no. 2, pp. 92-113, 1996, doi: https://doi.org/10.1002/sca.1996.4950180204.

[149] *TRACER, GenISys GmbH*. Munich, Germany. [Online]. Available: https://www.genisys-gmbh.com/tracer.html

[150] G. A. C. Jones, S. Blythe, and H. Ahmed, "Very high voltage (500 kV) electron beam lithography for thick resists and high resolution," *Journal of Vacuum Science & Technology B: Microelectronics Processing and Phenomena,* vol. 5, no. 1, pp. 120-123, 1987, doi: 10.1116/1.583844.

[151] S. Vlassov *et al.*, "Adhesion and Mechanical Properties of PDMS-Based Materials Probed with AFM: A Review," vol. 56, no. 1, pp. 62-78, 2018, doi: doi:10.1515/rams-2018-0038.

[152] "Problems Associated with the Electron Microscopy of Polymers," in *Electron Microscopy of Polymers*, G. H. Michler Ed. Berlin, Heidelberg: Springer Berlin Heidelberg, 2008, pp. 175-183.

[153]T. Haatainen, T. Mäkelä, J. Ahopelto, and Y. Kawaguchi, "Imprinted polymer stamps for UV-NIL," *Microelectronic Engineering,* vol. 86, no. 11, pp. 2293-2296, 2009/11/01/ 2009, doi: https://doi.org/10.1016/j.mee.2009.04.020.
[154]W. Zhou *et al.*, "Nanoimprint Lithography: A Processing Technique for Nanofabrication Advancement," *Nano-Micro Letters,* vol. 3, no. 2, pp. 135-140, 2011/06/01 2011, doi: 10.1007/BF03353663.
[155]W. S. Cleveland and S. J. Devlin, "Locally Weighted Regression: An Approach to Regression Analysis by Local Fitting," *Journal of the American Statistical Association,* vol. 83, no. 403, pp. 596-610, 1988/09/01 1988, doi: 10.1080/01621459.1988.10478639.
[156]W. S. Cleveland, "LOWESS: A Program for Smoothing Scatterplots by Robust Locally Weighted Regression," *The American Statistician,* vol. 35, no. 1, pp. 54-54, 1981, doi: 10.2307/2683591.
[157]W. S. Cleveland, "Robust Locally Weighted Regression and Smoothing Scatterplots," *Journal of the American Statistical Association,* vol. 74, no. 368, pp. 829-836, 1979/12/01 1979, doi: 10.1080/01621459.1979.10481038.
[158]S. Kasani, K. Curtin, and N. Wu, "A review of 2D and 3D plasmonic nanostructure array patterns: fabrication, light management and sensing applications," vol. 8, no. 12, pp. 2065-2089, 2019, doi: doi:10.1515/nanoph-2019-0158.
[159]T. J. Bruno and P. D. N. Svoronos, "CRC Handbook of Fundamental Spectroscopic Correlation Charts," 2005, doi: 10.1201/9780849332500.
[160]J. Li, S. K. Cushing, P. Zheng, F. Meng, D. Chu, and N. Wu, "Plasmon-induced photonic and energy-transfer enhancement of solar water splitting by a hematite nanorod array," *Nature Communications,* vol. 4, no. 1, p. 2651, 2013/10/18 2013, doi: 10.1038/ncomms3651.
[161]P. D. Nallathamby, T. Huang, and X.-H. N. Xu, "Design and characterization of optical nanorulers of single nanoparticles using optical microscopy and spectroscopy," *Nanoscale,* vol. 2, no. 9, p. 1715, 2010, doi: 10.1039/c0nr00303d.

[162]D. I. Yakubovsky, A. V. Arsenin, Y. V. Stebunov, D. Y. Fedyanin, and V. S. Volkov, "Optical constants and structural properties of thin gold films," *Opt. Express,* vol. 25, no. 21, pp. 25574-25587, 2017/10/16 2017, doi: 10.1364/OE.25.025574.

[163]E.-T. Hu *et al.*, "Effective method to study the thickness-dependent dielectric functions of nanometal thin film," *Opt. Lett.,* vol. 41, no. 21, pp. 4907-4910, 2016/11/01 2016, doi: 10.1364/OL.41.004907.

[164]D. Eschimèse, F. Vaurette, T. Mélin, and S. Arscott, "Precise tailoring of evaporated gold nanocones using electron beam lithography and lift-off," *Nanotechnology,* vol. 31, no. 22, p. 225302, 2020/03/13 2020, doi: 10.1088/1361-6528/ab746e.

[165]J. S. Weerakkody, S. Brenet, T. Livache, C. Herrier, Y. Hou, and A. Buhot, "Optical Index Prism Sensitivity of Surface Plasmon Resonance Imaging in Gas Phase: Experiment versus Theory," *The Journal of Physical Chemistry C,* vol. 124, no. 6, pp. 3756-3767, 2020/02/13 2020, doi: 10.1021/acs.jpcc.9b09973.

[166]C. Sönnichsen, T. Franzl, T. Wilk, G. von Plessen, and J. Feldmann, "Plasmon resonances in large noble-metal clusters," *New Journal of Physics,* vol. 4, no. 1, p. 93, 2002/11/14 2002, doi: 10.1088/1367-2630/4/1/393.

[167]D. Maystre, "Theory of Wood's Anomalies," vol. 167, 2012, p. 39.

[168]S. Savoia *et al.*, "Surface sensitivity of Rayleigh anomalies in metallic nanogratings," *Opt. Express,* vol. 21, no. 20, pp. 23531-23542, 2013/10/07 2013, doi: 10.1364/OE.21.023531.

[169]D. Khlopin *et al.*, "Lattice modes and plasmonic linewidth engineering in gold and aluminum nanoparticle arrays," *J. Opt. Soc. Am. B,* vol. 34, no. 3, pp. 691-700, 2017/03/01 2017, doi: 10.1364/JOSAB.34.000691.

[170]S. Hamdad, A. T. Diallo, M. Chakaroun, and A. Boudrioua, "The role of Rayleigh anomalies in the coupling process of plasmonic gratings and the control of the emission properties of organic molecules," *Scientific Reports,* vol. 12, no. 1, p. 3218, 2022/02/25 2022, doi: 10.1038/s41598-022-07216-1.

[171]R. Biswas, S. Neginhal, C. G. Ding, I. Puscasu, and E. Johnson, "Mechanisms underlying extraordinary transmission enhancement in subwavelength hole arrays," *J. Opt. Soc. Am. B,* vol. 24, no. 10, pp. 2589-2596, 2007/10/01 2007, doi: 10.1364/JOSAB.24.002589.

[172]V. Giannini, G. Vecchi, and J. Gómez Rivas, "Lighting Up Multipolar Surface Plasmon Polaritons by Collective Resonances in Arrays of Nanoantennas," *Physical Review Letters,* vol. 105, no. 26, p. 266801, 12/20/ 2010, doi: 10.1103/PhysRevLett.105.266801.

[173]J. Jatschka, A. Dathe, A. Csáki, W. Fritzsche, and O. Stranik, "Propagating and localized surface plasmon resonance sensing — A critical comparison based on measurements and theory," *Sensing and Bio-Sensing Research,* vol. 7, pp. 62-70, 2016/03/01/ 2016, doi: https://doi.org/10.1016/j.sbsr.2016.01.003.

[174]I. M. Pryce, Y. A. Kelaita, K. Aydin, and H. A. Atwater, "Compliant Metamaterials for Resonantly Enhanced Infrared Absorption Spectroscopy and Refractive Index Sensing," *ACS Nano,* vol. 5, no. 10, pp. 8167-8174, 2011/10/25 2011, doi: 10.1021/nn202815k.

[175]J. Jiang *et al.*, "Plasmonic nano-arrays for ultrasensitive bio-sensing," *Nanophotonics,* vol. 7, no. 9, pp. 1517-1531, 2018, doi: doi:10.1515/nanoph-2018-0023.

[176]J. Lin, Y. Zhang, J. Qian, and S. He, "A nano-plasmonic chip for simultaneous sensing with dual-resonance surface-enhanced Raman scattering and localized surface plasmon resonance," *Laser & Photonics Reviews,* vol. 8, no. 4, pp. 610-616, 2014/07/01 2014, doi: https://doi.org/10.1002/lpor.201400029.

[177]A. Lesuffleur, H. Im, N. C. Lindquist, and S.-H. Oh, "Periodic nanohole arrays with shape-enhanced plasmon resonance as real-time biosensors," *Applied Physics Letters,* vol. 90, no. 24, p. 243110, 2007, doi: 10.1063/1.2747668.

[178]G. C. Schatz, M. A. Young, and R. P. Van Duyne, "Electromagnetic Mechanism of SERS," in *Surface-Enhanced Raman Scattering: Physics and Applications*, K. Kneipp, M. Moskovits, and H. Kneipp Eds. Berlin, Heidelberg: Springer Berlin Heidelberg, 2006, pp. 19-45.

[179]A. A. Ensafi, "Chapter 1 - An introduction to sensors and biosensors," in *Electrochemical Biosensors*, A. A. Ensafi Ed.: Elsevier, 2019, pp. 1-10.
[180]V. Perumal and U. Hashim, "Advances in biosensors: Principle, architecture and applications," *Journal of Applied Biomedicine,* vol. 12, no. 1, pp. 1-15, 2014/01/01/ 2014, doi: https://doi.org/10.1016/j.jab.2013.02.001.
[181]V. Naresh and N. Lee, "A Review on Biosensors and Recent Development of Nanostructured Materials-Enabled Biosensors," *Sensors,* vol. 21, no. 4, p. 1109, 2021, doi: 10.3390/s21041109.
[182]C. R. Lowe, "Overview of Biosensor and Bioarray Technologies," in *Handbook of Biosensors and Biochips*, 2007.
[183]M. Prosa *et al.*, "Nanostructured Organic/Hybrid Materials and Components in Miniaturized Optical and Chemical Sensors," *Nanomaterials*, vol. 10, no. 3*,* doi: 10.3390/nano10030480.
[184]B. Sepúlveda, P. C. Angelomé, L. M. Lechuga, and L. M. Liz-Marzán, "LSPR-based nanobiosensors," *Nano Today,* vol. 4, no. 3, pp. 244-251, 2009/06/01/ 2009, doi: https://doi.org/10.1016/j.nantod.2009.04.001.
[185]P. D. B. i. E. (PDBe), ed.
[186]J. Hammond, N. Bhalla, S. Rafiee, and P. Estrela, "Localized Surface Plasmon Resonance as a Biosensing Platform for Developing Countries," *Biosensors,* vol. 4, no. 2, pp. 172-188, 2014, doi: 10.3390/bios4020172.
[187]P. A. D. Gonçalves, T. Christensen, N. Rivera, A.-P. Jauho, N. A. Mortensen, and M. Soljačić, "Plasmon–emitter interactions at the nanoscale," *Nature Communications,* vol. 11, no. 1, p. 366, 2020/01/17 2020, doi: 10.1038/s41467-019-13820-z.
[188]P. K. Jain, K. S. Lee, I. H. El-Sayed, and M. A. El-Sayed, "Calculated Absorption and Scattering Properties of Gold Nanoparticles of Different Size, Shape, and Composition: Applications in Biological Imaging and Biomedicine," *The Journal of Physical Chemistry B,* vol. 110, no. 14, pp. 7238-7248, 2006, doi: 10.1021/jp057170o.

[189]R. V. Rebois, P. Schuck, and J. K. Northup, "[2] - Elucidating Kinetic and Thermodynamic Constants for Interaction of G Protein Subunits and Receptors by Surface Plasmon Resonance Spectroscopy," in *Methods in Enzymology*, vol. 344, R. Iyengar and J. D. Hildebrandt Eds.: Academic Press, 2002, pp. 15-42.
[190]S. Deng, P. Wang, and X. Yu, "Phase-Sensitive Surface Plasmon Resonance Sensors: Recent Progress and Future Prospects," *Sensors,* vol. 17, no. 12, p. 2819, 2017, doi: 10.3390/s17122819.
[191]B. Instrument, "SPR Sensitivity and Detection Limit," Technical Note 2010.
[192]J. Zhou, Y. Wang, and G.-J. Zhang, "State-of-the-art strategies of surface plasmon resonance biosensors in clinical analysis: A comprehensive review," *Coordination Chemistry Reviews,* vol. 520, p. 216149, 2024/12/01/ 2024, doi: https://doi.org/10.1016/j.ccr.2024.216149.
[193]B. T. Cunningham *et al.*, "Label-Free Assays on the BIND System," *SLAS Discovery,* vol. 9, no. 6, pp. 481-490, 2004, doi: 10.1177/1087057104267604.
[194]A. R. Ferhan, B. K. Yoon, W.-Y. Jeon, and N.-J. Cho, "Biologically interfaced nanoplasmonic sensors," *Nanoscale Advances,* vol. 2, no. 8, pp. 3103-3114, 2020, doi: 10.1039/d0na00279h.
[195]D. Wild, *The Immunoassay Handbook: Theory and Applications of Ligand Binding, ELISA and Related Techniques*. Elsevier Science, 2013.
[196]J. I. E. Ltd, "Ligand bound Streptavidin homotetramer showing each asymmetric unit binding to individual biotin molecules.," in *Image generated Molsoft ICM browser.*, ed. https://www.jacksonimmuno.com/technical/products/groups/streptavidin.
[197]W. Liu, S. K. Samanta, B. D. Smith, and L. Isaacs, "Synthetic mimics of biotin/(strept)avidin," *Chemical Society Reviews,* vol. 46, no. 9, pp. 2391-2403, 2017, doi: 10.1039/c7cs00011a.
[198]Biorender.com, ed.
[199]T. Sano, S. Vajda, G. O. Reznik, C. L. Smith, and C. R. Cantor, "Molecular Engineering of

Streptavidin^a," *Annals of the New York Academy of Sciences,* vol. 799, no. 1, pp. 383-390, 1996, doi: 10.1111/j.1749-6632.1996.tb33229.x.

[200] Claire, Apurba, Edward, and M. Howarth, "How the biotin–streptavidin interaction was made even stronger: investigation via crystallography and a chimaeric tetramer," *Biochemical Journal,* vol. 435, no. 1, pp. 55-63, 2011, doi: 10.1042/bj20101593.

[201] B. J. Mills, E. M. Moussa, and F. Jameel, "Chapter 1: Monoclonal Antibodies: Structure, Physicochemical Stability, and Protein Engineering," Springer International Publishing, 2020, pp. 3-26.

[202] D. A. Quinteros, J. M. Bermúdez, S. Ravetti, A. Cid, D. A. Allemandi, and S. D. Palma, "Chapter 25 - Therapeutic use of monoclonal antibodies: general aspects and challenges for drug delivery," in *Nanostructures for Drug Delivery*, E. Andronescu and A. M. Grumezescu Eds.: Elsevier, 2017, pp. 807-833.

[203] Y. Xiao and S. N. Isaacs, "Enzyme-linked immunosorbent assay (ELISA) and blocking with bovine serum albumin (BSA)—not all BSAs are alike," *Journal of Immunological Methods,* vol. 384, no. 1-2, pp. 148-151, 2012, doi: 10.1016/j.jim.2012.06.009.

[204] R. J. Leatherbarrow and P. R. Edwards, "Analysis of molecular recognition using optical biosensors," *Current Opinion in Chemical Biology,* vol. 3, no. 5, pp. 544-547, 1999/10/01/ 1999, doi: https://doi.org/10.1016/S1367-5931(99)00006-X.

[205] N. J. De Mol and M. J. E. Fischer, "Surface Plasmon Resonance: A General Introduction," Humana Press, 2010, pp. 1-14.

[206] B. T. Cunningham, "Label-free optical biosensors: An introduction," in *Label-Free Biosensors: Techniques and Applications*, M. A. Cooper Ed. Cambridge: Cambridge University Press, 2009, pp. 1-28.

[207] "OPENSPR," in *1-Channel operational manual V4.1.01*, January 18, 2018, p. 60.

[208] M. N. Polyanskiy, "Refractiveindex.info database of optical constants," *Scientific Data,* vol. 11, no. 1, 2024, doi: 10.1038/s41597-023-02898-2.

[209] *Thermo Scientific Avidin-Biotin Technical Handbook*. Thermo Scientific, 2009, p. 51.
[210] P. C. Weber, D. H. Ohlendorf, J. J. Wendoloski, and F. R. Salemme, "Structural Origins of High-Affinity Biotin Binding to Streptavidin," *Science,* vol. 243, no. 4887, pp. 85-88, 1989/01/06 1989, doi: 10.1126/science.2911722.
[211] E. Ayan *et al.*, "Cooperative allostery and structural dynamics of streptavidin at cryogenic- and ambient-temperature," *Communications Biology,* vol. 5, no. 1, p. 73, 2022/01/20 2022, doi: 10.1038/s42003-021-02903-7.
[212] M. A.-O. Sarter, "Cooperative Change in the Internal Dynamics of Streptavidin Caused by Biotin Binding," (in eng), no. 1520-5207 (Electronic).
[213] N. Michael Green, "[5] Avidin and streptavidin," in *Methods in Enzymology*, vol. 184, M. Wilchek and E. A. Bayer Eds.: Academic Press, 1990, pp. 51-67.
[214] J. M. Marangoni, S.-C. Wu, D. Fogen, S.-L. Wong, and K. K. S. Ng, "Engineering a disulfide-gated switch in streptavidin enables reversible binding without sacrificing binding affinity," *Scientific Reports,* vol. 10, no. 1, 2020, doi: 10.1038/s41598-020-69357-5.
[215] J. M. Abad, M. Pita, and V. M. Fernández, "Immobilization of Proteins on Gold Surfaces," (in eng), no. 1940-6029 (Electronic).
[216] S. P. Boulos *et al.*, "Nanoparticle–Protein Interactions: A Thermodynamic and Kinetic Study of the Adsorption of Bovine Serum Albumin to Gold Nanoparticle Surfaces," *Langmuir,* vol. 29, no. 48, pp. 14984-14996, 2013/12/03 2013, doi: 10.1021/la402920f.
[217] "Biotin-Streptavidin Sensors Kit Tech Guide V 4.0." [Online]. Available: www.nicoyalife.com
[218] R. L. Rich and D. G. Myszka, "A survey of the year 2002 commercial optical biosensor literature," *Journal of Molecular Recognition,* vol. 16, no. 6, pp. 351-382, 2003, doi: 10.1002/jmr.649.
[219] R. L. Rich and D. G. Myszka, "Survey of the year 2007 commercial optical biosensor literature," (in eng), no. 0952-3499 (Print).
[220] Z. C. Ui and Y. Wan, "18 - Biofouling in membrane separation systems," in *Surfaces and Interfaces for*

Biomaterials, P. Vadgama Ed.: Woodhead Publishing, 2005, pp. 493-542.

[221] Y. Xia and G. M. Whitesides, "Self-assembled Monolayer Films: Microcontact Printing," in *Encyclopedia of Materials: Science and Technology*, K. H. J. Buschow *et al.* Eds. Oxford: Elsevier, 2001, pp. 8309-8314.

[222] B. Yu *et al.*, "Diagnostic and Prognostic Value of Interleukin-6 in Emergency Department Sepsis Patients," *Infection and Drug Resistance,* vol. Volume 15, pp. 5557-5566, 2022, doi: 10.2147/idr.s384351.

[223] M. Cecconi, L. Evans, M. Levy, and A. Rhodes, "Sepsis and septic shock," *The Lancet,* vol. 392, no. 10141, pp. 75-87, 2018/07/07/ 2018, doi: https://doi.org/10.1016/S0140-6736(18)30696-2.

[224] K. A. Fitzgerald, L. A. J. O'Neill, A. J. H. Gearing, and R. E. Callard, "IL-6," in *The Cytokine FactsBook and Webfacts (Second Edition)*, K. A. Fitzgerald, L. A. J. O'Neill, A. J. H. Gearing, and R. E. Callard Eds. London: Academic Press, 2001, pp. 69-74.

[225] M. Hibi, M. Murakami, M. Saito, T. Hirano, T. Taga, and T. Kishimoto, "Molecular cloning and expression of an IL-6 signal transducer, gp130," *Cell,* vol. 63, no. 6, pp. 1149-1157, 1990/12/21/ 1990, doi: https://doi.org/10.1016/0092-8674(90)90411-7.

[226] S. Gupta *et al.*, "Chemically Modified DNA Aptamers Bind Interleukin-6 with High Affinity and Inhibit Signaling by Blocking Its Interaction with Interleukin-6 Receptor," *Journal of Biological Chemistry,* vol. 289, no. 12, pp. 8706-8719, 2014, doi: 10.1074/jbc.m113.532580.

[227] O. Weiergräber *et al.*, "Soluble Human Interleukin-6 Receptor," *European Journal of Biochemistry,* vol. 234, no. 2, pp. 661-669, 1995, doi: 10.1111/j.1432-1033.1995.661_b.x.

[228] D. G. Myszka, "Improving biosensor analysis," (in eng), no. 0952-3499 (Print).

[229] R. L. Rich and D. G. Myszka, "Survey of the year 2000 commercial optical biosensor literature," *Journal of Molecular Recognition,* vol. 14, no. 5, pp. 273-294, 2001/09/01 2001, doi: https://doi.org/10.1002/jmr.547.

[230]P. Schuck, "USE OF SURFACE PLASMON RESONANCE TO PROBE THE EQUILIBRIUM AND DYNAMIC ASPECTS OF INTERACTIONS BETWEEN BIOLOGICAL MACROMOLECULES1," *Annual Review of Biophysics,* vol. 26, no. Volume 26, 1997, pp. 541-566, 1997, doi: https://doi.org/10.1146/annurev.biophys.26.1.541.
[231]M. Hentschel, M. Schäferling, X. Duan, H. Giessen, and N. Liu, "Chiral plasmonics," *Science Advances,* vol. 3, no. 5, p. e1602735, 2017, doi: 10.1126/sciadv.1602735.
[232]R. Tullius *et al.*, ""“Superchiral” Spectroscopy: Detection of Protein Higher Order Hierarchical Structure with Chiral Plasmonic Nanostructures," *Journal of the American Chemical Society,* vol. 137, no. 26, pp. 8380-8383, 2015/07/08 2015, doi: 10.1021/jacs.5b04806.
[233]F. Cui, Y. Yue, Y. Zhang, Z. Zhang, and H. S. Zhou, "Advancing Biosensors with Machine Learning," *ACS Sensors,* vol. 5, no. 11, pp. 3346-3364, 2020/11/25 2020, doi: 10.1021/acssensors.0c01424.
[234]Y. Chen, Y. Wang, Y. Zhang, X. Wang, C. Zhang, and N. Cheng, "Intelligent Biosensors Promise Smarter Solutions in Food Safety 4.0," *Foods,* vol. 13, no. 2, p. 235, 2024, doi: 10.3390/foods13020235.
[235]Y. Wang, W. Jing, N. Tao, and H. Wang, "Probing Single-Molecule Binding Event by the Dynamic Counting and Mapping of Individual Nanoparticles," *ACS Sensors,* vol. 6, no. 2, pp. 523-529, 2021/02/26 2021, doi: 10.1021/acssensors.0c02184.
[236]K. R. Okholm, S. W. Nooteboom, V. Lamberti, S. Dey, P. Zijlstra, and D. S. Sutherland, "Kinetics and dynamics of single-molecule multivalent interactions revealed by plasmon-enhanced fluorescence," *bioRxiv,* p. 2023.12.08.570798, 2023, doi: 10.1101/2023.12.08.570798.
[237]J. S. Danial, Y. Aguib, and M. H. Yacoub, "Advanced fluorescence microscopy techniques for the life sciences," *Global Cardiology Science and Practice,* vol. 2016, no. 2, 2016, doi: 10.21542/gcsp.2016.16.
[238]S. M. Hickey *et al.*, "Fluorescence Microscopy—An Outline of Hardware, Biological Handling, and

Fluorophore Considerations," *Cells,* vol. 11, no. 1, p. 35, 2021, doi: 10.3390/cells11010035.
[239] Y. Jeong, Y.-M. Kook, K. Lee, and W.-G. Koh, "Metal enhanced fluorescence (MEF) for biosensors: General approaches and a review of recent developments," *Biosensors and Bioelectronics,* vol. 111, pp. 102-116, 2018/07/15/ 2018, doi: https://doi.org/10.1016/j.bios.2018.04.007.
[240] T. Ribeiro, C. Baleizão, and J. P. S. Farinha, "Artefact-free Evaluation of Metal Enhanced Fluorescence in Silica Coated Gold Nanoparticles," *Scientific Reports,* vol. 7, no. 1, 2017, doi: 10.1038/s41598-017-02678-0.
[241] M. A. Badshah, N. Y. Koh, A. W. Zia, N. Abbas, Z. Zahra, and M. W. Saleem, "Recent Developments in Plasmonic Nanostructures for Metal Enhanced Fluorescence-Based Biosensing," *Nanomaterials,* vol. 10, no. 9, p. 1749, 2020, doi: 10.3390/nano10091749.
[242] J.-F. Li, C.-Y. Li, and R. F. Aroca, "Plasmon-enhanced fluorescence spectroscopy," *Chemical Society Reviews,* vol. 46, no. 13, pp. 3962-3979, 2017, doi: 10.1039/c7cs00169j.
[243] S. Wallace *et al.*, "Multiplexed Biosensing of Proteins and Virions with Disposable Plasmonic Assays," *ACS Sensors,* vol. 8, no. 9, pp. 3338-3348, 2023/09/22 2023, doi: 10.1021/acssensors.2c02238.
[244] O. Nur and M. Willander, "Chapter 3 - Conventional nanofabrication methods," in *Low Temperature Chemical Nanofabrication*, O. Nur and M. Willander Eds.: William Andrew Publishing, 2020, pp. 49-86.
[245] C. Shawn, Y. Makiuchi, and C. Che, "High-energy Electron Beam Lithography for Nanoscale Fabrication," InTech, 2010.
[246] S. Franssila and L. Sainiemi, "Reactive Ion Etching (RIE)," in *Encyclopedia of Microfluidics and Nanofluidics*, D. Li Ed. Boston, MA: Springer US, 2008, pp. 1772-1781.
[247] G. Kreindl, T. Glinsner, R. Miller, D. Treiblmayr, and R. Födisch, "High accuracy UV-nanoimprint lithography step-and-repeat master stamp fabrication for wafer level camera application," *Journal of Vacuum Science &*

Technology B, vol. 28, no. 6, pp. C6M57-C6M62, 2010, doi: 10.1116/1.3518914.
[248] G. K. Thomas Glinsner, and Michael Kast., "Nanoimprint Lithography," *Optik & Photonik,* vol. vol. 5, no. 2, 2011, doi: doi:10.1002/opph.201190097.
[249] J. Gim and L.-S. Turng, "A review of current advancements in high surface quality injection molding: Measurement, influencing factors, prediction, and control," *Polymer Testing,* vol. 115, p. 107718, 2022/11/01/ 2022, doi: https://doi.org/10.1016/j.polymertesting.2022.107718.
[250] C. Peixoto *et al.*, "Injection molding of high-precision optical lenses: A review," *Precision Engineering,* vol. 76, pp. 29-51, 2022/07/01/ 2022, doi: https://doi.org/10.1016/j.precisioneng.2022.02.002.
[251] M. R. Khosravani, S. Nasiri, and T. Reinicke, "Intelligent knowledge-based system to improve injection molding process," *Journal of Industrial Information Integration,* vol. 25, p. 100275, 2022/01/01/ 2022, doi: https://doi.org/10.1016/j.jii.2021.100275.
[252] S. Ebnesajjad, "10 - Injection Molding," in *Fluoroplastics (Second Edition)*, S. Ebnesajjad Ed. Oxford: William Andrew Publishing, 2015, pp. 236-281.

The End.